

# Large-Eddy simulation of nocturnal radiation fog: Advances in microphysical representation and process-level evaluation

Von der Fakultät für Mathematik und Physik  
der Gottfried Wilhelm Leibniz Universität Hannover

zur Erlangung des akademischen Grades  
Doktor der Naturwissenschaften  
Dr. rer. nat.

genehmigte Dissertation von

**M.Sc. Johannes Schwenkel**

2023

Referent: Prof. Dr. Björn Maronga (Leibniz Universität Hannover)  
1. Korreferent: Prof. Dr. Siegfried Raasch (Leibniz Universität Hannover)  
2. Korreferent: Prof. Dr. Gert-Jan Steeneveld (Wageningen University & Research)  
Tag der Promotion: 03. Mai 2023

# Abstract

Fog is characterized by the presence of liquid or solid water particles in the vicinity of Earth's surface, that leads to a reduction in visibility to less than 1 km. This reduced visibility poses a significant threat to humans, especially in transportation. However, numerical weather prediction (NWP) models still frequently fail to predict fog correctly. This can be attributed to small-scale processes, which interact with one another on different scales. The research presented in this thesis consists of four research articles and aims to represent, understand, and quantify the significant processes during the life cycle of fog using highly resolved large-eddy simulation (LES).

The first study investigates the effect of different microphysical parametrization on simulating fog. As found by other research, the number of cloud droplets is a crucial parameter determining the fog depth and the time of fog dissipation, which is, however, a fixed parameter in many numerical models. After major model development to include a prognostic equation of the cloud droplet number concentration and schemes for activation and diffusional growth, the error made by commonly used microphysical parameterizations (cloud bulk models) for simulating fog was evaluated. It was found that simulated fog reacts sensitively to the method of calculating supersaturation, which determines the number of activated droplets.

However, bulk cloud models like the one used in the first study are not suitable to remedy their immanent limitations, such as prescribing the shape of the cloud droplet size distribution (DSD) rather than simulating it. In the second study, an advanced method in cloud modeling (a so-called particle-based method) was applied for the first time to simulate fog. It was found that the shape of DSD in fog undergoes a temporal development. Moreover, compared to the particle-based microphysics, the bulk cloud model tends to overestimate the droplet number concentration but underrate droplet sedimentation.

The subject of the third study was a model intercomparison of LES and single-column models (SCMs) for a radiation fog event. The study revealed significant differences between the SCMs (which are based on NWP models), but the LES models also showed a non-uniform picture. The representation of microphysics has been identified as the primary source of uncertainty in the simulation of fog, but with surface-layer fluxes also contributing to the uncertainty.

The final study in this thesis discusses the influence of nocturnal fog on the evolution of the daytime boundary layer. The simulation results indicate that failing to resolve nocturnal fog leads to a faster boundary layer development, i.e., a higher temperature within the boundary layer and a higher inversion height during daytime.

**Keywords:** radiation fog, large-eddy simulation, cloud microphysics





# Contents

<b>List of Abbreviations</b>	<b>7</b>
<b>1 Introduction</b>	<b>9</b>
1.1 Structure of the foggy atmospheric boundary layer . . . . .	10
1.1.1 Appearance of fog and fog types . . . . .	10
1.1.2 Typical life cycle of radiation fog within the diurnal cycle . . . . .	10
1.1.3 Small-scale processes during fog . . . . .	12
1.2 State of the Art: Numerical modeling of fog . . . . .	17
1.2.1 Representing fog with a bulk cloud model . . . . .	18
1.2.2 Representing fog with a Lagrangian Cloud Model . . . . .	21
1.2.3 Model intercomparison . . . . .	23
1.2.4 Influence of nocturnal fog on daytime ABL . . . . .	24
1.3 Structure of this thesis . . . . .	26
<b>2 Methods</b>	<b>27</b>
2.1 Basics of the PALM Model system . . . . .	29
2.1.1 Declaration of Contributions . . . . .	29
2.1.2 Model Overview Article . . . . .	29
2.2 Bulk cloud model . . . . .	39
2.2.1 Activation . . . . .	40
2.2.2 Diffusional growth . . . . .	43
2.2.3 Sedimentation . . . . .	46
2.2.4 Collision and coalescence . . . . .	46
2.3 Lagrangian cloud model . . . . .	47
2.3.1 Boundary conditions and superdroplet initialization . . . . .	48
2.3.2 Transportation . . . . .	48
2.3.3 Activation and diffusional growth . . . . .	51
2.4 Land-surface model . . . . .	53
2.5 Radiation model . . . . .	54
<b>3 Impact of microphysical parameterizations on fog modeling</b>	<b>57</b>
3.1 Declaration of Contributions . . . . .	57
3.2 Research Article . . . . .	57
<b>4 Representation of fog with particle-based microphysics</b>	<b>75</b>
4.1 Declaration of Contributions . . . . .	75
4.2 Research Article . . . . .	75

<b>5</b>	<b>LES and SCM intercomparison of radiation fog</b>	<b>95</b>
5.1	Declaration of Contributions . . . . .	95
5.2	Research Article . . . . .	95
<b>6</b>	<b>Effect of nocturnal fog on daytime ABL development</b>	<b>111</b>
6.1	Declaration of Contributions . . . . .	111
6.2	Research Article . . . . .	111
<b>7</b>	<b>Concluding Remarks</b>	<b>131</b>
7.1	Summary . . . . .	131
7.2	Outlook . . . . .	133
	<b>Acknowledgements</b>	<b>137</b>
	<b>Bibliography</b>	<b>139</b>
	<b>Curriculum Vitae</b>	<b>149</b>

## List of Abbreviations

ABL	Atmospheric boundary layer
CBL	Convective boundary layer
CFD	Computational fluid dynamics
DSD	Drop size distribution
LES	Large-eddy simulation
LCM	Lagrangian cloud model
LPM	Lagrangian particle model
NBL	Nocturnal boundary layer
NWP	Numerical weather prediction
SBL	Stable boundary layer
SCM	Single column model
SGS	Sub-grid scale
TKE	Turbulent kinetic energy



# 1 Introduction

At first glance, fog appears as a calm meteorological phenomenon that immerses the landscape in a mystical veil (Fig. 1.1). In simple terms, fog is nothing but a cloud in the vicinity of Earth's surface. The presence of fog, however, leads to a significant reduction in visibility (to less than 1 km by definition) at ground levels. While moving through a fog layer, its mystical appearance turns into a safety hazard due to the reduced visibility. Especially in human transportation, whether by air, sea, or road, fog has caused significant damage throughout history. Moreover, economic losses due to fog (in particular by aviation delays) are in the same order of magnitude as for other extreme weather events, such as tornadoes or hurricanes (Gultepe et al., 2007).

Despite the resulting need for accurate fog forecasting, representation of fog is still poor in numerical weather prediction (NWP) models. This is mostly due to a multitude of complex and small-scale processes which are unresolved on the NWP-scale. Reducing this lack in representation with high-resolved large-eddy simulations (LES) and advanced model techniques, as well as assessing the impact of physical processes individually, are the objectives of this thesis. The remainder of this chapter will outline the general structure and life cycle of a typical atmospheric boundary layer with nocturnal radiation fog (Sec. 1.1), outline the research progress in modeling fog events, and motivate the specific issues addressed in this thesis (Sec. 1.2).



**Figure 1.1:** Rural landscape covered with shallow fog.

## 1.1 Structure of the foggy atmospheric boundary layer

### 1.1.1 Appearance of fog and fog types

According to meteorological institutions, fog is defined as a collection of suspended water droplets (or ice particles) close to Earth's surface that reduces people's visibility to below 1 km (e.g., American Meteorological Society, 2012). Fog can form wherever ground-level temperature reaches the dewpoint temperature. This can be caused by a wide variety of processes, which typically classify the fog types. Some of which are advection fog, mixing (or steam) fog, upslope fog, marine (or coastal) fog, stratus-lowering fog, and frontal fog, to mention some of the well-described fog types (Gultepe et al., 2007). In literature, however, many more types and subtypes of fog are defined, so this list is by no means exhaustive. The research in this thesis will solely focus on warm nocturnal radiation fog, which is the most common continental fog type in Europe and probably the most important type in terms of its socio-economic impact (Izett et al., 2019). Thus, for simplicity's sake, "fog" refers to warm (i.e., free of ice particles) nocturnal radiation fog, if not explicitly stated otherwise.

**Radiation fog** can form if longwave radiation emission from the surface outweighs the incoming solar radiation. Usually, this happens during the night and early morning hours, when incoming solar radiation is mostly absent. As a result, the radiation budget at the surface becomes negative, causing the surface to cool down. When the surface is colder than the air near the surface, the surface sensible heat flux cools the air. If the air temperature reaches the dewpoint temperature (i.e., the air becomes saturated with respect to water vapor), condensation of water vapor takes place. The formation of liquid water droplets marks the fog onset (in physical terms; by definition, fog onset is reached if the visibility decrease below 1 km).

In general, conditions that favor fog formation are clear skies in association with an anti-cyclone (Gultepe et al., 2007). Cloudless skies lead to a stronger surface cooling as compared to overcast conditions due to the lack of counter radiation. In mid-latitudes, the maximum in relative occurrence of fog is during the winter and transition months (e.g., Izett et al., 2019).

### 1.1.2 Typical life cycle of radiation fog within the diurnal cycle

Fog is a phenomenon of the atmospheric boundary layer (ABL). Thus, fog formation and its life cycle are strongly coupled to ABL processes. In addition, fog itself can influence the structure of the ABL.

Briefly summarized, the ABL is defined as the lower part of the troposphere. Hence, the ABL is significantly influenced by surface processes. Atmospheric flow is decelerated in the ABL due to its frictional drag, and as a consequence becomes turbulent in most cases. Moreover, Earth's surface acts as a source of heating or cooling, depending on circumstances. Atmospheric moisture is also significantly controlled by the surface: evapotranspiration from vegetation and the surface serves as the main source of atmospheric moisture. Conversely,

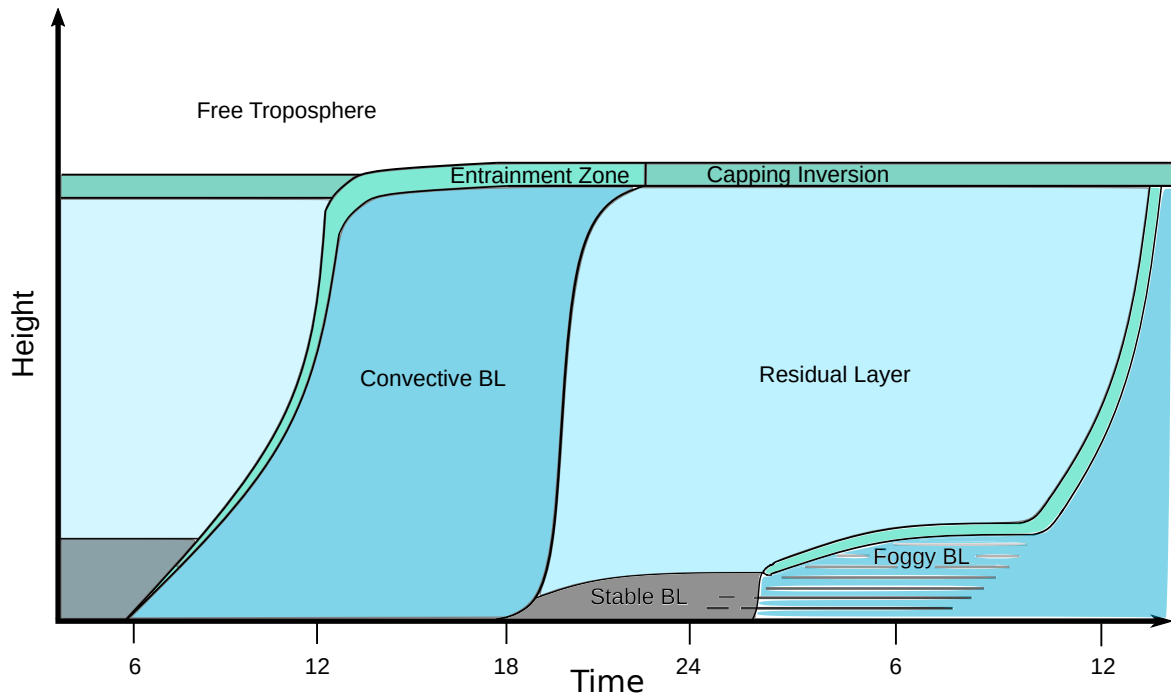


**Figure 1.2:** Sketch of the ABL development during a diurnal cycle including the formation of nocturnal radiation fog (based on Fig. 1.7 from Stull, 1988).

soil is a sink for moisture when liquid water in the form of rain or sedimentation of droplets deposits and runs off or seeps away.

The most common distinction of the different types of ABL involves three different atmospheric flow regimes: the convective boundary layer (CBL), the stable boundary layer (SBL), and the neutral or shear-driven boundary layer. The latter is characterized by constant potential temperatures throughout the ABL caused by negligible surface heating rates. This is usually observed during overcast conditions and at high background winds. However, within this thesis the focus are the CBL and SBL, both of which occur during a common diurnal cycle over land-surfaces in high-pressure regions. The temporal evolution of the different ABL regimes during the diurnal cycle and the formation of nocturnal fog is illustrated in Fig. 1.2.

The CBL develops during daytime when the sun heats the surface (Fig. 1.2). The surface becomes warmer than the air temperature, generating rising thermals (due to buoyancy force). This in turn leads to a mixed layer, where ABL properties (e.g., temperature, humidity, and pollutants) are constant with height. The CBL is capped by a temperature inversion, followed by the stably stratified free atmosphere. During daytime, the CBL grows mostly by encroachment, i.e., the warming of the mixed layer by the positive sensible surface heat flux. However, entrainment, i.e., the turbulent mixing of warmer air from the free atmosphere (or residual layer) into the CBL, also leads to ABL growth. These mixing processes are caused by wind shear generating turbulence and rising thermals penetrating the entrainment zone.

During evening transition (shortly before sunset) the CBL turns into a SBL. As incoming solar radiation weakens, surface warming comes to a halt. Surface radiative cooling and the

resulting negative surface heat flux causes a reduction in air temperature at the lowermost atmospheric levels. This stable stratification suppresses turbulence, and the flow may become laminar or intermittently turbulent for very weak wind conditions. For moderate wind velocities, however, turbulence is generated by wind shear within the SBL. In contrast to the CBL, the SBL has a much smaller vertical extent in the order of 10 m  $\sim$  100 m. Above the SBL, a residual layer remaining from the previous day's CBL is found. It is characterized by weak sporadic turbulence and a neutrally stratified temperature gradient. During the night, the near-surface temperature in the SBL continues to decrease due to longwave radiative cooling. If the temperature reaches the dewpoint temperature, fog can form in an aerosol-laden environment. In the formation stage, the fog is shallow and well-stratified. Consequently, effective cooling from the surface continues. Eventually, if the liquid water content grows sufficiently large, the fog becomes optically thick. Now, instead of the surface, the fog top experiences a radiative flux divergence, which is the differential increase of radiative flux leaving a volume compared to that entering it. As a consequence, radiative cooling at the fog top generates cold thermals that sink (top-down convection) and lead to a well-mixed uniform fog layer. The further fog development (i.e., the vertical growth rate) depends, among other factors such as non-local processes, on the interplay of the thermodynamic profiles in the residual layer, the strength of vertical mixing, and cloud microphysics.

A well-mixed fog such as this can extend for some several hundred meters vertically and has more in common with stratocumulus clouds than with a shallow, stably stratified mist layer (Stull, 1988). Deep fog can persist well into the morning, as much of the incoming solar radiation is reflected due to its high albedo. Especially during winter or in regions at high-latitudes, fog can persist for several days. After sunrise, the incoming solar radiation warms the interior of the fog, while the fog top is still cooled by radiative divergence. This may cause the fog to be lifted off the ground, causing it to possibly be reclassified as stratocumulus. Depending on the strength of the surface sensible heat flux and the thermodynamic profile of the ABL, the fog or stratocumulus may completely dissipate.

### 1.1.3 Small-scale processes during fog

So far, the conditions conducive to fog formation as well as a typical fog life cycle have been outlined. In this section, the complex processes during the presence of fog will be discussed, focusing on on microphysics, radiation, turbulence, and surface interactions. A sketch of these processes is shown in Fig. 1.3.

**Microphysics** in the atmosphere encompasses small-scale processes that govern the formation and evolution of cloud and precipitation particles, such as nucleation, condensation growth through vapor diffusion, collision and coalescence, and freezing and melting.

In the atmosphere, condensation of water vapor is contingent on the presence of aerosols. Homogeneous nucleation (i.e., condensation of water vapor without condensation nuclei) requires a relative humidity of several hundred percent, which does not occur in the ABL. However, the formation of liquid water in the atmosphere is observed at low supersaturations,



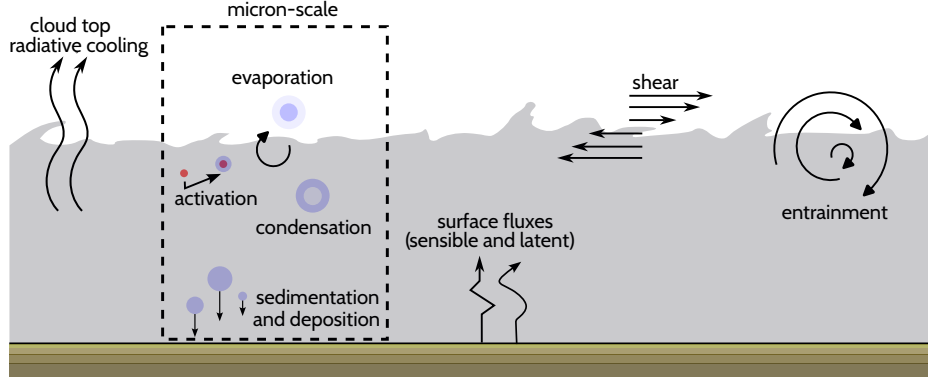


**Figure 1.3:** Sketch of relevant processes within fog.

i.e., at relative humidity of about 100%. Supersaturation  $S$  denotes the relative supersaturation above a plane water surface (further explanation follows) and is the ratio of water vapor mixing ratio  $q_v$  and saturation water mixing ratio  $q_s$ :

$$S = \frac{q_v - q_s}{q_s}. \quad (1.1)$$

The transition of aerosols into cloud droplets by means of diffusion of water molecules is called activation. Indeed, not all aerosols can act as so-called cloud condensation nuclei (CCNs). An aerosol's ability to be activated depends on its physiochemical properties as well as on the curvature of the resulting solution droplet. More precisely, the particle's equilibrium supersaturation (supersaturation at which the particle neither grows nor shrinks by condensation or evaporation, respectively) is determined by its properties and changes for different droplet solution radii. Two physical processes that have an opposite effect are responsible for this. On the one hand, the curvature effect increases the equilibrium supersaturation as the droplet radius decreases. On the other hand, the solution effect decreases the equilibrium supersaturation as the droplet radius decreases. In physical terms, the solution effect can be attributed to the presence of the dissolved aerosol, which causes a reduced concentration of water molecules. Consequently, the flow of water molecules from the solution droplet to the surrounding air decreases for more concentrated solutions (small droplets), allowing the presence of wetted aerosols (also known as haze particles). The underlying physics of the curvature effect can be understood from a molecular point of view: A strong curvature reduces the strength of inter-molecular bonds, as the number of neighboring water molecules is smaller compared to a plane surface.

Combining curvature and solution effects results in the so-called Köhler curve (Köhler, 1936), which describes the course of the equilibrium saturation  $S_{\text{eq}}$  on the droplet radius  $r$ :

$$S_{\text{eq}} = \exp \left( \frac{A}{r} - \frac{B}{r^3 - r_s^3} \right) - 1 \quad (1.2)$$

where  $r_s$  is the dry aerosol radius. The effect of the curvature is described by the first term of Eq. 1.2, where  $A = 2\sigma/(\rho_l R_v T)$ . Here,  $\sigma$  being the surface tension,  $\rho_l$  the liquid water mass density,  $R_v$  the specific gas constant of water vapor, and  $T$  the absolute temperature. The second term, where  $B = r_s^3 i \Phi \rho_s M_l / (\rho_l M_s)$ , considers the solution effect and includes physiochemical information about the aerosol. The number of atoms or molecules that dissolves in the droplet is given by the van't Hoff factor  $i$ . Moreover, the molar osmotic coefficient  $\Phi$  characterizes the deviation of a solute from ideal behavior. The mass density of the aerosol is termed  $\rho_s$ , while  $M_l$  and  $M_s$  are the molar masses of water and aerosol, respectively. The physics of the typical course of the Köhler curve are found in Earth's atmosphere. For very small radii, the solution effect is dominant, allowing for haze particles to exist below a relative humidity of 100%. For slightly larger radii, the curvature effect becomes more relevant and raises  $S_{\text{eq}}$  above a relative humidity of 100%. Consequently, slight supersaturations are required for the formation of cloud droplets. For even larger radii of more than 1-2  $\mu\text{m}$ , equilibrium saturation of the solution droplets becomes identical to that of a plane water surface (100%), rendering the solution and curvature effects negligible. As a consequence of both effects, solution and curvature, a maximum equilibrium supersaturation emerges. The so-called critical supersaturation is yielded by

$$S_{\text{crit}} = \sqrt{\frac{4A^3}{27B}}, \quad (1.3)$$

and reached at the critical radius, which in turn is calculated from

$$r_{\text{crit}} = \sqrt{\frac{3B}{A}}. \quad (1.4)$$

If the ambient air exceeds the critical supersaturation a wetted aerosol is able to grow beyond the critical radius and then becomes categorized as a cloud droplet. Hence, activation marks the onset of unhindered cloud droplet growth. Besides its microphysical impact on the individual development of a particle, activation (i.e., the process itself, the ambient supersaturation, and the properties of the aerosol distribution) essentially determines the number of cloud droplets and therefore also the size of droplets. As such, the microphysical processes outlined above have major implications concerning macroscopic cloud characteristics, such as the production of precipitation or optical properties.

Although activation describes whether cloud droplet growth can occur, the Köhler curve cannot be used to derive the time-dependent growth of a cloud droplet. Based on Fick's laws of diffusion (Fick, 1855), the growth ( $S > S_{\text{eq}}$ ) or shrinking ( $S < S_{\text{eq}}$ ) of a droplet can be calculated by

$$r \frac{dr}{dt} = \frac{S - S_{\text{eq}}}{F_k + F_D}, \quad (1.5)$$

with the coefficients  $F_D = \rho_l R_v T / (D e_s)$  and  $F_k = (L_v / (R_v T) - 1) L_v \rho_l / (kT)$ . The coefficient  $F_D$  describes the effect of diffusion of water molecules, where  $D$  is the molecular diffusion coefficient, and  $e_s$  is the saturation water vapor pressure. The process of thermal conduction

is included in  $F_k$ , with  $L_v$  being the latent heat of evaporation, and  $k$  the thermal conductivity of air.

Equation 1.5 can be applied for condensation and evaporation of aerosols and cloud droplets, and is the strongest physical mechanism for how droplets with small radii grow. Different approaches of transferring Eq. 1.5 into numerical models have been developed and will be presented in the next section (Sec. 1.2.1).

Beyond droplet growth, the motion of droplets significantly alters cloud development. In general, the motion of small droplets in a turbulent fluid can be approximated using Stokes drag force (Shaw, 2003). As sufficiently small droplets have short relaxation times  $\mathcal{O}(10^{-2}\text{s})$  (e.g., Mellado, 2017), it can be assumed that their horizontal velocity is identical to that of the surrounding flow. However, due to their inertia, droplets experience a vertical acceleration which is balanced by the drag of the surrounding fluid. Therefore, the droplet velocity vector  $U$  is given by

$$U = v + \tau_d g - \tau_d \frac{dv}{dt} + \mathcal{O}(\tau_d^2), \quad (1.6)$$

with  $v$  denoting the velocity vector of the air and  $g$  the gravitational acceleration. The droplet relaxation time is proportional to its radius squared and its defined as  $\tau_d^{-1} = 9\nu\rho_a/(2r^2\rho_l)$ , where  $\nu$  is the kinematic viscosity of the air and  $\rho_a$  is the density of dry air. For larger droplets ( $r \geq 30\mu\text{m}$ ) the relaxation time must be adjusted. However, as in fogs the radii of the droplets are small, Eq. 1.6 remains valid. The sedimentation velocity is represented by the second term on the right-hand side of Eq. 1.6. Droplets with typical radii observed in fogs obtain sedimentation velocities of  $3\text{--}18\text{ mm s}^{-1}$ . These velocities are small compared to those of rain droplets, yet due to missing updrafts and the long-term nature of fog, they remain sufficient to effectively create a downward liquid water flux.

In addition to diffusional growth droplets, droplets also grow by collision and coalescence. The combination of both is also called coagulation. The strength of coagulation increases proportionally to the fourth power of the radius. In contrast to convective clouds, where coagulation is a crucial mechanism for the growth of droplets and responsible for the generation of precipitation, it is of secondary importance within fog, where droplets remain relatively small (Bott et al., 1990; Gultepe et al., 2007; Boutle et al., 2018). For this reason, the presentation of this process is omitted in this work. The interested reader is referred to Pruppacher et al. (1998).

Aerosol-cloud interactions are not limited to the unilateral influence of aerosols on droplet formation. Once liquid has formed, it acts as the major sink for aerosols due to scavenging processes. There are two common mechanisms for in-cloud aerosol removal: nucleation and impaction scavenging (e.g., Pruppacher et al., 1998). As droplets form on aerosols, nucleation scavenging describes the reduction of the aerosol concentration due to activation. Impaction scavenging describes the collision and coalescence of a droplet with an aerosol. In-cloud scavenging in combination with sedimentation and wet deposition removes aerosol from the atmosphere. This in turn affects cloud and fog development as the number of aerosols which

can act as a CCN is reduced. While both nucleation and impaction scavenging are relevant, Flossmann et al. (1985) showed nucleation scavenging to be the dominant process. Especially in the presence of small droplets and the absence of precipitation, nucleation scavenging outweighs impaction scavenging.

**Radiation** As outlined previously, cloud top radiative cooling plays an important role in the development of nocturnal radiation fog. While the net longwave radiative flux inside a deep fog is close to zero as the liquid water acts as a black body on the infrared and upward and downward fluxes compensate each other, the diminishing downward flux on the fog top leads to a strong radiative flux divergence. This in turn causes an effective cooling by the cloud top. Thus, for an optical thick fog layer, cloud top cooling can be approximated as

$$\left(\frac{\partial T}{\partial t}\right)_{\text{Rad}} = \frac{1}{\rho_a c_p} \kappa \rho_a q_c F_0 \exp(-\kappa \text{LWP}), \quad (1.7)$$

where  $c_p$  is the heat capacity of dry air and  $q_c$  the cloud water mixing ratio (Larson et al., 2007). Assuming that the cloud top is not heated by the cloud base,  $F_0$  represents the net radiative flux at the cloud top, which can be calculated using the Stefan-Boltzmann law. The factor  $\kappa$  represents the absorptivity of the cloud and can be approximated with  $\kappa = r_e^{-1}$ , where  $r_e$  is the effective radius of the cloud droplet size distribution (DSD). The cloud drop effective radius is the weighted mean of the DSD and reflects the area weighted radius. The liquid water path, i.e., the vertically integrated amount of liquid, is denoted with LWP. Hence, the strength of cooling depends on the microphysical properties of the fog layer. While for stratocumulus and fog cloud top cooling is a major source for supersaturation and the generation of turbulence which drives entrainment (Mellado, 2017), radiative cooling and microphysics affecting each other non-linearly, exacerbating an analytic solution. For typical deep fog layers, cloud top cooling rates of  $4\text{-}6 \text{ K h}^{-1}$  are observed, leading to strong destabilization of the cloud layer.

A characteristic of fog is that it limits the visibility of humans. In general, the visibility (*vis*) which has the unit meter can be calculated using the Koschmieder's law (Koschmieder, 1924):

$$vis = \frac{1}{\beta_{\text{ext}}} \ln\left(\frac{1}{\epsilon}\right), \quad (1.8)$$

where  $\beta_{\text{ext}}$  is the horizontal extinction coefficient and  $\epsilon$  the brightness contrast threshold of the human eye. However, Koschmieder's law assumes a uniform atmosphere with constant  $\beta_{\text{ext}}$ , which is not valid in the presence of fog. Scattering and absorption of light on swollen aerosol particles and cloud droplets have the ability to decrease the visibility by approximately two orders of magnitude compared to clear-sky conditions. Consequently, Eq. 1.9 must be modified to account for the influence of liquid water. Based on observations, numerous approximations for the visibility within fog are found in literature. One of the most common

parameterizations has been derived by Gultepe et al. (2006)

$$vis = \frac{1002}{(n_c \rho_a q_l)^{0.6473}}, \quad (1.9)$$

where  $n_c$  is the cloud droplet number concentration and  $q_l$  is the liquid water mixing ratio. Note, Eq. 1.9 has been adapted to be used with SI units.

**Turbulent mixing and surface interactions** In contrast to other cloud types, the cloud base of fog is in direct physical contact with the surface. This leads to the outstanding importance of surface properties on the formation and evolution of fog (Jiusto, 1981), particularly turbulent fluxes of latent heat and sensible heat affecting fog development. Moreover, the surface is a source of momentum drag creating near-surface turbulence. The strength of the drag depends on the roughness length, which is a quantity describing the roughness of the surface (e.g., modified by vegetation, surface type, and canopy).

Surface heterogeneities (e.g., different surface types or orography) are able to modify the thermodynamic state of the ABL as well as induce secondary circulations. Subsequently, heterogeneities affect the fog layer, as found by Bergot (2016), who investigated the horizontal structure of a fog layer.

Via droplet interception, the surface (and its vegetation, especially by trees; Mazoyer et al., 2017) also has a direct influence on the microphysics. While enhancing the deposition rate, the canopy can be a sink for the fog lifetime, as it deprives liquid from the fog.

The effect of turbulence and its impact due to vertical mixing on fog is controversially discussed in literature (Roach, 1976; Duynkerke, 1999; Price, 2011; Maronga and Bosveld, 2017; Wainwright and Richter, 2021). On the one hand, some researchers argued that for fog formation turbulence is obstructive as it will preferentially cause saturation on the surface leading to dewfall (e.g., Price et al., 2018). This, however, will lower the near-surface humidity, preventing fog formation. On the other hand, observations and numerical models demonstrated that a certain amount of vertical mixing also can cause an effective saturation in the lowermost atmospheric levels and thus favoring fog formation (Gulpepe et al., 2007).

In general, the role of vertical mixing is complex and its feedback on fog often non-linear. If vertical mixing facilitates or impedes fog development, strengthening, and dissipation strongly depends on the atmospheric conditions (i.e., the thermodynamic profile of the atmosphere aloft). In case of a strong inversion layer at a relatively low altitude, entrainment of warm and dry air into the fog layer will cause in erosion of the fog by turbulent mixing. A deep residual layer that is close to saturation above the fog layer might strengthen the fog with increased vertical mixing.

## 1.2 State of the Art: Numerical modeling of fog

The research in atmospheric science has often been divided into the fields of theory, observations, and numerical modeling. While the first two of them have been used for more than a century, numerical modeling has become increasingly popular in the era of modern com-

puters. Frequently, atmospheric issues involve too many processes and scales to find analytic solutions. Although crucial for atmospheric science, observations often have limitations, either in the limited scope of their coverage or the accuracy of the process-level data they provide.

For the research on the physics of fog, high-resolved numerical models (e.g., LES) are powerful tools. In such models, the small-scale processes presented previously are translated into a complex system of equations, that are solved numerically. However, numerical models do not inevitably project the reality. Usually the choice of physical processes which have been included, neglected, or simplified have an impact on the model results. Moreover, even an ideal model that includes all processes accurately, would suffer from the numerical methods and their immanent limitations solving them (Stevens et al., 2001). Nonetheless, numerical models have already been shown to be able to illustrate a valuable image, allowing investigation of the process-level (which is impossible by observations) and ultimately improving weather forecasts.

In this study, an LES model is used to investigate the physics of fog. The major feature of LES is that it resolves all relevant turbulent structures and parameterizes only small-scale turbulence. The latter are more universal in nature compared to the energy containing eddies and located within the inertial subrange, which allows application of parametrizations based on the Kolmogorov theory.

For fog, in particular, an accurate representation of the interactions of turbulence, radiation, microphysics, and atmosphere-surface interplay on small spatial and temporal scales is crucial (e.g., Steeneveld et al., 2015). Even though the simulation of the SBL with weak turbulence (which is where fog typically forms) is a challenging task (Beare et al., 2006), LES has been proven as a convenient tool to study fog.

More than 20 years ago, Nakanishi (2000) successfully applied an LES model for the first time to investigate nocturnal radiation fog. He showed that his LES results could reasonably represent the evolution of fog compared to observations. Further, he claimed that the life cycle of fog can be divided into three stages: formation, strengthening, and dissipation. Nakanishi (2000) showed, that these stages are directly linked to the evolution of turbulent kinetic energy. In the recent years, additional studies of radiation fog with LES models have been published (among others Porson et al., 2011; Bergot, 2013, 2016; Maalick et al., 2016; Maronga and Bosveld, 2017; Boutle et al., 2018; Wærsted et al., 2019; Wainwright and Richter, 2021). Because a summary of all study results would go beyond the scope of this thesis, selected results (motivating the research question addressed in this thesis) are presented in the following.

### **1.2.1 Representing fog with a bulk cloud model**

The importance of microphysics processes on the life cycle of radiation fog has been discussed for several years (Pilié et al., 1975; Roach et al., 1976; Bott et al., 1990). Recently, numerous studies such as those of Stolaki et al. (2015); Maalick et al. (2016); Boutle et al. (2018); Poku et al. (2021) focused on aerosol-fog interactions with single-column models (SCMs)

or LES. However, all the cited studies have in common that they use a bulk approach for representing cloud microphysics. Bulk cloud models are characterized by the fact that the DSD is not explicitly represented, but parameterized by means of functions (exponential, gamma, or lognormal). By defining different species (such as cloud droplets, rain droplets, and possibly ice crystals, etc.) a further splitting of the DSD is made, reducing the radius-space where the function must fit. For each species, the temporal change of mass (one-moment scheme), or additionally number concentration (two-moment scheme) is calculated. These calculations are based on analytic solutions or parametrizations derived from spectral-bin models (the interested reader is referred to e.g., Khain et al., 2000; Grabowski et al., 2019). Bulk cloud models have been successfully applied for decades but are limited by their inherent assumptions made (Grabowski et al., 2019; Morrison et al., 2020).

There are different methods to consider for activation and diffusional growth in LES models using bulk parametrization for clouds. Considering supersaturations explicitly with the purpose to drive activation, condensation and evaporation would require a further restriction in the model time step. For the sake of numerical stability, if supersaturation depletion and production is resolved, the model time step must be smaller than the phase relaxation timescale

$$\Delta t < \Delta t_{\text{phase}} = 2\tau_{\text{phase}} \approx 2(4\pi DN\bar{r})^{-1}, \quad (1.10)$$

where  $N$  is the number of droplets, and  $\bar{r}$  is the arithmetic mean droplet radius (Árnason and Brown, 1971). For typical values, this results in  $\tau_{\text{phase}} \sim 0.1 - 10$  s (Grabowski and Wang, 2013). To prevent this restriction, and what has been historically sufficient for common temporal resolutions ( $\Delta t \geq 10$  s), is in numerical models the most simple approach and has been widely applied, the so-called saturation-adjustment scheme (Sommeria and Deardorff, 1977). The underlying assumption is, that all supersaturation is removed during one model time step, such that there is no supersaturation. Accordingly, the cloud water mixing ratio can be calculated diagnostically as

$$q_c = q_v - q_s. \quad (1.11)$$

As a side effect, saturation-adjustment mitigates the development of realistic supersaturations required for the calculation of the activation process. Hence, this scheme is frequently applied with a fixed number concentration for cloud droplets. However, it is also possible to account for the activation process while using saturation-adjustment (e.g., Seifert and Beheng, 2006). Usually this involves the calculation of a peak supersaturation, which is estimated by an approximation for the supersaturation development in an ascending adiabatic air parcel (e.g., Ghan et al., 1995; Abdul-Razzak et al., 1998; Cohard et al., 1998). Alternatively, if the time constraint of the phase relaxation timescale is satisfied, diffusional growth can be diagnosed (the so-called diagnostic approach) using (e.g., Khairoutdinov and Kogan, 2000)

$$\frac{dq_c}{dt} = 4\pi \frac{\rho_l}{\rho_a} \frac{S}{F_k + F_D} \int_0^\infty r f(r) dr. \quad (1.12)$$

The integral on the right-hand side expresses the product of droplet number concentration and arithmetic mean radius. The latter, however, depends on the assumed shape of the DSD function  $f$ .

For two-moment schemes, the number of activated cloud droplets is usually received using a parametrization originally found by Twomey (1959) (the so-called Twomey-type parametrization). Regardless if a peak supersaturation is estimated or an explicit supersaturation (with the inherent time constraint) is diagnosed, the general formulation of a such a parametrization is

$$N = N_0 S^{k_t}, \quad (1.13)$$

where  $N_0$  and  $k_t$  parameters depending on the aerosol distribution. In the majority of applied activation schemes, the supersaturation is limited to a maximum value at which all cloud-active aerosols are activated. While there are numerous variations of Eq. 1.13 (e.g., Cohard et al., 1998; Khvorostyanov and Curry, 2006), assuming different activation shapes, the general mechanism stays the same.

Saturation-adjustment (Eq. 1.11) is assumed to be applicable for most cloud simulations (Kogan and Martin, 1994). However, it violates the assumption of equilibrium for high-resolved models with a time step of less than 1 s (Thouren et al., 2012). The prevailing stable conditions during fog formation in particular need to be resolved using fine grid spacings due to small-scale turbulence. As a consequence of numerical stability, fine spatial resolutions potentially lower the time step of under a second in many fog simulations. The vast majority of the studies investigating fog (among others Nakanishi, 2000; Stolaki et al., 2015; Bergot, 2016; Maalick et al., 2016; Maronga and Bosveld, 2017; Boutle et al., 2018) applied a saturation-adjustment scheme in their microphysics.

- i. *But is saturation adjustment appropriate for simulating fog in LES as it crucially violates the assumption of equilibrium for very short time steps?*
- ii. *And how large is the effect of different methods to calculate supersaturation on diffusional growth of fog droplets?*

These are the first two questions that are addressed in the research article in Chapter 3.

Beyond the influence on diffusional growth, the feedback of different supersaturation calculations on activation are estimated to be even larger than on diffusional growth. The strong sensitivity of the fog strength to the cloud droplet number concentration was demonstrated by Stolaki et al. (2015); Maalick et al. (2016); Maronga and Bosveld (2017); Boutle et al. (2018). Using an SCM, Stolaki et al. (2015) quantified that doubling the initial aerosol concentration leads to an increase of 165% in the cloud droplet number concentration. Likewise, while reducing the initial aerosol concentration a drop of 65% for the cloud droplet number concentration was observed. In terms of fog strength, this results in 60% higher and 40% lower LWPs, respectively. A similar sensitivity to the cloud droplet number concentration was also found by Maalick et al. (2016) and Maronga and Bosveld (2017) using LES models. While Maalick et al. (2016) observed that the resulting differences in the cloud droplet



number concentration have a feedback on the fog life cycle (higher cloud droplet number concentration lead to later dissipation times) such a sensitivity to the life cycle was not observed by Maronga and Bosveld (2017). In general, the cloud droplet number concentration mainly depends on the activation process. However, activation cannot be solely defined by a linear relationship between the increase of aerosol and proportional increase of cloud droplets, as suggested by Eq. 1.2. Indeed, an increased concentration of cloud droplets leads to lower supersaturation, which subsequently results in lower activation rates (e.g., Twomey, 1959). This non-linear behavior underscores the significance of numerical modeling to comprehend the interaction between aerosols and clouds, yet it also raises the possibility of inaccuracies in the modeling of activation itself.

In a previous study, Thouron et al. (2012) already investigated the influence of different methods for calculating the supersaturation on the cloud droplet concentration using LES. For stratocumulus clouds Thouron et al. (2012) found out that, when using saturation-adjustment in combination with an approximated peak supersaturation, the number of activated cloud droplets is overestimated compared to diagnostic and a more advanced prognostic approach. Within the so-called prognostic approach for calculating the supersaturation, supersaturation is treated as a prognostic quantity rather than deriving it from the fields of temperature and water vapor pressure (see Sec 2). Moreover, Thouron et al. (2012) showed that the diagnostic and prognostic scheme performed relatively similarly throughout the stratocumulus deck. But only the latter approach was able to mitigate spurious cloud top activation.

- iii. *But how large is the effect of different supersaturation modeling approaches on aerosol activation in radiation fog?*

And moreover, in the presence of multiple shapes of the Twomey-type parametrizations (Eq. 1.13, e.g., Khvorostyanov and Curry, 2006):

- iv. *What is the impact of different activation schemes on the fog life cycle for a given aerosol environment?*

These questions will also be answered in the research article presented in Chapter 3.

### 1.2.2 Representing fog with a Lagrangian Cloud Model

To overcome the limitations of traditional bulk parametrizations enormous effort has been made in the last decade while developing a new kind of cloud microphysics scheme: Lagrangian Cloud Models (LCMs, Andrejczuk et al., 2008; Shima et al., 2009; Sölch and Kärcher, 2010; Riechelmann et al., 2012; Naumann and Seifert, 2015). The main idea of this approach is to represent aerosols and hydrometeors as particles instead as scalar quantities on an Eulerian grid. However, as even one cubic meter of cloudy air contains around  $10^8$  cloud droplets, the simulation of every hydrometeor individually is computationally impossible for a whole cloud or a cloud complex. This is why the concept of so-called superdroplets has been introduced (Shima et al., 2009), where one simulated particle (superdroplet) represents an ensemble of real cloud droplets with identical properties. Termed as weighting-factor

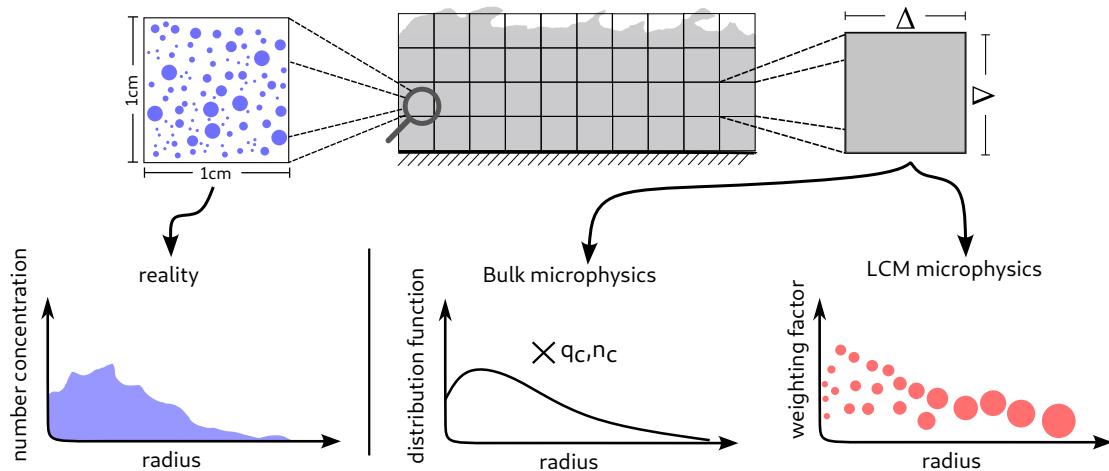


**Figure 1.4:** Discretization of an foggy ABL and the representation of the cloud size particle distribution therein by different microphysics schemes. For reference, the reality is also illustrated on the left, but the reference volume is much smaller than the reference volume of the numerical model (right gray box). The cloud droplet distribution in bulk cloud models (center) is assumed to follow an analytic function, the quantitative course of which depends on the cloud water mixing ratio ( $q_c$ ) and cloud droplet number concentration ( $n_c$ ). The shape of the function is prescribed by fixed parameters. In Lagrangian cloud models (right) the cloud distribution is given by the superdroplet ensemble (red dots), where the weighting-factor is the actual number of particles, which each superdroplet represents.

or multiplicity, this factor describes the number of real droplets or aerosols, which are presented by the superdroplet. In practice, LCMs are driven with several million superdroplets to ensure statistical convergence. This in turn causes high computational demands, so that applications currently take place exclusively in the research sector.

With the help of the LCM it is possible to solve microphysical processes according to their first principles instead of using parameterizations. In other words, the microphysical representation is particle-based and thus size resolved, while in traditional bulk approaches the DSD follows an analytic function. These differences between the representation of the DSD in LCMs and bulk cloud models is illustrated in Fig. 1.4.

For clarification, it must be noted that the microphysics is based solely on a Lagrangian approach. Temperature, humidity, and dynamics are still solved on the Eulerian grid and interpolated to the particle position. However, an active coupling is used, i.e., that microphysical processes as condensation or evaporation do impact the temperature and humidity on the Eulerian grid. Nonetheless, by means of first principles, activation and diffusional growth can be considered size-dependent for each simulated particle, i.e., Eq. 1.2 and 1.5 can be directly translated into the LCM. Moreover, the representation of sedimentation is also straight forward in LCMs, as the terminal fall velocity of each particle is explicitly calculated. LCMs have been successfully applied for warm shallow cumulus clouds (Shima et al., 2009; Riechelmann et al., 2012), stratus clouds (Andrejczuk et al., 2008), stratocumulus (Hoffmann and Feingold, 2019), cirrus clouds (Sölch and Kärcher, 2010) and lately (a 2-dimensional) cumulonimbus cloud (Shima et al., 2020). However, at the time the project started (2017), there were no published studies in which a LCM had been used to simulate a fog case. This is

not due to the lack of relevance of microphysical processes in fog, but rather to the high computational time required for a LCM application for high-resolution fog simulations. Initially, the question arose

- i. *How does a common Eulerian bulk cloud model compare to the sophisticated LCM in terms of fog strength and number concentration of cloud droplets?*

Apart from model advances in LCMs over traditional bulk approaches, LCMs immanently resolve the DSD, which is parameterized in bulk cloud models. The shape of the DSD in turn affects the strength of sedimentation within fog, as larger particles reveal higher fall velocities. Even though radiative cooling is generally found to be insensitive to the DSD itself, the DSD has a large indirect effect on cloud top cooling through modified sedimentation fluxes at the fog top (Roach et al., 1976). Observing fog in the New York area, Pilié et al. (1975) showed, that half of the fog events revealed a bimodal DSD with one mode at 2-3  $\mu\text{m}$  and a second mode between 6-12  $\mu\text{m}$  close to the surface. Aloft, the DSD becomes narrower with a decreasing mean radius and increasing height as long as the fog is stably stratified. Using a SCM, but with a sectional (also called spectral bin approach - the interested reader is referred to Grabowski et al., 2019) aerosol-microphysical representation, Bott et al. (1990) simulated size-resolved DSDs for fogs assuming different aerosol properties. Regardless of the chosen aerosol environment Bott et al. (1990) revealed bi-modal DSDs with a minimum at a radius of 4-6  $\mu\text{m}$ . In agreement with observations from Fuzzi et al. (1992), Bott et al. (1990) argued that this bi-modality separates the activated droplets from wetted aerosols. Based on observations on fog microphysics during a field campaign in the Po-Valley in Northern Italy, Wendisch et al. (1998) distinguished between two DSD stages for fog. In the initial stage during fog formation, the DSD is characterized by relatively small droplets. The second stage, termed the mass-transfer-stage, is dominated by larger droplets with radii in the range of 10-14  $\mu\text{m}$  and found to be bi-modal. The classification of different stages in fog DSDs was confirmed by Price (2011) observing fog in Cardington, United Kingdom. However, instead of bi-modal shapes within the mass-transfer-stage, Price (2011) found mostly platykurtic or skewed DSDs.

Conclusively, the observations reveal that the shape of fogs DSDs is neither constant in space nor in time. Already Price (2011) compromise the suitability of microphysical schemes that assume a constant spectral shape, as done in bulk cloud models by design.

- ii. *But how do DSDs develop in fog while explicitly simulated in a LCM?*
- iii. *And how do they match with the assumed DSD shapes in bulk cloud models?*

Chapter 4 will answer these questions, in which a LCM was used for the first time to study fog. Following up on our published research, an LCM was also applied on coastal fog by Richter et al. (2021).

### 1.2.3 Model intercomparison

A correct representation of individual physical processes within numerical models is indispensable. But the assessment of model performance (in physical terms) is challenging, par-

ticularly if relevant processes cannot be verified with observations due to missing techniques capturing the non-linear and multi-scale nature of the processes within fog. Hence, one tool to estimate model uncertainties are model intercomparisons. The first intercomparison study conducted by Bergot et al. (2007) of SCMs demonstrated that the model skill in simulating radiation fog was low. Even before fog onset, considerable large differences between the models have been observed. Moreover, Bergot et al. (2007) demonstrated that important processes such as dew deposition and fog sedimentation cannot be neglected. In practice, however, some SCMs - which in turn are based on operational weather forecast models - did not consider such processes at that time. After more than a decade in which methods in numerical models have been improved and physical processes included, the demand for a new intercomparison study of SCMs and LES modeling fog has recurred. In this study, which is presented in Chapter 5, the question of

- i. *How well can models simulate the development of radiation fog, and how large are the differences between the models?*

is evaluated. Even though parametrization for microphysics, radiation, and turbulent surface fluxes have been refined in recent years, significant differences between models and observations still exist (Teixeira, 1999; Tudor, 2010; Zhou et al., 2012; Román-Cascón et al., 2012; Steeneveld et al., 2015). Thus,

- ii. *Which of these processes are mostly responsible for the biases seen in current NWP models?*

will be addressed in this research. Boutle et al. (2018) showed that the Met Office Unified Model significantly overestimates droplet activation in fog. Designed for cloud types with significant updrafts, commonly used parameterizations assuming a minimum updraft velocity are unsuitable for the subtle supersaturations within fog. Hence, the general question arises:

- iii. *What level of complexity is required from NWP models to adequately simulate these processes during fog?*

All these questions are answered within the international model intercomparison study presented in Chapter 5, where the model, which was applied in the other research objectives of this thesis, is compared.

#### **1.2.4 Influence of nocturnal fog on daytime ABL**

Apart from fog-associated hazards, fog does alter the ABL properties during its presence. As presented in Fig. 1.2 deep fog can even cause that the NBL to become convective (e.g., Gulpe et al., 2007). Compared to a clear-sky NBL, the foggy NBL is characterized by an effective radiative cooling not at the surface, but at the fog top. Cooling rates of  $5 \text{ K h}^{-1}$  have been modeled (e.g., Maalick et al., 2016; Maronga and Bosveld, 2017) for fog, which significantly alter the thermodynamic structure within the NBL. Moreover, microphysical processes (see also Fig. 1.3) like the deposition of water droplets on the surface deprive humidity from the atmosphere.

With the help of observations and modeling techniques Vilà-Guerau de Arellano (2007) demonstrated the importance of NBL properties and the layer aloft of the early morning hours on daytime convection and the formation of shallow cumuli. This in turn has profound implications for studies and predictions using numerical models of atmospheric processes within the diurnal cycle if the bias made at night is propagated (at least to some extent) into the day. While modeling fog is quite challenging, the reasons for an incorrect representation are manifold. Small-scale processes must be parameterized adequately (Steenefeld et al., 2015) and initial conditions precisely included in the model (Rémy and Bergot, 2009). Even though great progress in the last decade has been made in modeling fog, many NWP models still fail to predict a significant amount of fog events (Steenefeld et al., 2015). For instance, Tudor (2010) failed to simulate a radiation fog event in Hungary in 2004 with the model ARPEGE (Déqué et al., 1994). Of course, such a model performance is unsuitable to study fog. But further, if it is intended to simulate a complete diurnal cycle or longer (as is usually done by NWP or climate models), the impact of a non-resolved fog event might distort the prediction.

The influence of a misrepresented (by a too-coarse spatial resolution) dry NBL on the daytime convection in LES was firstly studied by Van Stratum and Stevens (2015). Van Stratum and Stevens (2015) argued that this misrepresentation of the NBL has a negligible influence on the properties of a dry summer ABL during daytime. They showed that overestimating vertical mixing (as a result of too-large grid spacings) lead to slightly warmer CBLs, which prevents the formation of spurious clouds. Also, the deviations in the ABL temperature and boundary layer height were shown to be rather small (Van Stratum and Stevens, 2015). However, Van Stratum and Stevens (2015) did not consider the influence of radiation and humidity explicitly. Hence, the drawn conclusions can only be applied to atmospheric conditions where radiation and humidity play a minor role in the NBL. A follow-up study that accounted for radiation and humidity by means of a conceptual model, van Stratum and Stevens (2018) demonstrated that, overestimating vertical mixing at night will probably cause artificial low clouds or fog in numerical models. Furthermore, they suggest that the influence of non-resolved fog (assuming a maximum vertical extent of 50 m) is rather small (van Stratum and Stevens, 2018). Although, their implicit approach of considering the effect of unresolved fog is reasonable, they excluded conditions under which fog occurs mostly in Europe (fall, winter and spring, e.g., Izett et al., 2019). Rather, the study was designed to investigate whether daytime convection during summer is affected by the usage of low-resolution LESs.

Thus, prior research left the questions of

- i. *How large is the effect of nocturnal fog on the development of the daytime CBL?*
- ii. *Which small-scale processes (Fig. 1.3) are the most important for the differences observed?*
- iii. *And what conditions do amplify or mitigate the influence of fog on the CBL development?*

unanswered, and they have been addressed in Chapter 6.

### 1.3 Structure of this thesis

The present thesis mainly consists of four research articles in which the representation of radiation fog in numerical models is evaluated and the understanding of physical processes is improved. While addressing the previously stated research questions, the research articles can be briefly summarized as follows:

Chapter 3 describes a model improvement that was achieved by implementing a 2-moment bulk microphysics scheme including a parameterization for activation and supersaturation calculation. With those capabilities it is investigated how different schemes perform while simulating fog and the differences between the schemes are analyzed. The research article presented in Chapter 4 applied an advanced particle-based microphysics approach for the first time to simulate fog. Advantages compared to common microphysics schemes are elucidated. Moreover, the explicitly resolved DSDs within the fogs are studied. The third study (Chapter 5) is an international model intercomparison of the simulation of fog by SCMs and LESs in which the model used for the research objectives within this thesis is compared. It will present the differences among well-known numerical models and evaluate reasons for biases in simulating fog. The last study presented in Chapter 6 assesses the influence of nocturnal fog on the daytime ABL development. With the help of process-level analysis the most important physical mechanism causing differences between a foggy and a clear-sky ABL are identified. Prior to the presentation of the research articles, the used LES model is presented in Chapter 2. For this purpose, the relevant sections of latest published model description are included, which outline the model core. Subsequently, the bulk cloud model, the LCM, the land-surface model, and the radiation transfer model used in for this research are briefly summarized. The thesis is completed with concluding remarks and an outlook on subsequent research, which is given in Chapter 7.

## 2 Methods

As outlined in the introduction, numerical models are a powerful tool for studying fog processes. For ABL research, different types of numerical models are, in general, suitable. Typically, these model types are differentiated by their degree of precision in their simulation of atmospheric processes, whether they are fully parameterized or represented explicitly. Thus, they also inherently differ in the required resolution; in other words, the spatial and temporal distance within the atmospheric state must be calculated. Conversely, this implies that numerical models for atmospheric applications always require a trade-off between precision, computation time, and the size of the area being represented. For example, for a certain amount of computational resources it is possible to simulate the development of one cubic meter of cloudy air within one hour of real-time with very-high precision (e.g., on the millimeter-scale). Indeed, with a fixed amount of computing time, it is not possible to increase the spatial representation to encompass an entire cloud or cloud system (such as a cyclone) while maintaining the same level of accuracy in terms of spatial resolution. To simulate a cloud system, it would either be necessary to decrease the precision or dramatically increase computational resources. However, the latter is often impractical for most applications. Apart from a large variety of model subtypes or special model types, there are in general three methods to which most of the models can be assigned.

First is a method based on Reynolds-averaged Navier-Stokes (RANS) equations. The so-called RANS models fully parameterize the turbulence spectrum. The main advantage of this method is, that these models are computationally cost-efficient and can be applied for larger domains (e.g., on the mesoscale). However, RANS models solely predict mean quantities of the flow field and their results depend on quality of the parametrization for turbulence. Such parametrizations frequently suffer from limited applicability and can only represent the statistics of turbulence.

Second is the direct numerical simulation (DNS), where the Navier-Stokes equations are solved directly. DNS models are based on the idea that the complete turbulence spectrum is explicitly represented, i.e., from the largest scale eddies down to the size of the Kolmogorov dissipation length (Moin and Mahesh, 1998). This, however, causes a restriction to millimeters on the spatial resolution and to split-seconds on the temporal resolution. To capture realistic ABL phenomena, the largest eddies must also be represented, which causes a far-too-large number of points (so-called gridpoints) where numerical calculation must be carried out. Thus, DNS is still a tool for special applications at very low Reynolds numbers and small model domains.

Third is the compromise between RANS and DNS: large-eddy simulations (LES). Increasingly used within in the last 50 years, LES models are a suitable tool for studying ABL processes as they resolve the relevant turbulent structures explicitly but parameterize the

---

small-scale eddies (e.g., Ferziger, 1977). In the research studies presented in this thesis, the LES model system PALM was used for simulating fog. The PALM model system is being developed since more than 25 years. Nowadays the model includes (beyond the basic features of LES models) many features including an ocean model, a particle model, a wind-turbine model, an indoor model, a chemistry model, an aerosol model, several radiation models, a land-surface model, and a bulk cloud model, among others. In this chapter, however, only the components that were also used in the presented studies of this thesis are described.

For the model description in this thesis a hybrid style has been deliberately chosen, in which the basic principles, governing equations, the Subgrid-scale model, and the applied numerical methods are presented in the overview article on the PALM model system (Sec. 2.1). This is followed by a detailed description of the embedded model parts used for the representation of the liquid phase (bulk cloud model and LCM) and the newest model developments therein (as a part of the research projects presented in this thesis). Finally, the used (but not further developed) land-surface model and radiation model are briefly summarized.



## 2.1 Basics of the PALM Model system

### 2.1.1 Declaration of Contributions

The PALM model system 6.0 is a joint effort by several institutions and developers, most of which are authors of this paper. BM designed, prepared, and edited the manuscript with contributions by all listed co-authors. The section describing the implementation of the bulk cloud model as well as parts of the LCM section have been designed, implemented and written by JS.

### 2.1.2 Model Overview Article

©The authors 2020. CC BY 4.0 License

Geosci. Model Dev., 13, 1335–1372, 2020  
https://doi.org/10.5194/gmd-13-1335-2020  
© Author(s) 2020. This work is distributed under  
the Creative Commons Attribution 4.0 License.



Geoscientific  
Model Development  
Open Access  
EGU

## Overview of the PALM model system 6.0

**Björn Maronga<sup>1,2</sup>, Sabine Banzhaf<sup>3</sup>, Cornelia Burmeister<sup>4</sup>, Thomas Esch<sup>5</sup>, Renate Forkel<sup>6</sup>, Dominik Fröhlich<sup>7</sup>, Vladimir Fuka<sup>8</sup>, Katrin Frieda Gehrke<sup>1</sup>, Jan Geletić<sup>9</sup>, Sebastian Giersch<sup>1</sup>, Tobias Gronemeier<sup>1</sup>, Günter Groß<sup>1</sup>, Wieke Heldens<sup>5</sup>, Antti Hellsten<sup>10</sup>, Fabian Hoffmann<sup>1,a,b</sup>, Atsushi Inagaki<sup>11</sup>, Eckhard Kadasch<sup>12</sup>, Farah Kanani-Sühring<sup>1</sup>, Klaus Ketelsen<sup>13</sup>, Basit Ali Khan<sup>6</sup>, Christoph Knigge<sup>1,12</sup>, Helge Knoop<sup>1</sup>, Pavel Krč<sup>9</sup>, Mona Kurppa<sup>14</sup>, Halim Maamari<sup>15</sup>, Andreas Matzarakis<sup>7</sup>, Matthias Mauder<sup>6</sup>, Matthias Pallasch<sup>15</sup>, Dirk Pavlik<sup>4</sup>, Jens Pfafferoth<sup>16</sup>, Jaroslav Resler<sup>9</sup>, Sascha Rissmann<sup>17</sup>, Emmanuele Russo<sup>3,c,d</sup>, Mohamed Salim<sup>17,18</sup>, Michael Schrempf<sup>1</sup>, Johannes Schwenkel<sup>1</sup>, Gunther Seckmeyer<sup>1</sup>, Sebastian Schubert<sup>17</sup>, Matthias Sühring<sup>1</sup>, Robert von Tils<sup>1,4</sup>, Lukas Vollmer<sup>19,e</sup>, Simon Ward<sup>1</sup>, Björn Witha<sup>19,f</sup>, Hauke Wurps<sup>19</sup>, Julian Zeidler<sup>5</sup>, and Siegfried Raasch<sup>1</sup>**

<sup>1</sup>Institute of Meteorology and Climatology, Leibniz University Hannover, Hannover, Germany

<sup>2</sup>Geophysical Institute, University of Bergen, Bergen, Norway

<sup>3</sup>Institut für Meteorologie, Freie Universität Berlin, Berlin, Germany

<sup>4</sup>GEO-NET Environmental Services GmbH, Hannover, Germany

<sup>5</sup>German Aerospace Center (DLR), German Remote Sensing Data Center (DFD), Oberpfaffenhofen, Germany

<sup>6</sup>Karlsruhe Institute of Technology, IMK-IFU, Garmisch-Partenkirchen, Germany

<sup>7</sup>Research Center Human Biometeorology, Deutscher Wetterdienst, Freiburg, Germany

<sup>8</sup>Department of Atmospheric Physics, Faculty of Mathematics and Physics, Charles University, Prague, Czech Republic

<sup>9</sup>Institute of Computer Science, The Czech Academy of Sciences, Prague, Czech Republic

<sup>10</sup>Finnish Meteorological Institute, Helsinki, Finland

<sup>11</sup>School of Environment and Society, Tokyo Institute of Technology, Tokyo, Japan

<sup>12</sup>Deutscher Wetterdienst, Offenbach, Germany

<sup>13</sup>Software Consultant, Berlin, Germany

<sup>14</sup>Institute for Atmospheric and Earth System Research/Physics, Faculty of Science, University of Helsinki, Helsinki, Finland

<sup>15</sup>Ingenieuresellschaft Prof. Dr. Sieker mbH, Hoppegarten, Germany

<sup>16</sup>Hochschule Offenburg, Offenburg, Germany

<sup>17</sup>Geography Department, Humboldt-Universität zu Berlin, Berlin, Germany

<sup>18</sup>Faculty of Energy Engineering, Aswan University, Aswan, Egypt

<sup>19</sup>Carl von Ossietzky Universität Oldenburg, ForWind – Research Center of Wind Energy, Oldenburg, Germany

<sup>a</sup>currently at: Cooperative Institute for Research in Environmental Sciences, University of Colorado Boulder, Boulder, CO, USA

<sup>b</sup>currently at: NOAA Earth Systems Research Laboratory, Chemical Sciences Division, Boulder, CO, USA

<sup>c</sup>currently at: Oeschger Centre for Climate Change Research, University of Bern, Bern, Switzerland

<sup>d</sup>currently at: Climate and Environmental Physics, Physics Institute, University of Bern, Bern, Switzerland

<sup>e</sup>currently at: Fraunhofer Institute for Wind Energy Systems, Oldenburg, Germany

<sup>f</sup>currently at: energy & meteo systems GmbH, Oldenburg, Germany

**Correspondence:** Björn Maronga (maronga@muk.uni-hannover.de)

Received: 13 April 2019 – Discussion started: 7 June 2019

Revised: 12 November 2019 – Accepted: 19 January 2020 – Published: 20 March 2020

**Abstract.** In this paper, we describe the PALM model system 6.0. PALM (formerly an abbreviation for Parallelized Large-eddy Simulation Model and now an independent name) is a Fortran-based code and has been applied for studying a variety of atmospheric and oceanic boundary layers for about 20 years. The model is optimized for use on massively parallel computer architectures. This is a follow-up paper to the PALM 4.0 model description in Maronga et al. (2015). During the last years, PALM has been significantly improved and now offers a variety of new components. In particular, much effort was made to enhance the model with components needed for applications in urban environments, like fully interactive land surface and radiation schemes, chemistry, and an indoor model. This paper serves as an overview paper of the PALM 6.0 model system and we describe its current model core. The individual components for urban applications, case studies, validation runs, and issues with suitable input data are presented and discussed in a series of companion papers in this special issue.

## 1 Introduction

Since the early 1970s, the turbulence-resolving so-called large-eddy simulation (LES) technique has been increasingly employed for studying the atmospheric boundary layer (ABL) at large Reynolds numbers. While the earliest studies were performed at coarse grid spacings on the order of 100 m (Deardorff, 1970, 1973), today's supercomputers allow for large domain runs at fine grid spacings of 1–10 m (e.g., Kanda et al., 2004; Raasch and Franke, 2011; Sullivan and Patton, 2011, among many others) or even less (Sullivan et al., 2016; Maronga and Reuder, 2017; Maronga and Bosveld, 2017). LES models solve the three-dimensional prognostic equations for momentum, temperature, humidity, and other scalar quantities (such a chemical species). The principle of LES dictates a separation of scales. Turbulence scales larger than a chosen filter width are being directly resolved by LES models, while the effect of smaller turbulence scales on the resolved scales is fully parameterized within a so-called subgrid-scale (SGS) model. The filter width strongly depends on the phenomenon to be studied and must be chosen in such a way that at least 90 % of the turbulence energy can be resolved (Heus et al., 2010).

In a precursor paper (Maronga et al., 2015), we gave an overview of the Parallelized Large-eddy Simulation Model (PALM) version 4.0. PALM is a Fortran-based code and has been applied for a variety of atmospheric and oceanic boundary layers for about 20 years. The model is optimized for use on massively parallel computer architectures but can be used in principle also on small workstations and notebooks. The model domain is discretized in space using finite differences and equidistant horizontal grid spacings. The parallelization of the code is achieved by a 2-D domain decomposition

method along the  $x$  and  $y$  directions on a Cartesian grid with (usually) equally sized subdomains. Ghost layers are added at the side boundaries of the subdomains in order to account for the local data dependencies, which are caused by the need to compute finite differences at these positions. A Cartesian topography (complex terrain and buildings) is available in PALM, which is based on the mask method (Briscolini and Santangelo, 1989) and allows for explicitly resolving solid obstacles such as buildings and orography. PALM also has an ocean option, allowing for studying the ocean mixed layer where the sea surface is defined at the top of the model, and which includes a prognostic equation for salinity.

Furthermore, PALM has offered several embedded models which were described in the precursor paper, namely bulk cloud microphysics parameterizations, a Lagrangian particle model (LPM) which can be used for studying dispersion processes in turbulent flows, or as a Lagrangian cloud model (LCM) employing the superdroplet approach. Moreover, a plant canopy model can be used to study effects of plants as obstacles on the flow. A 1-D version of PALM can be switched on in order to generate steady-state wind profiles for 3-D model initialization.

Due to the enormous amount of data that come along with computationally expensive LES (in terms of the number of grid points and short time steps), the data handling plays a key role for the performance of LES models and for data analysis during post-processing. PALM is optimized to pursue the strategy of performing data operations like time or domain averaging to a great extent online instead of postpone such operations to a post-processing step. In this way, the data output (e.g., of huge 4-D data or temporal averages) can be significantly reduced. In order to allow the user to perform their own calculations during runtime, a user interface offers a wide range of possibilities, e.g., for defining user-defined output quantities. PALM allows data output for different quantities as time series, (horizontally averaged) vertical profiles, 2-D cross sections, 3-D volume data, and masked data. All data output files are in netCDF format, which can be processed by a variety of public domain and commercial software. The only exception is data output from the LPM, which is output in Fortran binary format for a better performance. For details about PALM's specifics, application scenarios, and validation runs, see Maronga et al. (2015) and references therein.

In the present paper, we describe the PALM model system version 6.0. Since version 4.0, the code has undergone massive changes and improvements. Above all, new components for applications of PALM in urban environments, so-called PALM-4U (PALM for urban applications) components, have been added in the scope of the Urban Climate Under Change [UC]<sup>2</sup> framework funded by the German Federal Ministry of Education and Research (Scherer et al., 2019b; Maronga et al., 2019). Besides, a turbulence closure based on the Reynolds-averaged Navier–Stokes (RANS) equations was added, enabling PALM to not only run in turbulence-

resolving (i.e., LES) but also in RANS mode where the full turbulence spectrum is parameterized. Originally, the name PALM referred to its parallelization as a special feature of the model. Nowadays, however, most of the existing LES models are parallelized.

Moreover, with the RANS mode implemented, PALM is more than an LES model, rendering the full name of the model inappropriate. As the name PALM has been established in the research community, we thus decided to drop the full name and use the abbreviation PALM as a proper name from now on. The model is now referred to as the PALM model system, consisting of the PALM model core and the PALM-4U components. For the motivation for developing the PALM-4U components and a description of model developments done within [UC]<sup>2</sup>, the reader is referred to Maronga et al. (2019). As the model core in version 4.0 was described in detail in the precursor paper, we will focus here on the changes in the model core and give an overview of all the new components that have been added to the model. The individual new PALM-4U components, case studies, validation studies, and issues with suitable input data are presented and discussed in a series of companion papers in this special issue.

The paper is organized as follows: Sect. 2 deals with the description of the model core, while Sect. 3 and Sect. 4 give details about the embedded modules in the PALM core and the PALM-4U components, respectively. Sect. 5 provides technical details, including recent developments in model operation, data structure of surface elements, I/O data handling, and optimization. The paper closes with conclusions in Sect. 6. Note that all symbols that will be introduced in the following are also listed in Tables 1–8.

## 2 PALM model core

In this section, we give a detailed description of the changes of the PALM model core starting from version 4.0. Here, we confine ourselves to the atmospheric version. Details about the ocean version are given by Maronga et al. (2015) and in Sect. 2.4. By default, PALM solves equations for up to seven prognostic variables: the velocity components  $u$ ,  $v$ , and  $w$  on a staggered Cartesian grid (staggered Arakawa C grid Harlow and Welch, 1965; Arakawa and Lamb, 1977), potential temperature  $\theta$ , SGS turbulence kinetic energy (SGS-TKE)  $e$  (in LES mode), water vapor mixing ratio  $q_v$ , and possibly a passive scalar  $s$ . Note that, in PALM 4.0, it was only possible to use either water vapor or the passive scalar as both used the same prognostic equation in the model code, while both are now fully separated and can be used simultaneously.

### 2.1 Governing equations of the PALM core

By default, PALM solves incompressible approximations of the Navier–Stokes equations, either in Boussinesq-

approximated form, filtered based on a spatial scale separation approach after Schumann (1975) (described in Maronga et al., 2015), or in an anelastic approximation, in which the flow is treated as incompressible but allowing for density variations with height, while variations in time are not permitted. This enables the application of PALM to simulate atmospheric phenomena that extend throughout the entire troposphere (e.g., deep convection). Both anelastic and Boussinesq-approximated forms are described by a single set of equations that only differ in the treatment of the density  $\rho$ . For the Boussinesq form,  $\rho$  is set to a constant value (and then drops out of most terms), while the anelastic form results from varying  $\rho$  with height during initialization.

In the following set of equations, angular brackets denote a horizontal domain average. A subscript 0 indicates a surface value. Note that the variables in the equations are implicitly filtered by the discretization (see above), but that the continuous form of the equations is used here for convenience. A double prime indicates SGS variables. The overbar indicates filtered quantities. The equations for the conservation of mass, momentum, thermal internal energy, moisture, and another arbitrary passive scalar quantity, filtered over a grid volume on a Cartesian grid, then read as

$$\frac{\partial \bar{u}_j \rho}{\partial x_j} = 0 \quad (1)$$

$$\begin{aligned} \frac{\partial \bar{u}_i}{\partial t} = & -\frac{1}{\rho} \frac{\partial \rho \bar{u}_i \bar{u}_j}{\partial x_j} - \varepsilon_{ijk} f_j \bar{u}_k + \varepsilon_{i3j} f_3 u_{g,j} - \frac{\partial}{\partial x_i} \left( \frac{\pi^*}{\rho} \right) \\ & + g \frac{\bar{\theta}_v - \theta_{v,\text{ref}}}{\theta_{v,\text{ref}}} \delta_{i3} - \frac{1}{\rho} \frac{\partial}{\partial x_j} \rho \left( \overline{u_i'' u_j''} - \frac{2}{3} e \delta_{ij} \right), \end{aligned} \quad (2)$$

$$\frac{\partial \bar{\theta}}{\partial t} = -\frac{1}{\rho} \frac{\partial \rho \bar{u}_j \bar{\theta}}{\partial x_j} - \frac{1}{\rho} \frac{\partial}{\partial x_j} \left( \rho \overline{u_j'' \theta''} \right) - \frac{l_v}{c_p \Pi} \chi_{q_v} \quad (3)$$

$$\frac{\partial \bar{q}_v}{\partial t} = -\frac{1}{\rho} \frac{\partial \rho \bar{u}_j \bar{q}_v}{\partial x_j} - \frac{1}{\rho} \frac{\partial}{\partial x_j} \left( \rho \overline{u_j'' q_v''} \right) + \chi_{q_v} \quad (4)$$

$$\frac{\partial \bar{s}}{\partial t} = -\frac{1}{\rho} \frac{\partial \rho \bar{u}_j \bar{s}}{\partial x_j} - \frac{1}{\rho} \frac{\partial}{\partial x_j} \left( \rho \overline{u_j'' s''} \right) + \chi_s. \quad (5)$$

Here,  $i, j, k \in \{1, 2, 3\}$ .  $u_i$  is the velocity components ( $u_1 = u, u_2 = v, u_3 = w$ ) with location  $x_i$  ( $x_1 = x, x_2 = y, x_3 = z$ ),  $t$  is time,  $f_i = (0, 2\Omega \cos(\phi), 2\Omega \sin(\phi))$  is the Coriolis parameter with  $\Omega = 0.729 \times 10^{-4} \text{ rad s}^{-1}$  being the Earth's angular velocity and  $\phi$  being the geographical latitude.  $u_{g,j}$  is the geostrophic wind speed components,  $\rho$  is the basic state density of dry air,  $\pi^* = p^* + \frac{2}{3} \rho e$  is the modified perturbation pressure with  $p^*$  being the perturbation pressure and  $e = \frac{1}{2} \overline{u_i'' u_i''}$ ,  $g = 9.81 \text{ m s}^{-2}$  is the gravitational acceleration,  $\delta$  is the Kronecker delta, and  $l_v = 2.5 \times 10^6 \text{ J kg}^{-1}$  is the specific latent heat of vaporization. The reference state  $\theta_{v,\text{ref}}$  in Eq. (2) can be set to be the horizontal average ( $\theta_v$ ), the initial state, or a fixed reference value. Furthermore,  $\chi_{q_v}$  and  $\chi_s$  are source/sink terms of  $q_v$  and  $s$ , respectively. The potential

**Table 1.** List of general model parameters.

Symbol	Value	Description
$c_0, c_1, c_2, c_3$	0.55, 1.44, 1.92, 1.44	Model constants in RANS turbulence parameterization
$c_p$	$1005 \text{ J kg}^{-1} \text{ K}^{-1}$	Specific heat capacity of dry air at constant pressure
$g$	$9.81 \text{ m s}^{-2}$	Gravitational acceleration
$l_v$	$2.5 \times 10^6 \text{ J kg}^{-1}$	Specific latent heat of vaporization
$Pr$	1	Prandtl number in RANS turbulence parameterization
$p_0$	1000 hPa	Reference air pressure
$R_d$	$287 \text{ J kg}^{-1} \text{ K}^{-1}$	Specific gas constant for dry air
$R_v$	$461.51 \text{ J kg}^{-1} \text{ K}^{-1}$	Specific gas constant for water vapor
$S_0$	$1368 \text{ W m}^{-2}$	Solar constant
$\alpha_{\text{Ch}}$	0.018	Charnock constant
$\epsilon_{\text{atm}}$	0.8	Atmospheric emissivity
$\kappa$	0.4	Von Kármán constant
$\nu$	$1.461 \times 10^{-5} \text{ m}^2 \text{ s}^{-1}$	Kinematic viscosity of air
$\pi$	3.14159 ...	Pi
$\sigma_e$	1.0	Model constant in RANS turbulence parameterization
$\sigma_\epsilon$	1.3	Model constant in RANS turbulence parameterization
$\sigma_{\text{SB}}$	$5.67 \times 10^{-8} \text{ W m}^{-2} \text{ K}^{-4}$	Stefan–Boltzmann constant
$\Omega$	$0.729 \times 10^{-4} \text{ rad s}^{-1}$	Angular velocity of the Earth

**Table 2.** List of general symbols.

Symbol	Dimension	Description
$F$	N	Random forcing term in parameterization of wave breaking
$N_{\text{chem}}$		Number of chemical species
$s$	$\text{kg m}^{-3}$	Passive scalar
$T$	K	Absolute air temperature
$U_s$	$\text{m s}^{-1}$	Wave amplitude in Stokes drift parameterization
$u_i$	$\text{m s}^{-1}$	Velocity components ( $u_1 = u, u_2 = v, u_3 = w$ )
$u_{g,i}$	$\text{m s}^{-1}$	Geostrophic wind components ( $u_{g,1} = u_g, u_{g,2} = v_g$ )
$u_s$	$\text{m s}^{-1}$	Stokes drift velocity
$u_{\text{tr}}$	$\text{m s}^{-1}$	Transport velocity used for radiation boundary conditions at the model outflow
$x_d$	m	Distance in $x$ direction used for radiation boundary conditions at the model outflow
$x_i$	m	Coordinate on the Cartesian grid ( $x_1 = x, x_2 = y, x_3 = z$ )
$z_w$	m	Wave height in Stokes drift parameterization
$\Delta$	m	Grid spacing
$\Delta x, \Delta y, \Delta z$	m	Grid spacings in $x, y,$ and $z$ directions
$\Delta t$	s	Time step of the LES model
$\delta$		Kronecker delta
$\theta$	K	Potential temperature
$\theta_v$	K	Virtual potential temperature
$\theta_{v,\text{ref}}$	K	Reference state of virtual potential temperature
$\lambda_w$	m	Wavelength in Stokes drift parameterization
$\Pi$		Exner function
$\pi^*$	hPa	Perturbation pressure
$\rho$	$\text{kg m}^{-3}$	Density of dry air (basic state)
$\rho_\theta$	$\text{kg m}^{-3}$	Potential density
$\omega$	$\text{s}^{-1}$	Rotation of velocity

temperature is defined as

$$\theta = T/\Pi, \quad (6)$$

with the absolute temperature  $T$  and the Exner function:

$$\Pi = \left(\frac{p}{p_0}\right)^{R_d/c_p}, \quad (7)$$

with  $p$  being the hydrostatic air pressure,  $p_0 = 1000$  hPa a reference pressure,  $R_d = 287 \text{ J kg}^{-1} \text{ K}^{-1}$  the specific gas constant for dry air, and  $c_p = 1005 \text{ J kg}^{-1} \text{ K}^{-1}$  the specific heat of dry air at constant pressure. The virtual potential temperature is defined as

$$\theta_v = \theta \left[ 1 + \left(\frac{R_v}{R_d} - 1\right) q_v - q_l \right], \quad (8)$$

with the specific gas constant for water vapor  $R_v = 461.51 \text{ J kg}^{-1} \text{ K}^{-1}$ , and the liquid water mixing ratio  $q_l$ . For the computation of  $q_l$ , see the descriptions of the embedded cloud microphysical models in Sect. 3.1 and 3.4.

## 2.2 Turbulence closures

By default, PALM employs a 1.5-order closure (LES mode) after Deardorff (1980) in the formulation by Moeng and Wyngaard (1988) and Saiki et al. (2000) (hereafter referred to as the Deardorff scheme). Details are given in Maronga et al. (2015). Since version 6.0, an alternative dynamic SGS closure can be used, which will be described in the following. Moreover, two turbulence closures are available in RANS mode (i.e., the full spectrum of turbulence is parameterized): a so-called TKE- $l$  and a TKE- $\epsilon$  closure, where  $l$  is a mixing length and  $\epsilon$  is the SGS-TKE dissipation rate.

### 2.2.1 Dynamic SGS closure

The dynamic SGS closure follows Heinz (2008) and Mokhtarpoor and Heinz (2017). In general, the dynamic SGS closure employs the same equations for calculating the SGS fluxes as the Deardorff scheme, assuming that the energy transport by SGS eddies is proportional to the local gradients of the mean resolved quantities and reads

$$\overline{u_i'' u_j''} - \frac{2}{3} e \delta_{ij} = -K_m \left( \frac{\partial \bar{u}_i}{\partial x_j} + \frac{\partial \bar{u}_j}{\partial x_i} \right) \quad (9)$$

$$\overline{u_i'' \theta''} = -K_h \frac{\partial \bar{\theta}}{\partial x_i} \quad (10)$$

$$\overline{u_i'' q_v''} = -K_h \frac{\partial \bar{q}_v}{\partial x_i} \quad (11)$$

$$\overline{u_i'' s''} = -K_h \frac{\partial \bar{s}}{\partial x_i}, \quad (12)$$

where  $K_m$  and  $K_h$  are the local SGS diffusivities of momentum and heat, respectively. In order to distinguish between

different filter operations, the overbar is used to denote variables that are filtered with the horizontal grid spacing  $\Delta$  in this subsection. While  $K_h$  is calculated as in the Deardorff scheme, a dynamic approach is applied to calculate  $K_m$ , viz.

$$K_m = c_* \Delta_{\max} \sqrt{e}, \quad (13)$$

where  $\Delta_{\max} = \max(\Delta_x, \Delta_y, \Delta_z)$ . Unlike in the Deardorff scheme,  $c_*$  is not a fixed value but is calculated at each time step for each grid cell. As for the Deardorff scheme,  $e$  is calculated using a prognostic equation:

$$\begin{aligned} \frac{\partial e}{\partial t} = & -\bar{u}_j \frac{\partial e}{\partial x_j} - \left( \overline{u_i'' u_j''} \right) \frac{\partial \bar{u}_i}{\partial x_j} + \frac{g}{\theta_{v,\text{ref}}} \overline{u_3'' \theta''} \\ & - \frac{\partial}{\partial x_j} \left[ u_j'' \left( e + \frac{p''}{\rho} \right) \right] - (0.19 + 0.74l/\Delta) \frac{e^{3/2}}{l}, \end{aligned} \quad (14)$$

with  $l$  being a mixing length. Note that, in the SGS closures,  $\theta_{v,\text{ref}}$  refers to either a given reference value or the local value of  $\bar{\theta}$ . The pressure term in Eq. (14) is parameterized as

$$\left[ u_j'' \left( e + \frac{p''}{\rho} \right) \right] = -2K_m \frac{\partial e}{\partial x_j}. \quad (15)$$

The left-hand side of Eq. (9) is called deviatoric subgrid stress. Using the rate of strain tensor  $S_{ij} = 0.5 \left( \frac{\partial \bar{u}_i}{\partial x_j} + \frac{\partial \bar{u}_j}{\partial x_i} \right)$ , it can be written as follows:

$$\tau_{ij}^d = \tau_{ij} - \frac{\tau_{nn}}{3} \delta_{ij} = -2K_m \bar{S}_{ij}, \quad (16)$$

where we used the summation convention. The subgrid stress can also be expressed as  $\tau_{ij} = \overline{u_i u_j} - \bar{u}_i \bar{u}_j$ . This expression makes clear why the subgrid stress has to be modeled, since only the second term of the right-hand side is known. Following Germano et al. (1991), a test filter is introduced, which is  $\Delta^T = 2\Delta$  in our case. The subgrid stress on the test filter scale then is  $T_{ij} = \overline{\widehat{u_i u_j}} - \widehat{\bar{u}_i} \widehat{\bar{u}_j}$ , where also the first term on the right-hand side is unknown (the hat denotes a filter operation with the width of the test filter). The difference between subgrid stress on the test filter level and the test-filtered subgrid stress is the resolved stress  $L_{ij} = T_{ij} - \widehat{\tau_{ij}} = \overline{\widehat{u_i u_j}} - \widehat{\bar{u}_i} \widehat{\bar{u}_j}$ . Both terms on the right-hand side are known, and  $L_{ij}$  can thus be calculated directly by application of the test filter to the resolved velocities on the grid cells. As described in Heinz (2008),  $c_*$  can be calculated via

$$c_* = - \frac{L_{ij}^d \widehat{S}_{ji}}{2\nu_*^T \widehat{S}_{mn} \widehat{S}_{nm}}, \quad (17)$$

where  $\nu_*^T = \Delta^T (L_{ii}/2)^2$  is the subtest-scale viscosity. The stability of the simulation is ensured by using dynamic bounds that keep the values of  $c_*$  in the range

$$|c_*| \leq \frac{23}{24\sqrt{3}} \frac{\sqrt{e}}{\Delta \sqrt{\widehat{S}_{ij} \widehat{S}_{ji}}}, \quad (18)$$

**Table 3.** List of SGS model symbols.

Symbol	Dimension	Description
$c_*$		Dynamic subgrid-scale coefficient
$e$	$\text{m}^2 \text{s}^{-2}$	Subgrid-scale turbulence kinetic energy (total turbulent kinetic energy in RANS mode)
$l$	$\text{m}$	Mixing length
$l_B$	$\text{m}$	Mixing length after Blackadar (1962)
$l_{\text{wall}}$	$\text{m}$	Minimum mixing length
$K_h$	$\text{m}^2 \text{s}^{-1}$	SGS eddy diffusivity of heat
$K_m$	$\text{m}^2 \text{s}^{-1}$	SGS eddy diffusivity of momentum
$L_{ij}$	$\text{m}^2 \text{s}^{-2}$	Resolved stress tensor
$S_{ij}$	$\text{s}^{-1}$	Strain tensor
$T_{ij}$	$\text{m}^2 \text{s}^{-2}$	Subtest-scale stress tensor
$\epsilon$	$\text{m}^2 \text{s}^{-3}$	SGS-TKE dissipation rate
$\nu_*^T$	$\text{m}^2 \text{s}$	Subtest-scale viscosity parameter
$\tau_{ij}$	$\text{m}^2 \text{s}^{-2}$	SGS stress tensor
$\tau_{d,ij}$	$\text{m}^2 \text{s}^{-2}$	Deviatoric SGS stress tensor

as derived by Mokhtarpoor and Heinz (2017). This model does not need artificial limitation of the range of  $c_*$  for stable runs and allows the occurrence of energy backscatter (i.e., negative values of  $K_m$ ). Unlike other dynamic models, this formulation of  $c_*$  is not derived using model assumptions for the subgrid stress and the stress on the test filter level but is derived as consequence of stochastic analysis (Heinz, 2008; Heinz and Gopalan, 2012).

### 2.2.2 RANS turbulence closures

For RANS mode, PALM offers two different turbulence closures – a TKE- $l$  and the standard TKE- $\epsilon$  closure (Mellor and Yamada, 1974, 1982) – to calculate the eddy diffusivities, which then describe diffusion by the complete turbulence spectrum. While the TKE- $l$  closure uses a single prognostic equation to calculate the TKE, the standard TKE- $\epsilon$  closure applies an additional prognostic equation for  $\epsilon$  in addition to the equation for  $e$ .

In the TKE- $l$  closure (e.g., Holt and Raman, 1988), the eddy diffusivities are calculated via  $e$  and  $l$  as

$$K_m = c_0 l \sqrt{e}, \quad (19)$$

$$K_h = \frac{K_m}{Pr}, \quad (20)$$

where  $Pr = 1$  denotes the Prandtl number and  $c_0 = 0.55$  denotes a model constant. The Prandtl number can be changed to a user-specific value for different stability regimes. Note that, in the case of RANS mode,  $e$  denotes the total turbulent kinetic energy as the full turbulence spectrum is parameterized. To calculate  $e$ , Eq. (14) is modified by introducing gradient approaches for the turbulent transport terms:

$$\begin{aligned} \frac{\partial e}{\partial t} = & -\bar{u}_j \frac{\partial e}{\partial x_j} + K_m \left( \frac{\partial \bar{u}_i}{\partial x_j} + \frac{\partial \bar{u}_j}{\partial x_i} \right) \frac{\partial \bar{u}_i}{\partial x_j} \\ & - \frac{g}{\theta_{v,\text{ref}}} K_h \frac{\partial \bar{\theta}_v}{\partial z} + K_e \frac{\partial^2 e}{\partial x_j^2} - \epsilon. \end{aligned} \quad (21)$$

Here,  $K_e = \frac{K_m}{\sigma_e}$  is the diffusivity of  $e$ , with the model constant  $\sigma_e = 1$  as default value, and  $\epsilon$  is calculated as

$$\epsilon = c_0^3 e \frac{\sqrt{e}}{l}. \quad (22)$$

The mixing length  $l$  is calculated using the mixing length after Blackadar (1962)  $l_B$  and the similarity function of momentum  $\Phi_m$  for stable conditions in the formulation of Businger–Dyer (see, e.g., Panofsky and Dutton, 1984):

$$l = \begin{cases} \min\left(\frac{l_B}{\Phi_m}, l_{\text{wall}}\right) & \text{for } \frac{z}{L} \geq 0, \\ \min(l_B, l_{\text{wall}}) & \text{for } \frac{z}{L} < 0, \end{cases} \quad (23)$$

with

$$l_B = \frac{\kappa z}{1 + \frac{\kappa z}{0.00027(u_{g,1}^2 + u_{g,2}^2)^{0.5}} f}, \quad \text{and} \quad (24)$$

$$\Phi_m = 1 + 5 \frac{z}{L}, \quad (25)$$

where  $\kappa = 0.4$  denotes the von Kármán constant,  $L$  the Obukhov length, and  $z$  the height above the surface. The mixing length is limited by  $l_{\text{wall}}$ , which is the distance to the nearest solid surface.

Aside from the TKE- $l$  closure, also a standard TKE- $\epsilon$  model is available as a turbulence closure. When choosing the standard TKE- $\epsilon$  model,  $K_m$  is calculated via

$$K_m = c_0^4 \frac{e^2}{\epsilon}. \quad (26)$$

The modeled TKE is calculated using Eq. (21) and an additional prognostic equation is used to calculate  $\epsilon$ :

$$\begin{aligned} \frac{\partial \epsilon}{\partial t} = & -u_j \frac{\partial \epsilon}{\partial x_j} + c_1 \frac{\epsilon}{e} K_m \left( \frac{\partial \bar{u}_i}{\partial x_j} + \frac{\partial \bar{u}_j}{\partial x_i} \right) \frac{\partial \bar{u}_i}{\partial x_j} \\ & - c_3 \frac{\epsilon}{e} \frac{g}{\theta_{v,\text{ref}}} K_h \frac{\partial \bar{\theta}_v}{\partial z} + K_\epsilon \frac{\partial^2 \epsilon}{\partial x_j^2} - c_2 \frac{\epsilon^2}{e}, \end{aligned} \quad (27)$$

where  $K_\epsilon = \frac{K_m}{\sigma_\epsilon}$  with  $\sigma_\epsilon = 1.3$  and  $c_1 = 1.44$ ,  $c_2 = 1.92$ , and  $c_3 = 1.44$  being model constants (e.g., Launder and Spalding, 1974; Oliveira and Younis, 2000). As the constants  $c_0 - c_3$  as well as  $\sigma_e$  and  $\sigma_\epsilon$  depend on the situation studied, they might need to be adjusted by the user.

## 2.3 Boundary conditions

### 2.3.1 Constant flux layer

Following Monin–Obukhov similarity theory (MOST), a constant flux layer assumption is used between the surface and the first computational grid level ( $k = 1$ ,  $z_{\text{mo}} = 0.5 \cdot \Delta z$ ). Using roughness lengths for heat, humidity, and momentum ( $z_{0,h}$ ,  $z_{0,q}$ , and  $z_0$ , respectively), MOST then provides surface fluxes of momentum (shear stress) and scalar quantities (heat and moisture flux) as bottom boundary conditions. In PALM, it is assumed that MOST can be applied locally, even though there is no theoretical foundation for this assumption. Hultmark et al. (2013), e.g., pointed out that this leads to a systematical overprediction of the mean shear stress. However, this local method has the advantage that surface heterogeneities can be prescribed at the surface, and therefore it has become standard in most contemporary LES codes.

The surface layer vertical profile of the horizontal wind velocity  $u_h = (\bar{u}^2 + \bar{v}^2)^{\frac{1}{2}}$  is predicted by MOST through

$$\frac{\partial u_h}{\partial z} = \frac{u_*}{\kappa z} \Phi_m \left( \frac{z}{L} \right), \quad (28)$$

where  $\Phi_m$  is the similarity function for momentum in the formulation of Businger–Dyer (see, e.g., Panofsky and Dutton, 1984):

$$\Phi_m = \begin{cases} 1 + 5 \frac{z}{L} & \text{for } \frac{z}{L} \geq 0, \\ (1 - 16 \frac{z}{L})^{-\frac{1}{4}} & \text{for } \frac{z}{L} < 0. \end{cases} \quad (29)$$

The scaling parameters  $\theta_*$  and  $q_*$  are defined by MOST as

$$\begin{aligned} \theta_* &= -\frac{\overline{w''\theta''_0}}{u_*}, \\ q_* &= -\frac{\overline{w''q''_0}}{u_*}, \end{aligned} \quad (30)$$

with the friction velocity  $u_*$  (defined through the square root of the surface shear stress) as

$$u_* = \left[ (\overline{u''w''_0})^2 + (\overline{v''w''_0})^2 \right]^{\frac{1}{4}}. \quad (31)$$

In PALM,  $u_*$  is calculated from  $u_h$  at  $z_{\text{mo}}$  by vertical integration of Eq. (28) over  $z$  from  $z_0$  to  $z_{\text{mo}}$ .

From Eqs. (28), (31), and a geometric decomposition of both the wind vector and  $u_*$ , it is possible to derive a formulation for the horizontal wind components, viz.

$$\frac{\partial \bar{u}}{\partial z} = \frac{-\overline{u''w''_0}}{u_* \kappa z} \Phi_m \left( \frac{z}{L} \right) \quad \text{and} \quad \frac{\partial \bar{v}}{\partial z} = \frac{-\overline{v''w''_0}}{u_* \kappa z} \Phi_m \left( \frac{z}{L} \right). \quad (32)$$

Vertical integration of Eq. (32) over  $z$  from  $z_0$  to  $z_{\text{mo}}$  then yields the surface momentum fluxes  $\overline{u''w''_0}$  and  $\overline{v''w''_0}$ .

The formulations above all require knowledge of the scaling parameters  $\theta_*$  and  $q_*$ . These are deduced from vertical integration of

$$\frac{\partial \bar{\theta}}{\partial z} = \frac{\theta_*}{\kappa z} \Phi_h \left( \frac{z}{L} \right) \quad \text{and} \quad \frac{\partial \bar{q}_v}{\partial z} = \frac{q_*}{\kappa z} \Phi_h \left( \frac{z}{L} \right) \quad (33)$$

over  $z$  from  $z_{0,h}$  to  $z_{\text{mo}}$ . The similarity function  $\Phi_h$  is given by

$$\Phi_h = \begin{cases} 1 + 5 \frac{z}{L} & \text{for } \frac{z}{L} \geq 0, \\ (1 - 16 \frac{z}{L})^{-1/2} & \text{for } \frac{z}{L} < 0. \end{cases} \quad (34)$$

Previously, the implementation of the constant flux layer involved a diagnostic–prognostic equation for  $L$ , based on data from the previous time step. Even though it was found that this method introduces only negligible errors, we decided to revise this procedure and calculate  $L$  based on using a Newton iteration method instead. By doing so, we can achieve a correct value of  $L$  which can be important when the model is coupled to a surface scheme. We also found that this does not increase the computational costs to a significant amount (usually less than 1%). Starting from PALM 6.0 (revision 3668), Newton iteration is the only available method. The Newton iteration method involves the calculation of a bulk Richardson number  $Ri_b$ . Depending on whether fluxes are prescribed or Dirichlet boundary conditions are used for temperature and humidity,  $Ri_b$  is related to  $L$  via

$$Ri_b = \frac{z_{\text{mo}}}{L} \cdot \begin{cases} \frac{\varphi_h}{\varphi_m^2} & \text{for Dirichlet conditions,} \\ \frac{1}{\varphi_m^3} & \text{for prescribed fluxes,} \end{cases} \quad (35)$$

where

$$\varphi_h = \log \left( \frac{z_{\text{mo}}}{z_{0,h}} \right) - \Psi_h \left( \frac{z_{\text{mo}}}{L} \right) + \Psi_h \left( \frac{z_{0,h}}{L} \right) \quad (36)$$

and

$$\varphi_m = \log \left( \frac{z_{\text{mo}}}{z_0} \right) - \Psi_m \left( \frac{z_{\text{mo}}}{L} \right) + \Psi_m \left( \frac{z_0}{L} \right) \quad (37)$$

are the integrated universal profile stability functions of  $\Psi_m$  and  $\Psi_h$  (see Paulson, 1970; Holtslag and De Bruin, 1988), so



that a (bulk) Richardson number can be defined:

$$Ri_b = \begin{cases} \frac{gz_{mo}(\bar{\theta}_{v,mo} - \theta_{v,0})}{u_h^2 \bar{\theta}_v} & \text{for Dirichlet conditions,} \\ -\frac{gz_{mo} w'' \bar{\theta}_v''}{\kappa^2 u_h^3 \bar{\theta}_v} & \text{for prescribed fluxes.} \end{cases} \quad (38)$$

The above equations are solved for  $L$  by finding the root of the function  $f_N$ :

$$f_N = Ri_b - \frac{z_{mo}}{L} \cdot \begin{cases} \frac{[\varphi_h]}{[\varphi_m]^2} & \text{for Dirichlet conditions.} \\ \frac{[\varphi_h]}{[\varphi_m]^3} & \text{for prescribed fluxes.} \end{cases} \quad (39)$$

The solution is then given by iteration of

$$L^{n+1} = L^n - \frac{f_N(L^n)}{f'_N(L^n)}, \quad (40)$$

with iteration step  $n$ , and

$$f'_N(L) = \frac{\partial f_N}{\partial L}, \quad (41)$$

until  $L$  meets a convergence criterion.

The surface fluxes of sensible and latent heat, as well as the surface shear stress, are then calculated using Eqs. (30) and (31). Note that for vertically oriented surfaces in combination with an interactive surface model switched on (see Sects. 3.5 and 4.5), the surface fluxes are calculated after Krayenhoff and Voigt (2007) as static stability considerations do not apply for such surface orientations (see also Resler et al., 2017). Also note that the above formulation can lead to violations of MOST for too-coarse grid spacings in some cases, particularly for setups of stable boundary layers, as the first grid layer might be located in the roughness sublayer of the surface layer. For a discussion of this issue and an improved boundary condition, see Basu and Lacser (2017) and Maronga et al. (2020).

In the case of the TKE- $\epsilon$  RANS closure, the boundary condition for  $e$ ,  $\epsilon$ , and  $K_m$  are

$$e = \left( \frac{u_*}{c_0} \right), \quad (42)$$

$$\epsilon = \frac{u_*^3}{\kappa z_{mo}}, \quad (43)$$

$$K_m = \kappa u_* z_{mo} \Phi_m^{-1} \left( \frac{z_{mo}}{L} \right). \quad (44)$$

### 2.3.2 Wave-dependent surface roughness

As the ocean surface in PALM is assumed to be flat and waves are not explicitly resolved, a Charnock parameterization can be switched on which relates the surface roughness lengths to the friction velocity as described in Beljaars (1994). This accounts for the fact that water surfaces become

**Table 4.** List of surface layer symbols.

Symbol	Dimension	Description
$L$	m	Obukhov length
$q_*$	kg kg <sup>-1</sup>	MOST humidity scale
$Ri_b$		Bulk Richardson number
$u_h$	ms <sup>-1</sup>	Absolute value of the horizontal wind
$z_{mo}$	m	Height above the surface where MOST is applied
$z_0$	m	Roughness length for momentum
$z_{0,h}$	m	Roughness length for heat
$z_{0,q}$	m	Roughness length for moisture
$\theta_*$	K	MOST temperature scale
$\Phi_h$		Similarity function for heat
$\Phi_m$		Similarity function for momentum
$\Psi_h$		Integrated similarity function for heat
$\Psi_m$		Integrated similarity function for momentum
$\varphi_h$		Integrated similarity function term for heat
$\varphi_m$		Integrated similarity function term for momentum

aerodynamically smooth for low wind speeds. For ocean surfaces, the roughness lengths are thus calculated for each surface grid point as

$$z_0 = \frac{0.11\nu}{u_*} + \alpha_{Ch} \frac{u_*^2}{g}, \quad (45)$$

$$z_{0,h} = \frac{0.4\nu}{u_*}, \quad (46)$$

$$z_{0,q} = \frac{0.62\nu}{u_*}, \quad (47)$$

with  $\alpha_{Ch} = 0.0018$  being the Charnock constant, and  $\nu = 1.461 \times 10^{-5} \text{ m}^2 \text{ s}^{-1}$  being the kinematic viscosity. Note that this parameterization is designed for large-scale models where waves are a subgrid-scale phenomenon. For fine grid spacings and/or large waves (in amplitude and wavelength), this parameterization can lead to erroneous roughness lengths and should not be switched on without rigorous testing.

### 2.3.3 Lateral boundary conditions

At lateral domain boundaries, various different conditions can be applied, which are listed in Table 9.

By default, cyclic boundary conditions apply at all lateral domain boundaries. Choosing an inflow boundary condition at one of the four domain boundaries requires to set an outflow condition at the opposing boundary while keeping the boundaries in perpendicular direction cyclic. An exception

is made in the case of model nesting, where inflow/outflow boundary conditions are set dynamically for each individual boundary grid point (see Sect. 4.8 and 4.9).

The simplest inflow condition is a purely laminar inflow using Dirichlet conditions at either domain boundary. A more sophisticated approach with fully developed turbulence already present at the inflow boundary can be achieved by using the turbulence-recycling method, which is implemented according to Lund et al. (1998) and Kataoka and Mizuno (2002). The turbulence-recycling method sets a fixed mean inflow condition at one side of the simulation domain and adds a turbulent signal from within the model domain to these mean profiles. This then creates a turbulent inflow (see Maronga et al., 2015). The turbulence-recycling method is currently only available at the left domain boundary, i.e., at  $x = 0$ .

The downside of the turbulence-recycling method is the requirement of an additional recycling area within the model domain which is purely needed to generate turbulence and cannot be used for data evaluation of the studied phenomenon. To avoid the necessity of including an additional recycling area within the simulation domain, a synthetic turbulence generator can be used instead of the turbulence-recycling method at the inflow boundary (Gronemeier et al., 2015). This turbulence generator is based on the method published by Xie and Castro (2008) with the modification of Kim et al. (2013) for divergence-free inflow. The turbulence-generation method calculates stochastic fluctuations from an arrayed random number. This is realized via given length scales that are added to the mean inflow profiles using a Lund rotation (Lund et al., 1998) and a given Reynolds stress tensor. In order to apply the synthetic turbulence generator, information on the turbulent length scales for the three wind components in the  $x$ ,  $y$ , and  $z$  directions, as well as the Reynolds stress tensor, is required. These information can be either obtained from idealized precursor simulations or from observations (Xie and Castro, 2008). In combination with the offline nesting (see Sect. 4.9), PALM also offers the possibility to compute turbulent length scales and Reynolds stress following the parameterizations described by Rotach et al. (1996).

At the outflow boundary, radiation conditions are used by default for the velocity components as proposed by Orlandi (1976). Velocity components are advected by a transport velocity  $u_{\text{tr}}$  which is calculated from the gradients of the transported velocity components normal to the boundary at the grid points next to the outflow boundary (see also Maronga et al., 2015). The transport velocity is restricted to  $0 \leq u_{\text{tr}} \leq \Delta/\Delta t$ , where  $\Delta t$  denotes the time step.

In cases with weak background wind in a convective boundary layer, it was found that using the radiation condition can lead to instabilities and strong self-intensifying inflow regimes at the outflow boundary (Gronemeier et al., 2017). In order to prevent such artificial inflow situations at the outflow boundary, an empirical approach can be used at

the outflow boundary, the so-called turbulent outflow condition (Gronemeier et al., 2017). Instead of transporting the velocity components via the radiation condition, instantaneous values of  $\bar{u}$ ,  $\bar{v}$ ,  $\bar{w}$ ,  $\bar{\theta}$ , and  $e$  are taken from a vertical plane situated at a distance  $x_d$  from the outflow boundary which are then mapped to the outflow boundary. By taking the information of the flow field from within the domain, occurring inflow regimes are disturbed and cannot intensify themselves as long as a proper  $x_d$  is chosen which needs to be a fair distance away from the outflow boundary. Note that the turbulent outflow condition can be transformed into the radiation condition, where  $u_{\text{tr}} = \Delta/\Delta t$  if  $x_d = 0$ . As for now, the turbulent outflow condition is only available at the right domain boundary.

## 2.4 Ocean option

PALM's ocean option has been extended to include wave effects to account for the Langmuir circulation, which can be optionally switched on. For this, the momentum equation is modified by including a vortex force and an additional advection by the Stokes drift following the theory by Craik and Leibovich (1976), similarly to McWilliams et al. (1997) and Skillingstad and Denbo (1995). Furthermore, a simple parameterization of wave-breaking effects has been included. The modified momentum equations for the ocean then reads

$$\begin{aligned} \frac{\partial \bar{u}_i}{\partial t} = & -(\bar{u}_j + u_{s,j}) \frac{\partial \bar{u}_i}{\partial x_j} - \varepsilon_{ijk} f_j (\bar{u}_k + u_{s,k}) \\ & + \varepsilon_{i3j} f_3 u_{g,j} - \frac{\partial \pi^*}{\partial x_i} + \varepsilon_{ijk} u_{s,j} \omega_k \\ & - g \frac{\bar{\rho}_\theta - \langle \rho_\theta \rangle}{\langle \rho_\theta \rangle} \delta_{i3} - \frac{\partial}{\partial x_j} \left( \overline{u_i'' u_j''} - \frac{2}{3} e \delta_{ij} \right) + F_i, \end{aligned} \quad (48)$$

where  $u_s$  is the Stokes drift velocity,  $\rho_\theta$  the potential density, and  $\omega_i = \varepsilon_{ijk} \frac{\partial u_k}{\partial x_j}$  the rotation of the velocity field.  $F$  is a random forcing term that represents the generation of small-scale turbulence by wave breaking. It should be kept in mind that the incompressibility assumption is used in the ocean option. It is assumed that wind stress and wave fields are in the same direction, and that the wave field is steady and monochromatic. The magnitude of the Stokes velocity along the wind stress direction is then given by

$$u_s = U_s \exp\left(\frac{4\pi z}{\lambda_w}\right), \quad (49)$$

with  $U_s = (\pi z_w / \lambda)^2 (g \lambda_w / 2\pi)^{1/2}$ , where  $z_w$  is the wave height and  $\lambda_w$  is the wavelength. The current implementation of wave effects strictly follows Noh et al. (2004), in particular the parameterization of wave breaking. Note that Noh et al. (2004) used an earlier version of PALM, where the programming of the wave effects was completely realized via PALM's user interface.

As part of the general code modularization effort, all ocean-related code has been put into one Fortran module, and

## 2.2 Bulk cloud model

In PALM a two-moment mixed-phase (the ice phase is implemented since 2021) bulk micro-physics scheme after Seifert and Beheng (2001, 2006) is implemented. However, the studies presented in this thesis apply non-freezing environmental conditions. Accordingly, a presentation of the ice and mixed-phase processes are omitted.

In the case that the bulk cloud model is turned on, prognostic equations for the total water mixing ratio  $q$

$$q = q_v + q_l, \quad (2.1)$$

and the liquid water potential temperature  $\theta_l$  (e.g. Emanuel, 1994)

$$\theta_l = \theta - \frac{L_v}{c_p \Pi} q_l \quad (2.2)$$

are solved (instead of water vapor mixing ratio  $q_v$  and potential temperature  $\theta$ ), where latent heat of evaporation is denoted with  $L_v$  and  $c_p$  is the heat capacity of dry air at constant pressure. The liquid water mixing ratio is defined as  $q_l = q_c + q_r$ , where  $q_c$  and  $q_r$  are the cloud and rain water mixing ratio, respectively. Moreover, based on Eq. 2.1 water vapor mixing ratio is derived as the difference of total water vapor mixing ratio and the liquid water mixing ratio  $q_v = q - q_l$ . Droplets of the size of rain droplets are not present in a relevant mass in the fog studies presented in this thesis and  $q_c \gg q_r$ . Thus, for simplicity sake, in the following, only processes relevant for the cloud water specie will be presented. The Exner function  $\Pi$  relates absolute temperature and potential temperature and is defined in Eq. 7 in the PALM overview article at the beginning of this section (see Sec. 2.1). Both,  $q$  and  $\theta_l$  are conserved quantities during wet adiabatic process, which implies that condensation and evaporation must not be considered for these variables.

The underlying assumption of a bulk scheme (see also Sec. 1.2.1) is to divide the spectrum into different species classes (cloud droplets and rain droplets). In the implemented scheme, the separation radius between cloud and rain droplets is  $r_{\text{sep}} = 40 \mu\text{m}$ . Moreover, instead of resolving the DSD it is parameterized in bulk cloud models by means of functions (exponential, gamma, or lognormal). The "two-moment" prefix signifies the solution of prognostic equations in terms of mass for the 0th moment, representing the number concentration, and the 1st moment, representing the cloud water mixing ratio. Thus, the equations predicting cloud droplet number and concentration  $n_c$  and cloud water mixing ratio  $q_c$  are expressed as follows:

$$\frac{\partial \bar{n}_c}{\partial t} = -\bar{u}_j \frac{\partial \bar{n}_c}{\partial x_j} - \frac{\partial}{\partial x_j} (\overline{u_j n_c}) + \chi_{n_c}, \quad (2.3)$$

$$\frac{\partial \bar{q}_c}{\partial t} = -\bar{u}_j \frac{\partial \bar{q}_c}{\partial x_j} - \frac{\partial}{\partial x_j} (\overline{u_j q_c}) + \chi_{q_c}. \quad (2.4)$$

The prognostic quantities of the bulk cloud model are defined on the Eulerian grid as scalar quantities. Accordingly, the same numerical methods for the transportation of these quan-

tities (first term of right-hand side of Eq. 2.3 and 2.4) as for the potential temperature and total water mixing ratio (see Sec. 2.1) are used. The SGS fluxes are calculated from:

$$\overline{u_j'' n_c''} = -K_h \frac{\partial \overline{n_c}}{\partial x_j}, \quad (2.5)$$

$$\overline{u_j'' q_c''} = -K_h \frac{\partial \overline{q_c}}{\partial x_j}, \quad (2.6)$$

where  $K_h$  is the eddy diffusivity coefficient for heat. The microphysical processes are included in the sink and source term  $\chi_{n_c}$  and  $\chi_{q_c}$ , respectively. The sink and source terms are given by

$$\chi_{n_c} = \left. \frac{\partial \overline{n_c}}{\partial t} \right|_{\text{act}} + \left. \frac{\partial \overline{n_c}}{\partial t} \right|_{\text{evap}} + \left. \frac{\partial \overline{n_c}}{\partial t} \right|_{\text{auto}} + \left. \frac{\partial \overline{n_c}}{\partial t} \right|_{\text{sed,c}}, \quad (2.7)$$

$$\chi_{q_c} = \left. \frac{\partial \overline{q_c}}{\partial t} \right|_{\text{cond}} + \left. \frac{\partial \overline{q_c}}{\partial t} \right|_{\text{evap}} + \left. \frac{\partial \overline{q_c}}{\partial t} \right|_{\text{sed,c}}, \quad (2.8)$$

which include the processes of activation (act), condensation (cond) and evaporation (evap), autoconversion (auto) and sedimentation (sed,c). In the following, the microphysical tendencies determining the sink/source term are presented. Note, that in agreement with the notation in Sec. 2.1 a double prime indicates SGS variables, while the overbar relates to filtered quantities. However, as not explicitly stated otherwise, filtered quantities are used in most equations. Hence, the overbar is omitted in the following.

### 2.2.1 Activation

The number of cloud droplets is crucially determined by activation. Due to the lack of explicit representation of aerosol and droplet size in bulk cloud models, the activation process must be parameterized. As for most bulk cloud models common Twomey-type parametrizations for activation in PALM are used. While being part of the first presented study (Chapter 3), three different formulations have been tested. However, only the first and the second method have been implemented to the default code.

(i) In agreement with the originally proposed shape of Twomey (1959) the scheme implies that Eq. 1.13 is translated to the model as

$$N_{\text{CCN}} = N_a S^{k_{\text{act}}}, \quad (2.9)$$

where  $N_{\text{CCN}}$  is the number of activated cloud condensation nuclei and  $N_a$  and  $k_{\text{act}}$  depend on the aerosol distribution and must be prescribed by the user. The supersaturation  $S$ , unless otherwise declared, is derived from the temperature and water vapor mixing ratio and calculated as

$$S = \frac{q_v}{q_s} - 1, \quad (2.10)$$

with  $q_s$  being the saturation water vapor mixing ratio. However, as the liquid water temperature is predicted, the saturation water vapor mixing ratio must be written as

$$q_s(T_1) = \frac{R_d}{R_v} \frac{e_s(T_1)}{p - e_s(T_1)}. \quad (2.11)$$

The saturation water vapor pressure is determined from an empirical relationship (Bougeault, 1981):

$$e_s(T_1) = 610.78 \exp \left[ \frac{17.269 \cdot (T_1 - 273.16)}{T_1} \right]. \quad (2.12)$$

Subsequently,  $q_s(T)$  is received using a first-order Taylor series expansion from  $q_s(T_1)$  (Sommeria and Deardorff, 1977):

$$q_s(T) = q_s(T_1) \frac{1 + \beta_t + q}{1 + \beta_t + q_s(T_1)}, \quad (2.13)$$

where  $\beta_t$  is

$$\beta_t = \frac{L_v^2}{R_v c_p T_1^2}. \quad (2.14)$$

(ii) A more advanced shape of Eq. 2.9 was implemented in the bulk cloud model. This advanced method allows to consider the physiochemical properties of the dry aerosol spectrum directly. Here the dry aerosol spectrum  $f(r_s)$  is assumed to follow up to three log-normal distributions (e.g., Jaenicke, 1993) which are given by

$$\frac{df(r_s)}{dr} = \sum_{i=1}^3 \frac{N_{a,i}}{r_s \sqrt{2\pi} \log(\sigma_{s,i})} \exp \left[ -\frac{\log(r_s/R_{s,i})^2}{2 \log(\sigma_{s,i})^2} \right], \quad (2.15)$$

where  $r_s$  is the dry aerosol radius and  $R_{s,i}$  the mean radius of the dry aerosol mode, respectively. The dispersion of the dry aerosol spectrum is denoted with  $\sigma_{s,i}$ . These parameters must be prescribed by the user. Based on the formulation of Khvorostyanov and Curry (2006) the number of activated aerosols is calculated from

$$N_{CCN}(S) = \frac{N_a}{2} [1 - \operatorname{erf}(u_s)], \quad (2.16)$$

$$u_s = \frac{\log(S_0/S)}{\sqrt{2} \log(\sigma_a)}. \quad (2.17)$$

The Gaussian error function is termed with "erf", and

$$S_0 = R_{s,i}^{-1+\beta_s} \left( \frac{4A^3}{27b} \right)^{1/2}, \quad (2.18)$$

$$\sigma_S = \sigma_{s,i}^{1+\beta_s}, \quad (2.19)$$

where  $S_0$  is the mean geometric supersaturation and  $\sigma_S$  the supersaturation dispersion (Khvorostyanov and Curry, 2006). The soluble fraction of the aerosol is prescribed with  $\beta_s$  and set to  $\beta_s=0.5$ , which implies that the soluble fraction of the aerosol is proportional to the mass of the aerosol. This value is used as a common parameter for the parametrization of activation in bulk models (e.g., Von der Emde and Wacker, 1993; Abdul-Razzak et al., 1998). The parameters  $A$  and  $b$  including effects of surface tension and the chemical properties of the aerosol are calculated from

$$A = \frac{2\sigma}{\rho_1 R_v T}, \quad (2.20)$$

$$b = \frac{i\rho_s M_1}{\rho_1 M_s}. \quad (2.21)$$

The temperature-dependence of the surface tension of water  $\sigma$  is taken into account by

$$\sigma = 7.61 \times 10^{-2} - 1.55 \times 10^{-4} \cdot (T - 273.15), \quad (2.22)$$

which is based on an empirical formulation (Eq. 5.120 in Straka, 2009). The van't Hoff factor  $i$  depends on the aerosol type.  $M_1$  and  $M_s$  are the molecular weight of water and of the aerosol, respectively.

**(iii)** For the research of the first study (see Sec. 3), a further activation scheme was applied. This method calculates a maximum supersaturation based on the function of supersaturation change in time. This function includes the change in supersaturation by lifting, release of latent heat due condensation and evaporation, and radiation. Following Cohard et al. (1998) the number of activated droplets is given by

$$N_{CCN}(S) = C S_{\max}^{k_C} \cdot F_C \left( \mu_C, \frac{k_C}{2} + \frac{k_C}{2} + 1; -\beta_C S_{\max}^2 \right), \quad (2.23)$$

where  $C$  is proportional to the total number concentration of CCNs that are activated, when  $S$  approaches infinity.  $F_C$  is the hypergeometric function. The parameters  $k_C$  and  $\mu_C$  and  $\beta_C$  are adjustable shape parameters associated with the characteristics of the aerosol size spectrum. More precisely, the parameters correspond to the mean geometric dry aerosol radius, the dispersion of the aerosol spectrum and the solubility of the aerosols (see Eq. 2.15). Therefore, this method is in general similar to the method described in (ii), but also approximate realistic activation tendencies if no realistic supersaturation can be derived from the fields of temperature and water vapor mixing ratio. Consequently, the maximum supersaturation is estimated as

$$S_{\max}^{k_C+2} F_C \left( \mu_C, \frac{k_C}{2} + \frac{k_C}{2} + 1; -\beta_C S_{\max}^2 \right) = \frac{(\phi_1 w + \phi_3 \frac{\partial T}{\partial t} |_{\text{rad}})^{3/2}}{2k_C \pi \rho_1 \phi_2 B_C(\frac{k_C}{2}, \frac{3}{2})}, \quad (2.24)$$

where  $w$  is the vertical velocity and  $B_C$  is the beta function, i.e., a series of gamma functions. The functions  $\phi_1$ ,  $\phi_2$  and  $\phi_3$  depend on the temperature and pressure and are yielded by

$$\phi_1 = \frac{g}{TR_d} \left( \frac{L_v}{c_p T} - 1 \right), \quad (2.25)$$

$$\phi_2 = \left( \frac{pR_v}{e_s R_d} + \frac{L_v}{R_v T^2 c_p} \right), \quad (2.26)$$

$$\phi_3 = \frac{L_v}{\rho R_v T^2 c_p}. \quad (2.27)$$

In practice, the function  $F_C$  can be tabulated, and the parameters within the functions  $\phi_1$ ,  $\phi_2$ , and  $\phi_3$  can be pre-calculated.

A further discussion of the differences between the activation parametrizations is part of the research presented in Sec. 3. Regardless of the method used to determine the number of activated droplets, the change in droplet number concentration is obtained by

$$\left. \frac{\partial n_c}{\partial t} \right|_{\text{acti}} = \max \left( \frac{N_{\text{CCN}} - n_c}{\Delta t}, 0 \right), \quad (2.28)$$

where  $n_c$  is the number of previously activated aerosols that are assumed to be equal to the number of pre-existing droplets. It must be mentioned, that in regions with significant droplet depletion by collision and coalescence the number of activated droplets might be overpredicted by Eq. 2.28 (Morrison et al., 2005). This effect is assumed to be negligible in fog, where collision and coalescence is weak.

### 2.2.2 Diffusional growth

To consider diffusional growth in bulk cloud models, different methods are available. In the following, the most common methods for condensation and evaporation, which have been tested for a fog case (see Sec. 3), are presented.

(i) In most bulk cloud models diffusional growth is presented as saturation-adjustment. This implies that all supersaturation is removed and converted into liquid water within a time step  $\Delta t$ . Therefore, diffusional growth is simply calculated as

$$q_c = \max(0, q - q_s), \quad (2.29)$$

where  $q_s$  is calculated from Eq. 2.13. That approach implies that the cloud water mixing ratio is calculated as a diagnostic quantity.

(ii) Moreover, diffusional growth of the cloud droplet specie can be treated by calculating the condensation rate diagnostically from (e.g., Khairoutdinov and Kogan, 2000). For that, Eq. 1.12 is used and translated into

$$\left. \frac{\partial q_c}{\partial t} \right|_{\text{cond}} = 4\pi \frac{\rho_l}{\rho} \frac{S}{F_k + F_D} R_c, \quad (2.30)$$

where  $R_c$  is the integral radius and given by

$$R_c = n_c \cdot \langle r_c \rangle. \quad (2.31)$$

The mean geometric radius  $\langle r_c \rangle$  of the assumed DSD is defined as (e.g., Eq. 14 in Seifert and Stevens, 2010)

$$\langle r_c \rangle = \frac{1}{n_c} \int_0^\infty r f_c(r) dr. \quad (2.32)$$

Assuming a gamma distribution for the cloud droplet distribution function  $f_c(r)$ , the mean geometric radius can be approximated as (Seifert and Beheng, 2001; Seifert and Stevens, 2010)

$$\langle r_c \rangle = \frac{\Gamma(\nu + 4/3)}{\Gamma(\nu + 1)} \left[ \frac{3}{4\pi\rho_l} \frac{q_c}{(\nu + 2)n_c} \right]^{1/3}. \quad (2.33)$$

Note, that the tuning factor as introduced by Seifert and Stevens (2010) to match results near the cloud base to a bin model has been neglected. Following Seifert and Beheng (2006) the shape parameter has been set to  $\nu = 1$ . The coefficients  $F_k$  and  $F_D$  of Eq. 2.30 consider the influence of thermal conduction and the diffusion of water vapor. They are calculated from

$$F_k = \left( \frac{L_v}{R_v T} - 1 \right) \frac{L_v \rho_l}{kT}, \quad (2.34)$$

$$F_D = \frac{\rho_l R_v T}{De_s}. \quad (2.35)$$

To consider the molecular diffusion coefficient of water vapor in air  $D$  an empirical relationship from Straka (2009) (their Eq. 5.2) is used:

$$D = 2.11 \times 10^{-5} \cdot \left( \frac{T}{273.15} \right)^{1.94} \cdot \frac{101325}{p}. \quad (2.36)$$

Moreover, the thermal conductivity of air  $k$  is calculated as in Rogers and Yau (1989):

$$k = 7.94048 \times 10^{-5} \cdot T + 2.27011 \times 10^{-2}. \quad (2.37)$$

For the treatment of diffusional growth using Eq. 2.30 the condensation timescale (see Eq. 1.10) must be considered. Hence, the model time step  $\Delta t$  must be smaller than  $\Delta t_{\text{phase}}$ . However, as for the simulations presented in this thesis the model setup causes a very small time step by the CFL-criterion ( $\Delta t \approx 0.1$  s) which already satisfies the condensation timescale. Thus, a further time restriction was not implemented.

**(iii)** Moreover, a so-called prognostic (or semi-analytic) supersaturation scheme (originally introduced by Clark, 1973) have been implemented and compared in Sec. 3. Instead of deriving the supersaturation from the fields of temperature and water vapor mixing ratio,



the absolute supersaturation  $\delta = q_v - q_s$  is treated as a dedicated prognostic field:

$$\frac{\partial \bar{\delta}}{\partial t} = -\bar{u}_j \frac{\partial \bar{\delta}}{\partial x_j} - \frac{\partial}{\partial x_j} (\overline{u_j'' \delta''}) + \chi_\delta. \quad (2.38)$$

The calculation of the SGS fluxes for the absolute supersaturation follows the formulation of Eq. 2.5 and is calculated as

$$\overline{u_j'' \delta''} = -K_h \frac{\partial \bar{\delta}}{\partial x_j}. \quad (2.39)$$

Beyond the advection of the absolute supersaturation (preferably with a monotonic advection scheme) the source/sink term includes the production and depletion of supersaturation due to vertical motion, radiation, and condensation/evaporation. Following Morrison and Grabowski (2008) and Grabowski and Morrison (2008) the source/sink term is calculated from:

$$\chi_\delta = A_s - \frac{\delta}{\tau_{\text{phase}}}, \quad (2.40)$$

where  $A_s$  is

$$A_s = -q_s \frac{\rho g w}{p - e_s} - \frac{dq_s}{dT} \cdot \left[ \frac{g w}{c_p} + \left( \frac{dT}{dt} \right)_{\text{rad}} \right]. \quad (2.41)$$

The temperature tendency by radiation  $(dT/dt)_{\text{rad}}$  is provided by the radiation model and assumed to be constant during one model time step. Moreover, following Morrison and Grabowski (2008) it is assumed that vertical motion and the change of  $dq_s/dT$  are constant during a model time step. The gravitational acceleration is denoted with  $g$  and the supersaturation relaxation timescale is

$$\tau_{\text{phase}} = (4\pi D n_c \langle r_c \rangle)^{-1}. \quad (2.42)$$

The reason for deriving an equation for the absolute supersaturation instead of the supersaturation  $S$  is, that a formulation of Eq. 2.41 for  $S$  is possible, but more complex (Morrison and Grabowski, 2008).

The condensation/evaporation rate is calculated by

$$\left. \frac{\partial q_c}{\partial t} \right|_{\text{cond}} = \frac{\delta}{\tau_{\text{phase}}} \left( 1 + \frac{dq_s}{dT} \frac{L_v}{c_p} \right)^{-1}. \quad (2.43)$$

In contrast to the explicit/diagnostic method [see method (ii)], the prognostic supersaturation scheme does not require further time constraints and can be also applied for  $\Delta t > 1$  s with an accurate calculation of the supersaturation development (which can be used for activation and diffusional growth).

### 2.2.3 Sedimentation

Sedimentation in the bulk cloud model is considered by calculating a sedimentation flux. In doing so, it is assumed that cloud droplets are log-normally distributed and falling in a Stoke regime (Ackerman et al., 2009). The sedimentation flux of cloud water mixing ratio and droplet concentration is calculated from

$$F_{q_c} = k_F \left( \frac{4}{3} \pi \rho_1 n_c \right)^{-2/3} (\rho q_c)^{5/3} \exp[5 \log(\sigma_g)^2], \quad (2.44)$$

$$F_{n_c} = k_F \left( \frac{4}{3} \pi \rho_1 / (q_c \rho) \right)^{-2/3} (n_c)^{1/3} \exp[5 \log(\sigma_g)^2], \quad (2.45)$$

where  $k_F = 1.2 \times 10^8 \text{ m}^{-1} \text{ s}^{-1}$  and  $\sigma_g = 1.3$  is the assumed dispersion of the DSD. The actual change in  $q_c$  and  $n_c$  in the grid box with index  $k$  is calculated by the vertical sedimentation flux divergence:

$$\left. \frac{\partial q_c}{\partial t} \right|_{\text{sed,c}} = \frac{F_{q_c}^{k+1} - F_{q_c}^k}{\rho} \Delta t \Delta z, \quad (2.46)$$

$$\left. \frac{\partial n_c}{\partial t} \right|_{\text{sed,c}} = \frac{F_{n_c}^{k+1} - F_{n_c}^k}{\rho} \Delta t \Delta z. \quad (2.47)$$

The length of a time step is denoted with  $\Delta t$  and the height of respective grid box with  $\Delta z$ . The sedimentation flux of the grid box with index  $k = 1$  is deposited to the ground and, if switched on, treated by the land-surface model.

### 2.2.4 Collision and coalescence

In bulk schemes, the collision of droplets is represented using collision rates derived from spectral bin models or analytical relationships. Typically, in fog, droplet growth by collision and coalescence is very weak due to the small droplet sizes. Thus, it is neglected frequently in fog simulations. In the bulk cloud model used here, a distinction is made between collision between cloud droplets (autoconversion), cloud droplets and raindroplets (accretion), and raindroplets itself (selfcollection). Since the latter two do not occur in fog, reference is made to the explanations in Maronga et al. (2015). Although, the study presented in Sec. 3 showed that this process is negligible small, the autoconversion process is presented for completeness, as it is not turned off explicitly.

The loss of  $q_c$  due to autoconversion is given by (Seifert and Beheng, 2001)

$$\left. \frac{\partial q_c}{\partial t} \right|_{\text{auto}} = - \frac{K_{\text{auto}}}{20 m_{\text{sep}}} \frac{(\mu_c + 2)(\mu_c + 4)}{(\mu_c + 1)^2} q_c^2 m_c^2 \cdot \left[ 1 + \frac{\Phi_{\text{auto}}(\tau_c)}{(1 - \tau_c)^2} \right] \rho_0, \quad (2.48)$$

where it is assumed that the new rain droplets have a size of  $r_{\text{sep}}$ , with the corresponding separation mass of  $m_{\text{sep}} = 2.6 \times 10^{-10} \text{ kg}$ . The depletion of cloud droplets can be yielded by

$$\left. \frac{\partial n_c}{\partial t} \right|_{\text{auto}} = - \rho \left. \frac{\partial q_c}{\partial t} \right|_{\text{auto}} \frac{2}{m_{\text{sep}}}. \quad (2.49)$$

Here,  $K_{\text{auto}} = 9.44 \times 10^9 \text{ m}^3 \text{ kg}^{-2} \text{ s}^{-1}$  is the autoconversion kernel and  $\mu_c = 1$  is a parameter describing the shape of the cloud droplet gamma distribution. The mean mass of the cloud droplets is defined as  $m_c = \rho q_c / n_c$ . Moreover, the autoconversion timescale  $\tau_c = 1 - q_c / (q_c + q_r)$  is considered in the autoconversion similarity function

$$\Phi_{\text{auto}} = 600 \cdot \tau_c^{0.68} (1 - \tau_c^{0.68})^3. \quad (2.50)$$

## 2.3 Lagrangian cloud model

The LCM in PALM is implemented as a feature of the Lagrangian particle model (LPM). By doing so, the LCM incorporates the code structure of the LPM and elements that can be applied to all particles, such as the method of interpolating the resolved flow to the particle position and the implementation of boundary conditions. Nevertheless, the LCM also consists of a significant amount of additional model parts, which mostly includes microphysical processes. For the research presented in this thesis the technical implementation of the particle model (sorting of Lagrangian particles, parallelization, and optimization) was not changed nor is it necessary to understand the research results. Thus, a description of this part is omitted. However, the interested reader is referred to section 4.2 of Maronga et al. (2015). Moreover, the LCM has the possibility to calculate droplet growth by collision and coalescence, which is not presented in this thesis. This mechanism, which is accurately represented by the LCM (Unterstrasser et al., 2017), but demanding a relatively large amount of computational resources, is irrelevant for fog and small droplets (see also Sec. 1.1.3). Thus, the interested reader is referred to Sec. 3.4.1 of Maronga et al. (2020).

All cloud resolving models must face the fact that a numerical representation of each aerosol or droplet individually is impossible, even for a very small cloud. Thus, all LCMs operate with the basic idea that one simulated particle (in the following, termed as superdroplet) represents an ensemble of identical aerosols or droplets (Shima et al., 2009). The size of this ensemble, i.e., the number of real particles which are represented by the superdroplet is called weighting-factor and denoted with  $A_{w,n}$ . The index  $n$  refers to the  $n$ -th superdroplet in the reference volume. While coupled to a dynamical model, the reference volume is the volume of the respective grid box where the particle is located at that time.

Within the particle model each superdroplet contains a number of certain properties. Beyond the weighting-factor, the information of their velocities, and the location in space each superdroplet has a dry aerosol radius  $r_{s,n}$  and a wet radius  $r_n$ . The latter one is the most relevant parameter for the LCM, as it determines the amount of liquid within the model. Accordingly, for a certain grid box with  $N_p$  superdroplets the liquid water mixing ratio is yielded by

$$q_l = \frac{1}{\rho_a \Delta V} \sum_{n=1}^{N_p} A_{w,n} \cdot \frac{4}{3} \pi \rho_l \cdot r_n^3. \quad (2.51)$$

In the following, empirical relationships are written as implemented in the model code, which

also imply that they correspond to SI units.

### 2.3.1 Boundary conditions and superdroplet initialization

For particles different boundary conditions can be prescribed at the model edges. At the top and bottom of the model particles can be reflected or absorbed. In the study presented in this thesis, absorption boundary conditions at the bottom have been chosen. Translated in physical terms they represent the deposition of cloud droplets. For the top of the model domain reflection boundary conditions have been applied. At the lateral edges, besides reflection and absorption conditions, cyclic boundary conditions can be used. As in all the presented studies of this thesis cyclic conditions have been applied for the flow, also particles are cyclically treated at the lateral edges in the study presented in Chapter 4.

To initialize the particle model, particles must be added to the model domain. Several degrees of freedom exist to steer the spatial and temporal release of particles (see Maronga et al., 2015). In this thesis however, a homogeneous set of particles throughout the model domain has been released at the start of the simulation. Similar to the bulk cloud model, the initial aerosol spectrum can be prescribed with up to three log-normal distributions (see Eq. 2.15). In contrast to the bulk cloud model, the aerosol spectrum is explicitly represented by the size distribution of the superdroplet population within the model. Accordingly, Eq. 2.15 is divided into  $N_p$  logarithmically spaced bins, i.e., one bin for each superdroplet in the grid-box. Those bins are located between a chosen minimum and maximum aerosol radius. The dry aerosol radius of a superdroplet is calculated as the geometric mean of the left and right boundary of the respective bin. The initial weighting-factor is determined as

$$A_{w,n} = \Delta V \cdot \Delta r_{s,n} \cdot \frac{df(r_{s,n})}{dr}, \quad (2.52)$$

where  $\Delta r_{s,n}$  is the bin width.

Since the Rosenbrock method requires a large amount of internal time steps (see below), if the superdroplet radius differs significantly from the equilibrium radius, the initial wet radius is approximated to the equilibrium radius after Eq. 14 in Khvorostyanov and Curry (2007) considering the initial environmental supersaturation:

$$r_n = \frac{b^{1/3} r_{s,n}}{-S^{1/3}} \left[ 1 + \left( \frac{A}{3b^{1/3} r_{s,n}} \right) (-S)^{-2/3} \right]^{-1}. \quad (2.53)$$

Note, that this approximation is only valid for supersaturations of  $S < -5\%$ . Thus, higher values are limited to this value.

### 2.3.2 Transportation

In contrast to Eulerian quantities, Lagrangian particles are not fixed on an Eulerian grid. Instead, particles can move independently from the grid over the whole model domain. The location of a particle  $X_i = (X, Y, Z)$  in Cartesian coordinates is achieved by integrating the

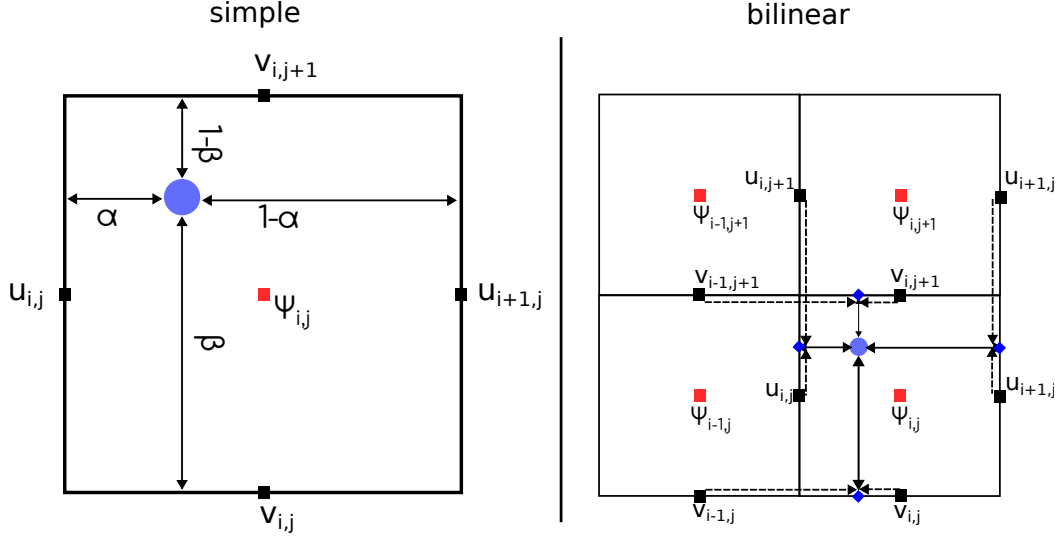


**Figure 2.1:** Illustration of the interpolation schemes "simple" and bilinear. For simplicity it is shown in two dimension (accordingly it is phrased bilinear but can be extended to the third dimension in the same way). The rectangular box represents a single grid cell with  $\psi_{i,j}$  representing scalar quantities defined at the center of a grid cell. The horizontal velocity components  $u$  and  $v$  are shifted by half a grid cell on the staggered C-grid. The blue diamonds in the bilinear method represent the points used for the interpolation.

particles velocity  $U_i = (U, V, W)$ :

$$\frac{dX_i}{dt} = U_i. \quad (2.54)$$

For the time integration two methods are currently implemented in the LPM. A first-order Euler forward step and a predictor-corrector scheme, which has a second-order accuracy and was part of model improvements within the research presented in this thesis. The predictor step calculates the change in particle position as

$$X_i^{t+1} = X_i^t + U_i^t(x_i^t)\Delta t, \quad (2.55)$$

where the exponent  $t$  and  $t + 1$  denotes the current and next time level, respectively. Subsequently, the corrector-step is applied including the information of the particle position of the predictor-step:

$$X_i^{t+1} = X_i^t + [U_i^{t+1}(X_i^{t+1}) + U_i^t(X_i^t)] \frac{\Delta t}{2}. \quad (2.56)$$

The application of such a scheme requires knowledge of the flow at the time level  $t + 1$ . In the LPM this is realized in such a way that the particle advection is called after the LES fields for the next time step are calculated.

The total particle velocity  $U_i$  is given by

$$U_i = u_{p,i} + \tilde{u}_{p,i} + \delta_{i3}U_\infty(r) \quad (2.57)$$

including the resolved-scale velocity based on the LES and interpolated to the particle position  $u_{p,i}$ , a subgrid-scale particle velocity part  $\tilde{u}_{p,i}$ , and the particle terminal fall speed  $U_\infty(r)$ . In theory, a prognostic calculation of the particle velocity considering the droplet relaxation time  $\tau_d$  (as in Eq. 1.6) would be possible. However, as  $\tau_d$  is very short (see Tab. 2.1) for small droplets this would require an infeasible short time step to resolve the droplet inertia correctly.

To achieve the resolved-scale particle velocity it can be selected between different interpolation methods. Previous to the research of this thesis the trilinear interpolation was implemented as the method of choice. For this method the particle velocity for each of the three velocity components is calculated linearly by the eight adjacent grid points. However, simulations revealed that the trilinear interpolation, which is considered to have a high accuracy, produce significant divergence in the particle concentration for a homogeneous initial particle concentration and an incompressible flow field. This particle concentration divergence in case of trilinear velocity interpolation was also reported by Grabowski et al. (2018). Thus, a method satisfying the incompressible condition described by Grabowski et al. (2018) was implemented in the LPM (for the proof of compliance with the divergence-free condition see their appendix A). This scheme, termed as "simple-interpolation" by Grabowski et al. (2018) makes use of the benefits of the staggered C-grid (see Se. 2.3 in Maronga et al., 2015) and considers for each velocity component only the weighted values of the adjacent grid points in the respective direction (Fig. 2.1). Subsequently, following Fig. 2.1 the interpolated particle velocity components are given by

$$u_p = \alpha \cdot u_{i+1,j,k} + (1 - \alpha)u_{i,j,k}, \quad (2.58)$$

$$v_p = \beta \cdot v_{i,j+1,k} + (1 - \beta)v_{i,j,k}, \quad (2.59)$$

$$w_p = \gamma \cdot w_{i,j,k+1} + (1 - \gamma)w_{i,j,k}. \quad (2.60)$$

Beyond the compliance of divergence-free condition, the simple-interpolation method requires substantial less computational time, as no sorting to find the adjacent grid points is needed, while this is required for the trilinear interpolation method. Depending on the application a reduction up to 20% of the total simulation cost was observed in cases where the LPM and its advection were the main consumer of computational resources.

For superdroplets, the subgrid-scale particle velocity  $\tilde{u}_{p,i}$  is based on the subgrid-scale kinetic energy of the flow and a stochastic velocity component, which includes a random term. Using the formulation of Sölch and Kärcher (2010) the subgrid-scale velocity is computed by

$$\tilde{u}_{p,i} = R_L \cdot \tilde{u}_{p,i}^{t-1} + \sqrt{1 - R_L^2} (\sqrt{e} \cdot \zeta). \quad (2.61)$$

Here, the Lagrangian autocorrelation coefficient  $R_L$  is

$$R_L = \exp(-\Delta t/\tau_L), \quad (2.62)$$

$r$ ( $\mu\text{m}$ )	$U_\infty(r)$ ( $\times 10^{-3} \text{ m s}^{-1}$ )	$\tau_d$ (s)
1	0.189	$1.0 \times 10^{-5}$
2	0.75	$4.0 \times 10^{-5}$
5	4.5	$2.5 \times 10^{-4}$
10	17.9	$1.0 \times 10^{-3}$
15	36.27	$2.2 \times 10^{-3}$
20	60.1	$4.0 \times 10^{-3}$
30	123.18	$9.1 \times 10^{-3}$
40	197.47	$1.6 \times 10^{-3}$

**Table 2.1:** Sedimentation velocities for spherical water droplets in air based on Eq. 2.64, and their relaxation time  $\tau_d$ . The droplet relaxation time is calculated assuming a kinematic viscosity of air to be  $\nu = 1.825 \times 10^{-5} \text{ m}^2\text{s}^{-1}$  and the air density to be  $\rho = 1.2 \text{ kgm}^{-3}$ .

with  $\tau_L$  being the Lagrangian fluid timescale:

$$\tau_L = K_m/e. \quad (2.63)$$

$K_m$  is the eddy diffusion coefficient for momentum and  $e$  is the subgrid-scale kinetic energy. Moreover, a random term is added where  $\zeta$  is a normal distributed random number with zero mean and unity standard deviation. By multiplying  $\zeta$  with  $\sqrt{e}$  the random term exhibits the same velocity variance as the SGS eddies, which is represented by  $e$ .

Based on an empirical relationship (Eq. 2 in Rogers et al., 1993) the terminal fall velocity of superdroplets are calculated by

$$U_\infty(r) = \begin{cases} 8000 \cdot r[1 - \exp(-24000 \cdot r)] & \text{for } r \leq 372.5 \mu\text{m}, \\ 9.65 - 10.43 \exp(-1200 \cdot r) & \text{for } r > 372.5 \mu\text{m}. \end{cases} \quad (2.64)$$

Based on that equation, sedimentation of droplets sizes typical for fog are given in Tab. 2.1. The second case of Eq. 2.64 is only demonstrated for completeness as such large droplet diameters are not observed in fog.

### 2.3.3 Activation and diffusional growth

A key advantage of using a LCM is that it eliminates the requirement for a separate activation scheme to determine the number of activated cloud droplets. Instead, Eq. 1.5 can be considered explicitly for each superdroplet. In this manner, a superdroplet can exceed or shrink below the critical radius, mirroring real-life observations. Thus, the diffusional growth of each superdroplet is calculated from

$$(r + r_0) \frac{dr}{dt} = \frac{S - A/r + br_s^3/r^3}{F_k + F_D} \cdot f_v(r). \quad (2.65)$$

For a numerically stable solution of Eq. 2.65 very short time steps are required, as its a so-called stiff differential equation. Accordingly, the time-integration is carried out with a fourth-order Rosenbrock method (Grabowski and Wang, 2013), which adjusts the internal time step for solving Eq. 2.65 properly. In practice, smaller radii require smaller time steps, while the time step can be increased for larger droplets. In contrast to other applications of the LPM, where particles have no feedback on the dynamics, the LCM is actively coupled to the LES. In other words, the thermodynamics influence the development of droplets, but microphysics also change dynamics due to the release of latent heat during condensation and evaporation. Hence, the change in radius by diffusion determines the change in the LES quantities water vapor mixing ratio,

$$\left(\frac{\partial q_v}{\partial t}\right)_{\text{cond}} = -\frac{1}{\rho_a \Delta V} \sum_{n=1}^{N_p} A_{w,n} \frac{4}{3} \pi \rho_l \frac{\widehat{r}_n^3 - r_n^3}{\Delta t}, \quad (2.66)$$

and the potential temperature,

$$\left(\frac{\partial \theta}{\partial t}\right)_{\text{cond}} = -\frac{L_v}{\Pi c_p} \left(\frac{\partial q_v}{\partial t}\right)_{\text{cond}}. \quad (2.67)$$

The symbol  $\widehat{(\cdot)}$  marks the radius after the calculation of diffusional growth. Accordingly, the last term in Eq. 2.66 represents the discrete change in radius within the time step of length  $\Delta t$ . The supersaturation  $S$  is calculated by the LES fields of water vapor mixing ratio and potential temperature with

$$S = \frac{e_a}{e_s} - 1. \quad (2.68)$$

The water vapor pressure is yielded from

$$e_a = \frac{q_v \cdot p}{q_v + R_d/R_v}. \quad (2.69)$$

The length-scale for gas-kinetic effects  $r_0$  becomes relevant for the droplet growth of small droplets (Mordy, 1959) and is yielded by

$$r_0 = \frac{D}{\beta_c} \cdot \sqrt{\frac{2\pi}{TR_v}}, \quad (2.70)$$

where  $\beta_c$  is the condensation coefficient and can be approximated with 0.036 (Rooth, 1957).

The last term of Eq. 2.65 represents the ventilation coefficient  $f_v$ , which becomes relevant for large droplets experiencing an accelerated evaporation in subsaturated environments. In the model this effect is only considered for droplets with a radius  $\geq 40 \mu\text{m}$ . Given that droplet sizes of this nature are rare for fogs and have not been observed in the studies presented, a more detailed discussion of the ventilation effect is omitted. However, the interested reader is referred to Chap. 7 of Rogers and Yau (1989).



## 2.4 Land-surface model

Many LES models apply idealized surface conditions with prescribed surface fluxes. In the simulations presented in this thesis, a full interactive land-surface model (LSM) was used. In particular for fog simulations, where interactions between atmosphere and surface become crucial as the surface energy budget is the main driver for fog formation, an LSM is indispensable for a correct fog presentation.

The LSM implementation in PALM is based on the formulation of the Tiled ECMWF Scheme for Surface Exchanges over Land (TESSEL/HTESSEL; Balsamo et al., 2009) and the simplified version as implemented in the LES model DALES (Heus et al., 2010). The main feature of the LSM is an energy balance solver for Earth's surface using a resistance parametrization for the surface fluxes

$$\frac{dT_0}{dt}C_0 = R_{\text{net}} - H - LE - G, \quad (2.71)$$

where  $C_0$  and  $T_0$  are the heat capacity and radiative temperature of the surface skin layer, respectively. The terms of the right-hand side (from left to right) of Eq. 2.71 denote the net surface radiation balance (see Sec. 2.5), the sensible surface heat flux, the latent surface heat flux, and the ground heat flux.

The surface sensible heat flux  $H$  is calculated as

$$H = -\rho c_p \frac{1}{r_a} (\theta_{\text{mo}} - \theta_0), \quad (2.72)$$

where  $r_a$  is the aerodynamic resistance. Based on the Monin-Obukhov similarity theory the aerodynamic resistance is given by

$$r_a = \frac{\theta_{\text{mo}} - \theta_0}{u_* \theta_*}, \quad (2.73)$$

where  $u_*$  and  $\theta_*$  are defined in Eq. 30 in Sec. 2.1. The latent heat flux  $LE$  is calculated as

$$LE = -\rho L_v \frac{1}{r_a + r_{\text{sf}}} [q_{\text{v,mo}} - q_{\text{s}}(T_0)], \quad (2.74)$$

where  $r_{\text{sf}}$  is the surface resistance. The water vapor mixing ratio at the height of  $z_{\text{mo}}$  is given with  $q_{\text{v,mo}}$ . If the surface type vegetation is used (vegetation is used as surface type for all presented studies within this thesis, for further types and description see Gehrke et al., 2021) a surface element can consist of patches of bare soil, vegetation and a liquid water reservoir. Hence, the total evapotranspiration can be written as (Viterbo and Beljaars, 1995)

$$LE = c_{\text{veg}}(1 - c_{\text{liq}})LE_{\text{veg}} + c_{\text{liq}}LE_{\text{liq}} + (1 - c_{\text{liq}})(1 - c_{\text{veg}})LE_{\text{soil}}, \quad (2.75)$$

where  $LE_{\text{veg}}$ ,  $LE_{\text{liq}}$ , and  $LE_{\text{soil}}$  are the latent surface heatflux components of the surface fraction covered with vegetation, liquid water, and bare soil, respectively. The surface fraction covered with vegetation is denoted with  $c_{\text{veg}}$  while  $c_{\text{liq}}$  represents the fraction covered with

liquid water. The liquid water reservoir represents the interception water stored on plants by precipitation, droplet deposition, and dewfall. The temporal change in the liquid water reservoir  $m_{\text{liq}}$  is calculated as

$$\frac{dm_{\text{liq}}}{dt} = \frac{LE_{\text{liq}}}{\rho_1 L_v}. \quad (2.76)$$

The maximum amount of water, which can be stored on plants is calculated as

$$m_{\text{liq,max}} = m_{\text{liq,ref}} \cdot c_{\text{veg}} \cdot LAI + (1 - c_{\text{veg}}), \quad (2.77)$$

where  $m_{\text{liq,max}}$  has a lower boundary of 1. The reference liquid water column for a single leaf is  $m_{\text{liq,ref}} = 0.2$  mm, and the leaf area index is denoted with  $LAI$ . Liquid water which exceeds the threshold is removed from the surface and infiltrated and treated with the underlying soil model (see below). The coverage of the surface by liquid is calculated as the fraction of the liquid water reservoir to the maximum storable plant water amount

$$c_{\text{liq}} = \frac{m_{\text{liq}}}{m_{\text{liq,max}}}. \quad (2.78)$$

The ground heat flux  $G$  is parameterized following a formulation of Duynkerke (1999)

$$G = \frac{\Lambda_{\text{skin}} \Lambda_{\text{soil}}}{\Lambda_{\text{skin}} + \Lambda_{\text{soil}}} (T_0 - T_{\text{soil},1}), \quad (2.79)$$

where  $\Lambda_{\text{soil}}$  and  $\Lambda_{\text{skin}}$  are the thermal conductivity of the top half of the uppermost soil-layer and between the canopy and soil-top, respectively. The second term of Eq. 2.79 depicts the temperature difference on the ground, where  $T_{\text{soil},1}$  is the temperature of the uppermost soil layer. Moreover, the surface is coupled to a multi-layer soil scheme, which solves prognostic equations for the soil temperature and the volumetric soil moisture. The grid configuration of the soil model is independent of the used grid layout for the atmosphere model and can be prescribed by the user. A detailed description of the soil model can be found in Gehrke et al. (2021).

## 2.5 Radiation model

The PALM Model System provides several radiation models. These range from very simple methods that assume a constant radiative forcing to complex radiative transfer models that are able to consider for the shading of buildings in urban environments. In the following the applied and coupled Rapid Radiative Transfer Model for global models (RRTMG; e.g., Clough et al., 2005) with its most important features for the herein presented research is summarized. Unlike all other embedded models, RRTMG is linked and used as an external library to PALM. Accordingly, PALM delivers relevant atmospheric quantities (see below) while RRTMG calculate the radiation transfer.

Radiation transfer can be understood as the interaction of radiation and matter and com-

prises the physical effects of absorption, scattering, and emission (Liou, 1980; Goody and Yung, 1989). While RRTMG has been coupled in its original form and because a full description of the radiation transfer model would be beyond the scope of this thesis, the following description focuses on a qualitative description of the radiation transfer and the coupling of the LES model PALM to RRTMG. A detailed description of RRTMG can be found at Iacono et al. (2000), Pincus et al. (2003) and Clough et al. (2005).

The radiation budget of the Earth's surface  $R_{\text{net}}$  is calculated as

$$R_{\text{net}} = \text{SW}_{\downarrow} - \text{SW}_{\uparrow} + \text{LW}_{\downarrow} - \text{LW}_{\uparrow}, \quad (2.80)$$

where  $\text{SW}_{\downarrow}$ ,  $\text{SW}_{\uparrow}$ ,  $\text{LW}_{\downarrow}$ , and  $\text{LW}_{\uparrow}$  are the shortwave incoming, shortwave outgoing, longwave incoming, and longwave outgoing fluxes, respectively. The short- and longwave fluxes are calculated by RRTMG based on the correlated-k method (Ambartsumian, 1936). In simple terms, the correlated-k method simplifies radiation transfer while absorption coefficients with similar values are grouped together (so-called spectral bands) rather than integrating the radiation transfer wavelength by wavelength. This is a common and well validated method, which is used by most of the modern radiation models, while it combines both high accuracy and a feasible amount of computational costs. RRTMG applies 16 and 14 spectral bands for the radiation transfer of longwave and shortwave, respectively. Those calculations are carried out for each vertical column of the model grid, while RRTMG calculates radiative fluxes and heating rates for each layer, i.e., for every grid box. As RRTMG requires information of the meteorological state of the atmosphere, PALM supplies the fields of pressure, temperature, water vapor mixing ratio, liquid water mixing ratio (and on demand ice water mixing ratio), and the effective droplet radius. Information of trace gas concentration as ozone and carbon dioxide are offered in a separate file by RRTMG, which are used by PALM as default. Note that the user can modify this trace gas concentration on demand. While the radiation transfer equation must be applied up to a large height, vertical profiles of temperature and pressure are extrapolated assuming standard profiles, which are also offered by RRTMG.

The presence of liquid water significantly alter the radiation transfer, as cloud particles absorb, emit and scatter radiation stronger than the clear-sky atmosphere. In PALM the coupling of radiation transfer and cloud microphysical properties, i.e., the DSD, is based on the cloud droplet effective radius, which is calculated as

$$r_{\text{eff}} = \begin{cases} \left( \frac{3q_c \rho}{4\pi n_c \rho_l} \right)^{1/3} \exp(\log(\sigma_g)^2) & \text{for the bulk cloud model,} \\ \frac{\int_0^{N_P} \pi r_n^3 A_{w,n}}{\int_0^{N_P} \pi r_n^2 A_{w,n}} & \text{for the LCM.} \end{cases} \quad (2.81)$$

The effective radius is subsequently limited to a lower boundary of  $2.5 \mu\text{m}$  and an upper boundary of  $60 \mu\text{m}$ .

The surface albedo for the surface type short grassland is calculated using a parametrization following Briegleb et al. (1986). Depending on the solar angle, the albedo for direct

long- and shortwave radiation are calculated as

$$\alpha_{\text{lw,dir}} = \frac{\alpha_{\text{lw,dif}} \cdot 1.1}{1 + 0.2\Psi}, \quad (2.82)$$

$$\alpha_{\text{sw,dir}} = \frac{\alpha_{\text{sw,dif}} \cdot 1.1}{1 + 0.2\Psi}, \quad (2.83)$$

where  $\Psi$  is the cosine of the solar zenith angle.

Calculating the radiation transfer is known to be a very computational demanding task. This is why the radiation model can be prescribed with a separate radiation time step  $\Delta t_{\text{rad}}$ , which might have larger values than the calculated time step for the dynamical model.

### **3 Large-eddy simulation of radiation fog with comprehensive two-moment bulk microphysics: impact of different aerosol activation and condensation parameterizations**

#### **3.1 Declaration of Contributions**

The numerical experiments were jointly designed by J. Schwenkel and B. Maronga. J. Schwenkel implemented the microphysics parameterizations, conducted the simulations and performed the data analysis. Results were jointly discussed. J. Schwenkel prepared the paper, with significant contributions by B. Maronga. Comments of Thierry Bergot (reviewer) and one anonymous referee helped to improve the final version of the manuscript.

#### **3.2 Research Article**

©The authors 2019. CC BY 4.0 License

Atmos. Chem. Phys., 19, 7165–7181, 2019  
https://doi.org/10.5194/acp-19-7165-2019  
© Author(s) 2019. This work is distributed under  
the Creative Commons Attribution 4.0 License.



Atmospheric  
Chemistry  
and Physics  
Open Access  
EGU

# Large-eddy simulation of radiation fog with comprehensive two-moment bulk microphysics: impact of different aerosol activation and condensation parameterizations

Johannes Schwenkel<sup>1</sup> and Björn Maronga<sup>1,2</sup>

<sup>1</sup>Institute of Meteorology and Climatology, Leibniz University Hannover, Hanover, Germany

<sup>2</sup>Geophysical Institute, University of Bergen, Bergen, Norway

**Correspondence:** Johannes Schwenkel (schwenkel@muk.uni-hannover.de)

Received: 27 October 2018 – Discussion started: 6 November 2018

Revised: 30 April 2019 – Accepted: 16 May 2019 – Published: 29 May 2019

**Abstract.** In this paper we study the influence of the cloud microphysical parameterization, namely the effect of different methods for calculating the supersaturation and aerosol activation, on the structure and life cycle of radiation fog in large-eddy simulations. For this purpose we investigate a well-documented deep fog case as observed at Cabauw (the Netherlands) using high-resolution large-eddy simulations with a comprehensive bulk cloud microphysics scheme. By comparing saturation adjustment with a diagnostic and a prognostic method for calculating supersaturation (while neglecting the activation process), we find that, even though assumptions for saturation adjustment are violated, the expected overestimation of the liquid water mixing ratio is negligible. By additionally considering activation, however, our results indicate that saturation adjustment, due to approximating the underlying supersaturation, leads to a higher droplet concentration and hence significantly higher liquid water content in the fog layer, while diagnostic and prognostic methods yield comparable results. Furthermore, the effect of different droplet number concentrations is investigated, induced by using different common activation schemes. We find, in line with previous studies, a positive feedback between the droplet number concentration (as a consequence of the applied activation schemes) and strength of the fog layer (defined by its vertical extent and amount of liquid water). Furthermore, we perform an explicit analysis of the budgets of condensation, evaporation, sedimentation and advection in order to assess the height-dependent contribution of the individual processes on the development phases.

## 1 Introduction

The prediction of fog is an important part of the estimation of hazards and efficiency in traffic and economy (Bergot, 2013). The annual damage caused by fog events is estimated to be the same as the amount caused by winter storms (Gultepe et al., 2009). Despite improvements in numerical weather prediction (NWP) models, the quality of fog forecasts is still unsatisfactory. The explanation for this is obvious: fog is a meteorological phenomenon influenced by a multitude of complex physical processes. Namely, these processes are radiation, turbulent mixing, atmosphere–surface interactions and cloud microphysics (hereafter referred to as microphysics), which interact on different scales (e.g., Gultepe et al., 2007; Haeffelin et al., 2010). The key issue for improving fog prediction in NWP models is to resolve the relevant processes and scales explicitly or – if that is not possible – to parameterize them in an appropriate way.

In recent years, various studies focused on the influence of microphysics on fog. In particular, the activation of aerosols (hereafter simply referred to as activation), which determines how many aerosols at a certain supersaturation get activated and hence can grow into cloud drops, is a key process and thus of special interest (e.g., Bott, 1991; Hammer et al., 2014; Boutle et al., 2018).

Stolaki et al. (2015) investigated and compared the influence of aerosols on the life cycle of a radiation fog event while using the one-dimensional (1-D) mode of the MESO-NH model with a two-moment warm microphysics scheme, after Geoffroy et al. (2008) and Khairoutdinov and Kogan (2000), and included an ac-

tivation parameterization after Cohard et al. (1998). In other fog studies, using single-column models, different activation schemes such as the simple Twomey power law activation in Bott and Trautmann (2002) and the scheme of Abdul-Razzak and Ghan (2000) (see Zhang et al., 2014) were applied. Furthermore, also more advanced methods such as sectional models have been used for an appropriate activation representation. Maalick et al. (2016) used the Sectional Aerosol module for Large Scale Applications (SALSA; Kokkola et al., 2008) in two-dimensional (2-D) studies for a size-resolved activation. Mazoyer et al. (2017) conducted, similar to Stolaki et al. (2015), simulations for the ParisFog Experiment with the MESO-NH model (for more information to the MESO-NH model, see Lac et al., 2018), but using the three-dimensional (3-D) large-eddy simulation (LES) mode and focusing on the drag effect of vegetation on droplet deposition. For the fog microphysics, they used the activation parameterizations after Cohard et al. (2000) in connection with saturation adjustment. As outlined above, several different activation parameterizations have been employed for simulating radiation fog. This raises the question how different methods affect the structure and life cycle of radiation fog. Furthermore, schemes that parameterize activation based on updrafts (typically done in NWP models) might fail for fog. Such schemes derive supersaturation as a function of vertical velocity, which is valid for convective clouds that are forced by surface heating but not for radiation fog, which is mainly driven by longwave radiative cooling in its development and mature phase (Maronga and Bosveld, 2017; Boutle et al., 2018).

Although great progress has been made to understand different microphysical processes in radiation fog based on numerical experiments, turbulence as a key process has been either fully parameterized (single-column models) or oversimplified (2-D LES). Since turbulence is a fundamentally 3-D process, the full complexity of all relevant mechanisms can only be reproduced with 3-D LESs (Nakanishi, 2000).

Moreover, a disadvantage of most former studies is the use of saturation adjustment, which implies that supersaturations are immediately removed within one time step. This approach is only valid when the timescale for diffusion of water vapor (on the order of 2–5 s) is much smaller than the model time step. This is the case in large-scale models where time steps are on the order of 1 min, but in LES of radiation fog, time steps easily go down to split seconds so that the assumption made for saturation adjustment is violated and might lead to excessive condensation (e.g., Lebo et al., 2012; Thouron et al., 2012). As a follow-up to these studies, which investigated the influence of different supersaturation calculations for deep convective cloud and stratocumulus, the present work investigates the effect of saturation adjustment on radiation fog.

As Mazoyer et al. (2017) and Boutle et al. (2018) stated that both LES and NWP models tend to overestimate the liquid water content and the droplet number concentration for

radiation fog, the following questions are derived from these shortcomings:

- i. Is saturation adjustment appropriate as it crucially violates the assumption of equilibrium? How large is the effect of different methods to calculate supersaturation on diffusional growth of fog droplets?
- ii. As the number of activated fog droplets is essentially determined by the supersaturation, how large is the effect of different supersaturation modeling approaches on aerosol activation and thus on the strength and life cycle of radiation fog (see Thouron et al., 2012)?
- iii. What is the impact of different activation schemes on the fog life cycle for a given aerosol environment?

In the present paper we will address the above research questions by employing idealized high-resolution LESs with atmospheric conditions based on an observed typical deep fog event with continental aerosol conditions at Cabauw (the Netherlands).

The paper is organized as follows: Sect. 2 outlines the methods used, that is, the LES modeling framework and the microphysics parameterizations used. Section 3 provides an overview of the simulated cases and model setup, while results are presented in Sect. 4. Conclusions are given in Sect. 5.

## 2 Methods

This section will outline the used LES model and the treatment of radiation and land–surface interactions, followed by a more detailed description of the bulk microphysics implemented in the Parallelized Large-Eddy Simulation Model (PALM) and the extensions made in the scope of the present study.

### 2.1 LES model with embedded radiation and land surface model

In this study the LES PALM (Maronga et al., 2015; revision 2675 and 3622) was used with additional extensions in the microphysics parameterizations. PALM has been successfully applied to simulate the stable boundary layer (BL) (e.g., during the first intercomparison of LES for stable BL – GABLS; Beare et al., 2006) as well as radiation fog (Maronga and Bosveld, 2017). The model is based on the incompressible Boussinesq-approximated Navier–Stokes equations and prognostic equations for total water mixing ratio, potential temperature and subgrid-scale turbulent kinetic energy (TKE). PALM is discretized in space using finite differences on a Cartesian grid. For the non-resolved eddies, a 1.5-order flux–gradient subgrid closure scheme after Deardorff (1980) is applied, which includes the solution of an additional prognostic equation for the

subgrid-scale TKE. Moreover, the discretization for space and time is done by a fifth-order advection scheme after Wicker and Skamarock (2002) and a third-order Runge–Kutta time-step scheme (Williamson, 1980), respectively. The interested reader is referred to Maronga et al. (2015) for a detailed description of the PALM.

In order to account for radiative effects on fog and the Earth's surface energy balance, the radiation code RRTMG (Clough et al., 2005) has been recently coupled to PALM, running as an independent single-column model for each vertical column of the LES domain. RRTMG calculates the radiative fluxes (shortwave and longwave) for each grid volume while considering profiles of pressure, temperature, humidity, liquid water, the droplet number concentration ( $n_c$ ) and the effective droplet radius ( $r_{\text{eff}}$ ). Compared to the precursor study of Maronga and Bosveld (2017), improvements in the microphysics parameterization introduced in the scope of the present study allow a more realistic calculation of the fog's radiation budget, as  $n_c$  is now represented as a prognostic quantity instead of the previously fixed value specified by the user. This involves an improved calculation of  $r_{\text{eff}}$ , entering RRTMG, which is given as

$$r_{\text{eff}} = \left( \frac{3q_l \rho}{4\pi n_c \rho_l} \right)^{\frac{1}{3}} \exp\left(\log(\sigma_g)^2\right), \quad (1)$$

where  $q_l$  is the liquid water mixing ratio,  $\rho$  is the density of air,  $\rho_l$  is the density of water and  $\sigma_g = 1.3$  is the geometric standard deviation of the droplet distribution. The effective droplet radius is the main interface between the optical properties of the cloud and the radiation model RRTMG. Note that 3-D radiation effects of the cloud are not implemented in this approach, which, however, could affect the fog development at the lateral edges during formation and dissipation phases when no homogeneous fog layer is present. As radiation calculations traditionally require enormous computational time, the radiation code is called at fixed intervals on the order of 1 min.

Moreover, PALM's land surface model (LSM) is used to calculate the surface fluxes of sensible and latent heat. The LSM consists of a multi-layer soil model, predicting soil temperature and soil moisture, as well as a solver for the energy balance of the Earth's surface using a resistance parameterization. The implementation is based on the ECMWF-IFS land surface parameterization (H-TESSSEL) and its adaptation in the DALES model (Heus et al., 2010). A description of the LSM and a validation of the model system for radiation fog are given in Maronga and Bosveld (2017).

## 2.2 Bulk microphysics

As a part of this study, the two-moment microphysics scheme of Seifert and Beheng (2001) and Seifert et al. (2006) implemented in PALM, basically only predicting the rain droplet number concentration ( $n_r$ ) and cloud water mixing ( $q_l$ ), was extended by prognostic equations for  $n_c$  and the cloud water

mixing ratio ( $q_c$ ). The scheme of Seifert and Beheng (2001) and Seifert et al. (2006) is based on the separation of the cloud and rain droplet scale by using a radius threshold of 40  $\mu\text{m}$ . This separation is mainly used for parameterizing coagulation processes by assuming different distribution functions for cloud and rain droplets. However, as collision and coalescence are weak in fog due to small average droplet radii, the production of rain droplets is negligible. Consequently, only the number concentration and mixing ratio of droplets (containing all liquid water and thus abbreviated with  $q_l$  here) are considered in the following. The budgets of the cloud water mixing ratio and number concentration are given by

$$\frac{\partial q_l}{\partial t} = -\frac{\partial u_i q_l}{\partial x_i} + \left(\frac{\partial q_l}{\partial t}\right)_{\text{activ}} + \left(\frac{\partial q_l}{\partial t}\right)_{\text{cond}} - \left(\frac{\partial q_l}{\partial t}\right)_{\text{auto}} - \left(\frac{\partial q_l}{\partial t}\right)_{\text{accr}} - \left(\frac{\partial q_l}{\partial t}\right)_{\text{sedi}}, \quad (2)$$

$$\frac{\partial n_c}{\partial t} = -\frac{\partial u_i n_c}{\partial x_i} + \left(\frac{\partial n_c}{\partial t}\right)_{\text{activ}} - \left(\frac{\partial n_c}{\partial t}\right)_{\text{evap}} - \left(\frac{\partial n_c}{\partial t}\right)_{\text{auto}} - \left(\frac{\partial n_c}{\partial t}\right)_{\text{accr}} - \left(\frac{\partial n_c}{\partial t}\right)_{\text{sedi}}. \quad (3)$$

The terms on the right-hand side represent the decrease or increase by advection, activation, diffusional growth, autoconversion, accretion and sedimentation (from left to right). Following Ackerman et al. (2009), cloud water sedimentation is parameterized, assuming that droplets have a log-normal distribution and follow a Stokes regime. This results in a sedimentation flux of

$$F_{q_l} = k_F \left(\frac{4}{3}\pi \rho_l n_c\right)^{-\frac{2}{3}} (\rho q_l)^{\frac{5}{3}} \exp(5\ln^2 \sigma_g), \quad (4)$$

with the parameter  $k_F = 1.2 \times 10^8 \text{ m}^{-1} \text{ s}^{-1}$  (Geoffroy et al., 2010). The main focus of this paper is to study the effect of different microphysical parameterizations of activation and condensation processes on microphysical and macroscopic properties of radiation fog. Those different activation and supersaturation parameterizations will be discussed in the following.

### 2.2.1 Activation

It is well known that the aerosol distribution and the activation process are of great importance for the life cycle of fog (e.g., Gultepe et al., 2007). The amount of activated aerosols determines the number concentration of droplets within the fog, which, in turn, has a significant influence on radiation through optical thickness as well as on sedimentation and consequently affects macroscopic properties of the fog, like, for instance, its vertical extent. For these reasons, a sophisticated treatment of the activation process is an essential prerequisite for the simulation of radiation fog. Several activation parameterizations for bulk microphysics models have been proposed in literature. In this work, three of



these activation schemes were compared with each other in order to quantify their effect on the development of a radiation fog event. The schemes considered in this scope are the activation scheme of Twomey (1959), which was used, for example, by Bott and Trautmann (2002) to simulate radiation fog, the scheme of Cohard et al., 1998 (used by, for example, Stolaki et al., 2015; Mazoyer et al., 2017), and the one by Khvorostyanov and Curry (2006). The latter two represent an empirical and analytical extension of Twomey's scheme, respectively. Consequently, these parameterizations are frequently termed Twomey-type parameterizations that have the following form:

$$N_{\text{CCN}}(s) = N_0 s^k, \quad (5)$$

where  $N_{\text{CCN}}$  values are the number of activated cloud condensation nuclei (CCN),  $N_0$  and  $k$  are parameters depending on the aerosol distribution, and  $s$  is the supersaturation. The three parameterizations considered in the present study are variations of Eq. (5) differing in mathematical complexity:

1. *Twomey (1959)*. The power law expression (Eq. 5) is well known and has been used for decades to estimate the number of activated aerosols for a given air mass in dependence of the supersaturation. A weakness of this approach is that the parameters  $N_0$  and  $k$  are usually assumed to be constant and are not directly linked to the microphysical properties. Furthermore, this relationship creates an unbounded number of CCN at high supersaturations.
2. *Cohard et al. (1998)*. This extended Twomey's power law expression by using a more realistic four-parameter CCN activation spectrum as shaped by the physiochemical properties of the accumulation mode. Although an extension to the multi-modal representation of an aerosol spectrum would be possible, all relevant aerosols that are activated in typical supersaturations within clouds and especially fog are represented in the accumulation mode (Cohard et al., 1998; Stolaki et al., 2015). Following Cohard et al. (1998) and Cohard and Pinty (2000), the activated CCN number concentration is expressed by

$$N_{\text{CCN}}(s) = C s^k \cdot F\left(\mu, \frac{k}{2}, \frac{k}{2} + 1; \beta s^2\right), \quad (6)$$

where  $C$  is proportional to the total number concentration of CCN that is activated when supersaturation  $s$  tends to infinity. Beside  $k$ , the parameters  $\mu$  and  $\beta$  are adjustable shape parameters associated with the characteristics of the aerosol size spectrum such as the geometric mean radius and the geometric standard deviation as well as with chemical composition and solubility of the aerosols. Thus, in contrast to the original Twomey approach, the effect of physiochemical properties on the aerosol spectrum are taken into account.

3. *Khvorostyanov and Curry (2006)*. This found an analytical solution to express the activation spectrum using Köhler theory. Therein, it is assumed that the dry aerosol spectrum follows a log-normal size distribution of aerosol  $f_d$ :

$$f_d = \frac{dN_a}{dr_d} = \frac{N_t}{\sqrt{2\pi} \ln \sigma_d r_d} \exp\left[-\frac{\ln^2(r_d/r_{d0})}{2 \ln^2 \sigma_d}\right]. \quad (7)$$

Here,  $r_d$  is the dry aerosol radius,  $N_t$  is the total number of aerosols,  $\sigma_d$  is the dispersion of the dry aerosol spectrum and  $r_{d0}$  is the mean radius of the dry particles. The number of activated CCN as a function of supersaturation  $s$  is then given by

$$N_{\text{CCN}}(s) = \frac{N_t}{2} [1 - \text{erf}(u)]; \quad u = \frac{\ln(s_0/s)}{\sqrt{2} \ln \sigma_s}, \quad (8)$$

where erf is the Gaussian error function, and

$$s_0 = r_{d0}^{-(1+\beta)} \left(\frac{4A_K^3}{27b}\right)^{1/2}, \quad \sigma_s = \sigma_d^{1+\beta}. \quad (9)$$

In this case,  $A_K$  is the Kelvin parameter and  $b$  and  $\beta$  depend on the chemical composition and physical properties of the soluble part of the dry aerosol.

Since prognostic equations were neither considered for the aerosols nor for their sources and sinks, a fixed aerosol background concentration was prescribed by setting parameters  $N_0$ ,  $C$  and  $N_t$  for the three activation schemes. The different nomenclature of the aerosol background concentration is based on the nomenclature used in the original literature.

The activation rate is then calculated as

$$\left(\frac{\partial n_c}{\partial t}\right)_{\text{activ}} = \max\left(\frac{N_{\text{CCN}} - n_c}{\Delta t}, 0\right), \quad (10)$$

where  $n_c$  is the number of previously activated aerosols that are assumed to be equal to the number of pre-existing droplets and  $\Delta t$  is the length of the model time step. Note that this method does not take into account reduction of CCN. However, this error can be neglected, since processes like aerosol washout and dry deposition are of minor importance for radiation fog. For all activation schemes it is assumed that every activated CCN becomes a droplet with an initial radius of 1  $\mu\text{m}$ . This results in a change of liquid water, which is considered by the condensation scheme and is described in the next section. Furthermore, we performed a sensitivity study with initial radii of 0.5 to 2  $\mu\text{m}$ , which showed that the choice of the initial radius had no impact on the results (not shown). This is consistent with the findings of Khairoutdinov and Kogan (2000) and Morrison and Grabowski (2007).

### 2.2.2 Condensation and supersaturation calculation

The representation of diffusional growth, evaporation and calculating the underlying supersaturation (which is the main driver for activation) is one of the fundamental tasks of cloud physics. Three different methods have been evaluated and widely discussed in the scientific community. Namely, these are the saturation adjustment scheme, the diagnostic scheme, where the supersaturation is diagnosed by the prognostic fields of temperature and water vapor, and a prognostic method for calculating the supersaturation following, for example, Clark (1973), Morrison and Grabowski (2007), and Lebo et al. (2012). Basically, the supersaturation is given by  $s = q_v/q_s - 1$ , while the absolute supersaturation (or water vapor surplus) is defined as  $\delta = q_v - q_s$ , where  $q_v$  is the water vapor mixing ratio and  $q_s$  is the saturation mixing ratio. In the following, these three methods are briefly reviewed.

1. *Saturation adjustment.* In many microphysical models, a saturation adjustment scheme is applied. The basic idea of this scheme is that all supersaturation is removed within one model time step and supersaturations are thus neglected. Saturation adjustment thus potentially leads to excessive condensation. Despite the many years of application of this scheme, its impact on microphysical processes is discussed controversially (e.g., Morrison and Grabowski, 2008; Thouron et al., 2012; Lebo et al., 2012). Saturation adjustment might hence especially be a source of error in fog simulations, where very small time steps are used due to small grid spacings, as already discussed. Using the saturation adjustment scheme,  $q_1$  represents a diagnostic value calculated by means of

$$q_1 = \max(0, q - q_r - q_s), \quad (11)$$

where  $q$  is the total water mixing ratio. The saturation mixing ratio, which is a function of temperature, is approximated in a first step by

$$q_s(T_1) = \frac{R_d}{R_v} \frac{e_s(T_1)}{p - e_s(T_1)}, \quad (12)$$

where  $T_1$  is the liquid water temperature and  $p$  is pressure.  $R_d$  and  $R_v$  are the specific gas constants for dry air and water vapor, respectively. For the saturation vapor pressure ( $e_s$ ) an empirical relationship of Bougeault (1981) is used. In a second step,  $q_s$  is corrected using a first-order Taylor series expansion of  $q_s$ :

$$q_s(T) = q_s(T_1) \frac{1 + \gamma q}{1 + \gamma q_s(T_1)}, \quad (13)$$

with

$$\gamma = \frac{L_v}{R_v c_p T_1^2}, \quad (14)$$

where  $c_p$  is the specific heat of dry air at constant pressure and  $L_v$  is the latent heat of vaporization. As previously mentioned, in each model time step, all supersaturation is converted into liquid water or, in subsaturated regions, the liquid water is reduced until saturation. In order to use this scheme with aerosol activation parameterizations, it is necessary to estimate the supersaturation (see Eq. 5). This can be achieved for the activation scheme of Cohard et al. (1998) following, for example, Thouron et al. (2012), Mazoyer et al. (2017) and Zhang et al. (2014), directly translating into a droplet number concentration by

$$s^{k+2} \cdot F(\mu, k/2, k/2 + 1, -\beta s) = \frac{\left(\phi_1 w + \phi_3 \frac{dT}{dt} \Big|_{\text{rad}}\right)^{\frac{3}{2}}}{2kC\pi\rho_l\phi_2 B\left(\frac{k}{2}, \frac{3}{2}\right)}, \quad (15)$$

where  $\phi_1$ ,  $\phi_2$  and  $\phi_3$  are functions of temperature and pressure and are given in Cohard et al. (1998) and Zhang et al. (2014).  $w$  is the vertical velocity and  $B$  is the beta function.

2. *Diagnostic supersaturation calculation.* Supersaturation is calculated diagnostically from  $q_v$  and temperature  $T$  (from which  $q_s$  can be derived). However, since it is assumed that the supersaturation is kept constant during one model time step, the diagnostic approach requires a very small model time step of

$$\Delta t \leq 2\tau, \quad (16)$$

due to stability reasons (Árnason and Brown Jr., 1971). Here,  $\tau$  is the supersaturation relaxation time which is approximated by

$$\tau \approx (4\pi D n_c \bar{r})^{-1}, \quad (17)$$

where  $\bar{r}$  is the average droplet radius, and  $D$  is the diffusivity of water vapor in air. Due to the low dynamic time step in the present study imposed by the Courant–Friedrichs–Lewy criterion (on the order of 0.1 s), however, the condensation time criterion is fulfilled, and no additional time-step decrease is needed. The rate of cloud water change due to condensation or evaporation is given by

$$\left(\frac{\partial q_1}{\partial t}\right)_{\text{cond}} = \frac{4\pi G(T, p)\rho_w}{\rho_a} s \int_0^{\infty} r f(r) dr \quad (18)$$

$$= \frac{4\pi G(T, p)\rho_w}{\rho_a} s r_c, \quad (19)$$

where  $r_c$  is the integral radius and  $G = \frac{1}{F_K + F_D}$  included the thermal conduction and the diffusion of water vapor (Khairoutdinov and Kogan, 2000). The density ratio of liquid water and the solute is given by  $\rho_w/\rho_a$ .

3. *Prognostic supersaturation.* The prognostic approach, which was first introduced by Clark (1973), includes an additional prognostic equation for the absolute supersaturation. Even though this requires solving one more prognostic equation, it mitigates the problem of spurious cloud-edge supersaturations and prevents inaccurate supersaturation caused by small errors in the advection of heat and moisture (Morrison and Grabowski, 2007; Grabowski and Morrison, 2004).

The temporal change of  $\delta$  is given by

$$\frac{\partial \delta}{\partial t} - \frac{1}{\rho} \nabla \cdot (u \rho \delta) = A - \frac{\delta}{\tau}, \quad (20)$$

with  $A$  being described by

$$A = -q_s \frac{\rho g w}{p - e_s} - \frac{dq_s}{dT} \cdot \left[ \frac{g w}{c_p} + \left( \frac{dT}{dt} \right)_{\text{rad}} \right], \quad (21)$$

with  $g$  being gravitational acceleration. The supersaturation relaxation time is given in Eq. (17). The second term on the left-hand side of Eq. (20) describes the change of the absolute supersaturation due to advection, while the right-hand side considers changes of  $\delta$  due to changes in pressure, adiabatic compression and expansion, and radiative effects (from left to right). By doing so, the predicted supersaturation is used for determining the number of activated droplets as well as the condensation and evaporation processes. Note that here the absolute supersaturation is taken, as using  $s$  would involve more terms and is more complex to solve (Morrison and Grabowski, 2007).

### 3 Case description and model setup

The simulations performed in the present study are based on an observed deep fog event during the night from 22 to 23 March 2011 at the Cabauw Experimental Site for Atmospheric Research (CESAR). The fog case is described in detail in Boers et al. (2013) and was used as a validation case for PALM by Maronga and Bosveld (2017). The CESAR site is dominated by rural grassland landscape and, although it is relatively close to the sea, continental aerosol conditions are commonly observed and are characterized by agricultural processes (Mensah et al., 2012).

The fog initially formed at midnight (as a thin near-surface layer), induced by radiative cooling, which also produced a strong inversion with a temperature gradient of 6 K between the surface and the 200 m tower level. In the following, the fog layer began to develop: at 03:00 UTC the fog had a vertical extension of less than 20 m then deepened rapidly to 80 m, reaching 140 m depth at 06:00 UTC. At 03:00 UTC, the visibility had also reduced to less than 100 m. After sunset (around 05:45 UTC) a further invigoration close to the ground was suppressed, and after 08:00 UTC the fog started

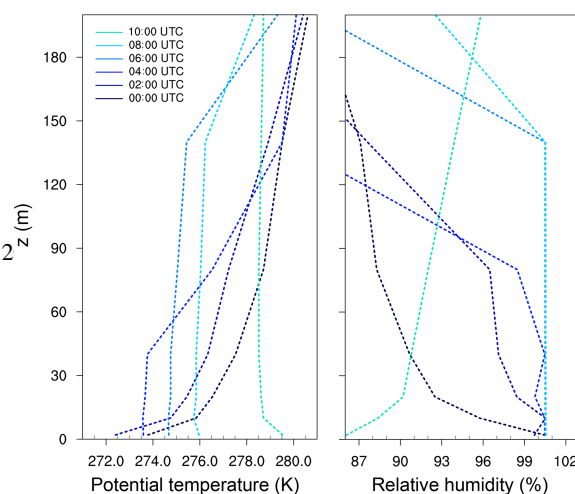


**Figure 1.** Profiles of potential temperature and relative humidity at different times, as observed at Cabauw.

to quickly evaporate due to direct solar heating of the surface. For details, see Boers et al. (2013).

The model was initialized as described in the precursor study of Maronga and Bosveld (2017). Profiles of temperature and humidity (see Fig. 1) were derived from the CESAR 200 m tower and used as initial profiles in PALM. A geostrophic wind of  $5.5 \text{ m s}^{-1}$  was prescribed based on the observed value at Cabauw at 00:00 UTC.

The land surface model was initialized with short grassland as surface type and four soil model layers at the depths of 0.07, 0.28, 1.0 and 2.89 m. The measured surface layer temperatures were interpolated to the respective levels, resulting in temperatures of 279.54, 279.60, 279.16 and 279.16 K for soil layers one to four, respectively. Furthermore, the initial soil moisture was set to the value at field capacity ( $0.491 \text{ m}^3 \text{ m}^{-3}$ ), which reflects the very wet soil and low water table in the Cabauw area. Moreover, the roughness length for momentum was prescribed to 0.15 m. Note that Maronga and Bosveld (2017) discussed that this value appears to be a little high given the season and wind direction. This does not play an important role in the present study, however, as we will not focus on direct comparison against observational data from Cabauw.

All simulations start at 00:00 UTC, before fog formation, and end at 10:15 UTC on the next morning after the fog layer has fully dissipated. Precursor runs are conducted for an additional 25 min using the initial state at 00:00 UTC, but without radiation scheme and LSM in order to allow the development of turbulence in the model without introducing feedback during that time (see Maronga and Bosveld, 2017).

Based on sensitivity studies of Maronga and Bosveld (2017), a grid spacing of  $\Delta = 1 \text{ m}$  was adopted for all simulations, with a model domain size

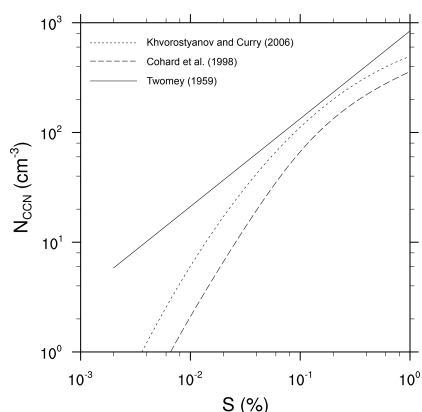


**Figure 2.** Activation spectrum for three different activation schemes of Twomey (1959), Cohard et al. (1998), and Khvorostyanov and Curry (2006) for a typical continental aerosol environment.

of  $768 \times 768 \times 384$  grid points in  $x$ ,  $y$  and  $z$  direction, respectively. Cyclic conditions were used at the lateral boundaries. A sponge layer was used starting at a height of 344 m in order to prevent gravity waves from being reflected at the top boundary of the model.

Table 1 gives an overview of the simulation cases. All cases were initialized with (identical) continental aerosol conditions. Case SAT represents a reference run with no activation scheme and thus a prescribed constant value of  $n_c = 150 \text{ cm}^{-3}$  (estimated from simulations of Boers et al., 2013). This case represents the same setup to the one described in Maronga and Bosveld (2017) except for modifications concerning the aerosol environment as outlined below. Condensation processes were treated here with the saturation adjustment scheme (Seifert et al., 2006). In order to evaluate the influence of saturation adjustment in a one-moment microphysics scheme on the development of radiation fog, identical assumptions were made in case DIA and PRG, except that diffusional growth was calculated with the diagnostic and prognostic method, respectively (see Sect. 2.2.2).

Moreover, as small differences in supersaturation can affect the number of activated droplets significantly, the impact of different methods for calculating supersaturation on CCN activation is investigated in a two-moment microphysics approach (see Sect. 4.2.2). Therefore, the simulations N2SAT, N2DIA and N2PRG were compared to each other. In all three cases the activation scheme of Cohard et al. (1998) is used and initialized as described below.

Furthermore, cases N1DIA–N3DIA used the activation schemes described in Sect. 2.2.1. To ensure comparability between the different schemes, all of them were initialized with a continental aerosol background described in Cohard et al. (1998), which is characterized by an

aerosol with the chemical composition of ammonium sulfate  $[(\text{NH}_4)_2\text{SO}_4]$ , a background aerosol concentration of  $842 \text{ cm}^{-3}$ , a mean dry aerosol radius of  $r_{d0} = 0.0218 \mu\text{m}$  and a dispersion parameter of the dry aerosol spectrum of  $\sigma_d = 3.19$ . For the Twomey activation scheme this results in  $N_0 = 842 \text{ cm}^{-3}$  and  $k = 0.8$ , which is a typical value for the exponent for continental air masses (e.g., Pruppacher and Klett, 1997, p. 289 et seq.). The Twomey activation scheme does not allow for taking aerosol properties into account. In contrast, the activation scheme of Cohard et al. (1998) requires the parameters  $C$ ,  $k$ ,  $\beta$  and  $\mu$  to be derived from the aerosol properties. Here, values of  $C = 2.1986 \times 10^6 \text{ cm}^{-3}$ ,  $k = 3.251$ ,  $\beta = 621.689$  and  $\mu = 2.589$  were used as described in Cohard and Pinty (2000). Finally, the activation scheme of Khvorostyanov and Curry (2006) can directly consider the aerosol properties, which are prescribed as previously mentioned. Using those different parameterizations resulted in different activation spectra, which are shown in Fig. 2. One can see that especially the CCN concentration is changed by using these different methods, such that this part of the study is equivalent to a sensitivity study of different CCN concentration but is realized by using different coexisting parameterizations.

## 4 Results

### 4.1 General fog life cycle and macrostructure

The reference case SAT is conducted with a constant droplet number concentration of  $n_c = 150 \text{ cm}^{-3}$ . The deepening of the fog layer can be seen in Fig. 3, which shows the profiles of the potential temperature, relative humidity and liquid water mixing ratio at different times.

The fog onset is at 00:55 UTC, defined by a visibility below 1000 m and a relative humidity of 100%. In the following the fog layer deepens and extends to a top of approximately 20 m at 02:00 UTC. However, at this point the stratification of the layer is still stable with a temperature gradient of 6 K between the surface and the fog top. The persistent radiative cooling of the surface and the fog layer leads to a further vertical development of the fog, which is accompanied with a regime transition from stable to convective conditions within the fog layer (see Fig. 3a). This starts as soon as the fog layer begins to become optically thick (at 03:30 UTC), and when radiative cooling at the fog top becomes the dominant process, creating a top-down convective boundary layer. The highest liquid water mixing ratio of  $q_1 = 0.41 \text{ g kg}^{-1}$  is achieved at 06:00 UTC at a height of 60 m (see Fig. 3c), while the fog layer in total reaches the maximum 1 h later at 07:00 UTC. The lifting of the fog, which is defined by a non-cloudy near-surface layer ( $q_1 \leq 0.01 \text{ g kg}^{-1}$ ), occurs at 08:45 UTC. At 11:30 UTC the fog is completely dissipated.

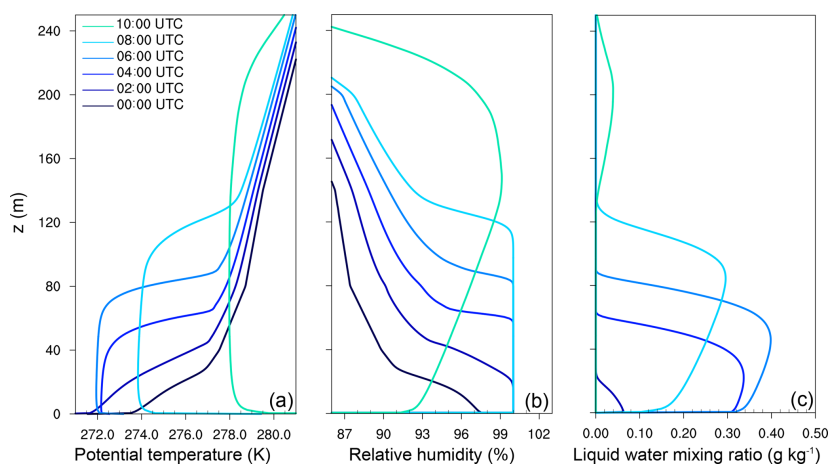


**Figure 3.** Profiles of potential temperature (a), relative humidity (b) and liquid water mixing ratio (c) at different times for the reference case REF.

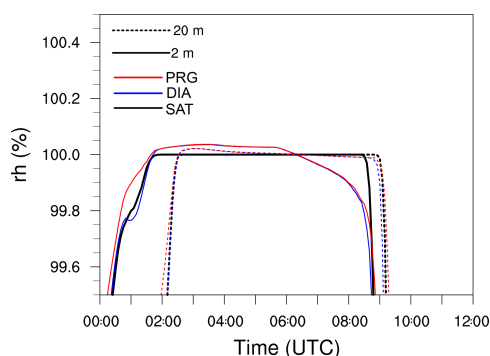


**Figure 4.** Time series of horizontally averaged relative humidity (rh) and supersaturation at height levels of 2 m (solid) and 20 m (dotted) for different methods in treating the supersaturation calculation.

#### 4.2 Influence of different supersaturation calculation

In this section we discuss the influence of three different methods considering supersaturation. Namely these are (as previously mentioned) saturation adjustment, a diagnostic supersaturation calculation and a prognostic method. In the first subsection a one-moment microphysics scheme is used and the impact of the different supersaturation methods is limited to the effect of diffusional growth. In the second part of this study those methods are applied in a two-moment microphysics scheme, considering the effect of such different approaches of supersaturation calculations for activation.

##### 4.2.1 One-moment microphysics scheme: impact of supersaturation calculation on diffusional growth

In this section we discuss the error introduced by using saturation adjustment for simulating radiation fog with a one-moment scheme in a LES. For this, we compare three simulations with identical setups (cases SAT, DIA, and PRG), which differ only in the way supersaturation is calculated and consequently the amount of condensed or evaporated liquid water. To isolate this effect, activation is neglected in all cases and  $n_c$  is set to a constant value of  $150 \text{ cm}^{-3}$  (a typical value in fog layers). The effect on different supersaturations driving the diabatic process of activation is discussed in Sect. 4.2.2. As mentioned before the time step is roughly 0.1 s, which is more than 1 order of magnitude smaller than the allowed values of 2–5 s for assuming saturation adjustment (Thouren et al., 2012). The present case hence is an ideal environment evaluating the error introduced by using saturation adjustment and by keeping all other parameters fixed.

Figure 4 shows time series of the horizontally averaged saturation (supersaturation) for cases SAT, DIA and PRG at selected heights close to the surface. In all cases saturation occurs simultaneously around 01:20 UTC. In case SAT, relative humidity does not exceed 100 % due to its limitation by saturation adjustment, while in case DIA and PRG, average supersaturations of 0.05 % are reached at a height of 2 m, which corresponds to typical values within fog (Hammer et al., 2014; Mazoyer et al., 2019; Boutle et al., 2018).

For cases DIA and PRG, starting from 06:15 UTC (in 2 m height) and 07:15 UTC (in 20 m height), supersaturations are removed and the air becomes subsaturated (on average). This is in contrast with case SAT, where the saturation adjustment approach keeps the relative humidity at 100 % as long as liq-

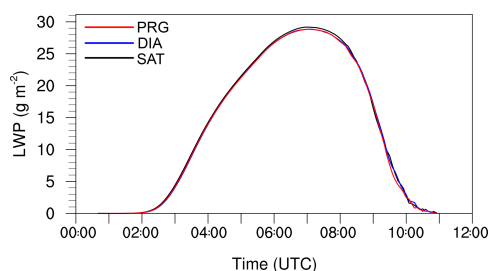


**Figure 5.** Time series of liquid water path (LWP) for cases using saturation adjustment, the diagnostic approach and a prognostic method for the diffusional growth.

liquid water is present (i.e., until the fog has dissipated). Around 06:00 UTC, which is shortly after sunrise, relative humidity drops rapidly in PRG and DIA as a direct consequence of direct solar heating of the surface and the near-surface air, preventing further supersaturation at these heights. While we cannot clearly identify the lifting of the fog in case DIA and PRG (due to the limited humidity range displayed), we note that for case SAT we can identify lifting times as a decrease of relative humidity around 08:45 UTC at 2 m height and around 09:10 UTC at 20 m height.

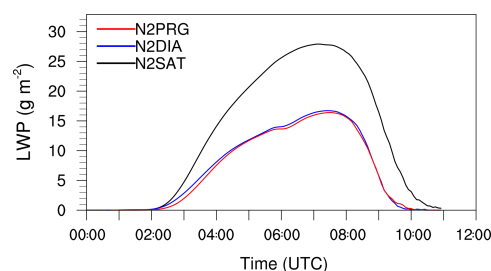
Besides this inherent difference in relative humidity, the general time marks (formation, lifting and dissipation, defined by Maronga and Bosveld, 2017) of the fog layer are identical for cases SAT, DIA and PRG.

Figure 5 shows the liquid water path (LWP) for all cases. Differences in the LWP appear between 04:00 and 11:00 UTC and do not exceed 1 % (lower values for cases DIA and PRG), indicating that the choice of the condensation scheme does not affect the total water content of the simulated fog layer.

It can be summarized that, although the assumptions of saturation adjustment are not valid for the simulation of fog when using a very small time step, the mean liquid water content is not changed by more than 1 % and the general fog structure is not altered when using a one-moment microphysics and neglecting supersaturation. This is probably due to the very small supersaturation that is not strong enough to generate a significant change in the effective droplet radius and which could possibly lead to stronger sedimentation or higher radiative cooling rates.

#### 4.2.2 Two-moment microphysics scheme: impact of supersaturation calculation on CCN activation

Even though different methods for calculating supersaturation which interacts with the diffusional growth are not strong enough to generate any noteworthy differences by using a one-moment microphysics (considering a constant value for  $n_c$ ), the impact of different methods modeling su-



**Figure 6.** Time series of LWP for simulations using saturation adjustment (N2SAT in black), the diagnostic scheme (N2DIA in blue) and the prognostic method (N2PRG in red). All cases use the activation scheme of Cohard et al. (1998).

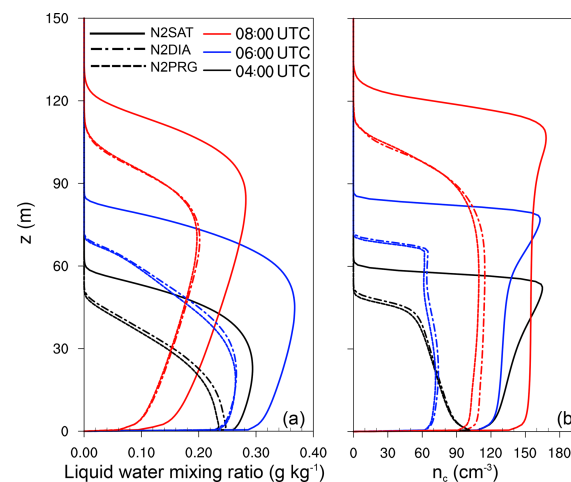


**Figure 7.** Profiles for liquid water mixing ratio (a) and droplet number concentration (b) at 04:00, 06:00 and 08:00 UTC.

persaturation on CCN activation by using a two-moment microphysics might be significant.

Figure 6 shows the LWP for simulations applying the activation scheme of Cohard et al. (1998) in conjunction with the usage of saturation adjustment (N2SAT), the diagnostic scheme (N2DIA) and the prognostic scheme (N2PRG) for calculating supersaturations. It can be seen that the prognostic and diagnostic methods produce similar LWP values. However, for case N2SAT the LWP is nearly 70 % higher than for the other two cases. In Fig. 7 profiles of the liquid water mixing ratio (left) and droplet number concentration (right) are shown. From that figure it can be seen that in case of N2SAT, both the fog height as well as the liquid water mixing ratios within the layer are higher than in N2DIA and N2PRG, respectively. However, small differences in  $q_1$  can also be found between N2DIA and N2PRG (e.g., at 06:00 UTC in the second third of the fog layer). This is explained by slightly higher values for the number concentration in case of N2DIA than in N2PRG. However, both are

**Table 1.** Overview of conducted simulations. The droplet number concentration  $n_c$  is only prescribed for simulations without activation scheme. In the simulations N1DIA–N3DIA,  $n_c$  is a prognostic quantity and is thus variable in time and space. The aerosol background concentration is abbreviated with  $N_{a,tot}$  and used to initialize the activation schemes. Note for the scheme after Cohard et al. (1998) a conversion to the parameter  $C$  must be applied, while for both other activation schemes this value is directly used to prescribe  $N_0$  and  $N_t$ , respectively.

No.	Simulation	Activation scheme	$n_c$ (cm <sup>-3</sup> )	$N_{a,tot}$ (cm <sup>-3</sup> )	Condensation scheme
1	SAT	None	150	None	Saturation adjustment
2	DIA	None	150	None	Diagnostic
3	PRG	None	150	None	Prognostic
4	N2SAT	Cohard et al. (1998)	Not fixed	842	Saturation adjustment
5	N2DIA	Cohard et al. (1998)	Not fixed	842	Diagnostic
6	N2PRG	Cohard et al. (1998)	Not fixed	842	Prognostic
7	N1DIA	Twomey (1959)	Not fixed	842	Diagnostic
8	N3DIA	Khvorostyanov and Curry (2006)	Not fixed	842	Diagnostic

at approximately 75 cm<sup>-3</sup> at 06:00 UTC. In contrast, in simulation N2SAT, a number concentration of 120 to 150 cm<sup>-3</sup> (at the top) is observed, which is about 60%–100% higher in comparison to N2DIA and N2PRG. These differences can be explained by the different methods for calculating the supersaturation, since activation is the main process altering the droplet number concentration. Therefore, we can implicitly derive from the droplet number concentration that the predicted and diagnosed supersaturations using the prognostic and diagnostic method are similar. These differences between N2SAT and N2DIA–N2PRG are, however, in good agreement with values reported for a stratocumulus case by Thouron et al. (2012). Their Fig. 2 shows that the number concentration of the diagnostic and prognostic method were also similar and the case with saturation adjustment overestimated the supersaturation and therefore the droplet number concentration. As the fog droplet number concentration has a crucial feedback on the overall LWP of the fog layer, the times of lifting and the time of its dissipation, the reported differences in  $n_c$  are significant regarding the accurate modeling and prediction of fog. The reason why the number concentration is such a critically parameter can be ascribed to their impact on sedimentation and radiative cooling, which is explained in more detail in Sect. 4.4.3.

In order to evaluate the possible effect of the grid spacing, in conjunction with different methods for calculating the supersaturation, on CCN activation, we repeated each of the cases N2SAT, N2DIA and N2PRG with two coarser grid spacings of 2 and 4 m. The general effect of the grid spacing on the temporal development and structure of radiation fog is discussed in detail in Maronga and Bosveld (2017). In this section, we will focus only on changes in LWP due to different supersaturation calculations at different spatial model resolutions. For isolating the effect of the grid spacing, all simulations with a coarser grid spacing were carried out with the same time step of 0.125 s, which corresponds to the average time step of the simulations at highest grid spacing of

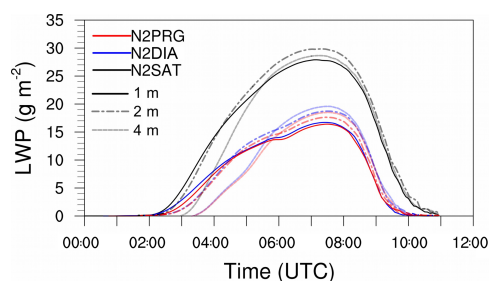


**Figure 8.** As in Fig. 6 but also for 2 m (dotted–dashed) and 4 m (dashed).

1 m. In this way, effects of different time steps induced by different grid spacings could be eliminated.

Figure 8 shows the LWP for all grid sensitivity runs. First of all, note that for 1 m grid spacing, the results reflect the results shown in Fig. 6 and discussed above (i.e., significantly higher LWP for case N2SAT than for cases N2DIA and N2PRG). Moreover, Fig. 8 reveals that these results are somewhat sensitive to changes in the grid spacing. For all cases we observe a tendency towards higher LWP values with increasing grid spacing, at least for cases N2DIA and N2PRG. These differences are, however, not larger than 4 g m<sup>-2</sup> and are thus significantly smaller than the observed differences found between the different methods to calculate supersaturation. Note, however, that the relative change in LWP with grid spacing is higher for case N2DIA than for case N2PRG. Quantitatively speaking, in case of 1 m grid spacing the relative difference of the LWP is 2.1% between N2DIA and N2PRG during the mature phase, while for the case with a grid spacing of 4 m it reaches 8.1%. This might be explained by the fact that the diagnostic scheme is very sensitive to small errors (e.g., induced by the numerical advection) in the temperature and humidity fields (e.g., Morrison and Grabowski, 2008; Thouron et al., 2012). A coarser



spatial resolution here can lead to larger error introduced by spurious supersaturation. We thus suppose that the increased differences (see Fig. 8) by larger grid spacings are induced by spurious supersaturation, which affect the CCN activation and hence influence the LWP of the fog layer.

Furthermore, we note that coarser grid spacings lead to a later fog formation time, which is in agreement with Maronga and Bosveld (2017) and can be ascribed to under-resolved turbulence near the surface at coarse grids.

In summary, we can thus conclude that the sensitivity to changes in the grid spacing is rather small, but it might imply differences in the LWP of the simulated fog layer of up to  $4 \text{ g m}^{-2}$ .

### 4.3 Two-moment microphysics scheme: comparison of different activation parameterizations

In numerous previous studies, the influence of aerosols and the activation process on the life cycle of fog was investigated (e.g., Bott, 1991; Stolaki et al., 2015; Maalick et al., 2016; Zhang et al., 2014; Boutle et al., 2018). Although all three activation schemes outlined in Sect. 2.2.1 are comparable power law parameterizations that are initialized with identical aerosol spectra, the effect on simulations of radiation fog is still unknown. Because changes in  $n_c$  due to different activation schemes have a considerable effect on the life cycle of fog, we might consider that even small differences in  $n_c$  might alter simulated fog layers significantly. This part of the study can be regarded as a sensitivity study of different CCN concentrations realized by applying different activation schemes, which is illustrated also in Fig. 2. However, from a model user's perspective, such a sensitivity is of great importance, as CCN concentrations are usually difficult (case studies) or even impossible (forecasting) to obtain, and model results thus might highly depend on the chosen activation parameterization.

### 4.4 LWP and $n_c$

Time series of the LWP for the reference run (case SAT) and the three different cases (N1DIA–N3DIA) are shown in Fig. 9a. The highest LWP occurs for case SAT, which also shows the highest  $n_c$  during the formation and mature phase in comparison with the other simulations (see Fig. 9b). The time series of  $n_c$  shown in Fig. 9b (representing runs with the three different aerosol activation parameterization schemes; see Table 1) reveal that, depending on the parameterization used, the a shift in  $n_c$  towards smaller or larger values is found. The quantitative differences in the number of activated aerosol by using the different activation schemes is due to a slightly different activation spectrum (see Fig. 2). A linear relationship between LWP and  $n_c$  can be found: a higher  $n_c$  leads to higher LWP, which is in agreement with other studies, like Boutle et al. (2018), for example. In principle, a similar qualitative development of  $n_c$  can be observed. While

$n_c$  increases during fog formation (with a local maximum with values between 70 and  $140 \text{ cm}^{-3}$ ), it remains nearly constant during the mature phase of the fog (values between 65 and  $145 \text{ cm}^{-3}$ ). We will see later see that activation here happens mostly at the top of the fog, but due to vertical mixing in the convective fog layer, cloud droplets are evenly distributed over a large vertical domain. Furthermore, the mixing layer is increasing in time so that there is no net change of the (averaged)  $n_c$  in the fog layer. As soon as the sun rises and the fog layers start to lift and turn into a stratocumulus cloud, all cases show a strong increase in  $n_c$ . This increase can be explained by stronger supersaturations induced by thermal updrafts in the developing surface-driven convective boundary layer due to surface heating by solar radiation. Moreover, we note that while the qualitative course of  $n_c$  is similar for all cases, the choice of the activation algorithm has an impact on the number of activated aerosols and thus on the strength of the fog layer, e.g., illustrated in Fig. 10 via  $q_l$ . This is due to the radiation effect of the droplets. The number of droplets to which a certain amount of liquid water is distributed plays an important role: the larger the number of droplets, the larger the radiation-effective surface and the higher also the optical thickness. As a result the cooling rate in fog with many small droplets is increased, allowing more water vapor to condense and the fog to grow stronger. By the same token, sedimentation also depends on the droplet radius and plays a major role in fog development. This will be further discussed below.

#### 4.4.1 Visibility

In Fig. 11 the simulated visibility is shown for the cases N1DIA–N3DIA in 2 m height together with the observed values at Cabauw (for illustration only). Visibility is calculated from the LES data following Gultepe et al. (2006) as

$$\text{vis} = \frac{1002}{(n_c \rho \ q_l)^{0.6473}}. \quad (22)$$

This visibility estimation (with  $n_c$  and  $q_l$  given in units of  $\text{cm}^{-3}$  and  $\text{g m}^{-3}$ , respectively) thus significantly depends on the droplet number concentration and the liquid water content. Unlike in the first part of this paper, analyzing visibility estimations from the simulations might illuminate the capability of LES to predict visibility. Figure 11 reveals that visibility follows the same general temporal developed for all cases, with a rapid decrease at fog formation, deepening and dissipation, with minimum values at around 100 m (which is close to the observed values). We also see noteworthy differences, particularly shortly before 02:00 UTC (before fog deepening) at around 05:45 UTC (shortly after sunrise). For both time marks, cases N1DIA–N3DIA display sudden increases in visibility, due to an fast decrease in  $n_c$  in 2 m height, which are not reproduced by case SAT, as  $n_c$  is fixed value in this case. The sudden increase in visibility around 00:45 UTC in the observations is possibly related to this pro-



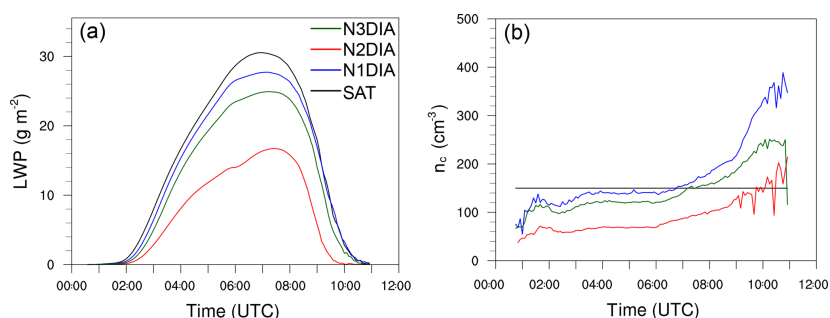


**Figure 9.** Time series of LWP and  $n_c$  (as a horizontal and vertical average of the fog layer) for the reference and N1DIA–N3DIA case.

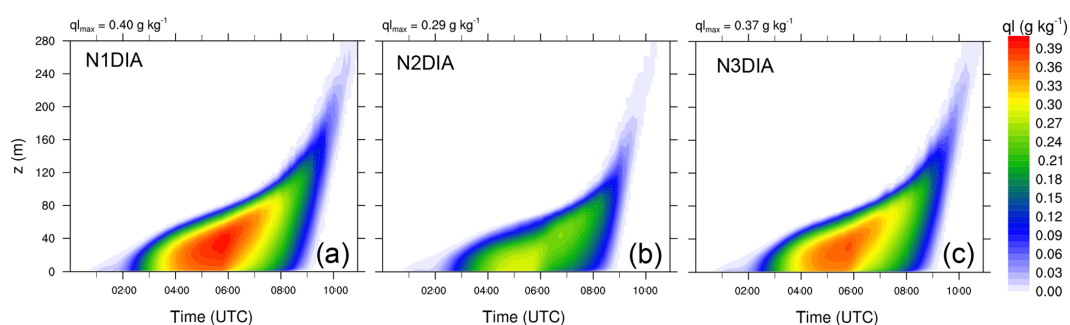


**Figure 10.** Height–time cross sections for the liquid water mixing ratio for N1DIA–N3DIA.

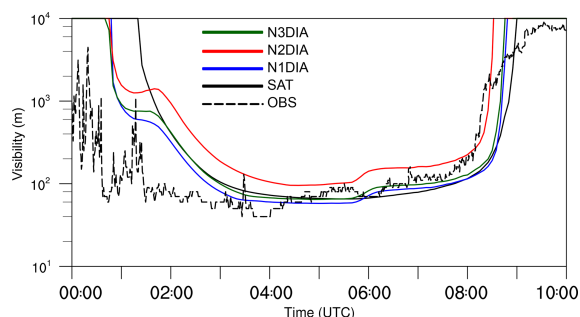


**Figure 11.** Time series of simulated visibility in 2 m height. Observations from Cabauw (dashed lines) were added for illustration only.

cess. Also, the time marks of formation and dissipation vary. For cases N1DIA–N3DIA, the formation time is significantly advanced compared to case SAT, while dissipation time only shows a small tendency towards earlier times, at least for N1DIA and N3DIA. Case N2DIA displays a different behavior, with a later fog formation and higher visibility and accordingly earlier dissipation time. This is in line with the findings discussed above (i.e., a much weaker fog layer that, as a direct consequence, can dissipate much faster). Other-

**Table 2.** Table of fog’s life cycle time marks.

Simulation	Onset	Maximum	Lifting	Dissipation
N1DIA	00:25 UTC	05:10 UTC	08:10 UTC	10:05 UTC
N2DIA	00:50 UTC	04:25 UTC	07:55 UTC	09:10 UTC
N3DIA	00:25 UTC	05:15 UTC	08:10 UTC	09:50 UTC

wise, all cases display almost identical visibility as soon as the fog has deepened.

#### 4.4.2 Time marks of the fog life cycle

The effect of the different droplet concentration (induced by the usage of different activation schemes) on the time marks of the fog life cycle is summarized in Table 2. While N1DIA and N3DIA have similar time marks, N2DIA stands out and shows a delayed onset by 25 min, while the maximum liquid water mixing ratio is reached 45 min earlier than in the other cases. Also lifting and dissipation are affected and occurred 15 and 40 min (with respect to simulation N3DIA) earlier. This is due to a lesser absolute liquid water mixing ratio which evaporates faster by the incoming solar radiation. Therefore, it can be concluded that the use of different activation schemes (if they change the droplet number concentration) has an effect on the time marks on the life cycle

as well as on the fog height and the amount of liquid water within the fog layer.

#### 4.4.3 Budgets of liquid water and droplet number concentration

In this section we will analyze the budgets of liquid water and droplet number concentration in physical terms. As in the preceding section, we will use the cases with different activation parameterizations, since they provide us a range of different CCN concentrations. Figure 12a shows the profiles of the liquid water mixing ratio at 04:00, 06:00 and 08:00 UTC, i.e. at different times during the mature phase of the fog. A detailed analysis of budgets at other stages of the life cycle of the fog is beyond the scope of this paper. The maximum  $q_l$  in the fog layer is reached at approximately 06:00 UTC at a height of 60 m. Afterwards a further vertical growth of the fog can be observed, where no further increase in liquid water takes place as a result of larger vertical extent of the mixing layer and due to rising temperatures after sunrise. Moreover, Fig. 12b and c show the liquid water budget during the mature phase of the fog at 06:00 UTC, when the fog was fully developed. Almost all three cases show identical values for condensation rates in the lowest part of the fog layer, with values being in the same order as the evaporation rates so that the net gain in this region appears to be small (see Fig. 12b). However, the N2DIA case (with the lowest  $n_c$ ) exhibits a generally lower absolute evaporation rate compared to both other cases, which can be attributed to the slightly higher mean values of the relative humidity (not shown) than in N1DIA and N3DIA. In the upper part of the fog layer, higher values of the condensation rate are observed (especially for N1DIA and N3DIA) with a concurrent decrease in evaporation rates, leading to differently strong deepening of the fog layer. At a height of approximately 80 m, a maximum of the evaporation rates can be observed, representing the presence of subsaturated regions at this height and the top of the fog. Larger differences can be observed in the sedimentation rates. First and foremost the sedimentation is proportional to the liquid water mixing ratio (see also Eq. 4). The strength of sedimentation also depends on the mean radius of the droplets, which increases with a decreasing number of activated drops. Here, a lower  $n_c$  for a given amount of liquid water leads to a higher mean radius, compared to a higher  $n_c$  where the same amount of water is distributed to more drops, decreasing the mean radius. Integrated over height, all three cases exhibit approximately the same sedimentation rates. Therefore, case N2DIA experiences the strongest loss of liquid water due to sedimentation (in relative terms). Moreover, Fig. 12c shows that sedimentation partially counteracts the gains caused by condensation at the upper edge of the fog. The net advection transports liquid water from the second third of the fog layer (position of the maximum) to higher levels. It can be summarized that all terms contribute significantly to the net change of the liq-

uid water mixing ratio, illustrating that all microphysical processes deserve a proper modeling for radiation fog. In the mature phase, however, sedimentation plays a key role, showing the highest values for the individual tendencies. As a result liquid water is slowly and constantly removed from the fog layer. These findings are in good agreement with previous investigations by Bott (1991).

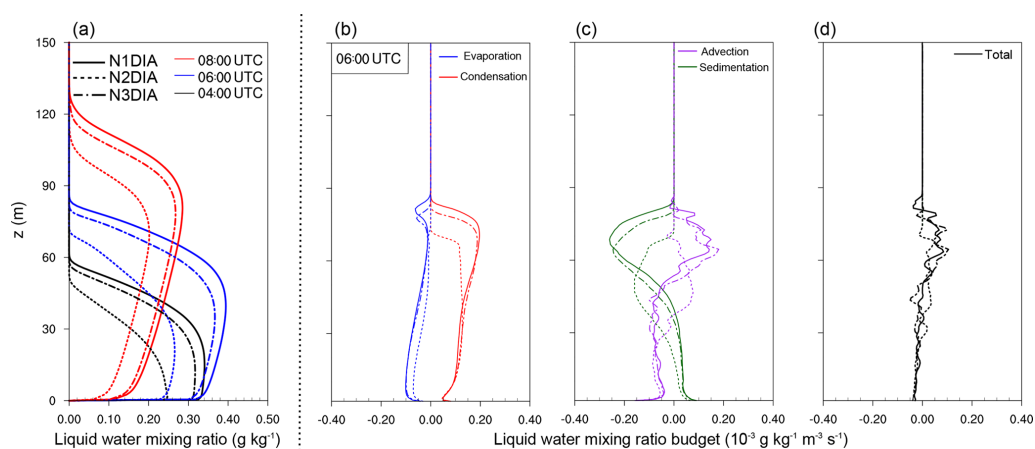
The sum of all tendencies, which is shown in Fig. 12d, is the height-dependent change of the liquid water. Also here it can be seen that in the lower 50 m the net tendency is negative, while in higher levels we observe a positive tendency so that the fog continues growing vertically while the liquid water content within the fog layer decreases.

Figure 13a additionally shows the profiles of  $n_c$ . We note that the profiles of the different cases differ quantitatively but not qualitatively. The stage of the fog can thus be identified in the profiles for all cases. At 04:00 UTC, the highest supersaturations occur close to the ground due to cooling of the surface and near-surface air, leading to high activation rates and therefore high  $n_c$  near the surface (not shown). At 06:00 UTC a well-mixed layer has developed that is driven by the radiative cooling from the fog top. While the turbulent mixing leads to a vertical well-mixed  $n_c$ , we note the maximum at the top, where the radiative cooling induces immense aerosol activation. This is further illustrated in the budget of the  $n_c$  in Fig. 13b and c, where instantaneous data at 06:00 UTC are shown. Here, we see clearly that aerosol activation at the top of the fog layer is the dominant process in the mature phase of the fog, while activation near the surface is comparably small. Evaporation of droplets, though small in magnitude, occurs only at the fog top, reflecting upward motions of foggy air penetrating the subsaturated air aloft where droplets then evaporate. Also, we see that both advection and sedimentation rates are much smaller than activation rates so that the net change in  $n_c$  is controlled by the activation near the fog top during the mature phase of the fog.

## 5 Conclusions

The main objective of this work was to investigate the influence of the choice of the supersaturation calculation and activation parameterizations used in LES models on the life cycle of simulated nocturnal deep radiation fog under typical continental aerosol conditions. For this purpose we performed a series of LES runs based on a typical deep fog event as observed at Cabauw (the Netherlands).

In the main part of this study we applied a two-moment microphysics scheme with an activation parameterization of Cohard et al. (1998) and investigated the influence of three different (but commonly used) supersaturation calculation methods, i.e., saturation adjustment, a diagnostic method, and a prognostic method, on the life cycle and LWP of the simulated fog event. From the results we found that in the case of saturation adjustment, nearly 60 % higher droplet



**Figure 12.** Profiles (instantaneously and horizontally averaged) of liquid water mixing ratio at 04:00, 06:00 and 08:00 UTC, and profiles of liquid water budget terms at 06:00 UTC.

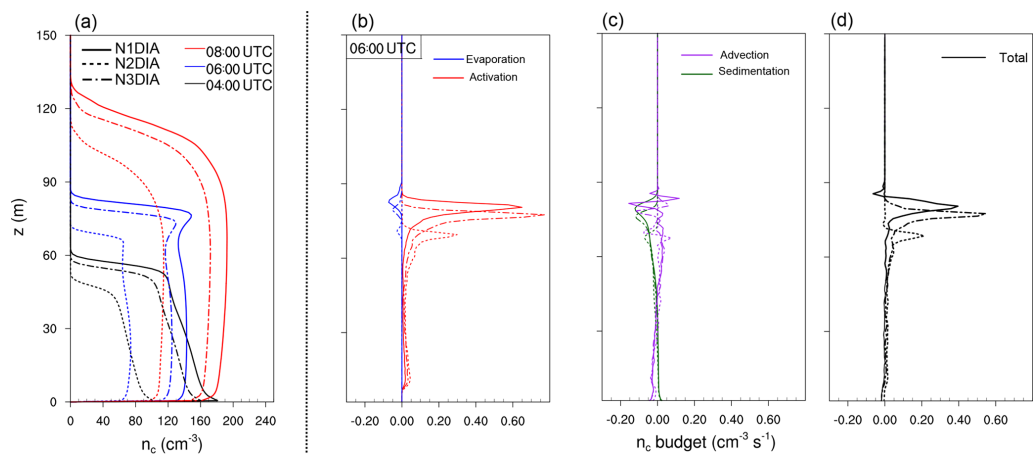


**Figure 13.** Profiles (instantaneously and horizontally averaged) of  $n_c$  at 04:00, 06:00 and 08:00 UTC, and profiles of  $n_c$  budget terms at 06:00 UTC.

number concentrations are produced in comparison with simulation with the diagnostic or prognostic method. This results in a more than 70 % higher LWP for the saturation adjustment case and a later occurrence of lifting and dissipation of the fog layer. An explanation for such differences between the schemes can be found in the general assumptions made within the methods. As saturation adjustment assumes that the complete water vapor surplus is removed within one time step, the supersaturation used for activation must be parameterized. In agreement with Thouron et al. (2012) we found that those values are higher than in the other cases, which leads to great feedback of the fog layer. Moreover, we found that the diagnostic method and the prognostic method yield similar results. However, in a grid spacing sensitivity study we observed that the relative differences between the prog-

nostic and diagnostic approach increase as the spatial resolution decreases. We assume that this is due to larger errors of spurious supersaturations which lead to an overestimation of activation in the diagnostic case. This in turn affects the sedimentation velocity as well as the effective radius and hence the radiative cooling, which results in higher values for the LWP.

In a further test, using a one-moment microphysics scheme, we compared the possible error introduced by using saturation adjustment in comparison with an diagnostic and prognostic method for calculating the supersaturation for diffusional growth, i.e., neglecting activation and prescribing a constant droplet number concentration. With these assumptions we were able to isolate the error introduced by saturation adjustment on condensation and evaporation. However,

the results showed that, although the model time step was inappropriate for the assumptions made during saturation adjustment, the differences in LWP are at most 1 % and the general life cycle is not affected. This could be attributed to the fact that the typical supersaturations in fog are in the range of a few tenths of a percent, and the resulting absolute differences are too small to induce further influence on dynamics, microphysics or radiation. This result implies that saturation adjustment is an acceptable method if no activation parameterization is available (with simultaneous consideration that the latter is highly recommended).

In a second part of our study, the effect of different activation schemes of Twomey (1959), Cohard et al. (1998), and Khvorostyanov and Curry (2006) on the simulated fog life cycle was investigated. Even though these parameterizations appear to be rather similar, our results indicate that the resulting number of activated aerosols (and consequently the number of droplets), known to be a crucial parameter for the fog development, can differ significantly. However, it must be mentioned that these differences are attributed to the fact that the CCN concentration is different for the investigated schemes. This part of the study can thus also be understood as a sensitivity study for different CCN concentrations realized by the usage of different activation schemes.

In order to get a deeper insight into the spatial and temporal development of deep radiation fog, we performed an additional analysis of budgets  $n_c$  and  $q_l$  during the mature phase of the fog for simulations with different aerosol activation parameterizations. We found that gain of liquid water is dominated by condensational growth throughout the fog layer with a maximum at the top of the fog layer (due to longwave radiative cooling) and by significant sedimentation of fog droplets from upper levels towards lower levels, while only little liquid water is lost by sedimentation (to the ground) and evaporation. The fact that the simulated cases display significant differences in the fog strength could be traced back to the differences in the condensational growth at the fog top, induced by different activation of CCN. For  $n_c$ , our simulations indeed indicate that activation is the dominant process, located in a narrow height level, while all other processes (i.e., evaporation, advection and sedimentation) were found to be comparably small. The amount of generated liquid water thus is a direct consequence of the strength of the activation process and is thus related to the number of CCN and accordingly the activation parameterization used in the model.

In summary, the present study indicates that the choice of the used supersaturation calculation can be a key factor for the simulation of radiation fog. In agreement with Thouron et al. (2012) we recommend using the prognostic approach to calculate the supersaturation for fog layer in case of a two-moment microphysics considering activation. With this, the effect of spurious cloud-edge supersaturation is mitigated and activation rates that are too large are omitted. Further, the choice of the chosen activation scheme has a notice-

able impact on the number concentration of CCN and hence on the LWP and fog layer depth. However, we have no means to give advice on which activation parameterization performs best. In order to give a more educated recommendation here, we would need observational data of size distributions from aerosol and fog droplets.

In order to overcome the remaining limitations of the present study that are related to microphysical parameterizations, we are currently working on a follow-up study in which we are revisiting this particular fog case using a Lagrangian particle-based approach to simulate the microphysics of droplets. This will allow for explicitly simulating the development of the 3-D droplet size distribution in the fog layer (e.g., Shima et al., 2009). This approach will also allow resolving all relevant microphysical processes such as activation and diffusional growth directly instead of parameterizing them. As such simulations are computationally very expensive, only a very limited number of simulations are feasible at the moment, so most future numerical investigations will – as in the present work – rely on bulk microphysics parameterizations. Based on the results using the Lagrangian approach, however, we hope to be able to give an educated recommendation on the best choice for such bulk parameterizations.

*Code availability.* The PALM used in this study (revision 2675 and revision 3622) is publicly available on <http://palm-model.org/trac/browser/palm?rev=2675> (last access: 28 May 2019) (PALM, 2019a) and <http://palm-model.org/trac/browser/palm?rev=3622> (last access: 28 May 2019) (PALM, 2019b), respectively. For analysis, the model has been extended and additional analysis tools have been developed. The extended code, as well as the job setups and the PALM source code used, are publicly available on <https://doi.org/10.25835/0067929> (PALM group, 2019c). All questions concerning the code-extension will be answered from the authors on request.

*Author contributions.* The numerical experiments were jointly designed by the authors. JS implemented the microphysics parameterizations, conducted the simulations and performed the data analysis. Results were jointly discussed. JS prepared the paper, with significant contributions by BM.

*Competing interests.* The authors declare that they have no conflict of interest.

*Acknowledgements.* This work has been funded by the German Research Foundation (DFG) under grant MA 6383/1-1, which is greatly acknowledged. All simulations have been carried out on the Cray XC-40 systems of the North-German Supercomputing Alliance (HLRN; <https://www.hlrn.de/>, last access: 28 May 2019).

*Financial support.* This research has been supported by the German Research Foundation (grant no. MA 6383/1-1).

The publication of this article was funded by the open-access fund of Leibniz Universität Hannover.

*Review statement.* This paper was edited by Barbara Ervens and reviewed by Thierry Bergot and one anonymous referee.

## References

- Abdul-Razzak, H. and Ghan, S. J.: A parameterization of aerosol activation: 2. Multiple aerosol types, *J. Geophys. Res.-Atmos.*, 105, 6837–6844, 2000.
- Ackerman, A. S., VanZanten, M. C., Stevens, B., Savic-Jovicic, V., Bretherton, C. S., Chlond, A., Golaz, J.-C., Jiang, H., Khairoutdinov, M., Krueger, S. K., Lewellen, D. C., Lock, A., Moeng, C.-H., Nakamura, K., Petters, M. D., Snider, J. R., Weinbrecht, S., and Zulauf, M.: Large-eddy simulations of a drizzling, stratocumulus-topped marine boundary layer, *Mon. Weather Rev.*, 137, 1083–1110, 2009.
- Árnason, G. and Brown Jr., P. S.: Growth of cloud droplets by condensation: A problem in computational stability, *J. Atmos. Sci.*, 28, 72–77, 1971.
- Beare, R. J., Macvean, M. K., Holtslag, A. A., Cuxart, J., Esau, I., Golaz, J.-C., Jimenez, M. A., Khairoutdinov, M., Kosovic, B., Lewellen, D., Lund, T. S., Lundquist, J. K., McCabe, A., Moene, A. F., Noh, Y., Raasch, S., and Sullivan, P.: An intercomparison of large-eddy simulations of the stable boundary layer, *Bound.-Lay. Meteorol.*, 118, 247–272, 2006.
- Bergot, T.: Small-scale structure of radiation fog: a large-eddy simulation study, *Q. J. Roy. Meteorol. Soc.*, 139, 1099–1112, 2013.
- Boers, R., Baltink, H. K., Hemink, H., Bosveld, F., and Moerman, M.: Ground-based observations and modeling of the visibility and radar reflectivity in a radiation fog layer, *J. Atmos. Ocean. Tech.*, 30, 288–300, 2013.
- Bott, A.: On the influence of the physico-chemical properties of aerosols on the life cycle of radiation fogs, *Bound.-Lay. Meteorol.*, 56, 1–31, 1991.
- Bott, A. and Trautmann, T.: PAFOG – a new efficient forecast model of radiation fog and low-level stratiform clouds, *Atmos. Res.*, 64, 191–203, 2002.
- Bougeault, P.: Modeling the trade-wind cumulus boundary layer. Part I: Testing the ensemble cloud relations against numerical data, *J. Atmos. Sci.*, 38, 2414–2428, 1981.
- Boutle, I., Price, J., Kudzsotsa, I., Kokkola, H., and Rönkkönen, S.: Aerosol-fog interaction and the transition to well-mixed radiation fog, *Atmos. Chem. Phys.*, 18, 7827–7840, <https://doi.org/10.5194/acp-18-7827-2018>, 2018.
- Clark, T. L.: Numerical modeling of the dynamics and microphysics of warm cumulus convection, *J. Atmos. Sci.*, 30, 857–878, 1973.
- Clough, S. A., Shephard, M. W., Mlawer, E. J., Delamere, J. S., Iacono, M. J., Cady-Pereira, K., Boukabara, S., and Brown, P. D.: Atmospheric radiative transfer modeling: A summary of the AER codes, *Short Communication, J. Quant. Spectrosc. Ra.*, 91, 233–244, 2005.
- Cohard, J.-M. and Pinty, J.-P.: A comprehensive two-moment warm microphysical bulk scheme. I: Description and tests, *Q. J. Roy. Meteorol. Soc.*, 126, 1815–1842, 2000.
- Cohard, J.-M., Pinty, J.-P., and Bedos, C.: Extending Twomey’s analytical estimate of nucleated cloud droplet concentrations from CCN spectra, *J. Atmos. Sci.*, 55, 3348–3357, 1998.
- Cohard, J.-M., Pinty, J.-P., and Suhre, K.: On the parameterization of activation spectra from cloud condensation nuclei microphysical properties, *J. Geophys. Res.-Atmos.*, 105, 11753–11766, 2000.
- Deardorff, J. W.: Stratocumulus-capped mixed layers derived from a three-dimensional model, *Bound.-Lay. Meteorol.*, 18, 495–527, 1980.
- Geoffroy, O., Brenguier, J.-L., and Sandu, I.: Relationship between drizzle rate, liquid water path and droplet concentration at the scale of a stratocumulus cloud system, *Atmos. Chem. Phys.*, 8, 4641–4654, <https://doi.org/10.5194/acp-8-4641-2008>, 2008.
- Geoffroy, O., Brenguier, J.-L., and Burnet, F.: Parametric representation of the cloud droplet spectra for LES warm bulk microphysical schemes, *Atmos. Chem. Phys.*, 10, 4835–4848, <https://doi.org/10.5194/acp-10-4835-2010>, 2010.
- Grabowski, W. W. and Morrison, H.: Toward the mitigation of spurious cloud-edge supersaturation in cloud models, *Mon. Weather Rev.*, 136, 1224–1234, 2008.
- Gultepe, I., Müller, M. D., and Boybeyi, Z.: A new visibility parameterization for warm-fog applications in numerical weather prediction models, *J. Appl. Meteor. Climatol.*, 45, 1469–1480, 2006.
- Gultepe, I., Tardif, R., Michaelides, S., Cermak, J., Bott, A., Bendix, J., Müller, M. D., Pagowski, M., Hansen, B., Ellrod, G., Jacobs, W., Toth, G., and Cober, S. G.: Fog research: A review of past achievements and future perspectives, in: *Fog and Boundary Layer Clouds: Fog Visibility and Forecasting*, Springer, 1121–1159, 2007.
- Gultepe, I., Hansen, B., Cober, S., Pearson, G., Milbrandt, J., Platnick, S., Taylor, P., Gordon, M., and Oakley, J.: The fog remote sensing and modeling field project, *B. Am. Meteorol. Soc.*, 90, 341–359, 2009.
- Haeffelin, M., Bergot, T., Elias, T., Tardif, R., Carrer, D., Chazette, P., Colomb, M., Drobinski, P., Dupont, E., Dupont, J.-C., Gomes, L., Musson-Genon, L., Pietras, C., Plana-Fattori, A., Protat, A., Rangognio, J., Raut, J.-C., Rémy, S., Richard, D., Sciare, J., and Zhang, X.: PARISFOG: shedding new light on fog physical processes, *B. Am. Meteorol. Soc.*, 91, 767–783, 2010.
- Hammer, E., Gysel, M., Roberts, G. C., Elias, T., Hofer, J., Hoyle, C. R., Bukowiecki, N., Dupont, J.-C., Burnet, F., Baltensperger, U., and Weingartner, E.: Size-dependent particle activation properties in fog during the ParisFog 2012/13 field campaign, *Atmos. Chem. Phys.*, 14, 10517–10533, <https://doi.org/10.5194/acp-14-10517-2014>, 2014.
- Heus, T., van Heerwaarden, C. C., Jonker, H. J. J., Pier Siebesma, A., Axelsen, S., van den Dries, K., Geoffroy, O., Moene, A. F., Pino, D., de Roode, S. R., and Vilà-Guerau de Arellano, J.: Formulation of the Dutch Atmospheric Large-Eddy Simulation (DALES) and overview of its applications, *Geosci. Model Dev.*, 3, 415–444, <https://doi.org/10.5194/gmd-3-415-2010>, 2010.
- Khairoutdinov, M. and Kogan, Y.: A new cloud physics parameterization in a large-eddy simulation model of marine stratocumulus, *Mon. Weather Rev.*, 128, 229–243, 2000.

- Khvorostyanov, V. I. and Curry, J. A.: Aerosol size spectra and CCN activity spectra: Reconciling the lognormal, algebraic, and power laws, *J. Geophys. Res.-Atmos.*, 111, D12202, <https://doi.org/10.1029/2005JD006532>, 2006.
- Kokkola, H., Korhonen, H., Lehtinen, K. E. J., Makkonen, R., Asmi, A., Järvenoja, S., Anttila, T., Partanen, A.-I., Kulmala, M., Järvinen, H., Laaksonen, A., and Kerminen, V.-M.: SALSA – a Sectional Aerosol module for Large Scale Applications, *Atmos. Chem. Phys.*, 8, 2469–2483, <https://doi.org/10.5194/acp-8-2469-2008>, 2008.
- Lac, C., Chaboureaud, J.-P., Masson, V., Pinty, J.-P., Tulet, P., Escobar, J., Leriche, M., Barthe, C., Aouizerats, B., Augros, C., Aumond, P., Auguste, F., Bechtold, P., Berthet, S., Bielli, S., Bosseur, F., Caumont, O., Cohard, J.-M., Colin, J., Couvreux, F., Cuxart, J., Delautier, G., Dauhut, T., Ducrocq, V., Filippi, J.-B., Gazen, D., Geoffroy, O., Gheusi, F., Honnert, R., Lafore, J.-P., Lebeaupin Brossier, C., Libois, Q., Lunet, T., Mari, C., Maric, T., Mascart, P., Mogé, M., Molinié, G., Nuissier, O., Pantillon, F., Peyrillé, P., Pergaud, J., Perraud, E., Pianezze, J., Redelsperger, J.-L., Ricard, D., Richard, E., Riette, S., Rodier, Q., Schoetter, R., Seyfried, L., Stein, J., Suhre, K., Taufour, M., Thouron, O., Turner, S., Verrelle, A., Vié, B., Visentin, F., Vionnet, V., and Wautelet, P.: Overview of the Meso-NH model version 5.4 and its applications, *Geosci. Model Dev.*, 11, 1929–1969, <https://doi.org/10.5194/gmd-11-1929-2018>, 2018.
- Lebo, Z. J., Morrison, H., and Seinfeld, J. H.: Are simulated aerosol-induced effects on deep convective clouds strongly dependent on saturation adjustment?, *Atmos. Chem. Phys.*, 12, 9941–9964, <https://doi.org/10.5194/acp-12-9941-2012>, 2012.
- Maalick, Z., Kühn, T., Korhonen, H., Kokkola, H., Laaksonen, A., and Romakkaniemi, S.: Effect of aerosol concentration and absorbing aerosol on the radiation fog life cycle, *Atmos. Environ.*, 133, 26–33, 2016.
- Maronga, B. and Bosveld, F.: Key parameters for the life cycle of nocturnal radiation fog: a comprehensive large-eddy simulation study, *Q. J. Roy. Meteor. Soc.*, 143, 2463–2480, 2017.
- Maronga, B., Gryschka, M., Heinze, R., Hoffmann, F., Kanani-Sühring, F., Keck, M., Ketelsen, K., Letzel, M. O., Sühring, M., and Raasch, S.: The Parallelized Large-Eddy Simulation Model (PALM) version 4.0 for atmospheric and oceanic flows: model formulation, recent developments, and future perspectives, *Geosci. Model Dev.*, 8, 2515–2551, <https://doi.org/10.5194/gmd-8-2515-2015>, 2015.
- Mazoyer, M., Lac, C., Thouron, O., Bergot, T., Masson, V., and Musson-Genon, L.: Large eddy simulation of radiation fog: impact of dynamics on the fog life cycle, *Atmos. Chem. Phys.*, 17, 13017–13035, <https://doi.org/10.5194/acp-17-13017-2017>, 2017.
- Mazoyer, M., Burnet, F., Denjean, C., Roberts, G. C., Haefelin, M., Dupont, J.-C., and Elias, T.: Experimental study of the aerosol impact on fog microphysics, *Atmos. Chem. Phys.*, 19, 4323–4344, <https://doi.org/10.5194/acp-19-4323-2019>, 2019.
- Mensah, A. A., Holzinger, R., Otjes, R., Trimborn, A., Mentel, Th. F., ten Brink, H., Henzing, B., and Kiendler-Scharr, A.: Aerosol chemical composition at Cabauw, The Netherlands as observed in two intensive periods in May 2008 and March 2009, *Atmos. Chem. Phys.*, 12, 4723–4742, <https://doi.org/10.5194/acp-12-4723-2012>, 2012.
- Morrison, H. and Grabowski, W. W.: Comparison of bulk and bin warm-rain microphysics models using a kinematic framework, *J. Atmos. Sci.*, 64, 2839–2861, 2007.
- Morrison, H. and Grabowski, W. W.: Modeling supersaturation and subgrid-scale mixing with two-moment bulk warm microphysics, *J. Atmos. Sci.*, 65, 792–812, 2008.
- Nakanishi, M.: Large-eddy simulation of radiation fog, *Bound.-Lay. Meteorol.*, 94, 461–493, 2000.
- PALM: revision 2675, available at: <http://palm-model.org/trac/browser/palm?rev=2675>, last access: 28 May 2019a.
- PALM: revision 3622, available at: <http://palm-model.org/trac/browser/palm?rev=3622>, last access: 28 May 2019b.
- PALM group: Dataset: Model Code, extended Code and Job Setup for publication, available at: <https://doi.org/10.25835/0067929>, last access: 28 May 2019c.
- Pruppacher, H. R. and Klett, J. D.: *Microphysics of clouds and precipitation*, Kluwer Academic Publishers, Dordrecht, Netherlands, 2nd revised edition, 1997.
- Seifert, A. and Beheng, K. D.: A double-moment parameterization for simulating autoconversion, accretion and selfcollection, *Atmos. Res.*, 59, 265–281, 2001.
- Seifert, A., Khain, A., Pokrovsky, A., and Beheng, K. D.: A comparison of spectral bin and two-moment bulk mixed-phase cloud microphysics, *Atmos. Res.*, 80, 46–66, 2006.
- Shima, S., Kusano, K., Kawano, A., Sugiyama, T., and Kawahara, S.: The super-droplet method for the numerical simulation of clouds and precipitation: A particle-based and probabilistic microphysics model coupled with a non-hydrostatic model, *Q. J. Roy. Meteor. Soc.*, 135, 1307–1320, 2009.
- Stolaki, S., Haefelin, M., Lac, C., Dupont, J.-C., Elias, T., and Masson, V.: Influence of aerosols on the life cycle of a radiation fog event. A numerical and observational study, *Atmos. Res.*, 151, 146–161, 2015.
- Thouron, O., Brenguier, J.-L., and Burnet, F.: Supersaturation calculation in large eddy simulation models for prediction of the droplet number concentration, *Geosci. Model Dev.*, 5, 761–772, <https://doi.org/10.5194/gmd-5-761-2012>, 2012.
- Twomey, S.: The nuclei of natural cloud formation part II: The supersaturation in natural clouds and the variation of cloud droplet concentration, *Pure Appl. Geophys.*, 43, 243–249, 1959.
- Wicker, L. J. and Skamarock, W. C.: Time-splitting methods for elastic models using forward time schemes, *Mon. Weather Rev.*, 130, 2088–2097, 2002.
- Williamson, J.: Low-storage runge-kutta schemes, *J. Comput. Phys.*, 35, 48–56, 1980.
- Zhang, X., Musson-Genon, L., Dupont, E., Milliez, M., and Carissimo, B.: On the influence of a simple microphysics parametrization on radiation fog modelling: A case study during parisfog, *Bound.-Lay. Meteorol.*, 151, 293–315, 2014.

# 4 Towards a Better Representation of Fog Microphysics in Large-Eddy Simulations Based on an Embedded Lagrangian Cloud Model

## 4.1 Declaration of Contributions

The numerical experiments were jointly designed by J. Schwenkel and B. Maronga. J. Schwenkel implemented new output quantities and was responsible for conception and realization of model improvements, conducted the simulations and performed the data analysis. Results were jointly discussed by J. Schwenkel and B. Maronga. J. Schwenkel prepared the paper, with significant contributions by B. Maronga. Comments of three anonymous referees helped to improve the final version of the manuscript.

## 4.2 Research Article

©The authors 2020. CC BY 4.0 License



Article

# Towards a Better Representation of Fog Microphysics in Large-Eddy Simulations Based on an Embedded Lagrangian Cloud Model

Johannes Schwenkel <sup>1,\*</sup>  and Björn Maronga <sup>1,2</sup><sup>1</sup> Institute of Meteorology and Climatology, Leibniz Universität Hannover, 30419 Hannover, Germany; maronga@muk.uni-hannover.de<sup>2</sup> Geophysical Institute, University of Bergen, 5020 Bergen, Norway

\* Correspondence: schwenkel@muk.uni-hannover.de

Received: 9 April 2020; Accepted: 30 April 2020; Published: 5 May 2020



**Abstract:** The development of radiation fog is influenced by multiple physical processes such as radiative cooling and heating, turbulent mixing, and microphysics, which interact on different spatial and temporal scales with one another. Once a fog layer has formed, the number of fog droplets and their size distribution have a particularly large impact on the development of the fog layer due to their feedback on gravitational settling and radiative cooling at the fog top, which are key processes for fog. However, most models do not represent microphysical processes explicitly, or parameterize them rather crudely. In this study we simulate a deep radiation fog case with a coupled large-eddy simulation (LES)–Lagrangian cloud model (LCM) approach for the first time. By simulating several hundred million fog droplets as Lagrangian particles explicitly (using the so-called superdroplet approach), we include a size-resolved diffusional growth including Köhler theory and gravitational sedimentation representation. The results are compared against simulations using a state of the art bulk microphysics model (BCM). We simulate two different aerosol backgrounds (pristine and polluted) with each microphysics scheme. The simulations show that both schemes generally capture the key features of the deep fog event, but also that there are significant differences: the drop size distribution produced by the LCM is broader during the formation and dissipation phase than in the BCM. The LCM simulations suggest that its spectral shape, which is fixed in BCMs, exhibits distinct changes during the fog life cycle, which cannot be taken into account in BCMs. The picture of the overall fog droplet number concentration is twofold: For both aerosol environments, the LCM shows lower concentrations of larger fog droplets, while we observe a higher number of small droplets and swollen aerosols reducing the visibility earlier than in the BCM. As a result of the different model formulation we observe higher sedimentation rates and lower liquid water paths for the LCM. The present work demonstrates that it is possible to simulate fog with the computational demanding approach of LCMs to assess the advantages of high-resolution cloud models and further to estimate errors of traditional parameterizations.

**Keywords:** cloud microphysics; lagrangian cloud model; large-eddy simulation; radiation fog

## 1. Introduction

The hazard emanating by fog and the damages caused to the society, whether in air, road, or sea transport, is estimated to be the same as those from winter storms [1]. Therefore, an accurate prediction of fog events is of major interest. However, it is still challenging to forecast fog accurately using numerical weather prediction (NWP) models [2–5]. This can be attributed to the fact that fog is influenced by multiple physical processes on different scales. Moreover, fog is typically covered by only a few grid points in NWP models, thus relying on the parameterization of many physical processes.



In recent years, several studies have focused on microphysical processes in fog [3,5–14]. Since the supersaturation in fog is low and the mean radius of fog droplets is rather small, collision and coalescence is a second order process, but the diffusional growth of the droplet population plays an important role. Nevertheless, as for all liquid clouds, heterogeneous nucleation must be considered first, which determines the number of cloud droplets and hence their size, depending on the number of aerosols. The basic understanding of this process, which is called activation of aerosols, is based on the theory of Köhler [15]. In addition to the number of aerosol, also its chemical composition, as well as the dry aerosol radius, influence the emergence of droplets. Depending on the number of droplets the fog layer will deepen or decay as, e.g., an increased optical thickness leads to a reduced visibility, an increased longwave cooling rate at the fog top, and a decreased sedimentation rate due to smaller droplet radii. However, as observations show that neither the number of fog droplets nor the spectral shape remains constant during the different fog stages [3,7,8,11]. To represent these processes in numerical models accurately, fundamental properties of single particles (e.g., aerosol mass and chemical composition, radius of droplets) must be considered. In general, the design of Eulerian models, where cloud physics quantities (such as the cloud water mixing ratio) are represented as integral values for a grid volume, prohibit this level of detail [16]. Even though much effort has been made in developing advanced parameterizations for the activation process in such models [17,18], those approaches are always limited [19]: First, models relying on bulk formulations must parameterize droplets size distribution and inherently the droplet effective radius. Second, the vast majority of bulk models assume that the spectral shape of the droplet size distribution is constant in space and time. Third, bulk schemes, regardless of which parameterization they use, can only represent activation with a non-physical discrete transition between aerosol and cloud droplets. Recent research [9,13,14,20–22] studied the influence of aerosols and microphysics on fog by using more or less advanced Eulerian cloud physics approaches. Moreover, Boutle et al. [5], Maalick et al. [10], Tonttila et al. [23] used sectional models which allows to represent aerosol-fog interactions in a detailed and interactive way. According to Stolaki et al. [9] and Maalick et al. [10], an increase in droplet number concentration and in the liquid water path can be found with increasing aerosol concentration. Boutle et al. [5] showed that NWP models typically overestimate the number of fog droplets, when using common activation parameterizations. Although all studies have contributed valuable insights in fog research and have highlighted that microphysical processes have a significant influence on the fog development, most of the studies cannot overcome the drawbacks of the usage of parameterizations. This study, where a three-dimensional large-eddy simulation (LES)–Lagrangian cloud model (LCM) approach is used to simulate a fog event, is a first effort to overcome this gap. As LCMs are a perfect tool to simulate microphysics by first principles [16], this study aims to simulate activation, diffusional growth and sedimentation of droplets explicitly and investigates the feedback of these processes on the life cycle of radiation fog in numerical models. In addition, we will examine the explicitly calculated particle size distributions of fog events and compare them with the assumed distributions of bulk approaches. This allows an evaluation of the bulk schemes and their shortcomings.

The paper is organized as follows. Section 2 briefly describes the Lagrangian and bulk microphysics models and their coupling to other modules followed by an outline of the numerical experiments. Results are presented in Section 3. A concluding discussion is given in Section 4.

## 2. Model and Numerical Experiments

### 2.1. LES Model with Radiation and Land Surface Scheme

In this study the Parallel large-eddy simulation model for atmospheric and oceanic flows (PALM; revision 4186) was used [24,25]. PALM has been successfully applied to simulate the stable boundary layer [26,27] as well as in precursor studies to simulate radiation fog [14,21].

The model formulation of PALM is based on the incompressible Boussinesq-approximated Navier-Stokes equations, prognostic equations for potential temperature, water vapor mixing ratio,

and subgrid-scale turbulence kinetic energy. Discretization in space and time on the Cartesian grid is achieved by finite differences using a fifth-order advection scheme after [28] and a third-order Runge-Kutta time stepping scheme [29], respectively. For the non-resolved eddies, a 1.5-order flux-gradient subgrid closure scheme after Deardorff [30] is applied, which includes the solution of an additional prognostic equation for the subgrid-scale turbulent kinetic energy. The interested reader is referred to Maronga et al. [24,25] for a detailed description of the PALM model.

Radiation is considered by the Rapid Radiation Transfer Model for Global Models (RRTMG), which is coupled to and that calculates radiative transfer for each vertical column of the LES [31]. RRTMG calculates the radiative fluxes (shortwave and longwave) for each grid volume while considering profiles of pressure, temperature, humidity, liquid water, and effective droplet radius ( $r_{\text{eff}}$ ). The latter, which is the major coupling between clouds and radiation (apart from the liquid water mixing ratio  $q_l$ ), is calculated by

$$r_{\text{eff}} = \begin{cases} \left( \frac{3 q_l \rho}{4\pi n_c \rho_l} \right)^{\frac{1}{3}} \exp(\log(\sigma_g)^2) & \text{for the bulk cloud model,} \\ \frac{\int_0^N \pi r_n^3 A_n}{\int_0^N \pi r_n^2 A_n} & \text{for the Lagrangian Cloud Model.} \end{cases} \quad (1)$$

Here,  $\rho$  is the density of air,  $\rho_l$  is the density of water,  $\sigma_g = 1.3$  is the geometric standard deviation of the droplet distribution,  $r_n$  is the radius of the simulated particle with the index  $n$ , and  $A_n$  is the weighting factor of the simulated particle, which is explained in the next subsection. The radiation code, which is computational demanding, is called only every 60 s representing a compromise between accuracy and required computing time.

Surfaces fluxes of sensible and latent heat are calculated with PALM's land surface model (LSM), which consists of an energy balance solver for the skin temperature and a multi-layer soil model, predicting soil temperature and soil moisture. A full description of the LSM and an application for the Cabauw setup can be found in Schwenkel and Maronga [14], Maronga and Bosveld [21], Maronga et al. [25], respectively.

## 2.2. Lagrangian Cloud Model

LCMs are a relatively new method for simulating cloud physical processes. As Grabowski et al. [16] pointed out, they have significant advantages over the traditional approaches (i.e., bulk and bin schemes): besides the advantages in terms of numerics and representation of different dimensions (i.e., aerosols), it is especially the physics that can be applied with its underlying equations instead of parameterizing it. The LCM uses so-called superdroplets, each representing an ensemble of identical real droplets, to treat cloud microphysics. Thus, each superdroplet has certain properties, which depict, among others, the number of droplets represented the superdroplet (the so-called weighting factor), the wet radius and dry aerosol radius of these droplets, the superdroplet's location in space, and its velocity. In contrast to the fixed positions of the numerical grid, superdroplets can move freely through the whole model domain. The velocity of each superdroplet is determined by

$$\frac{dX_{i,n}}{dt} = \bar{u}_i(X_{i,n}) - \delta_{i3}v(r_n), \quad (2)$$

where  $X_{i,n}$  is the position of a superdroplet with index number  $n$  in Cartesian coordinates ( $X_i$ ) = ( $X, Y, Z$ ) and  $(\bar{u}_i)$  =  $(\bar{u}, \bar{v}, \bar{w})$  represents the LES-resolved velocity interpolated to the superdroplets position, and  $v(r_n)$  is the terminal fall velocity. In contrast to former versions of the LCM, velocity interpolation to the particle position is done by using a simple interpolation scheme in combination with the predictor-corrector method as described in Grabowski et al. [32], which

has divergence-conserving character. Furthermore, sedimentation is calculated by approximating the fall velocity of droplets using an empirical relationship [33] depending on their size:

$$v(r) = \begin{cases} 8000 \text{ s}^{-1} \cdot r_n [1 - \exp(-24,000 \text{ m}^{-1} \cdot r_n)], & \text{for } r_n \leq 375.5 \text{ }\mu\text{m}, \\ 9.65 \text{ m s}^{-1} - [10.43 \text{ m s}^{-1} \cdot \exp(-1200 \text{ m}^{-1} \cdot r_n)], & \text{for } r_n > 375.5 \text{ }\mu\text{m}. \end{cases} \quad (3)$$

Moreover, boundary conditions for particles are set as follows: at the model top, reflection boundary conditions were used, which does not play an important role due to a sufficiently high model domain. At the bottom absorption boundary conditions are applied for particles, i.e., all liquid water contained by the superdroplet touching the surface is absorbed and transferred to the LSM. Furthermore, the inherent aerosol is depleted, representing the process of wet deposition due to gravitational settling. The LCM has been validated in different studies [34,35].

### 2.2.1. Diffusional Growth

The diffusional growth equation

$$(r_n + r_0) \frac{dr_n}{dt} = \frac{1}{F_K + F_D} \left( S - \frac{A}{r_n} + \frac{Br_{a,n}^3}{r_n^3 - r_{a,n}^3} \right), \quad (4)$$

is solved at each time step, and for each individual superdroplet. Here,  $S$  is the supersaturation in which the droplet resides based on the underlying LES fields of temperature and water vapor of the respective grid box. The dry aerosol radius is denoted as  $r_{a,n}$ . The length scale  $r_0 = 1.86 \text{ }\mu\text{m}$  includes gas-kinetic effects (e.g., [36]) and factors  $A$  and  $B$  are responsible for the consideration of curvature and solute effects, respectively. Thermal conduction and diffusion of water vapor in air is considered by the factors  $F_K$  and  $F_D$ .

Note, a detailed description of these factors and therein included constants can be found in the Appendix A. As Equation (4) is a stiff differential equation, a very small time step is required for an accurate and stable solution, especially during activation. We use a fourth-order Rosenbrock method [19] to adjust the internal time step for the integration of Equation (4). Solving the diffusional growth equation, which results in the release of latent heat, is the major coupling between the LCM and LES model. For more details the interested reader is referred to Maronga et al. [24] or Hoffmann et al. [37], where the underlying equations are explicitly given. The initialization of superdroplets as dry aerosols at the beginning of the simulation follows the described method by [19]. This can be briefly summarized: the dry aerosol spectrum is divided into  $N_p$  bins, where  $N_p$  is the number of superdroplets per grid box. Each superdroplet is assigned with the corresponding value of the mean dry radius of the aerosol distribution (plus a small random component). The weighting factor is initialized with the number density times the volume of the LES grid box. This results in a general aerosol spectrum that is reproduced in each grid box.

It must be mentioned that in this study collision and coalescence are neglected as the maximum radius of droplets is comparatively small in fogs (e.g., also neglected in Boutle et al. [5]). Therefore, diffusion of water vapor is the only mechanism that allow droplets to grow in our simulations.

### 2.3. Bulk Cloud Model

As bulk cloud model we use the state-of-the-art 2-moment microphysics scheme of Seifert and Beheng [38,39] with extension of Morrison et al. [40]. The first mentioned scheme based on the separation of the cloud and rain droplet scale by using a radius threshold of  $40 \text{ }\mu\text{m}$ . This separation is mainly used for parameterizing coagulation processes by assuming different distribution functions for cloud and rain droplets. However, as aforementioned collision and coalescence are weak in fog. Hence, autoconversion of cloud droplets is turned off.

The sedimentation process is parameterized assuming that droplets are log-normally distributed and follow a Stokes regime [41]. This results in a sedimentation flux of

$$F_{q_c} = k_F \left( \frac{4}{3} \pi \rho_l n_c \right)^{-\frac{2}{3}} (\rho q_l)^{\frac{5}{3}} \exp(5 \ln^2 \sigma_g), \quad (5)$$

with the parameter  $k_F = 1.2 \times 10^8 \text{ m}^{-1} \text{ s}^{-1}$  [42].

A diagnostic condensation scheme is used considering diffusional growth, following Khairoutdinov and Kogan [43]

$$\left. \frac{\partial q_c}{\partial t} \right|_{(\text{cond})} = \frac{4\pi G(T, P) \rho_l n_c}{\rho} S r_c, \quad (6)$$

where  $q_c$  is the cloud water mixing ratio,  $r_c$  is the mean droplet volume radius.

Activation of aerosols is represented by a parameterization following Khvorostyanov and Curry [18]. By doing so, physio-chemical properties of the background aerosol are considered and assumed that the aerosol follows a log-normal distribution of up to three modes [25]. The number of cloud droplets is calculated as

$$\left. \frac{\partial n_c}{\partial t} \right|_{\text{act}} = \max \left( \frac{N_{\text{CCN}} - n_c}{\Delta t}, 0 \right), \quad (7)$$

with  $N_{\text{CCN}}$  being the number of activated cloud condensation nuclei. Further,  $n_c$  is the number of previously activated aerosols that is assumed to be equal to the number of pre-existing droplets, and  $\Delta t$  is the model time step. Following Khairoutdinov and Kogan [43] and Seifert and Beheng [39], the initial cloud droplet radius is set to  $1 \mu\text{m}$ . A complete description of the recently implemented extensions is given in Maronga et al. [25].

#### 2.4. Numerical Experiments

To generate a deep fog event, which has been successfully validated against observations, atmospheric conditions from 22 to 23 March 2011 at the Cabauw Experimental Site for Atmospheric Research (CESAR) were used. The fog case is described in detail in Boers et al. [44] and was subject of various parameter studies [14,21,22].

The life cycle of the fog can be briefly summarized: the initial onset of the fog was midnight (as a thin near-surface fog layer) induced by radiative cooling, which also produced a strong inversion with a temperature gradient of 6 K between the surface and the 200 m tower-level. The fog layer began to develop so that the vertical extension was below 20 m at 0300 UTC, but then deepened rapidly to 80 m, and reaching 140 m depth at 0600 UTC. At 0300 UTC, also the visibility had reduced to less than 100 m indicating a deep fog layer. After sunrise (around 0545 UTC) a further reduction of the visibility close to the ground was suppressed due to warming of surface near air and after 0800 UTC the fog started quickly to evaporate. For details, see Boers et al. [44]; profiles of the initial conditions are also shown in Maronga and Bosveld [21] (their Figure 1).

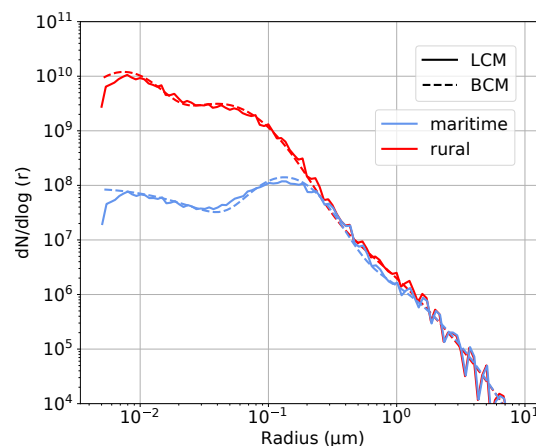


**Figure 1.** Maritime and rural initial dry aerosol distributions for the LCM and BCM.

The model was initialized as described in the precursor study of Maronga and Bosveld [21]. Profiles of temperature and humidity (see Schwenkel and Maronga [14], their Figure 1) were derived from the CESAR 200 m-tower and used as initial profiles in PALM. A geostrophic wind of  $5.5 \text{ m s}^{-1}$  was prescribed based on the observed value at Cabauw at 0000 UTC. The LSM was initialized with short grassland as surface type and four soil layers. The soil model layers, with depth levels at 0.07, 0.28, 1.0 and 2.89 m, were initialized using interpolations of temperature measurements to their respective depth. A more detailed description of the LSM setup, whose sensitivity to fog is not the subject of this study, can be found in Maronga and Bosveld [21].

All simulations start at 0000 UTC, before fog formation, and end at 1130 UTC after the fog layer has fully dissipated. Precursor runs are conducted for additional 25 min using the initial state at 0000 UTC, but without radiation scheme and LSM in order to allow the development of turbulence in model without introducing feedback during that time [21].

Based on the sensitivity studies of Maronga and Bosveld [21] and taking into account that using the LCM requires enormous computing time (approx.  $3 \times 10^5$  core hours), a grid spacing of  $\Delta = 2 \text{ m}$  was chosen. Note that simulations with  $\Delta = 1 \text{ m}$  and explicit activation representation using the LCM are not feasible with our current computer resources. Even though a grid spacing of  $\Delta = 2 \text{ m}$  leads to an underestimation of surface fluxes, which causes a delayed onset of the fog (comparatively to a case with  $\Delta = 1 \text{ m}$ ), the relevant features can be captured sufficiently well [21]. In  $x$ -,  $y$ -, and  $z$ -direction  $384 \times 384 \times 192$  grid points were used resulting in a domain size of 768 m for the horizontal and 400 m for the vertical. Cyclic conditions were used at the lateral boundaries. A sponge layer was used starting at a height of 344 m in order to prevent gravity waves from being reflected at the top boundary of the model. In the simulations presented here, the LCM was initialized with 32 superdroplets per grid box, which results in a total number of  $7.0 \times 10^8$  superdroplets for the whole model domain. The choice of this parameter based on current computational resources and a sensitivity study, which is presented in the Appendix A.

For this study, four high resolution simulations were conducted, where both the LCM and BCM were applied with maritime and rural aerosol conditions. All other model variables such as initial thermodynamic profiles, soil and radiation parameters, were kept constant throughout this study. Therefore, the model results are interpreted as being caused on the one hand by the different types of microphysics models (and their interactions with turbulent mixing, radiation, and the underlying surface) and on the other hand by different aerosol compositions.

The underlying aerosol conditions are defined after Jaenicke [45] and given by a three-modal distribution, which is shown in Table 1. Figure 1 shows the initial aerosol distribution of the LCM and BCM. Note, that the BCM does not simulate aerosols explicitly. Instead only the activation parameterization (see Section 2.3), determining the number of fog droplets, processing this information.

In contrast, the aerosol distribution in the LCM is displayed from the sum of all superdroplets, whereby each superdroplet is associated with a certain dry aerosol radius (see Section 2.2.1).

The used model parameter lists for PALM for all described cases, as well as the additional code parts used for data analysis in this study are included in the Supplementary Materials.

**Table 1.** Aerosol size distributions for maritime and rural conditions after Jaenicke [45]. Here, the type defines the chemical species,  $i$  depicts the mode,  $n_{a,i}$  is the number concentration of aerosol of that mode per cubic centimeter,  $r_{a,i}$  is the dry aerosol radius in microns and  $\ln \sigma_{a,i}$  is the logarithmic width of the distribution.

Aerosol	Type	$i$	$n_{a,i} \text{ (cm)}^{-3}$	$r_{a,i} \text{ (}\mu\text{m)}$	$\ln \sigma_{a,i}$
Maritime	NaCl	1	$1.33 \times 10^2$	0.0039	1.512
		2	$6.66 \times 10^1$	0.133	0.484
		3	$3.06 \times 10^0$	0.29	0.912
Rural	NH <sub>4</sub> NO <sub>3</sub>	1	$6.65 \times 10^3$	0.00739	0.518
		2	$1.47 \times 10^2$	0.0269	1.283
		3	$1.99 \times 10^3$	0.0419	0.612

### 3. Results

The main purpose of this study is to examine the influence of fog microphysics on the development of the fog layer, while comparing an innovative approach (LCM) against a common parameterization (BCM) for simulating cloud processes. Table 2 offers an overview of the conducted simulations.

**Table 2.** Overview of conducted simulations.

Name	Microphysical Model	Aerosol
LCM-R	Lagrangian cloud model	rural
LCM-M	Lagrangian cloud model	maritime
BCM-R	Bulk cloud model	rural
BCM-M	Bulk cloud model	maritime

#### 3.1. Time Series and Macroscopic Properties

Figure 2 shows time series of different quantities for the conducted simulations. The liquid water path (LWP) is a good indicator for the life cycle of the simulated fog (formation, deepening, strength and dissipation) Figure 2a reveals a great spread over the cases. Especially at the beginning of the mature phase the differences become apparent, whereby three aspects are particularly noteworthy. First, for rural conditions significantly higher values for the LWP can be observed compared to maritime conditions, which is also reported by other studies; e.g., [5,6,9,10]. Second, for both aerosol environments the LCM cases show a much lower LWP than cases with the BCM. Third, the maximum for the LCM simulation with rural conditions (LCM-R) is achieved about one hour later than in the simulation using the bulk model with rural conditions (BCM-R). In the following discussion, the reasons for this different development will be analyzed with respect to responsible and partly interacting physical processes.

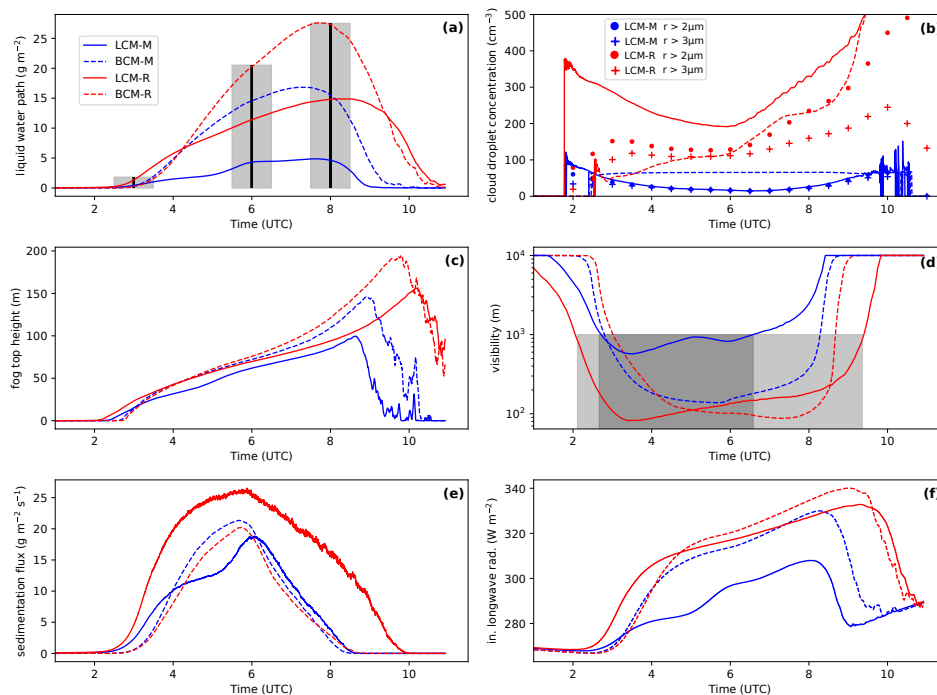


**Figure 2.** Temporal evolution of liquid water path (a), droplet number concentration averaged over the fog layer (b), fog top height (c), visibility at 2 m height (d), sedimentation rate at the surface and incoming longwave radiation (f). The vertical line and bars in (a) mark the time step and surface (e) of incoming longwave radiation in Figure 4. The shaded areas in (d) show the time frame where fog is present (applying the definition visibility < 1000 m) regarding LCM-M and LCM-R.

The visibility ( $vis$ ) at 2 m height can be used as a proxy to define the time periods where fog is present. Figure 2d illustrates this definition, using the  $vis$  parameterization after Gultepe et al. [46],

$$vis = \frac{1002}{(n_c \rho q_1)^{0.6473}}, \quad (8)$$

with  $n_c$  in units of  $\text{cm}^{-3}$  and  $q_1$  in units of  $\text{g kg}^{-1}$ , returns  $vis$  in m. The grey shaded areas mark ( $vis < 1000$  m) the onset and the start of the dissipation phase of the fog for the LCM cases. In contrast to the BCM simulations, where the visibility drops down fast and reaches values below 1000 m, the visibility for the LCM cases decreases earlier and more continuously and may be an evidence of already swollen aerosols reducing the visibility before saturation is attained, but still are too small to affect longwave radiation [5,47,48]. Note that for the visibility parameterization in case of the LCM particles with a radii larger or equal  $1 \mu\text{m}$  are considered. Using the visibility as the criterion for the occurrence of fog, we see an about 70 min earlier onset of the fog for LCM-R (see Figure 2d) than in BCM-R. In contrast, the onset of fog for the LCM simulation with maritime conditions (LCM-M) and simulation with the bulk model and maritime aerosol background (BCM-M) takes place at the same time. However, the earlier formation of liquid water can also be found for LCM-M (see Figure 2b).

The time-height cross-sections in Figure 3 give a convenient overview of the time-vertical structure of the simulated fogs. In general, all simulations show that fog forms somewhat after 0200 UTC and deepens rapidly. The sun rises around 0545 UTC, where the fog has already expanded to a vertical extent of about 50–70 m. Subsequently, the fog layer is lifted between 0815–0945 UTC due to heating at the surface and near surface air. By the end of the simulations the fog is completely dissipated. For LCM-M the fog persists longer in the near surface layers.



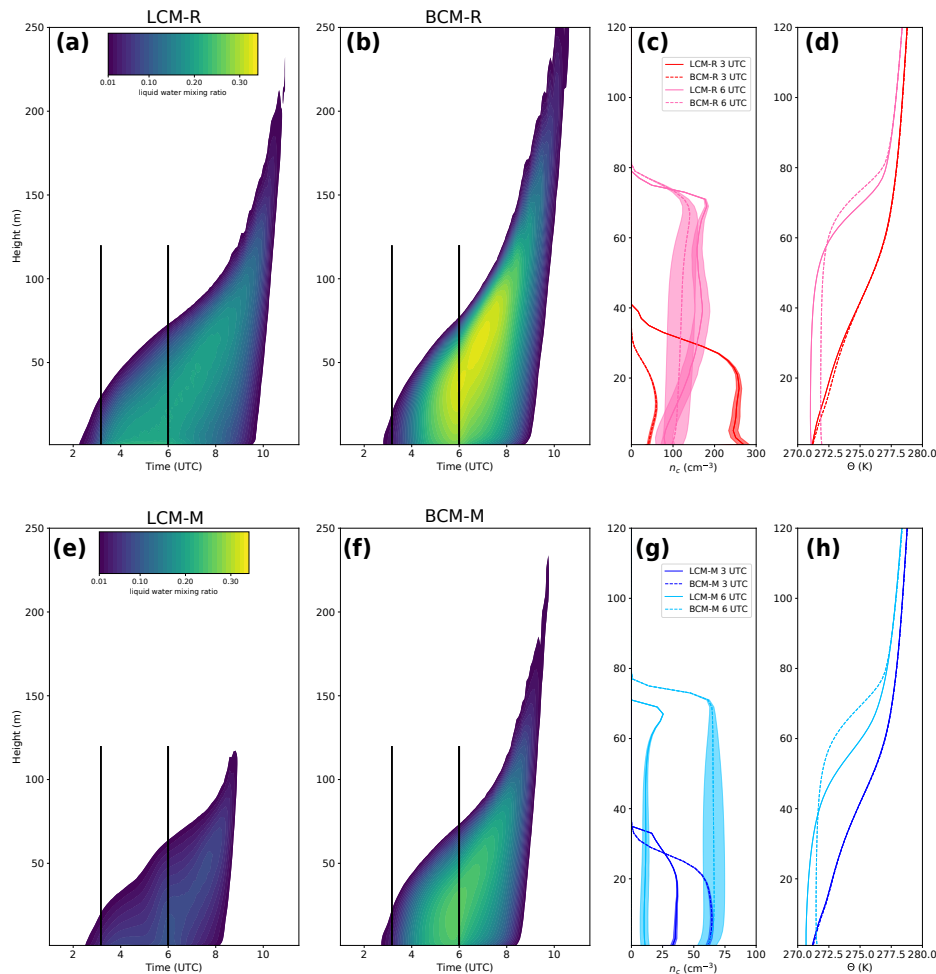


**Figure 3.** Time-height cross-section of liquid water ratio (horizontally averaged) for rural (top panel) (a,b) and maritime (bottom panel) (e,f) aerosol conditions. In the left column results for LCM cases and on the right column for BCM cases are shown. Profiles on the right hand side display  $n_c$  (c,g) and potential temperature  $\theta$  (d,h) at the marked times (black vertical line in the cross-section). The shaded areas (c,g) show the liquid water mixing ratio as a qualitative measure. Here, areas of the same size represent equal values for  $q_l$ .

Furthermore, it can be observed that the respective BCM cases predict a higher lifting level, i.e., the formation or advection of liquid water to higher layers. However, the overall height of the fog shows almost no significant differences between the simulations (see Figure 2c). As mentioned before, the simulations with the LCM produce liquid water earlier, which results primarily in an earlier increase in fog height. During the mature phase, however, all simulations show very similar fog heights with maximum values of about 40–100 m. Only the simulation LCM-M reveals a deviation from the other cases with an about 10 m lower maximum fog height at the corresponding times. This can be explained by the fact that in this case the fog layer has significantly lower LWP and is optically thinner caused by a fewer number of fog droplets (see Figure 2f). This finding is in agreement with previous observations, who found a positive correlation between fog height and number of fog droplets [10].

Furthermore, the concentration of fog droplets plays an important role for the development of fog, as it controls the droplet effective radius, which in turn has feedback to sedimentation rate



and to the point in time when the fog becomes optically thick and radiatively active [5]. As Figure 2b illustrates, the averaged (over the whole fog layer) droplet concentration in the fog depends mainly on the aerosol concentration. However, note that for the LCM simulations all particles larger than  $1\ \mu\text{m}$  were counted as fog droplets, which is consistent to the treatment on the BCM. This assumption probably include some swollen and not activated aerosols to avoid the calculation of the critical radius at each time step for every superdroplet. Moreover, the development of the number of particles with radii larger than  $r = 2\ \mu\text{m}$  (dots) and  $r = 3\ \mu\text{m}$  (plus sign) for the LCM simulations is shown. For LCM-M and BCM-M the number concentration of droplets (except during the initial phase in LCM-M) does not exceed  $70\ \text{cm}^{-3}$ . However, as the number of droplets for BCM-M is almost constant throughout the simulation, LCM-M shows a significant variation of the number of droplets in time. First, the overall concentration of droplets decreases during fog development to values of  $15\text{--}20\ \text{cm}^{-3}$ . This reduction can be explained by the continuous sedimentation of droplets, which are permanently removed from the model when a superdroplet touches the surface and consequently the underlying aerosol (which is also absorbed) can not act as CCN anymore. That this process affects the fog layer has already been reported by Bott [6]. During the mature phase of the fog the concentration of droplets stays constant, but increases around 0700 UTC due to onset of convection by solar heating at the surface, leading to higher supersaturations. In contrast, the droplet number concentration for LCM-R is higher than for BCM-R. Indeed, this results in a number concentration of  $200\text{--}340\ \text{cm}^{-3}$  for LCM-R during the formation and mature phase. Generally, a similar behavior as for LCM-M in the course of the number concentration can be observed. The number of droplets decreases, but starts to increase around 0600 UTC. In contrast, BCM-R initially has significant lower droplet concentrations (approximately  $60\text{--}150\ \text{cm}^{-3}$  during formation and mature phase) followed by a persistent increase (but with different slopes) in the amount of droplets. However, the time series of the droplet number concentration of LCM-R (solid line) includes a large number of swollen and not activated aerosols, as we observe a much lower concentration of particles with a radius larger than  $2\ \mu\text{m}$ . Figure 3 (right columns) shows profiles of  $n_c$  and potential temperature at 0300 UTC and 0600 UTC. For both shown periods,  $n_c$  is higher for LCM-R. Moreover, for LCM-R and LCM-M, a maximum at the cloud top occurs during the mature phase (0600 UTC). The development of such a profile is characteristic for deep fog, due to the high cooling rates at the top of the fog layer, which produce high supersaturations and thus lead to high activation rates [10]. This maximum is also apparent in a slightly attenuated manner for BCM-R. LCM-M and BCM-M show the opposite behavior with respect to the droplet number concentration. Thus, BCM-M exhibit a higher  $n_c$  for 0420 UTC as well as for 0600 UTC. Also the profiles of the potential temperature clearly show the transition of the initial phase with a stably stratified fog layer to a well mixed fog layer. Although, Stolaki et al. [9] and Maalick et al. [10] found a positive correlation between the droplet number concentration and LWP, our study shows that the LWP of BCM-R exceeds the LWP of LCM-R. This observation, however, does not take into account the size distribution and the differences in other physical processes, which are discussed in the following. For both aerosol environments, we observe lower temperatures for the LCM within the fog layer compared to the runs with BCM. This is explained by optically thicker fog in the respective BCM cases, which suppresses stronger radiative cooling. Moreover, the process of entrained warm air from above the inversion height into the mixed layer leads to warming of the mixing layer. The effect of warming due to entrainment is stronger (due to higher inversion heights) for the cases using the BCM. However, our analysis showed that the effect of radiative cooling is much larger.

Furthermore, sedimentation is a crucial process for the development of fog. Here again, we note differences among the simulated cases. Despite a lower LWP, LCM-R shows significantly higher sedimentation rates (up to three times) compared to BCM-R (see Figure 2e). As we compare the sedimentation rates for the BCM simulations, we observe a quite similar course, but with slightly higher values for BCM-M. These higher sedimentation rates are caused by higher mean volume droplet radii for BCM-M (see Figure 4). The sedimentation rate of LCM-M reveals the lowest absolute values of all simulations. However, in relative terms (regarding the LWP), the fog layer in LCM-M experiences

the highest loss of liquid water due to sedimentation. The deviations in the sedimentation rates between the models is caused by inherent differences in the microphysics parameterizations. While BCMs parameterize the sedimentation flux with a fixed assumption of the shape of the distribution, the LCM calculates the gravitational settling velocity explicitly for each superdroplet depending on its size. It is assumed that the latter method is superior and we can thus reason that the BCM underestimates the sedimentation rates. In the BCM the sedimentation rate depends on the diagnostic quantities of  $q_l$  and  $r_c$ , but also on the spectral width (see Equation (5)). Since bulk models inherently must make assumptions concerning the shape of the distribution, the spectral width must either be prescribed or calculated. In this study, the spectral width is prescribed with  $\sigma_g = 1.3$ , which is an appropriate value for stratiform clouds [41] and thus commonly used in bulk models. This, however, impairs the calculation of the sedimentation flux, as the spectral shape of the droplet size distributions is found to be variable over time [3,7]. Even though the spectral width might crucially affect the sedimentation rates, which was also reported by Zhang et al. [49], a sensitivity study of this parameter is beyond the scope of this paper. In addition, the process of sedimentation also involves wet deposition of aerosols, which can only be represented by the LCM in this study.

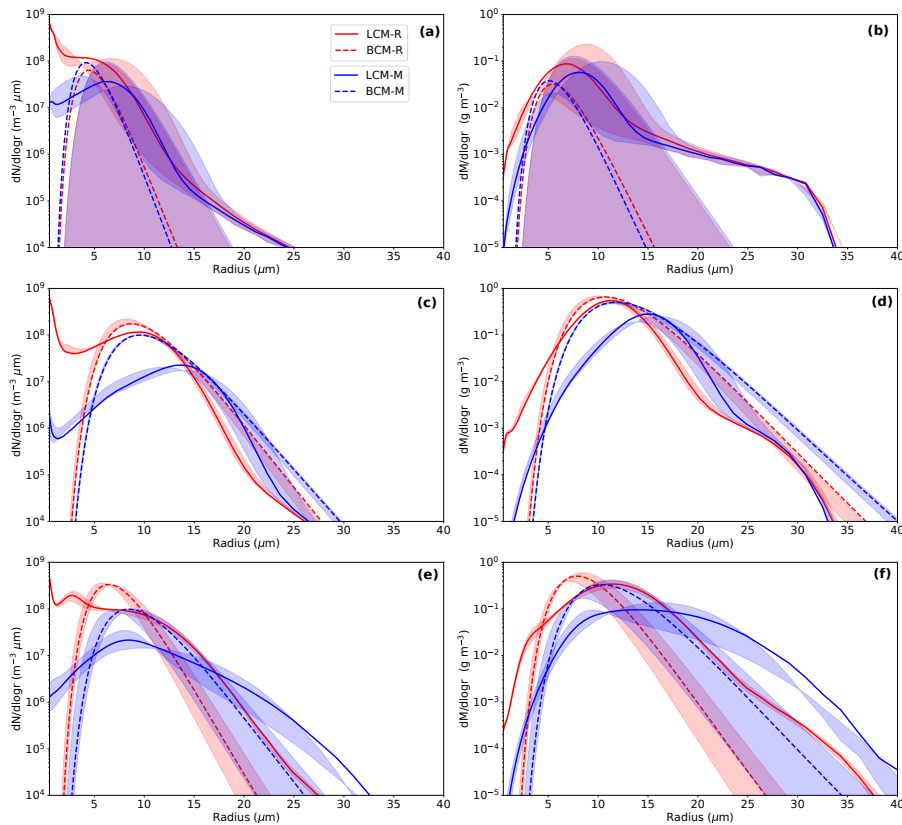


**Figure 4.** Instantaneous drop size distributions of number and mass density at 0300 UTC (a,b), 0600 UTC (c,d) and 0800 UTC (e,f) averaged over the fog layer of the simulations listed in Table 2. The shaded area indicates the shift of the spectrum in an interval of 1 h around the discrete value.

### 3.2. Microphysics

Figure 4 shows the particle number and mass density functions in their logarithmic forms of  $dN/dlogr$  and  $dM/dlogr$  ( $log$  stands for  $log_{10}$ ) at 0300 UTC, 0600 UTC and 0800 UTC for both LCM and BCM. In contrast to the LCM, where the size distribution is derived explicitly by the sum of all droplets within a discrete radius interval, the bulk model has a preset shape (in this case following

a log-normal distribution), whose quantitative course is defined by the liquid water mixing ratio, the mean geometric radius and the spectral width [41].

As shown in Figure 4 (top panel) the droplet distributions at 0300 UTC of the LCM cases are broader (corresponding to an width of approximately  $\sigma_g = 1.5$  considering a log-normal distribution) than those of the BCM simulations. Already within the first 60 min of the fog life cycle, despite of a very thin fog layer in stable stratified conditions, droplets with a radius of up to 25  $\mu\text{m}$  have formed. However, large droplets, only a few in concentration, are likely caused by the presence of large aerosols. Furthermore, the size distributions of the LCM simulations reveal different shapes caused by the different aerosol environments. On the one hand, LCM-R shows its maximum at very small particles radii, which account for a large amount of the total number concentration as shown in Figure 2, which can be assumed to be swollen and not activated aerosols. On the other hand, LCM-M shows an increase in the number concentration up to radii of  $r = 8 \mu\text{m}$ . This findings concerning the different number concentrations is an agreement with previous observations [1,6]. However, LCM-M as well as LCM-R show a change in kurtosis at a radius of 14  $\mu\text{m}$ . As we compare the BCM simulations with the LCM simulations, it becomes apparent that also the BCM cases are still at the beginning of the formation phase at 0300 UTC, indicated by large shift of the distribution within one hour (illustrated by shaded areas). One main difference between the microphysics schemes is that small droplets and swollen aerosols in the BCM are not included by design. Although the influence of the amount of small droplets on the fog may be small, the question of how many droplets are activated and therefore will compete for supersaturation and eventually grow to larger droplets is crucial, as it affects both the sedimentation rate and optical thickness. In regard on the different aerosol environments, Figure 4 shows that already at this early stage BCM-M exceeds the number concentration of LCM-M. In contrast, LCM-R has an overall higher droplet concentration than BCM-R. Additionally, the mass density distribution (Figure 4, right column) shows, which droplets of the distribution contribute the largest fraction of the total mass of liquid water. For both LCM simulations we observe a maximum at approximately 10  $\mu\text{m}$ . This, however, is not surprising, as in comparison to convective clouds, fog droplets are rather small [1].

Examining the size distributions at 0600 UTC and 0800 UTC (see Figure 4c,e) we see some changes of essential features and spectral shape. In general, the spectrum is shifted towards larger radii. Moreover, we see that both LCM-R and LCM-M obtain two peaks (bi-modal shape), where the first one is located at very small radii and the second one at 10  $\mu\text{m}$  and 15  $\mu\text{m}$ , respectively. In both LCM simulations a decrease of small droplets and an increase in the range of droplets with  $r = 10 \mu\text{m}$  can be observed. Furthermore, the comparison displays that LCM-R shows an order of magnitude higher droplet concentration of particles with  $r \approx 10 \mu\text{m}$  than LCM-M. In contrast, the number of droplets with a radius of about  $r = 20 \mu\text{m}$  is higher in LCM-M than in LCM-R. This can be attributed to the fact that with a small number of activated aerosols the water vapour surplus is distributed over fewer droplets and thus individual droplets can grow more vigorously.

At 0800 UTC we observe a decrease of the mean modal radius for all simulations compared to the microphysical conditions at 0600 UTC. Especially the shape of the distribution of LCM-M has significantly changed from a bi-modal shape to a more platykurtic distribution, especially for LCM-M. This involves also a change in the spectral shape, which could be best approximated with  $\sigma_g = 1.4$  assuming a log-normal distribution for the LCM cases. Such changes in the shape of the fog size distributions have been also observed by Wendish et al. [7] and Price [3]. Moreover, LCM-M, albeit much lower in total liquid mass, shows the presence of larger droplets with  $r \approx 40 \mu\text{m}$  (see Figure 4f). Further, the number of very small and large droplets is underestimated in the BCM compared to the LCM. This behavior is an intrinsic feature of the bulk model, as their spectrum is parameterized and can only follow a logarithmic distribution by design. Overall, the explicitly simulated spectra by the LCM are (at least at 0300 UTC and 0800 UTC) broader than the resulting BCM spectra. This explains, among the differences in the calculation, the higher sedimentation rates for the LCM observed in Figure 2e, which are explicitly resolved in the LCM but follows a parameterization in the bulk model.

Although adjusting the shape parameter within this parameterizations could lead to different results, tuning this parameter seems arbitrary and not a practical way. The derivation of a parameterization for a dynamic calculation based on results of the LCM would be a logical next step, but, this is beyond the scope of the present study.

Figure 5 shows the number and mass density distributions at 2 m height at 0600 UTC as they are often measured and thus simulated at this level [3,6]. Note, that the spectra taken during any other time periods as shown before, would not contribute further insights to the points discussed here. While the spectrum of BCM-R and BCM-M in 2 m height is nearly the same as the averaged distribution over the whole fog, the spectrum of LCM-R and LCM-M shows a more distinct bi-modal shape in 2 m height with a minimum at  $r \approx 1.9 \mu\text{m}$  and  $r \approx 1.2 \mu\text{m}$ , respectively. This minimum separates the activated an unactivated (but swollen) aerosols [6] and is a good agreement with the values by Mazoyer et al. [12] who reported a critical diameter of  $3.8 \mu\text{m}$ . Differences in the spectrum of LCM-R and LCM-M between the 2 m level and the whole fog layer might be explained by the fact, that the latter involve a broader range of prevailing supersaturations, e.g., at the fog top, or due to updrafts within the convective fog layer, which has been reported to play also a role in fogs [50]. Indeed, such a bi-modal shape is in agreement with the particle distributions simulated by Bott [6] and observed by Price [3], which include two modes with maxima at very small particles sizes ( $r \approx 1 \mu\text{m}$ ) and ( $r \approx 10 \mu\text{m}$ ) even though they reported a slightly higher separation radius producing the minimum at approximately  $r = 5 \mu\text{m}$  (their Figure 9) and  $r = 3 - 4 \mu\text{m}$  (their Figures 9–10), respectively.

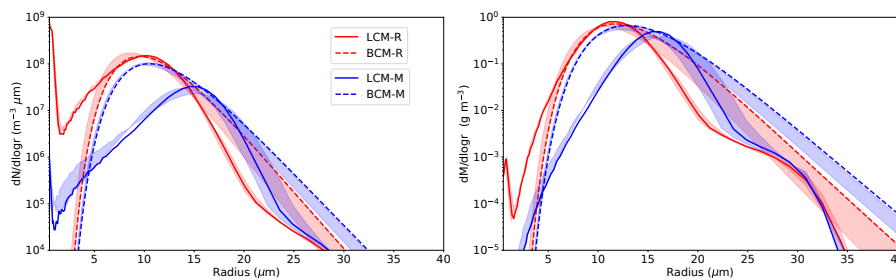


**Figure 5.** Instantaneous drop size distributions at 0600 UTC at 2 m height of the simulations listed in Table 2. The shaded area indicates the shift of the spectrum in an interval of 1 h around the discrete value.

#### 4. Conclusions

In this study we applied a LCM-LES approach for the first time to simulate a complete life cycle of a radiation fog event. These results were compared against simulations using a traditional bulk model. In this way, we could show the importance of a proper representation of microphysical processes for the development of radiation fogs in numerical models. Furthermore, we were able to investigate the evolution of droplet size distributions in fogs while taking advantage of the explicit resolving character of the LCM. These were contrasted with the assumed size distributions of bulk models in order to assess their shortcomings.

For the overall development of the radiation fog we made five major observations with significant differences among the models and aerosol environments. First, the onset of fog in BCMs is delayed by up to 70 min compared to the LCM simulations for the case studied. Second, BCMs tend to overestimate the liquid water path as the LCM suggests much lower values for both aerosol environments. Third, the amount of liquid water (in relative terms to the overall LWP), which is sedimented during the fog, is significantly higher using the LCM than the BCM. Fourth, as already found in former studies [9,10], a higher aerosol loading leads to higher fog droplet concentrations and a more dense fog layer with a higher overall LWP. Fifth, the temporal evolution of the overall number of fog droplets within the fog layer differs notably. For the LCM simulations (both aerosol environments) the number of medium

sized fog droplets is lower than for the BCM simulations, while we observe the opposite for small droplets and swollen aerosols.

All these observations can be linked to microphysical processes and how they are represented within the models. As BCMs are not capable to simulate the gradual transition from aerosols to fog droplets, they fail to resolve the swelling of aerosols, which consequently results in a delayed production of liquid water and reduction in visibility. Also our LCM results suggest that the number of actual fog droplets is lower than predicted by the BCM as many aerosols have swollen in size but not activated due to low supersaturations. This is in general agreement with results found by Boutle et al. [5], who used a sophisticated Eulerian bin approach to simulate aerosols and fog droplets. Moreover, as the spectral shape and the width of the fog distribution must be prescribed and assumed to be constant (in space and time) in the BCM, such models are incapable of representing different microphysical stages of the fog associated with various spectral shapes. In contrast, our LCM simulations suggest that the droplet size distributions develops during the life cycle (gamma shaped, bi-modal and platykurtic), which is also found in observations of other fog cases [3,7]. This in turn also influences the process of fog droplet sedimentation, which is quite differently represented in the schemes. The LCM resolves the settling velocity of each superdroplet individually, whereas the BCM calculates a sedimentation flux based on the parameterized distribution. These differences of the model formulation cause, besides different results of the sedimentation fluxes, that the removal of aerosol due to wet deposition is considered in the LCM but excluded in the BCM by design. However, this process potentially interacts in turn with the development of the fog layer as it changes the underlying aerosol conditions.

In summary, the present study demonstrates for the first time that today's high performance computing facilities allows for performed coupled LES-LCM studies of fog processes and are a useful tool for studying fog microphysics at a unprecedented level of detail. In the future the proposed modeling approach has great potential to be validated against field measurements. For doing so, future measurement campaigns must be designed in such a way that the local aerosol background and drop size distributions are measured at various locations and times. To our knowledge such data sets are currently lacking or rare.

**Supplementary Materials:** The complete list of parameters for all presented simulations as well as the output files and modified code parts used in addition to the standard code base of PALM are available online at <https://doi.org/10.25835/0030614>.

**Author Contributions:** The numerical experiments were jointly designed by the authors. J.S. implemented output quantities and model improvements, conducted the simulations and performed the data analysis. Results were jointly discussed. J.S. prepared the paper, with significant contributions by B.M. All authors have read and agreed to the published version of the manuscript.

**Funding:** This research has been supported by the German Research Foundation (grant no. MA 6383/1-3). The publication of this article was funded by the Open Access fund of Leibniz Universität Hannover.

**Acknowledgments:** The authors thank the three reviewers for their critical and valuable comments which helped to improve the manuscript. All simulations were carried out on the computer clusters of the North-German Supercomputing Alliance (HLRN). Python3.6 was used for data analysis and visualization. The PALM code can be accessed under [www.palm-model.org](http://www.palm-model.org).

**Conflicts of Interest:** The authors declare no conflict of interest. The funders had no role in the design of the study; in the collection, analyses, or interpretation of data; in the writing of the manuscript, or in the decision to publish the results.

## Abbreviations

The following abbreviations are used in this manuscript:

BCM	Bulk cloud model
CCN	Cloud condensation nuclei
LCM	Lagrangian cloud model
LES	Large-eddy simulation
LSM	land surface model
LWP	Liquid water path
NWP	Numerical weather prediction
PALM	Parallel large-eddy simulation model for atmospheric and oceanic flows
RRTMG	Rapid Radiation Transfer Model for Global Models
UTC	Coordinated Universal Time
<i>vis</i>	visibility

## Appendix A. Sensitivity Study: Number of Superdroplets

We performed three-dimensional large-eddy simulations of a radiation fog event with different microphysics schemes. By using particle-based microphysics illustrated by explicit simulated Lagrangian particles, the general question arises how many of those particles are required for a convergent solution. Due to the extremely high computing time requirements of the simulations presented in the main part of this paper, some simplifications were made in the sensitivity studies. Mainly the curvature and solution effects of the aerosol were neglected, which leads to the elimination of the internal particle time step for the diffusional growth equation. Therefore, a comparatively large time step of 0.2 s could be used. The prescribed initial number concentration was set to  $600 \text{ cm}^{-3}$ . All other parameters were left constant. Four simulations were carried out with concentrations of 8, 16, 32 and 64 superdroplets per grid box. Figure A1 shows that the overall liquid water path is sensitive to the used number of superdroplets. However, increasing the superdroplet number leads to decreasing differences between the simulations. It can be seen that the results converge and satisfactory results are achieved with a superdroplet number of 32 particles per grid box. Deriving the superdroplet concentration to the physical space, yields concentrations of 0.5, 1, 2 and 4 superdroplets per cubic-meter. Compared to other studies using the LCM approach, this number is at the cutting-edge of current LCM applications [16,37].

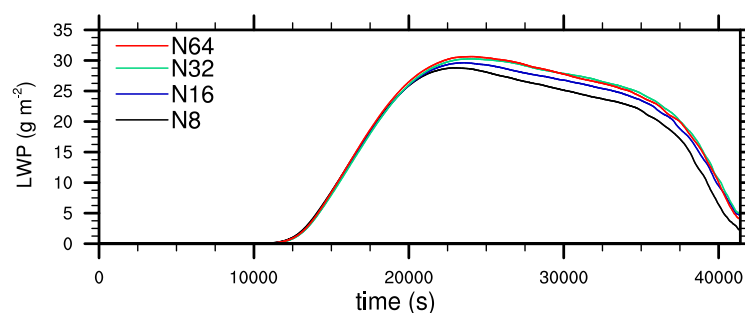


**Figure A1.** Time series of liquid water path for the sensitivity studies with different superdroplet concentrations.

## References

1. Gultepe, I.; Hansen, B.; Cober, S.; Pearson, G.; Milbrandt, J.; Platnick, S.; Taylor, P.; Gordon, M.; Oakley, J. The fog remote sensing and modeling field project. *Bull. Am. Meteor. Soc.* **2009**, *90*, 341–359, doi:10.1175/2008BAMS2354.1.



2. Gultepe, I.; Tardif, R.; Michaelides, S.; Cermak, J.; Bott, A.; Bendix, J.; Müller, M.D.; Pagowski, M.; Hansen, B.; Ellrod, G.; et al. Fog research: A review of past achievements and future perspectives. *Pure Appl. Geophys.* **2007**, *164*, 1121–1159, doi:10.1007/s00024-007-0211-x.
3. Price, J. Radiation fog. Part I: Observations of stability and drop size distributions. *Bound.-Layer Meteorol.* **2011**, *139*, 167–191, doi:10.1007/s10546-010-9580-2.
4. Wilkinson, J.M.; Porson, A.N.; Bornemann, F.J.; Weeks, M.; Field, P.R.; Lock, A.P. Improved microphysical parametrization of drizzle and fog for operational forecasting using the Met Office Unified Model. *Q. J. R. Meteorol. Soc.* **2013**, *139*, 488–500, doi:10.1002/qj.1975.
5. Boutle, I.; Price, J.; Kudzotsa, I.; Kokkola, H.; Romakkaniemi, S. Aerosol-fog interaction and the transition to well-mixed radiation fog. *Atmos. Chem. Phys.* **2018**, *18*, 7827–7840, doi:10.5194/acp-18-7827-2018.
6. Bott, A. On the influence of the physico-chemical properties of aerosols on the life cycle of radiation fogs. *Bound.-Layer Meteorol.* **1991**, *56*, 1–31, doi:10.1007/BF00119960.
7. Wendish, M.; Mertes, S.; Heintzenberg, J.; Wiedensohler, A.; Schell, D.; Wobrock, W.; Frank, G.; Martinsson, B.G.; Fuzzi, S.; Orsi, G.; et al. Drop size distribution and LWC in Po valley fog. *Contrib. Atmos. Phys.* **1998**, *71*, 87–100.
8. Niu, S.; Liu, D.; Zhao, L.; Lu, C.; Lü, J.; Yang, J. Summary of a 4-year fog field study in northern Nanjing, Part 2: Fog microphysics. *Pure Appl. Geophys.* **2012**, *169*, 1137–1155, doi:10.1007/s00024-011-0344-9.
9. Stolaki, S.; Haeffelin, M.; Lac, C.; Dupont, J.C.; Elias, T.; Masson, V. Influence of aerosols on the life cycle of a radiation fog event. A numerical and observational study. *Atmos. Res.* **2015**, *151*, 146–161, doi:10.1016/j.atmosres.2014.04.013.
10. Maalick, Z.; Kühn, T.; Korhonen, H.; Kokkola, H.; Laaksonen, A.; Romakkaniemi, S. Effect of aerosol concentration and absorbing aerosol on the radiation fog life cycle. *Atmos. Environ.* **2016**, *133*, 26–33, doi:10.1016/j.atmosenv.2016.03.018.
11. Thies, B.; Egli, S.; Bendix, J. The Influence of Drop Size Distributions on the Relationship between Liquid Water Content and Radar Reflectivity in Radiation Fogs. *Atmosphere* **2017**, *8*, 142, doi:10.3390/atmos8080142.
12. Mazoyer, M.; Burnet, F.; Denjean, C.; Roberts, G.C.; Haeffelin, M.; Dupont, J.C.; Elias, T. Experimental study of the aerosol impact on fog microphysics. *Atmos. Chem. Phys.* **2019**, *19*, 4323–4344, doi:10.5194/acp-19-4323-2019.
13. Poku, C.; Ross, A.; Blyth, A.; Hill, A.; Price, J. How important are aerosol–fog interactions for the successful modelling of nocturnal radiation fog? *Weather* **2019**, *74*, 237–243, doi:10.1002/wea.3503.
14. Schwenkel, J.; Maronga, B. Large-eddy simulation of radiation fog with comprehensive two-moment bulk microphysics: Impact of different aerosol activation and condensation parameterizations. *Atmos. Chem. Phys.* **2019**, *19*, 7165–7181, doi:10.5194/acp-19-7165-2019.
15. Köhler, H. The nucleus in and the growth of hygroscopic droplets. *Trans. Faraday Soc.* **1936**, *32*, 1152–1161.
16. Grabowski, W.W.; Morrison, H.; Shima, S.I.; Abade, G.C.; Dziekan, P.; Pawlowska, H. Modeling of Cloud Microphysics: Can We Do Better? *Bull. Am. Meteorol. Soc.* **2019**, *100*, 655–672, doi:10.1175/BAMS-D-18-0005.1.
17. Cohard, J.M.; Pinty, J.P.; Bedos, C. Extending Twomey’s analytical estimate of nucleated cloud droplet concentrations from CCN spectra. *J. Atmos. Sci.* **1998**, *55*, 3348–3357, doi:10.1175/1520-0469(1998)055<3348:ETSAEO>2.0.CO;2.
18. Khvorostyanov, V.I.; Curry, J.A. Aerosol size spectra and CCN activity spectra: Reconciling the lognormal, algebraic, and power laws. *J. Geophys. Res. Atmos.* **2006**, *111*, doi:10.1029/2005JD006532.
19. Hoffmann, F.; Raasch, S.; Noh, Y. Entrainment of aerosols and their activation in a shallow cumulus cloud studied with a coupled LCM–LES approach. *Atmos. Res.* **2015**, *156*, 43–57, doi:10.1016/j.atmosres.2014.12.008.
20. Porson, A.; Price, J.; Lock, A.; Clark, P. Radiation fog. Part II: Large-eddy simulations in very stable conditions. *Bound.-Layer Meteorol.* **2011**, *139*, 193–224, doi:10.1007/s10546-010-9579-8.
21. Maronga, B.; Bosveld, F. Key parameters for the life cycle of nocturnal radiation fog: A comprehensive large-eddy simulation study. *Q. J. R. Meteorol. Soc.* **2017**, *143*, 2463–2480, doi:10.1002/qj.3100.
22. Steeneveld, G.J.; de Bode, M. Unravelling the relative roles of physical processes in modelling the life cycle of a warm radiation fog. *Q. J. R. Meteorol. Soc.* **2018**, *144*, 1539–1554, doi:10.1002/qj.3300.
23. Tonttila, J.; Maalick, Z.; Raatikainen, T.; Kokkola, H.; Kühn, T.; Romakkaniemi, S. UCLALES–SALSA v1.0: A large-eddy model with interactive sectional microphysics for aerosol, clouds and precipitation. *Geosci. Model Dev.* **2017**, *10*, 169–188, doi:10.5194/gmd-10-169-2017.

24. Maronga, B.; Gryschka, M.; Heinze, R.; Hoffmann, F.; Kanani-Sühring, F.; Keck, M.; Ketelsen, K.; Letzel, M.O.; Sühring, M.; Raasch, S. The Parallelized Large-Eddy Simulation Model (PALM) version 4.0 for atmospheric and oceanic flows: Model formulation, recent developments, and future perspectives. *Geosci. Model Dev.* **2015**, doi:10.5194/gmd-8-2515-2015.
25. Maronga, B.; Banzhaf, S.; Burmeister, C.; Esch, T.; Forkel, R.; Fröhlich, D.; Fuka, V.; Gehrke, K.F.; Geletič, J.; Giersch, S.; et al. Overview of the PALM model system 6.0. *Geosci. Model Dev.* **2020**, *13*, 1335–1372, doi:10.5194/gmd-13-1335-2020.
26. Beare, R.J.; Macvean, M.K.; Holtslag, A.A.; Cuxart, J.; Esau, I.; Golaz, J.C.; Jimenez, M.A.; Khairoutdinov, M.; Kosovic, B.; Lewellen, D.; et al. An intercomparison of large-eddy simulations of the stable boundary layer. *Bound.-Layer Meteorol.* **2006**, *118*, 247–272, doi:10.1007/s10546-004-2820-6.
27. Maronga, B.; Knigge, C.; Raasch, S. An Improved Surface Boundary Condition for Large-Eddy Simulations Based on Monin–Obukhov Similarity Theory: Evaluation and Consequences for Grid Convergence in Neutral and Stable Conditions. *Bound.-Layer Meteorol.* **2020**, *174*, 297–325, doi:10.1007/s10546-019-00485-w.
28. Wicker, L.J.; Skamarock, W.C. Time-splitting methods for elastic models using forward time schemes. *Mon. Weather Rev.* **2002**, *130*, 2088–2097, doi:10.1175/1520-0493(2002)130<2088:TSMFEM>2.0.CO;2.
29. Williamson, J. Low-storage runge-kutta schemes. *J. Comput. Phys.* **1980**, *35*, 48–56, doi:10.1016/0021-9991(80)90033-9.
30. Deardorff, J.W. Stratocumulus-capped mixed layers derived from a three-dimensional model. *Bound.-Layer Meteorol.* **1980**, *18*, 495–527, doi:10.1007/BF00119502.
31. Clough, S.A.; Shephard, M.W.; Mlawer, E.J.; Delamere, J.S.; Iacono, M.J.; Cady-Pereira, K.; Boukabara, S.; Brown, P.D. Atmospheric radiative transfer modeling: A summary of the AER codes, Short Communication. *J. Quant. Spectrosc. Radiat. Transf.* **2005**, *91*, 233–244, doi:10.1016/j.jqsrt.2004.05.058.
32. Grabowski, W.W.; Dziekan, P.; Pawlowska, H. Lagrangian condensation microphysics with Twomey CCN activation. *Geosci. Model Dev.* **2018**, *11*, 103–120, doi:10.5194/gmd-11-103-2018.
33. Rogers, R.R.; Baumgardner, D.; Ethier, S.A.; Carter, D.A.; Ecklund, W.L. Comparison of Raindrop Size Distributions Measured by Radar Wind Profiler and by Airplane. *J. Appl. Meteorol.* **1993**, *32*, 694–699, doi:10.1175/1520-0450(1993)032<0694:CORSDM>2.0.CO;2.
34. Riechermann, T.; Noh, Y.; Raasch, S. A new method for large-eddy simulations of clouds with Lagrangian droplets including the effects of turbulent collision. *New J. Phys.* **2012**, *14*, 065008.
35. Hoffmann, F. The effect of spurious cloud edge supersaturations in Lagrangian cloud models: An analytical and numerical study. *Mon. Weather Rev.* **2016**, *144*, 107–118, doi:10.1175/MWR-D-15-0234.1.
36. Kogan, Y.L. The Simulation of a Convective Cloud in a 3-D Model With Explicit Microphysics. Part I: Model Description and Sensitivity Experiments. *J. Atmos. Sci.* **1991**, *48*, 1160–1189, doi:10.1175/1520-0469(1991)048<1160:TSAACC>2.0.CO;2.
37. Hoffmann, F.; Noh, Y.; Raasch, S. The Route to Raindrop Formation in a Shallow Cumulus Cloud Simulated by a Lagrangian Cloud Model. *J. Atmos. Sci.* **2017**, *74*, 2125–2142, doi:10.1175/JAS-D-16-0220.1.
38. Seifert, A.; Beheng, K.D. A double-moment parameterization for simulating autoconversion, accretion and selfcollection. *Atmos. Res.* **2001**, *59*, 265–281, doi:10.1016/S0169-8095(01)00126-0.
39. Seifert, A.; Beheng, K.D. A two-moment cloud microphysics parameterization for mixed-phase clouds. Part 1: Model description. *Meteorol. Atmos. Phys.* **2006**, *92*, 45–66, doi:10.1007/s00703-005-0112-4.
40. Morrison, H.; Curry, J.A.; Shupe, M.D.; Zuidema, P. A New Double-Moment Microphysics Parameterization for Application in Cloud and Climate Models. Part II: Single-Column Modeling of Arctic Clouds. *J. Atmos. Sci.* **2005**, *62*, 1678–1693, doi:10.1175/JAS3447.1.
41. Ackerman, A.S.; VanZanten, M.C.; Stevens, B.; Savic-Jovicic, V.; Bretherton, C.S.; Chlond, A.; Golaz, J.C.; Jiang, H.; Khairoutdinov, M.; Krueger, S.K.; et al. Large-eddy simulations of a drizzling, stratocumulus-topped marine boundary layer. *Mon. Weather Rev.* **2009**, *137*, 1083–1110, doi:10.1175/2008MWR2582.1.
42. Geoffroy, O.; Brenguier, J.L.; Burnet, F. Parametric representation of the cloud droplet spectra for LES warm bulk microphysical schemes. *Atmos. Chem. Phys.* **2010**, *10*, 4835–4848, doi:10.5194/acp-10-4835-2010.
43. Khairoutdinov, M.; Kogan, Y. A new cloud physics parameterization in a large-eddy simulation model of marine stratocumulus. *Mon. Weather Rev.* **2000**, *128*, 229–243, doi:10.1175/1520-0493(2000)128<0229:ANCPPI>2.0.CO;2.



44. Boers, R.; Baltink, H.K.; Hemink, H.; Bosveld, F.; Moerman, M. Ground-based observations and modeling of the visibility and radar reflectivity in a radiation fog layer. *J. Atmos. Ocean Technol.* **2013**, *30*, 288–300, doi:10.1175/JTECH-D-12-00081.1.
45. Jaenicke, R. Tropospheric Aerosols. In *Aerosol-Cloud-Climate Interactions*; Hobbs, P.V., Ed.; Academic Press: San Diego, CA, USA, 1993; pp. 1–31.
46. Gultepe, I.; Müller, M.D.; Boybeyi, Z. A New Visibility Parameterization for Warm-Fog Applications in Numerical Weather Prediction Models. *J. Appl. Meteorol. Climatol.* **2006**, *45*, 1469–1480, doi:10.1175/JAM2423.1.
47. Hammer, E.; Gysel, M.; Roberts, G.C.; Elias, T.; Hofer, J.; Hoyle, C.R.; Bukowiecki, N.; Dupont, J.C.; Burnet, F.; Baltensperger, U.; et al. Size-dependent particle activation properties in fog during the ParisFog 2012/13 field campaign. *Atmos. Chem. Phys.* **2014**, *14*, 10517–10533, doi:10.5194/acp-14-10517-2014.
48. Elias, T.; Dupont, J.C.; Hammer, E.; Hoyle, C.R.; Haefelin, M.; Burnet, F.; Jolivet, D. Enhanced extinction of visible radiation due to hydrated aerosols in mist and fog. *Atmos. Chem. Phys.* **2015**, *15*, 6605–6623, doi:10.5194/acp-15-6605-2015.
49. Zhang, X.; Musson-Genon, L.; Dupont, E.; Milliez, M.; Carissimo, B. On the influence of a simple microphysics parametrization on radiation fog modelling: A case study during parisfog. *Bound.-Layer Meteorol.* **2014**, *151*, 293–315, doi:10.1007/s10546-013-9894-y.
50. Pilié, R.; Mack, E.; Kocmond, W.; Eadie, W.; Rogers, C. The life cycle of valley fog. Part II: Fog microphysics. *J. Appl. Meteorol.* **1975**, *14*, 364–374, doi:10.1175/1520-0450(1975)014<0364:TLCOVF>2.0.CO;2.



© 2020 by the authors. Licensee MDPI, Basel, Switzerland. This article is an open access article distributed under the terms and conditions of the Creative Commons Attribution (CC BY) license (<http://creativecommons.org/licenses/by/4.0/>).



## 5 Demystify: a large-eddy simulation (LES) and single-column model (SCM) intercomparison of radiation fog

### 5.1 Declaration of Contributions

IB analysed the submitted results and wrote the manuscript. IB, WA, RB, AB, LD, RF, TG, EG, AH, AI, IK, JoS, and GJS ran the model simulations. JoS prepared, implemented required output quantities and conducted simulations for the PALM model as well as provided simulation results for the PALM model. All authors contributed to the discussion, understanding and presentation of results, as well as the preparation of the manuscript.

### 5.2 Research Article

©The authors 2022. CC BY 4.0 License



## Demistify: a large-eddy simulation (LES) and single-column model (SCM) intercomparison of radiation fog

Ian Boutle<sup>1</sup>, Wayne Angevine<sup>2</sup>, Jian-Wen Bao<sup>3</sup>, Thierry Bergot<sup>4</sup>, Ritthik Bhattacharya<sup>5</sup>, Andreas Bott<sup>6</sup>, Leo Ducongé<sup>4</sup>, Richard Forbes<sup>7</sup>, Tobias Goecke<sup>8</sup>, Evelyn Grell<sup>9</sup>, Adrian Hill<sup>1</sup>, Adele L. Igel<sup>10</sup>, Innocent Kudzotsa<sup>11</sup>, Christine Lac<sup>4</sup>, Bjorn Maronga<sup>12</sup>, Sami Romakkaniemi<sup>11</sup>, Juerg Schmidli<sup>5</sup>, Johannes Schwenkel<sup>12</sup>, Gert-Jan Steeneveld<sup>13</sup>, and Benoît Vié<sup>4</sup>

<sup>1</sup>Met Office, Exeter, UK

<sup>2</sup>CIRES, University of Colorado, and NOAA Chemical Sciences Laboratory, Boulder, USA

<sup>3</sup>NOAA Physical Sciences Laboratory, Boulder, USA

<sup>4</sup>CNRM, Université de Toulouse, Météo-France, CNRS, Toulouse, France

<sup>5</sup>Institute for Atmospheric and Environmental Sciences, Goethe University Frankfurt, Frankfurt, Germany

<sup>6</sup>Institute of Geosciences, University of Bonn, Bonn, Germany

<sup>7</sup>European Centre for Medium-Range Weather Forecasts, Reading, UK

<sup>8</sup>Deutscher Wetterdienst, Offenbach, Germany

<sup>9</sup>CIRES, University of Colorado, and NOAA Physical Sciences Laboratory, Boulder, USA

<sup>10</sup>Department of Land, Air and Water Resources, University of California, Davis, USA

<sup>11</sup>Finnish Meteorological Institute, Kuopio, Finland

<sup>12</sup>Institute of Meteorology and Climatology, Leibniz University Hannover, Hannover, Germany

<sup>13</sup>Meteorology and Air Quality Section, Wageningen University, Wageningen, Netherlands

**Correspondence:** Ian Boutle (ian.boutle@metoffice.gov.uk)

Received: 4 October 2021 – Discussion started: 15 October 2021

Revised: 2 December 2021 – Accepted: 3 December 2021 – Published: 10 January 2022

**Abstract.** An intercomparison between 10 single-column (SCM) and 5 large-eddy simulation (LES) models is presented for a radiation fog case study inspired by the Local and Non-local Fog Experiment (LANFEX) field campaign. Seven of the SCMs represent single-column equivalents of operational numerical weather prediction (NWP) models, whilst three are research-grade SCMs designed for fog simulation, and the LESs are designed to reproduce in the best manner currently possible the underlying physical processes governing fog formation. The LES model results are of variable quality and do not provide a consistent baseline against which to compare the NWP models, particularly under high aerosol or cloud droplet number concentration (CDNC) conditions. The main SCM bias appears to be toward the overdevelopment of fog, i.e. fog which is too thick, although the inter-model variability is large. In reality there is a subtle balance between water lost to the surface and water condensed into fog, and the ability of a model to accurately simulate this process strongly determines the quality of its forecast. Some NWP SCMs do not represent fundamental components of this process (e.g. cloud droplet sedimentation) and therefore are naturally hampered in their ability to deliver accurate simulations. Finally, we show that modelled fog development is as sensitive to the shape of the cloud droplet size distribution, a rarely studied or modified part of the microphysical parameterisation, as it is to the underlying aerosol or CDNC.

## 1 Introduction

Most operational numerical weather prediction (NWP) centres will list errors in fog forecasting amongst their top model problems, with the requirement for improvement considered high priority (Hewson, 2019). The key customer driving this is the aviation sector, with  $\approx 40\%$  of all delays ( $\approx 50\%$  of weather-related delays) at busy airports (such as London Heathrow, Paris CDG, San Francisco, and New Delhi) being due to low-visibility events. In the best case, these delays are inconvenient for passengers and expensive for airline operators (Cook and Tanner, 2015; Kulkarni et al., 2019). However, in the worst case, fog can also be a significant danger and is the second most likely cause of weather-related accidents (Gultepe et al., 2019; Leung et al., 2020).

Despite this importance, there is no international community working together on improving fog modelling. The Global Atmospheric System Studies (GASS) panel facilitates projects which draw together researchers from around the globe to work on specific and targeted process studies. Utilising large-eddy simulation (LES) and single-column (SCM) versions of NWP models, previous projects (including under GABLS and GCSS) have made significant advances in the understanding, and modelling of stable boundary layers (Beare et al., 2006; Cuxart et al., 2006), turbulent clouds (van der Dussen et al., 2013; Neggers et al., 2017), and aerosol–cloud interactions (Hill et al., 2015). A new GASS project related to fog modelling therefore presents an opportunity to form a community and address the challenges together, building on the previous understanding of the multitude of processes at play in radiation fog.

A previous intercomparison of radiation fog in SCM models (Bergot et al., 2007) demonstrated that even before fog onset there were considerable differences between models, and it found the model skill to be low. The current intercomparison considers a new generation of NWP SCM models, with more complex physical parameterisations, and for the first time will compare LES models for the same radiation fog event. The key questions to be considered include the following:

- How well can models simulate the development of radiation fog?
- What are the key processes governing the development of radiation fog, i.e. aerosol, cloud microphysics, radiation, turbulence, dew deposition, something else?
- Which of these processes are mostly responsible for the biases seen in current NWP models?
- What level of complexity is required from NWP models to adequately simulate these processes?

The initial phase of work, documented in this paper, will constrain the surface properties and focus primarily on the atmospheric development of fog. This will document the current

state of LES and NWP fog modelling within the community and provide guidance on opportunities for improvements applicable to many models. Further stages of the project will then consider feedbacks through the land surface, more complicated cases with non-local forcing, and the representation of fog in climate models, something which has rarely been looked at in the literature.

## 2 Intercomparison design and participants

The first intensive observational period (IOP1) of the Local and Non-local Fog Experiment (LANFEX; Price et al., 2018) presented a relatively simple case of fog forming in a nocturnal stable boundary layer, developing over several hours into turbulent, optically thick fog. However, NWP modelling of this event (Boutle et al., 2018) showed significant errors in the structure and evolution of the fog. Therefore we base the intercomparison around a slightly idealised version of IOP1. The case is based at the Met Office observational site at Cardington, UK ( $52.1015^\circ$  N,  $0.4159^\circ$  W), and occurred on the night of 24–25 November 2014. Models are initialised from the 17:00 UTC radiosonde profile and forced throughout the night by the observed surface skin temperature (measured with an infra-red radiation thermometer; Price et al., 2018). No other forcing is used to keep the case simple and allow for maximum participation amongst modelling centres. This makes the case identical to the LES case presented in Boutle et al. (2018), which showed good agreement with a 3D NWP model, and testing has shown little difference to SCM results from applying advective forcing derived from the radiosondes (not shown). Forcing with surface temperature also constrains the problem to an atmospheric one, focussing on the cloud, radiation, and turbulence interaction. In reality, patchy fog began to form around 18:00 UTC, with persistent fog and visibilities around 100 m from 20:00 UTC for 12 h before clearance. The real clearance was driven by a bank of overlying cloud cover arriving at the site, which we do not attempt to represent in the simplified case.

Because of the sensitivity to cloud and aerosol processes previously discussed in Boutle et al. (2018), we request two simulations from all participants. For models which do not represent aerosol processing, the cloud droplet number concentration (CDNC) should be prescribed (if possible) as follows:

- c10: fixed cloud droplet number concentration of  $10\text{ cm}^{-3}$
- c50: fixed cloud droplet number concentration of  $50\text{ cm}^{-3}$ .

For models which do represent aerosol processing, the accumulation mode aerosol should be prescribed as follows:

- a100: initial accumulation mode ( $0.15\text{ }\mu\text{m}$  diameter,  $\sigma = 2$ ) aerosol of  $100\text{ cm}^{-3}$

- a650: initial accumulation mode (0.15  $\mu\text{m}$  diameter,  $\sigma = 2$ ) aerosol of  $650 \text{ cm}^{-3}$ .

Experiments c10 and a100 will be referred to as “low” aerosol/CDNC simulations, whilst c50 and a650 will be referred to as “high” aerosol/CDNC simulations. The aerosol set-up is complicated slightly, as some of the more sophisticated aerosol processing models also require specification of the Aitken and coarse mode aerosols, which are prescribed (as in Boutle et al., 2018) as  $1000 \text{ cm}^{-3}$  with a mean diameter of  $0.05 \mu\text{m}$  and  $2 \text{ cm}^{-3}$  with a mean diameter of  $1 \mu\text{m}$ . Vié et al. (2022) discuss how it is only really sensible to impose these additional aerosols in models which represent prognostic supersaturation of liquid water; otherwise excessive activation of the Aitken mode aerosol into cloud droplets occurs.

Although the surface temperature is specified, many models still require some parameterisation of the surface characteristics (to estimate the turbulent fluxes into the atmosphere), which is set as a flat, homogeneous, grass surface with the following parameters:

- momentum roughness length ( $z_{0m}$ ): 0.1 m
- heat roughness length ( $z_{0h}$ ): 0.001 m
- leaf area index: 2
- albedo: 0.25
- emissivity: 0.98.

This set-up is derived from the characteristics of the Cardington site (Price et al., 2018). Evapotranspiration should be unrestricted (i.e. like a sea surface) to avoid complexities associated with soil moisture and land-surface models, although in practice the observed fluxes are into the surface for most of the night, and so this simplification should be of limited importance if the models can reproduce this behaviour.

Table 1 shows the model configurations that have been submitted and are analysed in this paper, whilst Tables 2 and 3 give some further relevant details about the set-ups of the LES and SCM models respectively.

### 3 Results

#### 3.1 Liquid water path evolution

Figure 1 presents an initial view of the submitted models, separated by their class (LES or SCM) and aerosol or CDNC (low or high). As there is no higher-level cloud in any of the simulations, any non-zero liquid water path is attributable to fog. This is consistent with the observations until 08:00 UTC, when the upper level cloud arrived at the site and is responsible for the sharp increase in liquid water path (LWP) after this time (which should not be reproduced by the simulations). The first thing to note is that all models do at least form fog, but beyond this there is very little consistency between models.

The observations are most consistent with the low aerosol/CDNC set-up. For the SCM runs, only MiFog, Meso-NH, UM, and d91 have liquid water path (LWP) evolution in line with the observations, although PaFog, IFS, and WRF are only just outside the observational range. The other models considerably overestimate the LWP. In general, the LES runs are in closer agreement with each other and the observations, but considerable spread exists between them for the high aerosol/CDNC runs. With the exception of ICON and FV3-GFS (which does not represent variable CDNC), all models show substantial variation between the low and high aerosol/CDNC set-ups, producing higher LWP with greater aerosol/CDNC.

To leading order, the dominant factor in determining the LWP evolution of all models is the rate at which water is deposited from the atmosphere to the surface. The observations (see Boutle et al., 2018, Fig. 4a) are broadly constant at around  $20 \text{ g m}^{-2} \text{ h}^{-1}$  throughout the night, and most models achieve this value despite the wildly varying LWP (possibly because the water deposition is constrained by the long-wave cooling of the atmosphere). Because the water deposition rate is strongly affected by the LWP, we must therefore normalise it before comparing the models, which is shown in Fig. 2. This shows a clear link between the deposition rate and LWP – models which do not deposit enough water onto the surface end up with LWP values which are too high, and models which deposit too much water onto the surface end up with LWP values which are too low.

The reasons for the varying water deposition rate are very model dependent, although we can try to summarise some consistent themes in the SCMs:

- *Models which do not represent cloud droplet sedimentation.* These models (FV3-GFS, COSMO, IFS) are significantly hampered by their lack of this process, which is likely to be the dominant mechanism of water removal in reality. IFS is able to compensate to a certain extent by autoconverting significant amounts of fog into precipitation and removing it that way, which explains its lower LWP than COSMO or FV3-GFS, which are unable to do this. Improvements here should be easy to achieve via modifications to the microphysical parameterisation.
- *Models which produce excessive positive surface latent heat flux (Fig. 5).* These models (WRF, COSMO) will always struggle to deposit enough water through microphysical processes because it is being constantly replenished via evaporation from the surface. Understanding the mechanisms behind this error can be tricky, as it may not simply be an issue with the turbulent exchange parameterisations but could also be a feedback. For example, as discussed in Boutle et al. (2018), forming fog which is slightly too optically thick can drive an erroneous positive flux, which in turn leads to further development of thicker fog.

**Table 1.** Modelling centres, lead participants, models, and model simulations submitted. The \* denotes the SCMs that have the physics package and vertical resolution of operational NWP models.

Institution	Model	Type	Experiments submitted	Lead participant	Reference
Bonn University	MiFog	SCM	a100, a650	Andreas Bott	Bott et al. (1990)
Bonn University	PaFog	SCM	a100, a650	Andreas Bott	Bott and Trautmann (2002)
CIRES/NOAA	WRF	SCM*	c10, c50, a100, a650	Wayne Angevine	Angevine et al. (2018)
UC Davis	RAMS	LES	c10, c50, a100, a650	Adele Igel	Cotton et al. (2003)
DWD	ICON	SCM*	c10, c50	Tobias Goecke	Bařtak Duran et al. (2021)
ECMWF	IFS	SCM*	c10, c50	Richard Forbes	Ahlgimm and Forbes (2014)
FMI	UCLA-SALSA	LES	a100, a650	Innocent Kudzotsa	Tonttila et al. (2017)
Frankfurt University	COSMO	SCM*	c10, c50	Ritthik Bhattacharya	Baldauf et al. (2011)
Hannover University	PALM	LES	a100, a650	Johannes Schwenkel	Maronga et al. (2020)
Met Office	Unified Model	SCM*	c10, c50	Ian Boutle	Bush et al. (2020)
Met Office	MONC	LES	c10, c50, a100, a650	Adrian Hill	Dearden et al. (2018)
Meteo France	Meso-NH	SCM*	c10, c50, a100, a650	Leo Duconge	Lac et al. (2018)
Meteo France	Meso-NH	LES	c10, c50, a100, a650	Leo Duconge	Lac et al. (2018)
NOAA	FV3-GFS	SCM*	c300	Evelyn Grell	Firl et al. (2020)
Wageningen University	d91	SCM	c10, c50	Gert-Jan Steeneveld	Duynkerke (1991)

**Table 2.** LES model details: horizontal ( $dx$ ) and vertical ( $dz$ ) grid length, type of aerosol processing, microphysics parameterisation details, and type of sub-grid turbulence scheme (TKE = turbulent kinetic energy closure).

Model	Grid length ( $dx$ , $dz$ )	Aerosol processing	Microphysics type	Prognostic supersaturation	Cloud droplet settling	Sub-grid turbulence
RAMS	4 m, 1.5 m	Accumulation	Bulk	N	Y	TKE
UCLA-SALSA	4 m, 1.5 m	Full	Bin	Y	Y	Smagorinsky
PALM	1.5 m, 1.5 m	Accumulation	Bulk	N	Y	TKE
MONC	4 m, 1.5 m	Accumulation	Bulk	N	Y	Smagorinsky
Meso-NH	4 m, 1.5 m	Accumulation	Bulk	N	Y	TKE

– *The precise nature of the microphysical parameterisations responsible for water deposition.* Even models which represent all processes and maintain a low latent heat flux (ICON, UM, Meso-NH) can have large discrepancies because of how the different water deposition rates feed back onto model evolution. This suggests that more work is required on the basic observations, understanding and modelling of water deposition. For example Meso-NH is the only model to represent turbulent deposition of droplets in addition to sedimentation, giving it one of the highest deposition rates.

The LES models may be closer in their behaviour but still show some similar traits to the SCMs. In particular, the models with the highest deposition rates tend to have the lowest LWP, and visa-versa. However, the mechanism by which this is achieved can be considerably different between the models. RAMS-c10 for example has a significant positive latent heat flux which is balanced by a larger cloud droplet sedimentation rate than any other LES to give an overall water deposition rate and LWP comparable to the other models. Differences like this show why it is difficult to use the LES as process models because although they are producing more

consistent behaviour, the processes by which they achieve it are not consistent.

The one LES (and indeed SCM) model which does not appear to follow the pattern is Meso-NH-c10, which has one of the highest water deposition rates of any of the models, yet manages to achieve a reasonable fog simulation in all cases. This arises because it simulates a very low effective radius (Fig. 3), resulting in very strong absorption and emission from the fog layer, helping the fog to grow despite the high water deposition. The reason for the low effective radius appears to be the use of the Martin et al. (1994) parameterisation with a default “land” set-up; i.e. it is using a high ( $300\text{ cm}^{-3}$ ) assumed CDNC value in the effective radius parameterisation, rather than the actual CDNC used by the microphysical parameterisation. The Meso-NH-a100 simulation, which has a consistent link between cloud droplet number and effective radius, shows a response more consistent with the other models. This highlights the importance of using consistent assumptions between radiation and microphysical parameterisations.

The RAMS-a100 simulation has almost the opposite effect, with a high effective radius resulting in a very low LWP. This however arises because the model rapidly depletes all



**Table 3.** SCM model details: height of lowest model level and number of levels below 150 m, type of aerosol processing, microphysics parameterisation details, and type of sub-grid turbulence scheme (EDMF = eddy-diffusivity mass-flux closure, K1 = local first order closure, NL = non-local/counter-gradient transport, and \* = modified for SCM as in Buzzi et al., 2011).

Model	Grid length (lowest level, levels below 150 m)	Aerosol processing	Microphysics type	Prognostic supersaturation	Cloud droplet settling	Sub-grid turbulence
MiFog	0.5 m, 61	Full	Bin	Y	Y	TKE
PaFog	0.5 m, 61	Full	Bulk	Y	Y	TKE
WRF	12 m, 6	Accumulation	Bulk	N	Y	TKE+EDMF
ICON	10 m, 3	None	Bulk	N	Y	TKE
IFS	10 m, 6	None	Bulk	N	N	EDMF
COSMO	10 m, 7	None	Bulk	N	N	TKE*
Unified Model	2.5 m, 6	None	Bulk	N	Y	K1+NL
Meso-NH	5 m, 7	Accumulation	Bulk	N	Y	TKE
FV3-GFS	21 m, 3	None	Bulk	N	N	EDMF
d91	3.3 m, 27	None	Bulk	N	Y	K1

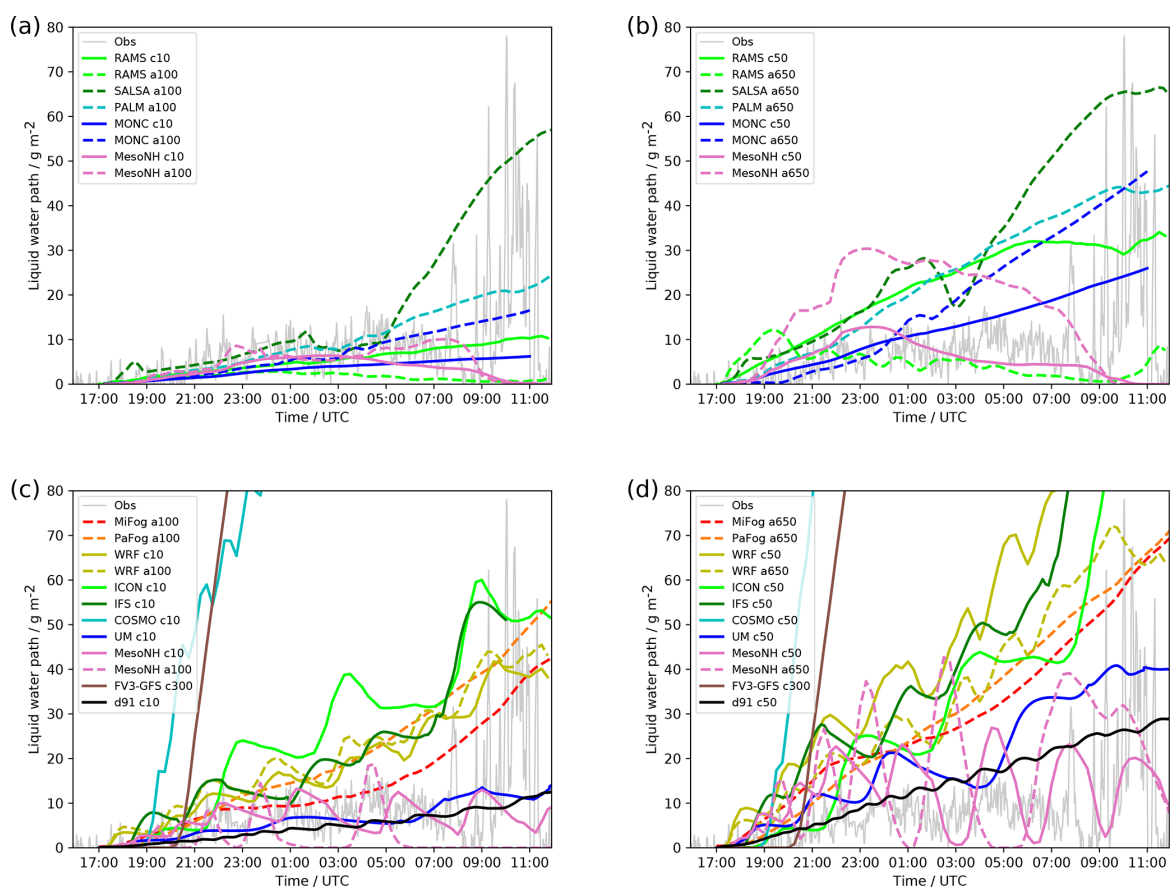


**Figure 1.** Liquid water path observed and modelled by (a) low aerosol/CDNC LES, (b) high aerosol/CDNC LES, (c) low aerosol/CDNC SCMs, and (d) high aerosol/CDNC SCMs.



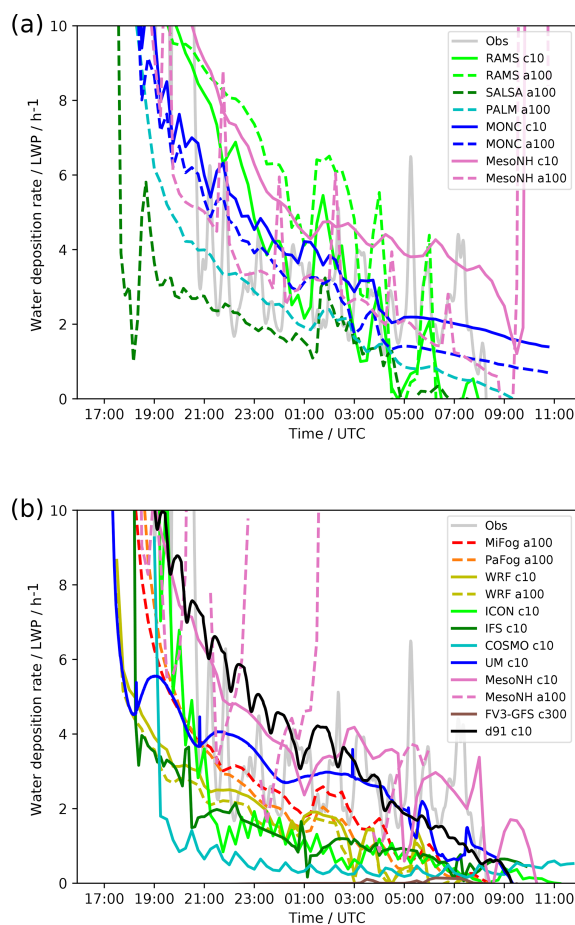


**Figure 2.** Water deposition rate divided by liquid water path observed and modelled by (a) low aerosol/CDNC LES and (b) low aerosol/CDNC SCMs.

of the aerosol in the atmosphere and therefore has nothing to activate into cloud droplets. As a consequence, after the initial fog formation, no new small droplets are formed, but the droplets which do exist grow in size and sediment out, resulting in a very low liquid water path. This is particularly noticeable in the RAMS-a650 simulation, which has the lowest LWP of any model in the “high” experiment. Figure 4b shows that this is linked to a very low CDNC, despite the high initial aerosol concentration, because most of the aerosol has been depleted. Figure 4b also shows an interesting clustering between the full aerosol processing models, which predict CDNC values in the range  $40\text{--}60\text{ cm}^{-3}$ , and the accumulation only models which predict CDNC values in the range  $70\text{--}90\text{ cm}^{-3}$ . This shows that even though the latter group are only considering a subset of the full aerosol distribution, they may still be overestimating the activation occurring in the fog layer. However, Fig. 1b and d show that this clus-

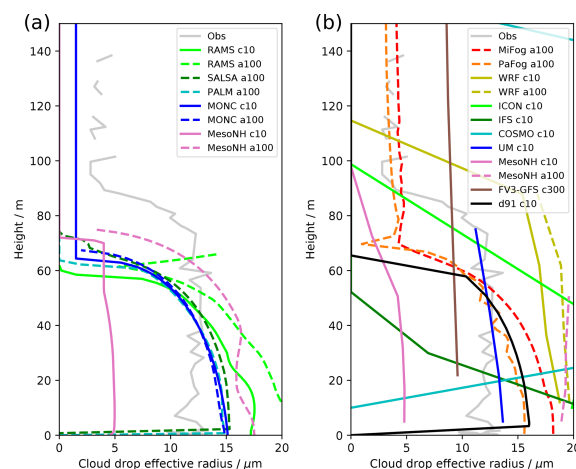


**Figure 3.** Effective radius observed and simulated by the low aerosol/CDNC (a) LES and (b) SCMs at 00:00 UTC.

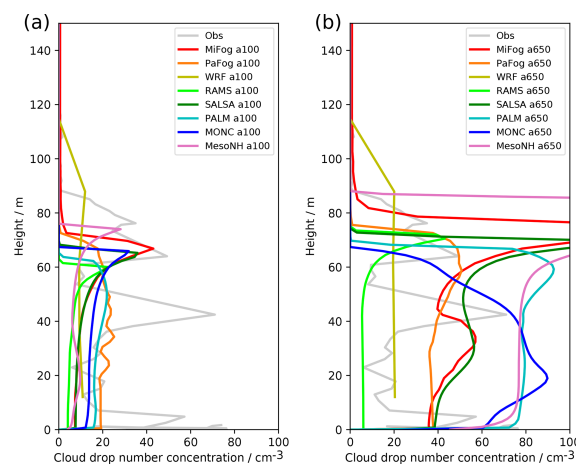


**Figure 4.** CDNC observed and from the aerosol processing models at 00:00 UTC for (a) low aerosol and (b) high aerosol.

tering in the CDNC value does not equate to a clustering in the LWP evolution, demonstrating that there are larger differences between the models than the predicted CDNC value.

It is worth briefly discussing the oscillations in LWP seen in the SCM models. This is a known feature of fog SCM simulations and has been discussed previously by Tardif (2007). Long-wave (LW) cooling from the fog top is the key driver of the fog layer deepening. However, with the coarse vertical grid of the SCM models, the fog can only deepen in discrete units, when the top grows by a single model level. The LWP therefore erodes, by loss of moisture and heating from the surface, until such time as the fog can jump up a level, leading to a large increase in LWP as the water vapour in the level above is available for condensation. Hence the oscilla-

tions are created. All of the SCMs with coarse vertical grids show some oscillations, although the severity of them differs significantly. By far the simulation to suffer most is Meso-NH-a, which appears to have a further complicating feedback from the microphysics. When the fog top jumps up a level, the increase in LWP triggers significant precipitation formation, which quickly removes a large amount of water from the atmosphere. This microphysical feedback does not disappear when running Meso-NH-a at higher vertical resolution, whereas the oscillations in Meso-NH-c do (not shown) due to its use of different microphysical parameterisations.

### 3.2 Surface fluxes and boundary layer structure

A key feature of this fog event, and indeed many fog events, is the slow transition from a stable boundary layer with optically thin fog to a well-mixed boundary layer with optically thick fog. How this transition evolves is of key interest from a forecasting perspective as it will determine the depth and intensity of the fog layer and ultimately its duration into the following morning.

Interestingly, the LES models show greater variability in the surface sensible heat flux (Fig. 5a) than they did for the liquid water path. Whilst there is some hint towards the expected trend that models which are optically thickest (PALM, Meso-NH-c10) will generate a positive sensible heat flux and well-mixed fog layer first, RAMS-c10 sits as a clear outlier here generating the strongest positive sensible heat flux whilst having one of the thinnest (optically and physically) fog layers. It achieves this by forming a shallow but well-mixed layer in which the fog exists (Fig. 6a), capped by a strong inversion. RAMS does indeed have a higher downwelling LW radiation, which would promote development of a well-mixed fog layer. However, why it keeps this layer shallow and does not grow deeper like it does in Meso-NH is interesting, suggesting lower entrainment across the inversion. The result is that RAMS has the lowest fog top of all the LES models (Fig. 7a).

The SCMs show a similar trend to the LES models, with many producing a positive surface sensible heat flux and well-mixed boundary layer structure (Figs. 5c and 6b). However, those SCMs with close to zero sensible heat flux do maintain a stable potential temperature profile throughout the fog layer. As always, there are interesting outliers. The IFS in particular appears to manage a stable profile with a positive sensible heat flux. However, this is likely a consequence of the low vertical resolution as there are only two vertical levels within the fog layer at this stage, the first of which is well-mixed and the second is stabilised by cloud top entrainment. It is also worth discussing FV3-GFS, which is the only model which produces a negative sensible heat flux. This is possibly due to its poor vertical resolution, with the lowest model level being approximately double the height of any other model, meaning the lowest-level temperature is very warm relative to the surface. In its default set-up, FV3-GFS

also produced a very negative latent heat flux, which prevented any fog formation. Therefore a lower limit of zero on the latent heat flux was imposed in their simulations to enable fog to form.

### 3.3 Forecasting considerations

In terms of fog impact, particularly to the aviation sector, correctly modelling fog clearance after sunrise is key to forecasting airfield clearance time and allowing full take off/landing rates to resume. There are a number of aspects of the intercomparison which complicate the simulation of the morning transition. Firstly, the unrestricted evaporation is unrealistic for a true land surface – soil moisture availability and resistance to evapotranspiration in grass will always result in less latent heat flux than our idealised set-up will produce. Secondly, the observed surface temperature warming is representative of fog which has dissipated in reality for a number of reasons not simulated by the LES and SCMs (particularly overlying cloud cover, which is responsible for the observed increase in LWP after 08:00 UTC). However, comparison between how the models deal with this situation can still provide some useful insights. As shown in Fig. 1, MesoNH-LES is the only model which completely dissipates the fog during the morning. Most models' fog evolution seems broadly unaffected by the increasing surface temperature and short-wave radiation, except for SALSA, in which it drives a large increase in LWP. There are essentially two competing mechanisms at work here. The increase in surface temperature will drive a strong positive surface moisture flux, promoting fog development. However, direct short-wave heating of the fog layer and heating due to the rise in surface temperature and positive surface heat flux will counteract this. The consequences for fog development are therefore model dependent, based on the relative importance of these processes.

If the surface temperature was not prescribed, the key quantity driving dissipation would be the downwelling short-wave radiation (as this would drive the surface heating), which is shown in Fig. 8. The figure shows that the degree of variation between models is large (over  $250 \text{ W m}^{-2}$ ), with similar uncertainty between the LES and SCM models. To leading order, the key reason for differences in the downwelling short-wave (SW) is the LWP at sunrise – the models with the highest LWP have the lowest downwelling SW and vice versa. Optical properties of the fog appear to be much less significant here – for example comparing the UM and Meso-NH-c10 SCM simulations; Meso-NH-c10 only has a slightly smaller LWP, which offsets against its much smaller effective radius to result in almost identical downwelling SW evolution. What is clear is that there is a huge range in potential fog evolution and dissipation times driven by differences in the fog development during the night-time. Having knowledge of how realistic a model forecast of fog development through the night-time is (e.g. via real-time observations) may enable a forecaster to understand how reliable

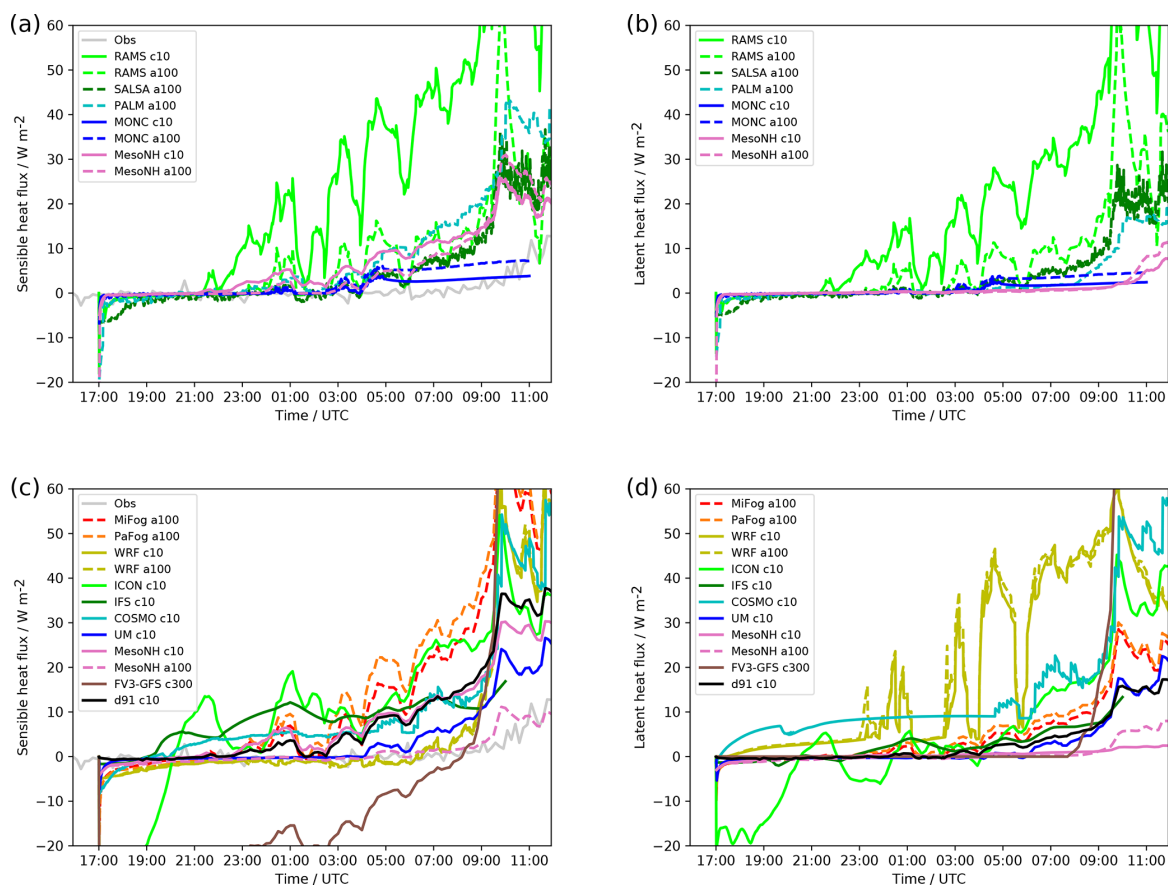


**Figure 5.** Sensible (a, c) and latent (b, d) heat flux observed and modelled by (a, b) low aerosol/CDNC LES and (c, d) low aerosol/CDNC SCMs.

the forecast for morning dissipation is. For example, real-time equivalents of many of the observations presented here, such as radiosonde profiles, liquid water path measurement, surface heat, moisture, and radiation fluxes, would enable a much better assessment of how the fog is developing than traditional screen-level observations can provide. A comparison of these to model diagnostics will enable an assessment of whether the model is over- or under-developing fog (optically or physically) and therefore whether it is likely to dissipate earlier or later in the morning than forecast.

Another forecasting consideration is whether the fog will indeed dissipate or whether it will lift into low stratus. In reality, this is governed by many factors not included in this intercomparison, such as non-local advective effects or overlying cloud cover. However, some features such as fog depth and entrainment at the fog top should be captured. Figure 9 shows the cloud base height ( $q_c > 0.01 \text{ g kg}^{-1}$ ) during the morning period for the LES and SCM models, demonstrating that there is significant variety in model simulation of this behaviour. Whilst most models keep the fog firmly on

or near the ground, Meso-NH LES and COSMO SCM lift the cloud base significantly, with cloud base height exceeding 60 m (the threshold typically used by aviation for instigating low-visibility procedures) by 08:00–09:00 UTC. The difference here (and elsewhere) between Meso-NH LES and SCM is of particular interest because the physics package of both models is identical, meaning that differences must arise because of the lower vertical resolution in SCM, or because the 1D parameterised turbulence in the SCM is acting differently to the 3D resolved turbulence in the LES. In general, the dissipation results appear much more closely tied to individual models rather than characteristics of the set-up or development of the fog during the night. All models which provide both interactive and non-interactive aerosol set-ups do the same thing in both set-ups, and whilst for most this is to not break the fog, for Meso-NH it is to lift the fog. Similarly, for models which produce excessive LWP during the night, most do not break it, whilst COSMO lifts it. A more focussed intercomparison on the dissipation phase is likely

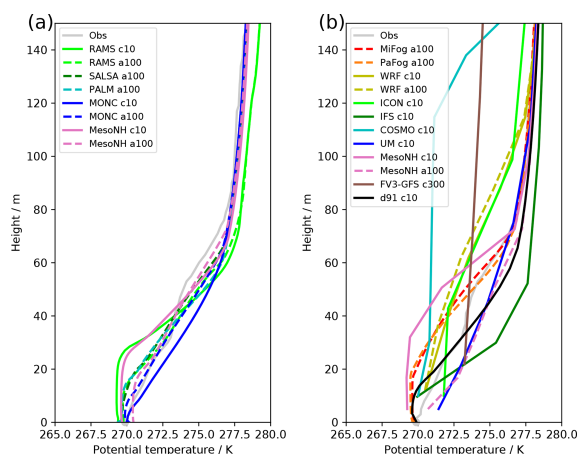


**Figure 6.** Potential temperature observed and simulated by (a) the low aerosol/CDNC LES models and (b) the low aerosol/CDNC SCMs at 00:00 UTC.

required to fully understand this model-dependent behaviour and link it to physical processes.

Finally, we discuss some of the typical metrics used by decision makers when forecasting fog events. Figure 10a shows the visibility as predicted by all models incorporating a visibility parameterisation. The visibility parameterisation is model dependent, with those used listed in Table 4. Some parameterisations utilise a direct empirical link between cloud water content and visibility, whilst others attempt to calculate the extinction coefficient directly based on the aerosol distribution and atmospheric humidity. Models for which the vertical resolution does not give a grid level at the screen-level height (1.5–3 m) either use values at the lowest model level (Table 4) or first produce input variables to the visibility parameterisation at this level via interpolation. Given the differences seen elsewhere in the fog evolution, the level of agreement between models here is somewhat surprising. Most models are forecasting visibility in the 100–300 m range for most of the night, in line with observations. IFS and PALM are forecasting slightly larger visibilities ( $\approx 500$  m) but still below the thresholds typically used by aviation decision makers (600 m), whilst only Meso-NH produces visibilities below 100 m. Most models also retain low visibilities well into the morning period, with only Meso-NH, IFS, and eventually the UM forecasting a clearance in this metric. The consistent behaviour may, in part, be due to the tight linkage between screen-level and surface variables in many models, as with the surface temperature prescribed, the screen-level temperature does not deviate far from the observations (Fig. 10b). However, it also raises caution against the use and interpretation of such variables if they can seemingly produce such similar results despite such obvious differences in the actual simulation of fog within the models. To truly understand and interpret an NWP fog forecast requires

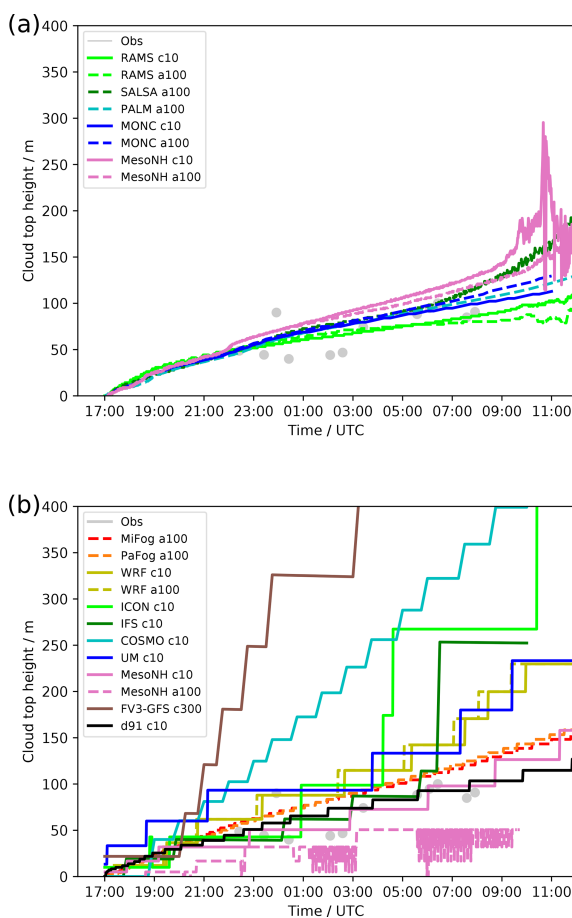


**Figure 7.** Fog top height observed and modelled by (a) low aerosol/CDNC LES and (b) low aerosol/CDNC SCMs.

much more than simply looking at the predicted visibility, especially in more marginal cases than this one.

Table 4 shows for all models the onset and dissipation time of the fog event and the maximum height reached by the fog layer. This summarises many of the themes discussed so far in the paper. The initiation of fog is handled well by all models, with the initiation happening between 17:00 and 18:00 UTC in all but two of the models. Many models show that low visibility (LVP) occurs some time after fog onset, demonstrating that the models are able to capture an initial period of thin fog where visibility remains good. The dissipation phase is much poorer, with most models persisting fog until the end of the simulation. Only a minority of models break the fog during the morning period and with no consistency in how this is done – some lifting it into stratus, whilst others clear it entirely. Whilst a few models do thin the fog sufficiently for LVP to end, it would clearly be very difficult to provide guidance to customers based on this ensemble set.

**Table 4.** Selected forecasting metrics for each model, as observed, and the mean and range of results for the LES and SCM models combined. Fog onset/dissipation is defined by liquid water below 60 m, whilst typical airfield low-visibility procedures (LVPs) are defined by visibility < 600 m and cloud base < 60 m. “> 12” denotes models which did not dissipate fog by the end of the simulation.

	Fog onset	LVP start	Fog dissipation	LVP end	Max fog top (m)	Visibility parameterisation
<b>Observations</b>		17:45		08:04	≈ 100 <sup>b</sup>	
MiFog SCM a100	17:00	17:11	> 12	> 12	153	Physical: Bott (2021)
PaFog SCM a100	17:15	18:25	> 12	> 12	159	Physical: Bott (2021)
WRF SCM c10	17:30		> 12		230	
WRF SCM a100	17:30		> 12		230	
RAMS LES c10	17:30		> 12		110	
RAMS LES a100	17:30		> 12		95	
ICON SCM c10	17:30	18:49	11:45	> 12	503	Empirical: Kunkel (1984)
IFS SCM c10	17:52	18:37	> 12	06:37	253	Physical <sup>c</sup> : Gultepe et al. (2006)
SALSA LES a100	17:10		> 12		196	
COSMO SCM c10	19:00		08:00		489	
PALM LES a100	17:00	19:09	> 12	> 12	130	Empirical: Gultepe et al. (2006)
UM SCM c10	17:01	18:41	> 12	11:08	233	Physical: Clark et al. (2008)
MONC LES c10	17:30		> 12		113	
MONC LES a100	17:30		> 12		129	
MesoNH SCM c10	17:15	17:15	> 12	09:19	158	Empirical <sup>c</sup> : Kunkel (1984)
MesoNH SCM a100	17:45	17:45	06:00	05:30	51	Physical <sup>c</sup> : similar to Bott (2021)
MesoNH LES c10	17:30		09:15		295	
MesoNH LES a100	17:30		08:45		271	
FV3-GFS SCM c300	20:15		> 12		622	
d91 SCM c10	17:04	17:10	> 12	> 12	127	Empirical: Kunkel (1984)
LES mean	17:23		09:00 <sup>a</sup>		167	
LES range	00:30		00:30 <sup>a</sup>		200	
SCM mean	17:44	17:59	08:35 <sup>a</sup>	08:08 <sup>a</sup>	267	
SCM range	03:15	01:39	05:45 <sup>a</sup>	05:38 <sup>a</sup>	571	

<sup>a</sup> Dissipation statistics are only calculated from the models which dissipated fog during the morning. <sup>b</sup> Recorded around 08:00 UTC just before the fog dissipated.

<sup>c</sup> Parameterisations are applied at the lowest model level (Table 3) rather than the screen level.

The mean fog depth simulated by the SCMs is approximately 100 m higher than that from the LES and at the very top end of the LES range. This is symptomatic of the SCM behaviour in producing fog which is too thick, a characteristic that will likely lead to fog persisting for too long into the daytime.

#### 4 Microphysics parameterisation sensitivity

To explore some of the themes and relationships shown in Sect. 3.1, in this section we focus on two SCMs (COSMO and UM) and one LES (MONC), modifying several parameterisations to confirm the speculated reasons for fog differences. The first and most simple test, using the UM, is to switch off cloud droplet sedimentation entirely (similar to COSMO, FV3-GFS, or IFS). This is shown in Fig. 11.

The removal of cloud droplet sedimentation leads to large increases in the liquid water path for both CDNC values. Clearly the presence or absence of cloud drop sedimentation is more important than the prescription of CDNC value. This also confirms why models which do not represent this process produce a fog layer which is too thick.

Whilst implementing cloud droplet sedimentation in models which do not have it is ultimately the most physically realistic way of improving fog simulation, we can also investigate, using COSMO, how simulations might be improved with the parameterisations at hand. The autoconversion in COSMO (Seifert and Beheng, 2001) is proportional to the 4th power of cloud water content and therefore produces very little autoconversion at low water contents. Reducing the power (to 3.1) allows the autoconversion rate to be increased at low water contents. As shown in Fig. 11, the consequence of this is a much improved fog simulation, again confirming that the rate of water loss from the atmosphere is the dominant mechanism governing the fog LWP. This also shows why IFS, which uses the autoconversion (power 2.47) of Khairoutdinov and Kogan (2000), is able to produce lower and more realistic LWP evolution without cloud droplet sedimentation. It is worth clarifying again that this is not a realistic model improvement we would suggest implementing – fog droplets are small, and the collision-coalescence process is rare; therefore autoconversion should not be happening.

For models which do simulate cloud droplet sedimentation, how sensitive is the fog development to the precise



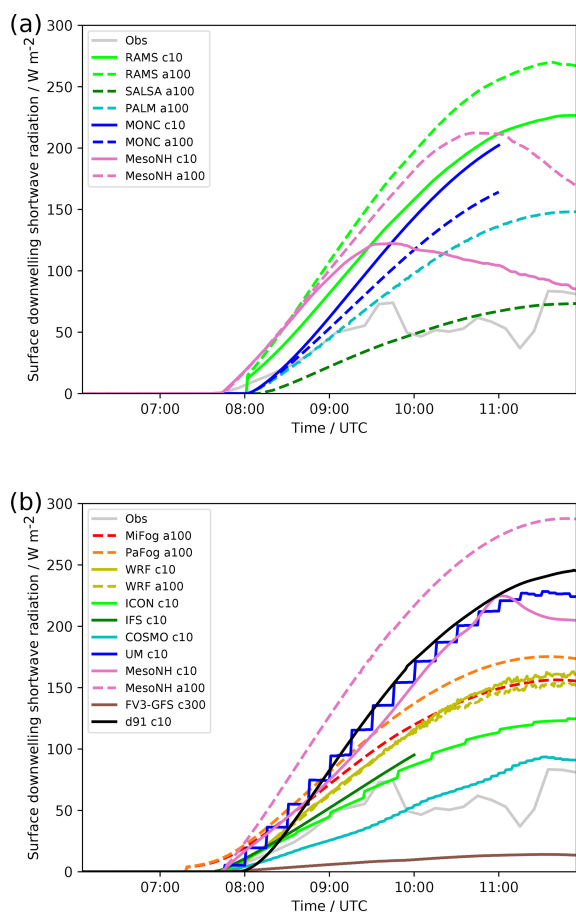


**Figure 8.** Surface downwelling short-wave radiation observed and modelled by (a) low aerosol/CDNC LES and (b) low aerosol/CDNC SCMs.

details of the parameterisation? This is explored with the MONC LES by varying the shape parameter,  $\mu$ , used in the cloud droplet size distribution:

$$N(D) = N_0 D^\mu e^{-\lambda D}, \quad (1)$$

where  $N$  is the number of drops of diameter  $D$ ,  $N_0$  is the intercept parameter, and  $\lambda$  is the slope parameter. Miles et al. (2000) have shown that  $\mu$  in the range 2–5 is most commonly found in stratiform clouds, but values in the range 0–25 have been found in observations. The default value used in MONC is  $\mu = 2.5$ , and Fig. 12 shows a sensitivity study varying  $\mu$  between 0 and 10.

Once again, this relatively minor change to part of the microphysical parameterisation can have a similar sized effect on fog evolution to the prescribed CDNC value, showing the importance of fundamental parameterisation development. It is also interesting to note that with the reduction of  $\mu$ , which increases droplet sedimentation rates, it is actually possible

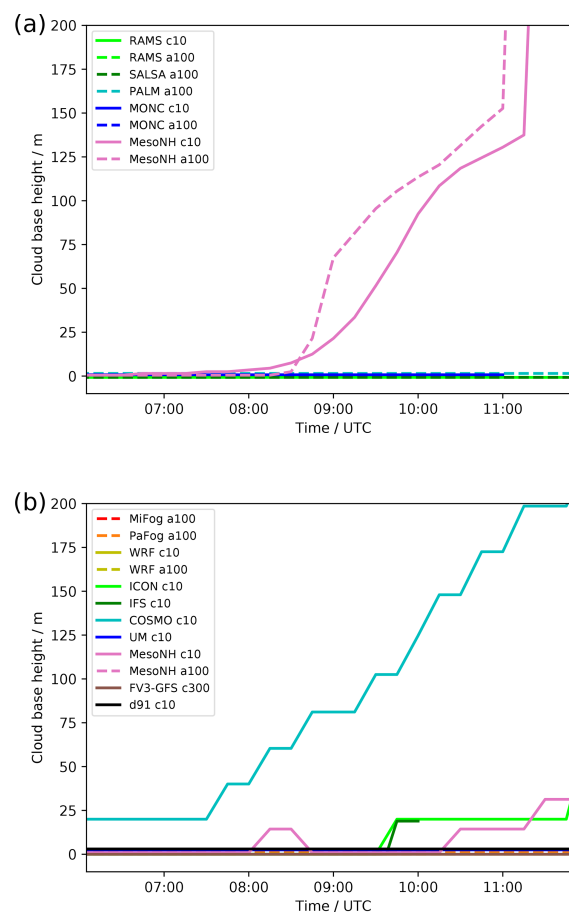


**Figure 9.** Cloud base height modelled by (a) low aerosol/CDNC LES and (b) low aerosol/CDNC SCMs.

to produce a fog layer which is too thin – no other model has shown this so far. This acts to highlight why even when all processes are represented within a model, large differences in fog evolution can still be seen because the fog evolution is so sensitive to small parameterisation changes.

This section has shown that even for a highly constrained scenario, the microphysics of fog remains a very uncertain process. We could, for example, recommend that future field campaigns focus on ascertaining with better accuracy the parameters of bulk microphysics parameterisations (for example  $\mu$ ). However, existing observations show that frequently size distributions are bimodal in nature (Wendisch et al., 1998; Price, 2011), and therefore we should question whether microphysics parameterisations imposing a Gamma distribution are even the appropriate tool for fog simulation. Bin microphysics parameterisations (such as that employed in SALSA or MiFog) offer a better ability to simulate the evolution of the size distribution, and certainly these models are among the best performing in this intercomparison.

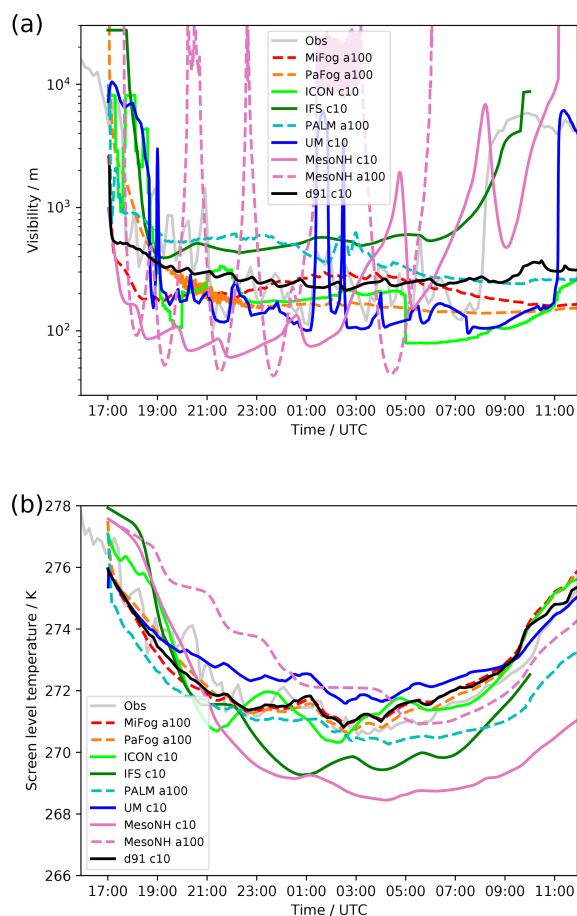


**Figure 10.** (a) Visibility and (b) screen level temperature, observed and predicted by all models including a specific visibility parameterisation.

Recently, Schwenkel and Maronga (2020) demonstrated the use of a Lagrangian cloud model (LCM) for fog simulation and found (consistent with this work) that the LCM tended to produce greater sedimentation rates and lower liquid water paths than a bulk scheme due to its evolution of the size distribution. However, bin schemes and LCMs are likely to be prohibitively expensive for operational implementation, and therefore how to best represent this behaviour in operational models remains an open question. They also contain many more degrees of freedom, and thus it is important that future observational campaigns focus not just on the mean value of microphysical parameters but also the time and space variability of the full size distribution to allow accurate evaluation of bin schemes and LCMs.

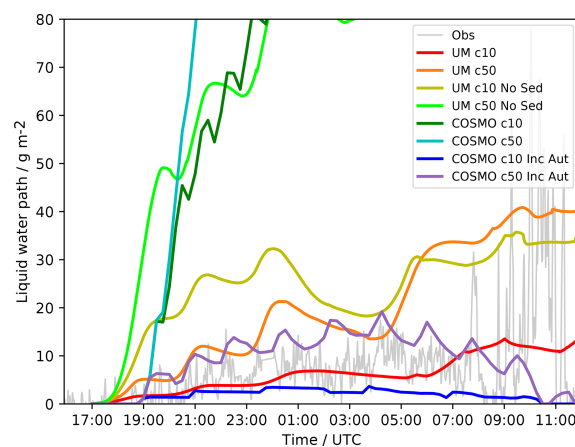


**Figure 11.** Liquid water path observed and modelled with low and high CDNC values, from the UM with or without cloud droplet sedimentation and COSMO with low and high autoconversion rates (see caption).

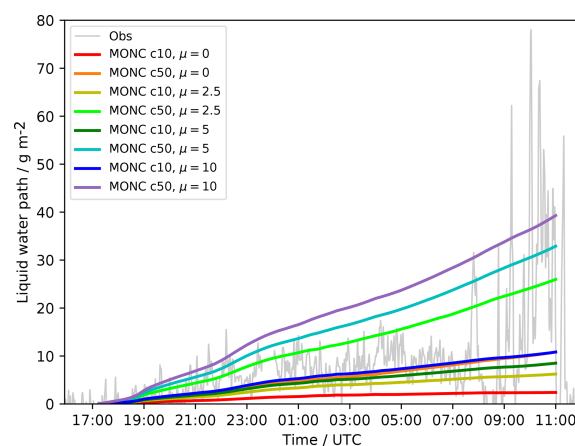


**Figure 12.** Liquid water path observed and modelled by MONC with low and high CDNC values, with varied values of the shape parameter  $\mu$  (see caption).

## 5 Conclusions

If nothing else, this paper has highlighted why fog remains such a difficult forecasting challenge. The level of comparability between our most detailed process models – LES – is much lower than has been seen in previous intercomparison studies of other boundary-layer or cloud regimes (Beare et al., 2006; van der Dussen et al., 2013). This is largely due to the huge role microphysics plays in fog development and uncertainties inherent in the representation of a process which is still entirely parameterised in LES. However, there were also strong differences seen in the surface fluxes and turbulent structure within the LES models. Whilst through-

out the bulk of the fog layer the simulations were well enough resolved, near the surface the sub-filter-scale flux clearly becomes dominant and provides an additional source of uncertainty not seen with higher-level clouds. This effectively means that LES cannot be considered an adequate baseline (or truth) against which to compare NWP models. Therefore our first recommendation must be for continued investment in observational understanding of real fog events, particularly to understand the high-frequency (in time and space) variability that exists in fog. This must be linked to continued development of LES models to a state at which they can provide an adequate substitute for real observations.

For the SCMs, it is clear that improvements have been made since the previous intercomparison of Bergot et al. (2007) as a very good consistency between models in the fog onset phase was achieved. However, after onset the NWP SCMs are of highly variable quality, but there appears to be a general trend for the overdevelopment of fog; i.e. models produce fog which is too physically and optically thick, too quickly. There are some simple improvements (such as the inclusion of cloud droplet sedimentation) which should be applied to some models, but further improvements could require some significant parameterisation development. This work has given some guidance as to where that work should be focussed as we have shown that fundamental parameterisations (such as cloud microphysics) are as uncertain and important in simulating fog development as implementing new feedback processes (such as aerosol interaction). However, there are still fundamental questions on the interaction between cloud, radiation, and turbulence in fog which require further investigation. Additionally, these conclusions are only drawn for a single case, and therefore it is important to continue the intercomparison of models on a wider range of cases, in different geographic locations, and with different forcings.

Regarding forecasting applications, this work has shown that the early stages of fog development crucially impact its decay phase the following morning. This suggests that if real-time comparison of NWP forecast to observations can be conducted during the night-time, it could be used to help determine how accurate the NWP dissipation forecasts will be, allowing them to be manually adapted to give the best guidance to customers. Success has been seen with techniques like this in the past (Bergot, 2007), and with new and emerging observational platforms (such as UAVs), more detailed measurements of the fog properties (e.g. real-time droplet spectra) could further improve customer guidance.

**Data availability.** The data are available from the authors upon request.

**Author contributions.** IB analysed the submitted results and wrote the manuscript. IB, WA, RB, AB, LD, RF, TG, EG, AH, AI, IK, JoS, and GJS ran the model simulations. All authors contributed to the discussion, understanding and presentation of results, as well as the preparation of the manuscript.

**Competing interests.** The contact author has declared that neither they nor their co-authors have any competing interests.

**Disclaimer.** Publisher's note: Copernicus Publications remains neutral with regard to jurisdictional claims in published maps and institutional affiliations.

**Acknowledgements.** Wayne Angevine thanks Greg Thompson of NCAR for help in understanding and setting parameters in the Thompson microphysics schemes in WRF.

**Financial support.** Juerg Schmidli was supported by the Hans Ertel Centre for Weather Research of DWD (The Atmospheric Boundary Layer in Numerical Weather Prediction) grant number 4818DWDP4. Ritthik Bhattacharya was supported by MeteoSwiss (project number 123001738). This work used resources of the Deutsches Klimarechenzentrum (DKRZ) granted by its Scientific Steering Committee (WLA) under project ID bb1096. Innocent Kudzotsa and Sami Romakkaniemi were supported by the Horizon 2020 Research and Innovation Programme (grant no. 821205). Johannes Schwenkel was supported by the German Research Foundation (grant no. MA 6383/1-2).

**Review statement.** This paper was edited by Johannes Quaas and reviewed by Robert Tardif and one anonymous referee.

## References

- Ahlgrimm, M. and Forbes, R.: Improving the representation of low clouds and drizzle in the ECMWF model based on ARM observations from the Azores, *Mon. Weather Rev.*, 142, 668–685, 2014.
- Angevine, W. M., Olson, J., Kenyon, J., Gustafson, W. I., Endo, S., Suselj, K., and Turner, D. D.: Shallow Cumulus in WRF Parameterizations Evaluated against LASSO Large-Eddy Simulations, *Mon. Weather Rev.*, 146, 4303–4322, <https://doi.org/10.1175/MWR-D-18-0115.1>, 2018.
- Baldauf, M., Seifert, A., Förstner, J., Majewski, D., Raschendorfer, M., and Reinhardt, T.: Operational Convective-Scale Numerical Weather Prediction with the COSMO Model: Description and Sensitivities, *Mon. Weather Rev.*, 139, 3887–3905, <https://doi.org/10.1175/MWR-D-10-05013.1>, 2011.
- Bašták Ďurán, I., Köhler, M., Eichhorn-Müller, A., Maurer, V., Schmidli, J., Schomburg, A., Klocke, D., Göcke, T., Schäfer, S., Schlemmer, L., and Dewani, N.: The ICON Single-Column Mode, *Atmosphere*, 12, 906, <https://doi.org/10.3390/atmos12070906>, 2021.



- Beare, R. J., MacVean, M. K., Holtslag, A. A. M., Cuxart, J., Esau, I., Golaz, J.-C., Jimenez, M. A., Khairoutdinov, M., Kosovic, B., Lewellen, D., Lund, T. S., Lundquist, J. K., McCabe, A., Moene, A. F., Noh, Y., Raasch, S., and Sullivan, P.: An Intercomparison of Large-Eddy Simulations of the Stable Boundary Layer, *Bound.-Lay. Meteorol.*, 118, 247–272, <https://doi.org/10.1007/s10546-004-2820-6>, 2006.
- Bergot, T.: Quality assessment of the Cobel-Isba numerical forecast system of fog and low clouds, *Pure Appl. Geophys.*, 164, 1265–1282, [https://doi.org/10.1007/978-3-7643-8419-7\\_10](https://doi.org/10.1007/978-3-7643-8419-7_10), 2007.
- Bergot, T., Terradellas, E., Cuxart, J., Mira, A., Liechti, O., Mueller, M., and Nielsen, N. W.: Intercomparison of Single-Column Numerical Models for the Prediction of Radiation Fog, *J. Appl. Meteorol. Climatol.*, 46, 504–521, <https://doi.org/10.1175/JAM2475.1>, 2007.
- Bott, A.: Comparison of a spectral microphysics and a two-moment cloud scheme: Numerical simulation of a radiation fog event, *Atmos. Res.*, 262, 105787, <https://doi.org/10.1016/j.atmosres.2021.105787>, 2021.
- Bott, A. and Trautmann, T.: PAFOG – a new efficient forecast model of radiation fog and low-level stratiform clouds, *Atmos. Res.*, 64, 191–203, [https://doi.org/10.1016/S0169-8095\(02\)00091-1](https://doi.org/10.1016/S0169-8095(02)00091-1), 2002.
- Bott, A., Sievers, U., and Zdankowski, W.: A Radiation Fog Model with a Detailed Treatment of the Interaction between Radiative Transfer and Fog Microphysics, *J. Atmos. Sci.*, 47, 2153–2166, [https://doi.org/10.1175/1520-0469\(1990\)047<2153:ARFMWA>2.0.CO;2](https://doi.org/10.1175/1520-0469(1990)047<2153:ARFMWA>2.0.CO;2), 1990.
- Boutle, I., Price, J., Kudzotsa, I., Kokkola, H., and Romakkaniemi, S.: Aerosol–fog interaction and the transition to well-mixed radiation fog, *Atmos. Chem. Phys.*, 18, 7827–7840, <https://doi.org/10.5194/acp-18-7827-2018>, 2018.
- Bush, M., Allen, T., Bain, C., Boutle, I., Edwards, J., Finnenkoetter, A., Franklin, C., Hanley, K., Lean, H., Lock, A., Manners, J., Mittermaier, M., Morcrette, C., North, R., Petch, J., Short, C., Vosper, S., Walters, D., Webster, S., Weeks, M., Wilkinson, J., Wood, N., and Zerroukat, M.: The first Met Office Unified Model–JULES Regional Atmosphere and Land configuration, *RAL1, Geosci. Model Dev.*, 13, 1999–2029, <https://doi.org/10.5194/gmd-13-1999-2020>, 2020.
- Buzzi, M., Rotach, M. W., Holtslag, M., and Holtslag, A. A.: Evaluation of the COSMO-SC turbulence scheme in a shear-driven stable boundary layer, *Meteor. Z.*, 20, 335–350, <https://doi.org/10.1127/0941-2948/2011/0050>, 2011.
- Clark, P. A., Harcourt, S. A., Macpherson, B., Mathison, C. T., Cusack, S., and Naylor, M.: Prediction of visibility and aerosol within the operational Met Office Unified Model. I: Model formulation and variational assimilation, *Q. J. Roy. Meteorol. Soc.*, 134, 1801–1816, <https://doi.org/10.1002/qj.318>, 2008.
- Cook, A. J. and Tanner, G.: The cost of passenger delay to airlines in Europe – consultation document, available at: <https://westminsterresearch.westminster.ac.uk/item/q4qq5/the-cost-of-passenger-delay-to-airlines-in-europe-consultation-document> (last access: 1 January 2022), 2015.
- Cotton, W. R., Pielke Sr., R. A., Walko, R. L., Liston, G. E., Tremback, C. J., Jiang, H., McAnelly, R. L., Harrington, J. Y., Nicholls, M. E., Carrio, G. G., and McFadden, J. P.: RAMS 2001: Current status and future directions, *Meteorol. Atmos. Phys.*, 82, 5–29, <https://doi.org/10.1007/s00703-001-0584-9>, 2003.
- Cuxart, J., Holtslag, A. A. M., Beare, R. J., Bazile, E., Beljaars, A., Cheng, A., Conangla, L., Ek, M., Freedman, F., Hamdi, R., Kerstein, A., Kitagawa, H., Lenderink, G., Lewellen, D., Mailhot, J., Mauritsen, T., Perov, V., Schayes, G., Steeneveld, G.-J., Svensson, G., Taylor, P., Weng, W., Wunsch, S., and Xu, K.-M.: Single-Column Model Intercomparison for a Stably Stratified Atmospheric Boundary Layer, *Bound.-Lay. Meteorol.*, 118, 273–303, <https://doi.org/10.1007/s10546-005-3780-1>, 2006.
- Dearden, C., Hill, A., Coe, H., and Choullarton, T.: The role of droplet sedimentation in the evolution of low-level clouds over southern West Africa, *Atmos. Chem. Phys.*, 18, 14253–14269, <https://doi.org/10.5194/acp-18-14253-2018>, 2018.
- Duynkerke, P. G.: Radiation Fog: A Comparison of Model Simulation with Detailed Observations, *Mon. Weather Rev.*, 119, 324–341, [https://doi.org/10.1175/1520-0493\(1991\)119<0324:RFACOM>2.0.CO;2](https://doi.org/10.1175/1520-0493(1991)119<0324:RFACOM>2.0.CO;2), 1991.
- Firl, G., Carson, L., Bernardet, L., Heinzeller, D., and Harrold, M.: Common Community Physics Package Single Column Model v4.0 User and Technical Guide, available at: <https://dtcenter.org/GMTB/v4.0/scm-ccpp-guide-v4.pdf> (last access: 1 January 2022), 2020.
- Gultepe, I., Muller, M. D., and Boybeyi, Z.: A New Visibility Parameterization for Warm-Fog Applications in Numerical Weather Prediction Models, *J. Appl. Meteorol. Climatol.*, 45, 1469–1480, <https://doi.org/10.1175/JAM2423.1>, 2006.
- Gultepe, I., Sharman, R., Williams, P. D., Zhou, B., Ellrod, G., Minnis, P., Trier, S., Griffin, S., Yum, S. S., Gharabaghi, B., Feltz, W., Temimi, M., Pu, Z., Storer, L. N., Kneringer, P., Weston, M. J., Chuang, H.-y., Thobois, L., Dimri, A. P., Dietz, S. J., Franca, G. B., Almeida, M. V., and Neto, F. L. A.: A Review of High Impact Weather for Aviation Meteorology, *Pure Appl. Geophys.*, 176, 1869–1921, <https://doi.org/10.1007/s00024-019-02168-6>, 2019.
- Hewson, T.: Use and Verification of ECMWF Products in Member and Co-operating States (2018), ECMWF Technical Memoranda, <https://doi.org/10.21957/jgz6nh0uc>, 2019.
- Hill, A. A., Shipway, B. J., and Boutle, I. A.: How sensitive are aerosol-precipitation interactions to the warm rain representation?, *J. Adv. Model. Earth Syst.*, 7, 987–1004, <https://doi.org/10.1002/2014MS000422>, 2015.
- Khairoutdinov, M. and Kogan, Y.: A New Cloud Physics Parameterization in a Large-Eddy Simulation Model of Marine Stratocumulus, *Mon. Weather Rev.*, 128, 229–243, 2000.
- Kulkarni, R., Jenamani, R. K., Pithani, P., Konwar, M., Nigam, N., and Ghude, S. D.: Loss to Aviation Economy Due to Winter Fog in New Delhi during the Winter of 2011–2016, *Atmosphere*, 10, 198, <https://doi.org/10.3390/atmos10040198>, 2019.
- Kunkel, B. A.: Parameterization of Droplet Terminal Velocity and Extinction Coefficient in Fog Models, *J. Appl. Meteorol. Climatol.*, 23, 34–41, [https://doi.org/10.1175/1520-0450\(1984\)023<0034:PODTVA>2.0.CO;2](https://doi.org/10.1175/1520-0450(1984)023<0034:PODTVA>2.0.CO;2), 1984.
- Lac, C., Chaboureaud, J.-P., Masson, V., Pinty, J.-P., Tulet, P., Escobar, J., Leriche, M., Barthe, C., Aouizerats, B., Augros, C., Aumond, P., Auguste, F., Bechtold, P., Berthet, S., Bielli, S., Bosseur, F., Caumont, O., Cohard, J.-M., Colin, J., Couvreux, F., Cuxart, J., Delautier, G., Dauhut, T., Ducrocq, V., Filippi, J.-B., Gazen, D., Geoffroy, O., Gheusi, F., Honnert, R., Lafore, J.-P., Lebeaupin Brossier, C., Libois, Q., Lunet, T., Mari, C., Maric, T., Mascart, P., Mogé, M., Molinié, G., Nuissier, O., Pan-

- tillon, F., Peyrillé, P., Pergaud, J., Perraud, E., Pianezze, J., Redelsperger, J.-L., Ricard, D., Richard, E., Riette, S., Rodier, Q., Schoetter, R., Seyfried, L., Stein, J., Suhre, K., Taufour, M., Thouron, O., Turner, S., Verrelle, A., Vié, B., Visentin, F., Vionnet, V., and Wautelet, P.: Overview of the Meso-NH model version 5.4 and its applications, *Geosci. Model Dev.*, 11, 1929–1969, <https://doi.org/10.5194/gmd-11-1929-2018>, 2018.
- Leung, A. C. W., Gough, W. A., and Butler, K. A.: Changes in Fog, Ice Fog, and Low Visibility in the Hudson Bay Region: Impacts on Aviation, *Atmosphere*, 11, 186, <https://doi.org/10.3390/atmos11020186>, 2020.
- Maronga, B., Banzhaf, S., Burmeister, C., Esch, T., Forkel, R., Fröhlich, D., Fuka, V., Gehrke, K. F., Geletič, J., Giersch, S., Gronemeier, T., Groß, G., Heldens, W., Hellsten, A., Hoffmann, F., Inagaki, A., Kadasch, E., Kanani-Sühring, F., Ketelsen, K., Khan, B. A., Knigge, C., Knoop, H., Krč, P., Kurppa, M., Maamari, H., Matzarakis, A., Mauder, M., Pallasch, M., Pavlik, D., Pfafferoth, J., Resler, J., Rissmann, S., Russo, E., Salim, M., Schrempf, M., Schwenkel, J., Seckmeyer, G., Schubert, S., Sühring, M., von Tils, R., Vollmer, L., Ward, S., Witha, B., Wurps, H., Zeidler, J., and Raasch, S.: Overview of the PALM model system 6.0, *Geosci. Model Dev.*, 13, 1335–1372, <https://doi.org/10.5194/gmd-13-1335-2020>, 2020.
- Martin, G. M., Johnson, D. W., and Spice, A.: The Measurement and Parameterization of Effective Radius of Droplets in Warm Stratocumulus Clouds, *J. Atmos. Sci.*, 51, 1823–1842, [https://doi.org/10.1175/1520-0469\(1994\)051<1823:TMAPOE>2.0.CO;2](https://doi.org/10.1175/1520-0469(1994)051<1823:TMAPOE>2.0.CO;2), 1994.
- Miles, N. L., Verlinde, J., and Clothiaux, E. E.: Cloud Droplet Size Distributions in Low-Level Stratiform Clouds, *J. Atmos. Sci.*, 57, 295–311, [https://doi.org/10.1175/1520-0469\(2000\)057<0295:CDSIDL>2.0.CO;2](https://doi.org/10.1175/1520-0469(2000)057<0295:CDSIDL>2.0.CO;2), 2000.
- Neggers, R. A. J., Ackerman, A. S., Angevine, W. M., Basile, E., Beau, I., Blossey, P. N., Boutle, I. A., de Bruijn, C., Cheng, A., van der Dussen, J., Fletcher, J., dal Gesso, S., Jam, A., Kawai, H., Kumar, S., Larson, V. E., Lefebvre, M.-P., Lock, A. P., Meyer, N. R., de Roode, S. R., de Rooy, W., Sandu, I., Xiao, H., and Xu, K.-M.: Single-column model simulations of subtropical marine boundary-layer cloud transitions under weakening inversions, *J. Adv. Model. Earth Syst.*, 9, 2385–2412, <https://doi.org/10.1002/2017MS001064>, 2017.
- Price, J.: Radiation Fog. Part I: Observations of Stability and Drop Size Distributions, *Bound.-Lay. Meteorol.*, 139, 167–191, <https://doi.org/10.1007/s10546-010-9580-2>, 2011.
- Price, J., Lane, S., Boutle, I., Smith, D., Bergot, T., Lac, C., Duconge, L., McGregor, J., Kerr-Munslow, A., Pickering, M., and Clark, R.: LANFEX: a field and modelling study to improve our understanding and forecasting of radiation fog, *Bull. Amer. Meteor. Soc.*, 99, 2061–2077, <https://doi.org/10.1175/BAMS-D-16-0299.1>, 2018.
- Schwenkel, J. and Maronga, B.: Towards a Better Representation of Fog Microphysics in Large-Eddy Simulations Based on an Embedded Lagrangian Cloud Model, *Atmosphere*, 11, 466, <https://doi.org/10.3390/atmos11050466>, 2020.
- Seifert, A. and Beheng, K. D.: A double-moment parameterization for simulating autoconversion, accretion and selfcollection, *Atmos. Res.*, 59–60, 265–281, [https://doi.org/10.1016/S0169-8095\(01\)00126-0](https://doi.org/10.1016/S0169-8095(01)00126-0), 2001.
- Tardif, R.: The Impact of Vertical Resolution in the Explicit Numerical Forecasting of Radiation Fog: A Case Study, *Pure Appl. Geophys.*, 164, 1221–1240, <https://doi.org/10.1007/s00024-007-0216-5>, 2007.
- Tonttila, J., Maalick, Z., Raatikainen, T., Kokkola, H., Kühn, T., and Romakkaniemi, S.: UCLALES–SALSA v1.0: a large-eddy model with interactive sectional microphysics for aerosol, clouds and precipitation, *Geosci. Model Dev.*, 10, 169–188, <https://doi.org/10.5194/gmd-10-169-2017>, 2017.
- van der Dussen, J. J., de Roode, S. R., Ackerman, A. S., Blossey, P. N., Bretherton, C. S., Kurowski, M. J., Lock, A. P., Neggers, R. A. J., Sandu, I., and Siebesma, A. P.: The GASS/EUCLIPSE model intercomparison of the stratocumulus transition as observed during ASTEX: LES results, *J. Adv. Model. Earth Syst.*, 5, 483–499, <https://doi.org/10.1002/jame.20033>, 2013.
- Vié, B., Ducongé, L., Lac, C., Bergot, T., and Price, J.: LES simulations of LANFEX IOPI radiative fog event: prognostic vs. diagnostic supersaturation for CCN activation, *Q. J. Roy. Meteorol. Soc.*, in preparation, 2022.
- Wendisch, M., Mertes, S., Heintzenberg, J., Wiedensohler, A., Schell, D., Wobrock, W., Frank, G., Martinsson, B. G., Fuzzi, S., Orsi, G., Kos, G., and Berner, A.: Drop size distribution and LWC in Po Valley fog, *Contr. Atmos. Phys.*, 71, 87–100, 1998.

## **6 On the effect of nocturnal radiation fog on the development of the daytime convective boundary layer: A large-eddy simulation study**

### **6.1 Declaration of Contributions**

The numerical experiments were jointly designed by J. Schwenkel and B. Maronga. J. Schwenkel had the general idea for the process-analysis. J. Schwenkel was responsible for conception and realization, conducted the simulations and performed the data analysis. Results were jointly discussed by J. Schwenkel and B. Maronga. J. Schwenkel prepared the paper, with significant contributions by B. Maronga. In the role as reviewer the comments of Marie Mazoyer and Christine Lac helped to improve the final version of the manuscript.

### **6.2 Research Article**

©The authors 2022. CC BY 4.0 License

## RESEARCH ARTICLE

# On the effect of nocturnal radiation fog on the development of the daytime convective boundary layer: A large-eddy simulation study

Johannes Schwenkel<sup>1</sup>  | Björn Maronga<sup>1,2</sup>

<sup>1</sup>Institute of Meteorology and  
Climatology, Leibniz University  
Hannover, Hannover, Germany

<sup>2</sup>Geophysical Institute, University of  
Bergen, Bergen, Norway

**Correspondence**

J. Schwenkel, Institute of Meteorology  
and Climatology, Leibniz University  
Hannover, Hannover, Germany.

Email:

[schwenkel@meteo.uni-hannover.de](mailto:schwenkel@meteo.uni-hannover.de)

**Funding information**

German Research Foundation,  
Grant/Award Number: MA 6383/1-2

**Abstract**

The potential effect of failing to predict nocturnal deep radiation fog on the development of the daytime convective boundary layer (CBL) is studied using large-eddy simulations. Typical spring and autumn conditions for the mid-latitudes are used to perform simulations in pairs. Fog formation is allowed in one simulation of each pair (nocturnal fog [NF]) and is suppressed in the other (clear sky [CS]). This allows for the identification of properties (temperature, humidity, boundary-layer depth), conditions, and processes in CBL development that are affected by fog. Mixing-layer temperatures and boundary-layer depths immediately after fog dissipation in CSs are shown to be up to 2.5 K warmer and 200 m higher, respectively, than the NF counterparts. Additionally, greater water vapor mixing ratios are found in the CSs. However, owing to greater temperatures, relative humidities at the CBL top are found to be less in CSs than in the corresponding NFs. This relative humidity difference might be an indication that cloud formation is suppressed to some extent. The magnitude of the differences between CSs and NFs during the day is mainly correlated to the fog depth (in terms of duration and liquid water path), whereas the key processes responsible for differences are the atmospheric long-wave cooling of the fog layer (for temperature development) and droplet deposition (for water vapor mixing ratio development).

**KEYWORDS**

boundary-layer development, diurnal cycle, large-eddy simulation, misrepresenting fog, PALM, radiation fog, turbulence

## 1 | MOTIVATION

Fog is a cloud in the vicinity of the Earth's surface characterized by a reduction of visibility to less than 1 km. Despite the rather small vertical extent, low wind speeds and

negligible amount of precipitation compared with other clouds, fog still poses a threat to human life, especially in transportation (Haeffelin *et al.*, 2010). Fundamental and applied research have significantly improved fog forecasts and contributed to a broader and deeper understanding of

This is an open access article under the terms of the Creative Commons Attribution-NonCommercial-NoDerivs License, which permits use and distribution in any medium, provided the original work is properly cited, the use is non-commercial and no modifications or adaptations are made.

© 2022 The Authors. *Quarterly Journal of the Royal Meteorological Society* published by John Wiley & Sons Ltd on behalf of the Royal Meteorological Society.

fog at the process level in the last decades. However, common numerical weather prediction (NWP) models still fail to predict a significant amount of fog events (Steenefeld *et al.*, 2015). Radiation fog is the most common continental fog type (e.g., Bergot, 2013). The misrepresentation of the life cycle of this type of fog (i.e., its onset, depth, and dissipation), as well as a lack of representation in NWP models, can be caused by several factors. A number of complex, small-scale processes (such as turbulent mixing, land–atmosphere interactions, aerosol and cloud microphysics, and radiation) that interact on different scales must be resolved or parametrized correctly (Steenefeld *et al.*, 2015). Likewise, the atmospheric conditions must be known precisely, because fog formation is sensitive to changes in temperature, humidity or soil moisture. An incorrect representation of subtle supersaturations could be generated from even small deviations in the forcing data and fog might fail to be predicted accurately (Rémy and Bergot, 2009). Capturing small-scale processes and precisely representing multilayered forcing data are hampered by the relatively large grid spacing commonly used in NWP.

Apart from the hazards associated with it, the presence of deep fog significantly alters the properties of the nocturnal boundary layer (NBL). The NBL is typically characterized by a stable stratification and weak forcings. These characteristics result in low or sometimes intermittent turbulence (Fernando and Weil, 2010). In contrast, convection can be triggered in the NBL by deep fog because the fog layer is optically thick to long-wave radiation; the atmosphere is destabilized from above because the net radiative loss occurs at the top of the fog (e.g., Nakanishi, 2000). Because of this energy loss, the sign of the turbulent sensible surface heat flux (SHF) is the opposite of what would typically be expected in the stable-stratified NBL and increased turbulence is produced. Therefore, differences between the stable NBL (SNBL) and foggy NBL might be caused by diabatic processes, such as modified long-wave cooling, short-wave absorption, turbulent mixing and entrainment, reduction of the total water content through droplet settling, and modified dewfall. Although the SNBL is quickly transformed into a convective boundary layer (CBL) after sunrise, the daytime convection might be influenced by the propagation of NBL properties into the day (Vilà-Guerau de Arellano, 2007).

In a previous study, van Stratum and Stevens (2015) found that the error resulting from misrepresenting the dry summertime SNBL (due to too coarse grid spacings) in large-eddy simulations (LESs) has a negligible influence on the daytime convection and bulk properties of the CBL. In a follow-up study by van Stratum and Stevens (2018), it was shown using a conceptual model that, even when humidity and radiation are accounted for, it is

unlikely that fog or low clouds are formed during the night as a consequence of the overestimation of vertical mixing. The influence of non-resolved fog (assuming a maximum vertical extent of 50 m) for the summertime CBL development was also evaluated in their study as rather small. However, these studies were designed to discover if daytime convection is significantly influenced by the usage of low-resolution LESs, which the SNBL is not correctly resolved with. In addition to insufficient grid spacings, there are numerous other reasons for nocturnal fog to be misrepresented (e.g., inappropriate microphysical parametrization, errors in the initial conditions). Recently, it was shown in the model intercomparison of Boutle *et al.* (2022) that even sophisticated models revealed a large spread in simulating fog characteristics. Smith *et al.* (2018) demonstrated that, beyond model inefficiencies, subtle changes in humidity in the residual layer and wind-driven vertical mixing can have a significant impact on the development of radiation fog. Thus, this study is meant to complement the valuable results of van Stratum and Stevens (2018) by evaluating the physical effect of nocturnal fog on CBL development. Unlike van Stratum and Stevens (2015), the van Stratum and Stevens (2018) meteorological conditions for the transition months are applied because such conditions are more typical for nocturnal fog in the midlatitudes (Izett *et al.*, 2019). Spring and autumn conditions in the midlatitudes are associated with weaker incoming solar radiation to dissipate the fog layer after sunrise. An inadequate representation of such conditions is hence more likely to cause a stronger effect on CBL development.

In this article, the following questions will be answered:

1. What are the effects of nocturnal radiation fog on the development of the daytime CBL?
2. How long do these effects persist?
3. Which conditions and parameters amplify or reduce the influence of fog on CBL development?
4. What processes are responsible for differences observed?

To answer these questions, idealized LESs are performed in pairs (with and without fog formation possible). The diurnal cycle of a typical fog event observed at Cabauw (Netherlands) is modeled in the simulations. Radiative conditions between February and April are used. With the help of LESs, the diurnal cycle and the physical processes within the boundary layer (BL) can be modeled realistically and are less dependent on parametrizations compared to one-dimensional approaches.

Unfortunately, to examine the entire parameter space and obtain conclusions for all conceivable meteorological

situations prone to fog formation would be computationally uneconomical and, therefore, beyond the scope of this study. The objective of this work is rather to provide a quantitative estimate of the possible errors in simulating the daytime CBL properties induced by the absence of a deep fog event during night. Hence, our study is limited to one (but representative for typical local radiation fog) case setup, neglecting surface heterogeneities, trees, and orography. Moreover, we confine the cases investigated to situations with a deep nocturnal radiation fog that completely dissipates after sunrise. Thus, to investigate the influence of a fog layer that turns into a long-lasting stratus deck after dissipation is beyond the scope of this article.

The article is structured as follows: Background on the LES model and the setup of the numerical experiments used in this study are provided in Section 2. The results of the numerical experiments are presented in Section 3. Finally, a discussion and conclusion of this study is provided in Section 4.

## 2 | METHODOLOGY

### 2.1 | Model

In this study we use the PALM model system 6.0 (revision 4792) (Maronga *et al.*, 2020a). The model core is based on the incompressible Boussinesq-approximated Navier–Stokes equations, prognostic equations for potential temperature, and the total water mixing ratio. Discretization in space and time on the Cartesian grid is achieved by finite differences using a fifth-order advection scheme after Wicker and Skamarock (2002) and a third-order Runge–Kutta time-stepping scheme (Williamson, 1980), respectively. For the non-resolved eddies, a 1.5-order flux-gradient subgrid closure scheme after Deardorff (1980) is applied, which includes the solution of an additional prognostic equation for the subgrid-scale turbulence kinetic energy. The influence of different subgrid-scale models is discussed in Maronga and Li (2022).

Moreover, using embedded models considering land-surface interactions, radiative transfer, and cloud microphysics, as well as the interactions among the model parts, PALM has the ability to cover the most important physical processes involved in fog development and the diurnal cycle. The land-surface model (LSM) consists of an energy balance solver for the skin temperature  $T_0$  and a multilayer soil model, predicting the soil temperature and the soil moisture content. A rigorous description and evaluation of the PALM's LSM implementation are given by Gehrke *et al.* (2021). A coupling of the Rapid Radiation Transfer Model for Global Models (RRTMG) (Clough

*et al.*, 2005) to PALM achieves the radiative transfer (in one-dimensional mode) for each vertical grid column. In particular, RRTMG calculates the radiative fluxes (short wave and long wave) for each grid volume while considering profiles of pressure, temperature, humidity, liquid water, and effective droplet radius. Three-dimensional radiation effects are neglected. Prognostic equations for the cloud droplet number concentration and cloud water mixing ratio as well as all cloud microphysical processes are described by using the embedded two-moment bulk cloud model based on parametrization formulated by Seifert and Beheng (2001; 2006). This scheme is extended by a parametrization for activation and a diagnostic treatment for diffusional growth based on the equations presented in Morrison *et al.* (2005).

In previous studies, PALM has been successfully applied to represent the stable BL (Beare *et al.*, 2006; Couvreux *et al.*, 2020; Maronga *et al.*, 2020b), radiation fog (Maronga and Bosveld, 2017; Schwenkel and Maronga, 2019; Boutle *et al.*, 2022), and diurnal cycles (Gehrke *et al.*, 2021).

### 2.2 | Numerical experiments

The design of the numerical experiments is based on the concept of running pairs of simulations, one allowing fog to form (in the following termed nocturnal fog [NF]) and the other where formation of liquid water is prohibited (in the following termed clear sky [CS]). Otherwise, identical initial conditions are applied. The initial conditions of the numerical experiments follow the idealized case used by Maronga and Bosveld (2017, fig. 4), which in turn is based on the observations of a deep radiation fog event from March 22–23, 2011, at the Cabauw Experimental Site for Atmospheric Research in the Netherlands. The initial profiles can be summarized as follows: Starting at  $T_0 = 276$  K, a stable stratified BLr of 50 m with an initial temperature gradient of  $\gamma_{bl} = 0.08$  K·m<sup>-1</sup> is followed by a residual layer with  $\gamma_{rl} = 0.01$  K·m<sup>-1</sup>. In this study, the model domain size is vertically extended (up to 1,230 m) in order to cover the vertical extent of the CBL developing during daytime. The value of  $\gamma_{rl}$  of the residual layer is used until the model top. Moreover, relative humidity (RH) decreases from 95% at the first grid level to 90% at 50 m and 85% at 400 m height. Subsequently, the water vapor mixing ratio decreases in such a way that RH reaches a value of 50% at 800 m and stays constant afterwards.

For all numerical experiments, cyclic conditions are used at the lateral boundaries, whereas at the model top the wind speed is fixed to the geostrophic value (varying for different parameter runs). In addition, a sponge layer is applied starting at a height of 1,000 m in order to prevent



gravity waves from being reflected at the top boundary of the model. The simulation start time is varied from around 2100 UTC to 0300 UTC but with a fixed end at 1600 UTC. The LSM is initialized with a short grassland canopy and an eight-layer soil configuration as suggested by Gehrke *et al.* (2021). The bulk cloud model, which also includes a scheme for activation, is initialized with a background aerosol concentration of  $100 \text{ cm}^{-3}$  composed of ammonium sulfate. Note that in real, continental environments, aerosol concentrations are typically higher. However, as our dry aerosol radius is relatively large, this aerosol concentration does illustrate the relevant fraction of aerosol, which can act as cloud condensation nuclei. As a result, an average droplet concentration of approximately  $80 \text{ cm}^{-3}$  (varying in space and time) is found in our simulations. We consider droplet deposition by sedimentation, assuming that droplets are distributed log-normally and falling in a Stokes regime (Ackerman *et al.*, 2009). Aerosol scavenging due to droplet deposition is not included; this effect is discussed, for example, in Schwenkel and Maronga (2020). Also, we do not consider turbulent droplet deposition by vegetation, which was modeled, for example, by Mazoyer *et al.* (2017). Further global parameters for simulation steering can be found in Table 1.

The difficulty of representing the diurnal cycle accurately is, on the one hand, to have sufficiently small grid spacings to simulate the weak turbulence and relatively small eddies at night. On the other hand, the model domain must be large enough to capture the largest eddies during the day (Brown *et al.*, 2002). Given limited computational resources, this combination is always a trade-off between precision and costs. In this study, a novel but simple approach is used, which can briefly be phrased as “cyclic-restart,” a mixture between the cyclic-fill method after restarting of the simulation. This method implies that the simulation is stopped once the BL has reached a height of 350 m for the first time, which corresponds to 2.5 times the horizontal model domain size and provides a proxy for the minimum horizontal extension needed to resolve the largest turbulent eddies. The threshold of 350 m is reached in the simulations between 0930 UTC and 1230 UTC, depending on the specific parameter case. Thereafter, the model domain is extended horizontally by a factor of 2.5. For this procedure, the so-called cyclic-fill method is used; that is, the added areas are filled cyclically with the state of the atmosphere at the end of where the precursor run has stopped (Figure 1). This procedure requires non-integer factors for the domain extension, as otherwise all turbulent structures are numerically identical and will develop undisturbed up to the last decimal place equally. In addition, the cloud model is also switched on for the CSs during restart, so that the formation of BL clouds during daytime is not suppressed. However, none of the experiments

**TABLE 1** Model parameters and initial conditions of the numerical experiments for all large-eddy simulations (unless otherwise explicitly stated)

Description	Symbol	Value
Grid spacing (m)	$\Delta$	3.0
Vertical model extent (m)	$H$	1,230
Horizontal model extent (m)		
Nighttime	$L_{x,y}$	810
Daytime	$L_{x,y}$	2,025
Surface pressure (hPa)	$p_0$	1,040
Skin temperature (K)	$\theta_0$	276.0
Roughness length (cm)	$z_0$	5
Surface humidity ( $\text{g} \cdot \text{kg}^{-1}$ )	$q_0$	5.5
Time-step radiation (s)	$\Delta t_{\text{rad}}$	60.0
Short-wave albedo	$\alpha$	0.14
Aerosol concentration ( $\text{cm}^{-3}$ )	$N_a$	100.0
Mean aerosol radius ( $\mu\text{m}$ )	$r_a$	0.012
Geometric standard deviation of aerosol distribution	$\sigma_a$	1.8
Skin-layer conductivity ( $\text{W} \cdot \text{m}^{-2} \cdot \text{K}^{-1}$ )	$\Lambda$	4.0
Soil moisture ( $\text{m}^3 \cdot \text{m}^{-3}$ )	$m_k$	0.4
Saturation moisture ( $\text{m}^3 \cdot \text{m}^{-3}$ )	$m_{\text{sat}}$	0.6

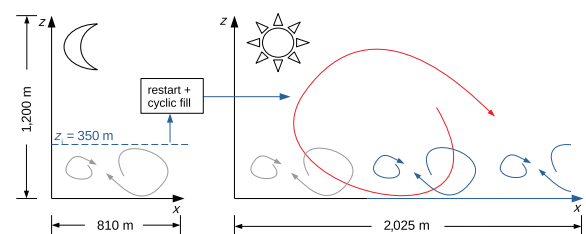


**FIGURE 1** Domain layout and termination criterion of night- and daytime simulation [Colour figure can be viewed at [wileyonlinelibrary.com](http://wileyonlinelibrary.com)]

conducted is found to feature the development of daytime clouds.

Based on sensitivity studies (Section 3.1), an isotropic grid spacing of  $\Delta = 3 \text{ m}$  is used; similar grid spacings for simulating the SBL or fog are used, for example, by Beare *et al.* (2006) and Wærsted *et al.* (2019). As outlined before,

TABLE 2 Overview of simulation pairs conducted

Simulation-pair name	$R_{sw,max}$ ( $W \cdot m^{-2}$ )	Day of the year	Simulation start time (UTC)	Geostrophic wind ( $m \cdot s^{-1}$ )
<i>Parameter simulations</i>				
<b>R700S21U5.5</b>	700	March 23	2100	5.5
R700S21U2.8	700	March 23	2100	2.75
R700S21U1.4	700	March 23	2100	1.375
R700S23U5.5	700	March 23	2300	5.5
R700S01U5.5	700	March 23	0100	5.5
R700S03U5.5	700	March 23	0300	5.5
R500S21U5.5	500	February 21	2100	5.5
R600S21U5.5	600	March 7	2100	5.5
R800S21U5.5	800	April 7	2100	5.5
R900S21U5.5	900	April 21	2100	5.5
<i>Additional simulations for process analysis</i>				
R600S21U2.8	600	February 21	2100	2.75
R800S21U2.8	800	April 7	2100	2.75
R600S23U2.8	600	February 21	2300	2.75
R800S23U2.8	800	April 7	2300	2.75
R800S23U5.5A200	800	April 21	2300	5.5
R600S21U5.5A50	600	February 21	2100	5.5
R600S21U5.5A25	600	March 7	2100	5.5

Note: The baseline simulation pair is indicated in bold.

we work with two different model domains in each simulation. The nighttime domain has  $270 \times 270 \times 225$  grid points in  $x$ -,  $y$ -, and  $z$ -directions, respectively, while the daytime domain is running on  $675 \times 675 \times 225$  grid points. Accordingly, the nighttime domain is  $810 \text{ m} \times 810 \text{ m}$  and the daytime domain covers  $2,025 \text{ m} \times 2,025 \text{ m}$  horizontally. The vertical model extent is the same for both layouts and ends at  $1,230 \text{ m}$  (by applying grid stretching above  $500.0 \text{ m}$ , but limiting the vertical grid spacing to a maximum of  $15 \text{ m}$ ).

In the parameter simulations we vary the geostrophic wind speed in order to represent different strengths or turbulent mixing. Furthermore, we vary the day of the year to account for different solar radiation forcing (both intensity and length of the day). Finally, we are also implicitly varying the fog thickness by prescribing different simulation start times (but all being after sunset). Thus, the fog has more time to develop vertically during nighttime until sunrise. The range of parameters represents a broad spectrum of possible meteorological conditions in which nocturnal radiation fog is likely to form. However, cases in which the fog does not completely dissipate and turns into a low-level

stratus cloud are excluded in order to be able to link the appearing differences between CS and NF unambiguously to the presence of fog during nighttime. All parameter simulation pairs conducted are listed in Table 2. The nomenclature of the simulation pairs is as follows: First, the maximum incoming solar radiation at noon (e.g., R700 is equal to approximately  $700 \text{ W} \cdot \text{m}^{-2}$ ) is given. Second, the starting point of the simulation is declared (e.g., S21 means a model start at solar noon 2100 UTC). Third, the geostrophic wind conditions are stated (e.g., U5.5 implies a geostrophic wind speed of  $5.5 \text{ m} \cdot \text{s}^{-1}$ ). For the purpose of analyzing processes that are responsible for differences between CS and NF, we added seven further simulation pairs (see Table 2), consisting of cross-combinations of the previous cases; for example, lower wind speeds and with a different day of the year, and different background aerosol conditions from  $25$  to  $200 \text{ cm}^{-3}$  (indicated with capital A). In the following,  $\delta$  is used to denote the difference of a quantity between the CS and NF cases, where  $\Delta$  is the grid spacing. Since case R700S21U5.5 is closest to the conditions of the Cabauw observations, we define it as the baseline simulation pair.



### 2.3 | Analysis of process contributions of temperature and humidity budget

This section describes how we separate the modeled temperature and humidity tendencies into contributions from different physical processes. By doing so, we are able to evaluate processes responsible for differences between CS and NF caused by the presence of fog. The general approach is similar to the method applied by Wærsted *et al.* (2019) assessing processes leading to fog dissipation. In general, assuming horizontal homogeneity and neglecting non-local processes, the temperature within the atmosphere within the analysis height  $H_a$  is changed by the SHF, long- and short-wave radiation divergence ( $R_{lw} + R_{sw}$ ), and by microphysics ( $F_{micro}$ ); that is, the release of latent heat due to condensation or evaporation. In this study we choose  $H_a = 1,000$  m, which is the model domain up to the sponge and larger than the maximum modeled BL heights (BLHs) of all simulations. Choosing  $H_a$  larger than the BLHs of all parameter simulations implicitly eliminates the contribution by mixing with the free atmosphere for changes in temperature and water vapor mixing ratio. Thus, the temperature budget within  $H_a$  (in the following, differences averaged over  $H_a$  are denoted with angle brackets) can be written as

$$\left\langle \frac{d\theta}{dt} \right\rangle = SHF + R_{lw} + R_{sw} + F_{micro}. \quad (1)$$

Analogously, the water vapor mixing ratio within  $H_a$  is altered by the turbulent latent surface heat flux (LHF), which can be split into a contribution by the evapotranspiration of the vegetation ( $LHF_{veg}$ ) and by the condensation or evaporation of dew ( $LHF_{liq}$ ).  $F_{micro}$  includes condensation (evaporation) of water vapor to liquid (of liquid to water vapor) and contributes as a loss (gain) for the water vapor budget. The water vapor mixing ratio budget for the modeled atmosphere is

$$\left\langle \frac{dq}{dt} \right\rangle = LHF_{veg} + LHF_{liq} + F_{micro}. \quad (2)$$

For a time-integrated analysis of process contributions we integrate up to the point in time where the temperature and humidity difference within  $H_a$  after fog dissipation (i.e., within the analysis period) differs the most between CS and NF (hereafter denoted by  $t_{a,\theta}$  and  $t_{a,q}$ , respectively). In this regard,  $F_{micro}$  can be substituted by the deposition of fog droplets ( $F_{dep}$ ) assuming that all condensed water that has not been deposited to the surface has been evaporated again after fog dissipation. How the right-hand side terms of Equations 1 and 2 are derived from the model output is documented in the Appendix.

## 3 | RESULTS

### 3.1 | Sensitivity study

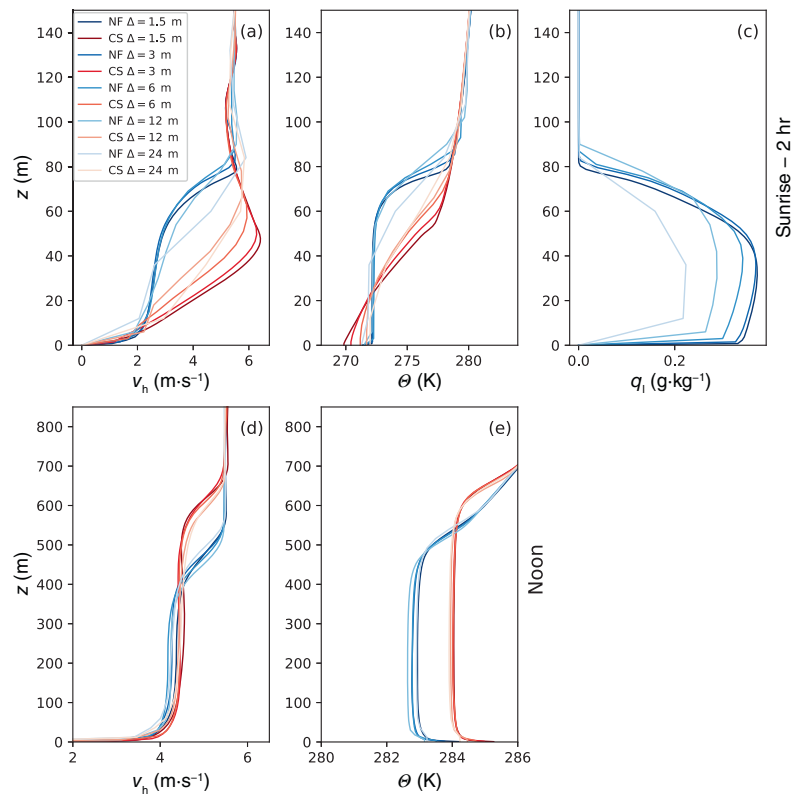
We first present the results of a grid sensitivity study of the baseline simulation. Based on these results, the grid spacings for the parameter studies are selected. For this purpose, we perform simulations with isotropic grid spacings of  $\Delta = 1.5, 3.0, 6.0, 12.0, 24.0$  m. As outlined earlier, the NBL is known to be especially sensitive to the numerical grid resolution due to possibly underresolved turbulence. Figure 2 shows profiles for the horizontal wind velocity, potential temperature, and liquid water mixing ratio of the sensitivity simulations 2 hr before sunrise (upper row) and at noon (1200 UTC, lower row). The most obvious differences can be observed during night in both wind speed and potential temperature, with pronounced differences between a foggy convective NBL and an SNBL. Additionally, large differences are found among the cases using different grid spacings, especially for the CSs at night (Figure 2a,b). Those differences are caused by an overestimation in vertical mixing when using too coarse grid spacings, leading to underestimation of the near-ground temperature gradient (Figure 2b; see (van Stratum and Stevens, 2015)). Even though the differences are smaller for the NFs, since the NBL is convectively evoked by the deep fog we observe up to 40% lower liquid water mixing ratios for larger grid spacings. However, the profiles of  $q_l$  between cases with  $\Delta = 1.5$  m and  $\Delta = 3.0$  m match quite well; thus, we conclude that the fog is sufficiently resolved with  $\Delta = 3.0$  m.

At noon (1200 UTC), where both NFs and CSs are convective, simulation results are less sensitive to the chosen grid spacing. Especially for the CSs, the temperature profiles are quite similar and do not show the deviation observed during the night (Figure 2), which is in line with the findings of van Stratum and Stevens (2015). However, for the NFs we observe deviations up to 0.5 K for  $\theta$  in the BL. As we want to investigate the influence of a foggy NBL on daytime convection as precisely as possible, such errors as found for grid spacing larger than  $\Delta = 3.0$  m in the representation of fog are not negligible. Based on these sensitivity studies, we used a grid spacing of 3.0 m for the parameter studies.

### 3.2 | Diurnal cycle

To identify processes that cause NF affecting the CBL development and to determine which meteorological conditions intensify or mitigate this impact, we employ a set of parameter simulations in which we vary the radiation conditions, the wind speed, and the fog depth (see Table 2).

**FIGURE 2** Profiles (horizontally averaged) of the horizontal wind velocity, (a,c) potential temperature (b,d) liquid water mixing ratio (e) for different grid spacings of the baseline simulations 2 hr before sunrise (upper row) and at noon (lower row) [Colour figure can be viewed at [wileyonlinelibrary.com](http://wileyonlinelibrary.com)]



We conduct simulations for five different days of the year between February and end of April, three different wind speeds ( $u_g = 5.5, 2.75, \text{ and } 1.375 \text{ m}\cdot\text{s}^{-1}$ ), and four different fog depths implicitly achieved by using various simulation starting points (2100, 2300, 0100, and 0300 UTC); that is, by varying the length of the night where short-wave radiation is absent.

We simulate the diurnal cycle (starting at night until 1600 UTC of the next day) for different parameter study pairs. The general BL development during the diurnal cycle, which differs for the individual parameter cases, is outlined exemplarily for the baseline simulation in Figure 3 in terms of the vertical velocity shown as instantaneous cross-section for three different stages (top row: at night 0500 UTC, during fog; center row: shortly after dissipation around 1100 UTC; and bottom row: in a fully developed CBL at 1400 UTC) during the diurnal cycle. At night, a well-mixed fog layer (marked by contour lines) with a height of 80 m in the NF (left column) has developed, whereas the CS (right column) exhibits a somewhat lower BLH and lower vertical wind speeds (shear driven) due to a stable stratification. After sunrise, the fog completely dissipates (at 1100 UTC) and the mixing layer reaches a BLH of 290 m, whereas the BLH in the CS is as high as 480 m. At 1400 UTC, both BLs are cloud free and convective. The CS, however, exhibits a 150 m deeper BL.

Figure 4 shows time series for simulation pairs in which the day of the year, and hence incoming solar radiation conditions, is varied. The LWP (Figure 4a) of the fog layers increases equally in all simulations as long as sunlight is absent. Beginning with sunrise in the R900S21U5.5, the LWP growth rate decreases and subsequently the LWP starts to decrease. By time the fog (the green shaded areas show the time where fog exists by definition; i.e., visibility is less than 1,000 m at 2 m height) lifts and remains as a low-level cloud for 1–3 hr until the liquid water has been completely dissipated. The presence of fog and low-level clouds significantly alters the near-surface radiation balance (Figure 4b). On the one hand, at night, the surface radiation balance is less negative in the NFs compared with the CSs; that is, surface cooling rates are stronger in cases without fog as the fog layer intensifies long-wave counter-radiation. On the other hand, after sunrise, the effect of an increased atmospheric albedo (i.e., the relatively light fog layer) outweighs the increased atmospheric long-wave radiation for the NF, resulting in higher net surface radiation values for the CS.

The focus in this study will be on the differences within the period after all liquid water is dissipated in the NFs and the surface short-wave radiation balance is the same for NFs and CSs (defined by  $|\delta R_{\text{sw,in}}| < 2 \text{ W}\cdot\text{m}^{-2}$ ). Using a threshold of  $|\delta R_{\text{sw,in}}| = 0 \text{ W}\cdot\text{m}^{-2}$  is not feasible, as different

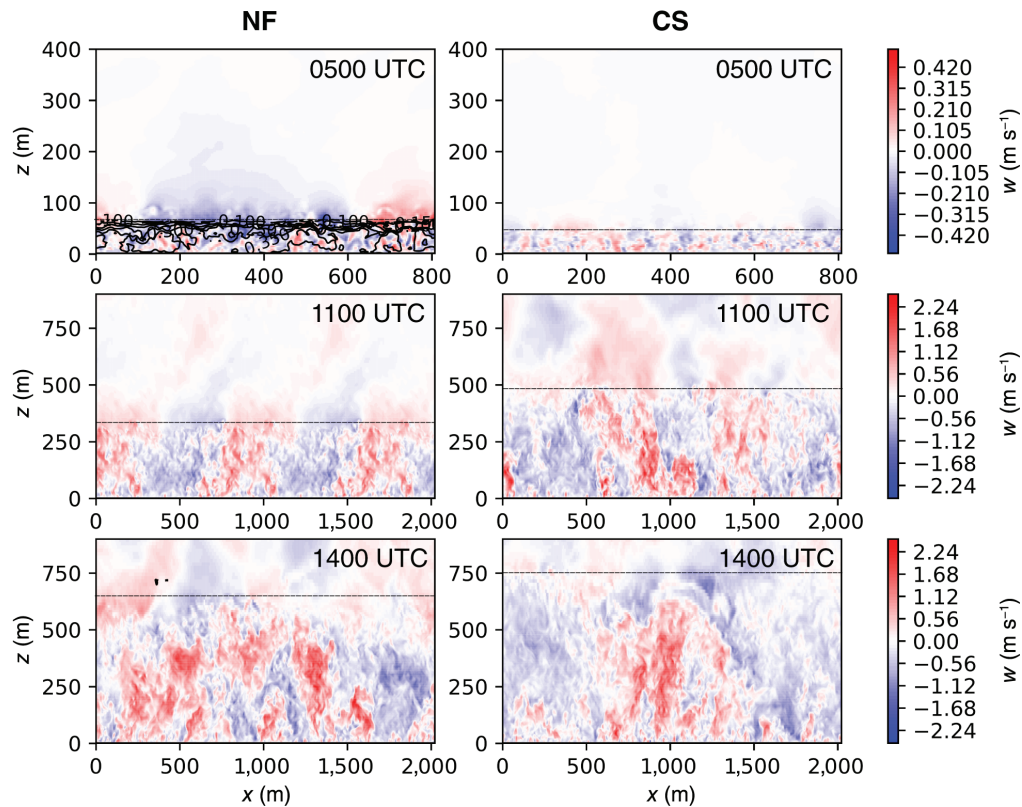


**FIGURE 3** Instantaneous  $x$ - $z$  sections for vertical velocities at  $y = 0$  m for nocturnal fog (NF, left column) and clear sky (CS, right column) at 0500 UTC (top row), 1100 UTC (center row), and 1400 UTC (bottom row) for the baseline simulation. The black dashed lines indicate the domain-averaged boundary-layer height. Contour lines for the foggy case at 0500 UTC show the liquid water mixing ratio [Colour figure can be viewed at [wileyonlinelibrary.com](http://wileyonlinelibrary.com)]

temperature and humidity profiles cause slight deviations in the incoming solar radiation between NFs and CSs. The length of the analysis period is shaded in Figure 4c,d. Shown are the differences of the 2 m potential temperature (c) and BLH (d) between the NFs and CSs.

Although the radiative forcing (sunrise, zenith, and thus strength of incoming solar radiation), is considerably modified within the parameter cases, we observe the same qualitative temperature trend for all simulations (Figure 4c). At 2300 UTC the fog has formed in the NFs within the first grid level and about 0.8 K higher temperatures appear for the CSs near the ground. As long as the fog top is shallow, the radiative cooling rate ( $3\text{--}4\text{ K}\cdot\text{hr}^{-1}$ ) of the fog cools the near-surface layers. However, during the night, after fog has become optically thick and deeper, which suppresses net surface cooling and amplifies vertical mixing, higher near-surface temperatures in the NFs are observed (up to 2 K). Indeed, as long as the CSs are stably stratified this tendency in the temperature deviation is only present for the near-surface regions. An analysis for the temperature within  $H_a$  exhibits also

higher temperatures for the CSs during the night, as the vertically integrated cooling is stronger for the NFs (see next section). Maximum differences between CSs and NFs in the 2-m temperature can be found shortly after sunrise, showing a deviation up to 4.5 K. Afterwards, at the beginning of the analysis period, differences between 2.5 and 2.0 K are simulated, which decrease (exponentially) down to deviations between 0.5 and 2.0 K at 1600 UTC. The decline of the differences can be explained by approximately 25% larger values of the Bowen ratio ( $B = \text{SHF}/\text{LHF}$ ) in the NFs; that is, in the NFs; more energy is transferred into sensible heat, whereas in the CSs more energy is transferred into latent heat after fog dissipation (will be shown later).

Furthermore, in all simulation pairs, the BLH is higher for CSs than with the NFs within the analysis period. The deviations are in the range of 150.0–200.0 m at the beginning of the analysis period and, in contrast to the exponential temperature declination, tend to decrease linearly (discussed later) in time, yielding deviations between 200 m and 100 m at 1600 UTC. However, for

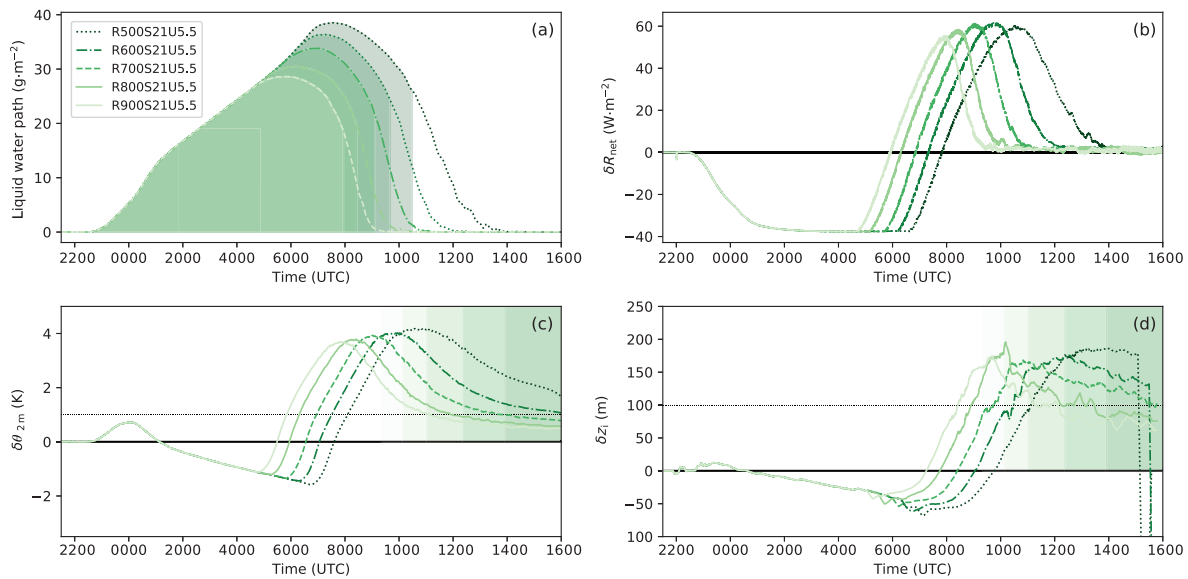


**FIGURE 4** Time series for parameter studies R500S21U5.5–R900S21U5.5 showing the liquid water path of the fog for (a) the nocturnal fog (NF) case and the deviations (clear sky [CS] minus NF) of the (b) surface radiation balance, (c) potential temperature at 2 m, and (d) boundary-layer height (BLH). The BLH is calculated as an average over 10 min. Shaded areas in (a) indicate the period of fog (by definition of visibility at 2 m height). Shaded areas in (c) and (d) mark the analysis period, with the same radiative forcing between CS and NF [Colour figure can be viewed at [wileyonlinelibrary.com](http://wileyonlinelibrary.com)]

R500S21U5.5 (corresponding to end of February), no decrease in BLH is observed, which can be explained by the low incoming solar radiation at the time of fog dissipation insufficient to compensate the deviations. The collapse of the BLH deviations for the simulations R500S21U5.5 and R600S21U5.5 marks the decay of daytime convection due to a negative surface net radiation. As a result, we observe that the absolute differences in temperature and BLH increase with decreasing incoming solar radiation. But it must be mentioned that the available solar incoming radiation, being the major forcing for the SHF and known to be the prime process for fog dissipation (Wærsted *et al.*, 2019), is thus also correlated to the fog depth and life time.

Within the parameter runs (based on the radiation conditions for mid-March) for lower turbulent mixing (Figure 5) as well as different fog depths (implicitly induced by later simulation starts; Figure 6), we also observe higher 2-m temperatures as well as larger BLH for all parameter runs within the analysis period for the CS compared to the NF. Both cases with lower turbulent mixing (achieved by prescribing lower geostrophic wind speeds) reveal an earlier fog formation (about 30 min). Decreased turbulent mixing enhances surface cooling and, as a result, air becomes supersaturated earlier, which was also simulated in, for example, Bergot and Guedalia (1994) and Steeneveld and de Bode (2018). Once fog has formed, higher turbulent mixing accelerates the vertical propagation by stronger entrainment and a subsequent

cooling of entrained air masses down to saturation. Figure 5a shows that lower turbulent mixing cases lead to lower LWPs, as the vertical development is retarded. Despite the higher LWP for the baseline simulation, a higher temperature within the BL and stronger mixing favor an earlier fog dissipation for this case (30 min to 1 hr earlier with respect to R700S21U2.8 and R700S21U1.4). Indeed, the effect of turbulent mixing on the life cycle of fog is controversially discussed in the literature (Bergot and Guedalia, 1994). In contrast to our findings, Smith *et al.* (2018) reported that stronger turbulent mixing weakens fog development during the night. Conclusively, turbulent mixing can facilitate or impede fog development and dissipation, which strongly depends on the thermodynamic profile of the overlying air (whether mixed air is close to saturation or relatively dry and warm) (Wainwright and Richter, 2021). It is noteworthy that simulation pairs with a geostrophic wind of 2.75 and 1.375 m·s<sup>-1</sup> show only very small differences between each other in terms of LWP. This non-linear behavior indicates that the NF cases with lower turbulent mixing experience a transition in the turbulence regime as soon as deep fog has formed. From this point on, vertical mixing triggered by cloud-top cooling prevails over vertical mixing caused by wind shear. Although the fog development behaves similarly, decreased turbulent mixing leads to increased nocturnal 2-m temperature deviations between NFs and CSs. Though the NF cases for both decreased mixing cases

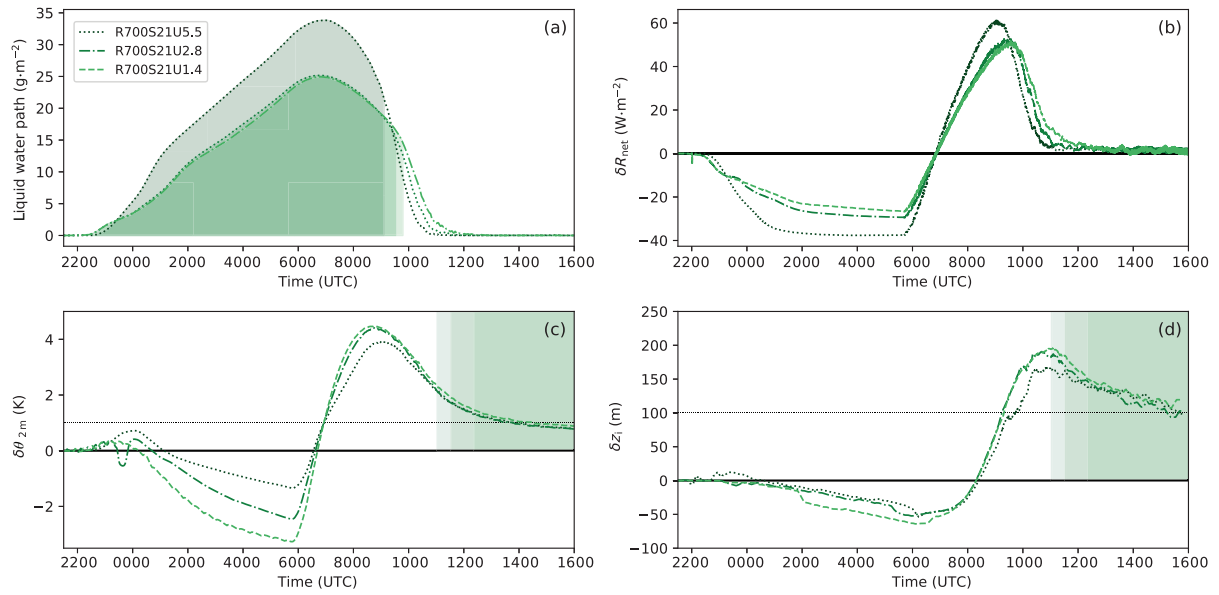


**FIGURE 5** Same as Figure 4, but for parameter studies R700S21U1.4–R700S21U5.5 [Colour figure can be viewed at [wileyonlinelibrary.com](http://wileyonlinelibrary.com)]

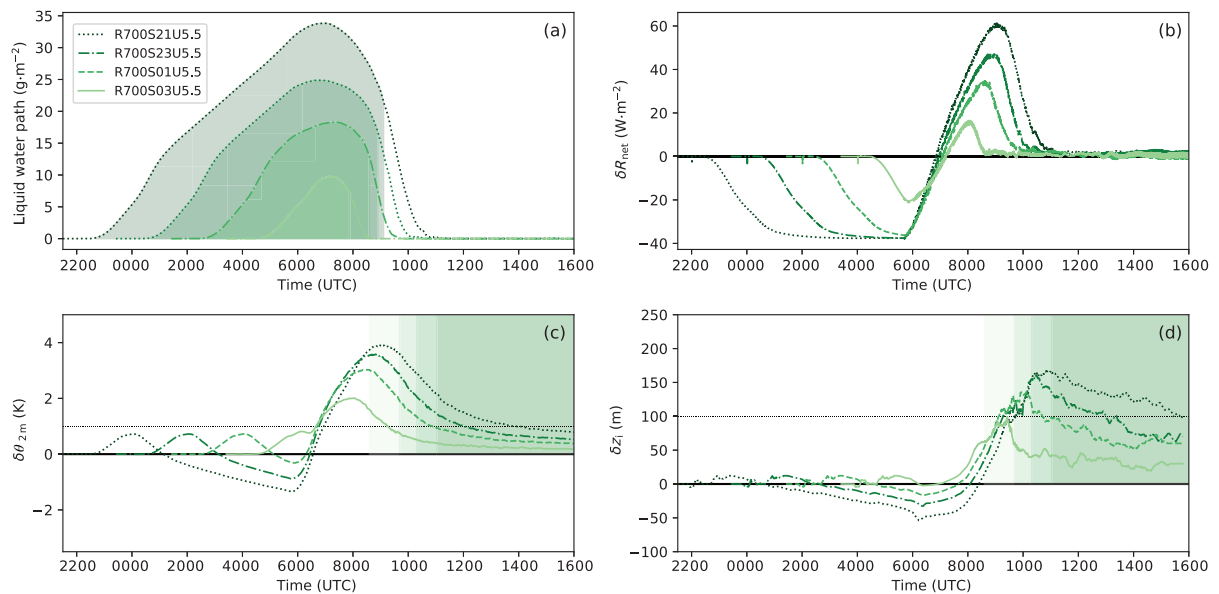


**FIGURE 6** Same as Figure 4, but for parameter studies R700S21U5.5–R700S03U5.5 [Colour figure can be viewed at [wileyonlinelibrary.com](http://wileyonlinelibrary.com)]

show a very similar BL structure, those differences are caused by the enhanced cooling of near-surface air due to a decreased vertical heat transport for R700S21U1.4. Nevertheless, within the analysis period, all simulations, regardless of the strength of turbulent mixing, reveal nearly identical deviations for the 2-m temperature and BLH. This is explained by the fact that a larger LWP

(after sunrise) causes stronger differences in the radiation balance (see Section 3.3), which counteracts an earlier dissipation due to stronger vertical mixing.

Furthermore, the simulations with different fog depths show distinctly different LWPs and also fog heights (not shown). The later the simulation starts, the less time the fog layer has until sunrise and, therefore, the less time to



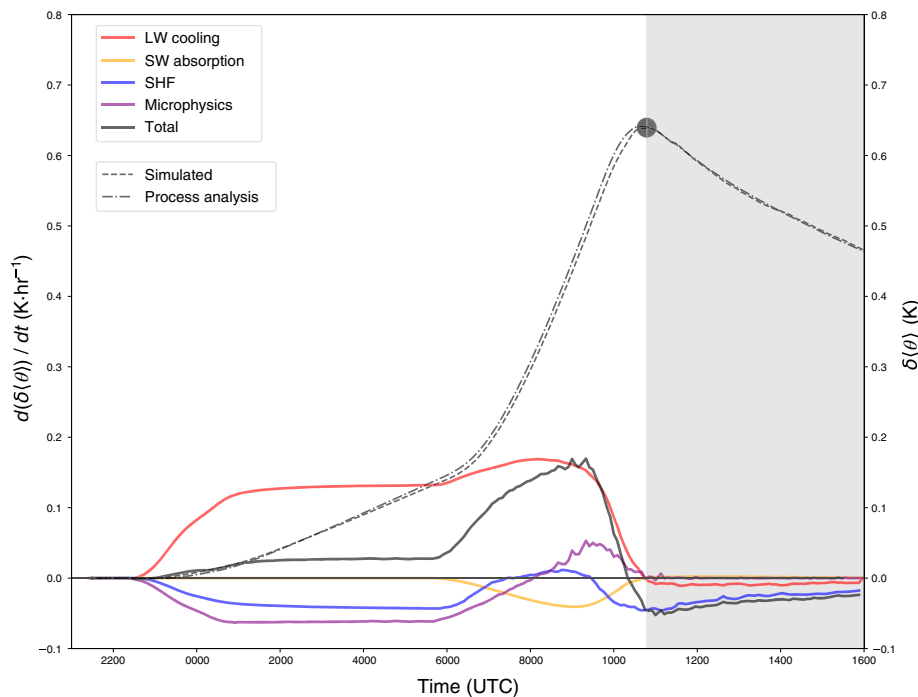


**FIGURE 7** Time series for the differences of clear sky (CS) minus nocturnal fog (NF) in process-level contributions on temperature integrated over height  $H_a$  for the baseline simulation. The black solid line shows the total heating rate of CS minus NF, and the other lines represent the process contributions outlined in Equation (1). The right y-axis shows the simulated temperature difference within  $H_a$ , and the temperature difference by the process analysis is shown. The black marker shows the point in time where the maximum temperature difference after fog dissipation occurs. The gray shaded area marks the time span without fog. LW, long wave; SHF, sensible surface heat flux; SW, short wave [Colour figure can be viewed at [wileyonlinelibrary.com](http://wileyonlinelibrary.com)]

develop before the BL warms up. Accordingly, the simulation (NF case) that starts at 0300 UTC has a maximum LWP of  $10 \text{ g}\cdot\text{m}^{-2}$  and maximum fog height of 92 m, whereas for the simulation lasting the longest the LWP is three times higher with twice the fog height. Additionally, different simulation starting times also shorten the period in which surface cooling of the BL occurs (by a shorter nocturnal phase) and thus lead to higher BL temperatures with later simulation starts. Again, as in the parameter studies for different days of the year, higher LWPs lead to a later dissipation after sunrise—for example, as also found by Toledo *et al.* (2021)—of the fog layer and correlate with stronger differences between the NF and CS in temperature and BLH. Likewise, for the cases where the fog lasts the shortest and remains relatively thin, rather small differences from the comparison of CSs and NFs can be seen, but these nevertheless persist until the end of the analysis period. In summary, we can conclude that all NFs generally tend to lower BL temperatures as well as lower BLHs than the CSs do within the analysis period.

### 3.3 | Process-level analysis

Up to this point, we analyzed the parameter simulations pairs individually while changing only one of the parameters day of the year, starting point and geostrophic wind speed at a time. Indeed, the change of a single parameter (e.g., the day of the year) alters several interacting processes, for example, the absolute incoming solar radiation, the time of sunrise and consequently the depth of fog layer as well as the fog dissipation time. Therefore, we address this section to analyze which processes are the most important for the potential of fog to alter CBL development during daytime. Besides, we want to identify key parameters which crucially control the strength of the fog impact.

#### 3.3.1 | Process-level analysis on temperature

Following the approach presented in Section 2.3, Figure 7 shows time series for differences in heating/cooling rates

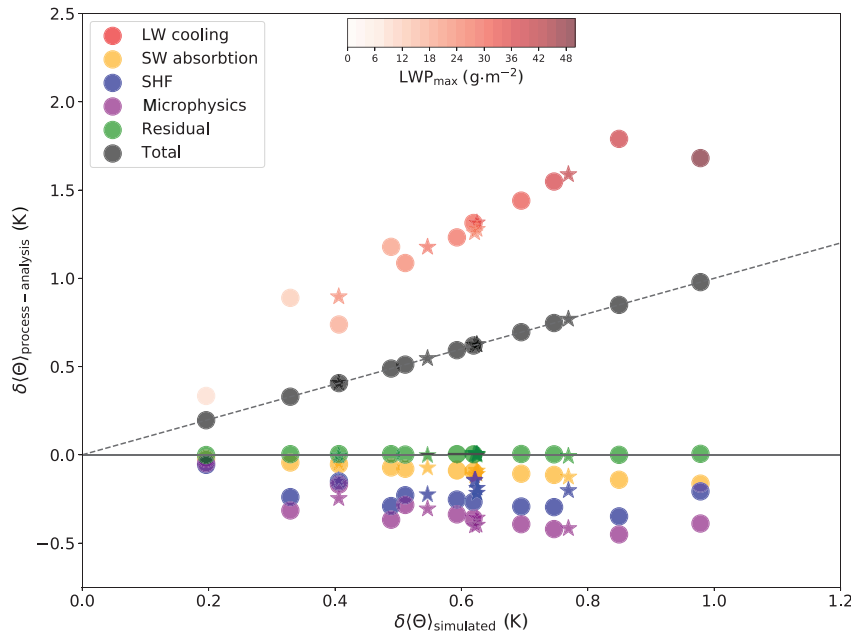


FIGURE 8

Integrated-in-time temperature differences within the air volume from the surface to contributions by atmospheric long-wave (LW) cooling, atmospheric short-wave (SW) absorption, surface sensible heat flux (SHF), latent heat, and residual versus maximum bulk temperature difference. Each dot represents the difference within a simulation pair at  $t_{a,\theta}$ . The sum of all contributions is shown by the black marker. The different opacity for LW cooling markers indicate the maximum liquid water path (LWP) of the fog layer. Simulations with lower wind speeds are marked by asterisks [Colour figure can be viewed at [wileyonlinelibrary.com](http://wileyonlinelibrary.com)]

for the baseline simulation pair. The simulated and expected (by the contributions of the process analysis) temperature differences are illustrated with the black dashed and dotted lines on the right axis. Moreover, the time-integrated process analysis for all simulation pairs is shown in Figure 8.

The temperature difference between CS and NF increases in time until the fog is dissipated (Figure 7). Initially, the absolute heating rate is relatively constant at  $0.025 \text{ K}\cdot\text{hr}^{-1}$ . After sunrise, however, the slope increases sharply as effective cooling occurs in the case of NF as a consequence of the evaporation of the fog layer. At the maximum we found a  $0.62 \text{ K}$  higher temperature for CS compared with NF. Note that the temperature difference within the BL might be up to two times (or more) the value as the BLH is about the half (or even less) of  $H_a$  at that time. After fog dissipation, the temperature difference within  $H_a$  is decreasing linearly associated with negative total cooling (quasi-constant) rates for CS minus NF. The quasi-constant difference in the heating-rate can also explain the linear decrease in BLHs (Figures 4–6). Growth of the BL is mainly caused by encroachment. Consequently, a constant difference in the heating-rate difference (between CS and NF) causes a linear decrease in BLH difference. Comparing the simulated temperature trend with the contributions achieved by Equation (1), we see that the temperature budget closes well during the diurnal cycle. This rather small differences might be caused by the approximation assumptions made for Equation (A1). Starting from fog formation until fog dissipation, radiative cooling reveals the largest net

warming rates ( $\approx 0.13 \text{ K}\cdot\text{hr}^{-1}$ ) between CS and NF. As, after fog formation, the CS has higher water vapor mixing ratios (leading to a stronger long-wave emission), radiative cooling is higher than for NF during daytime.

This behavior is also found for all the other parameter runs; that is, the difference in long-wave cooling leads to most of the BL temperature differences between the NFs and CSs (Figure 8). At maximum this is by  $+1.75 \text{ K}$ , reflecting the strong emission of long-wave radiation at the fog top in the NFs, which cools the BL. While for CS conditions the atmospheric long-wave cooling is comparatively small (in our case about  $0.6 \text{ K}\cdot\text{hr}^{-1}$ ), cooling rates increase rapidly in the presence of fog (up to  $6.0 \text{ K}\cdot\text{hr}^{-1}$ ). As clouds are almost a black body within the infrared spectrum, the strength of radiative cooling correlates to the optical depth, which in turn depends on the cloud depth, the water content, and droplet size distribution (Mellado, 2017). Thus, unsurprisingly, we observe a correlation (to some extent) of the strength of radiative cooling to the maximum LWP. However, besides the strength of cooling rates, the temperature change by long-wave cooling depends on the lifetime of the fog (which is, inter alia, linked to the depth of the fog but might also be affected by turbulent mixing). The contribution by microphysics is mitigating the warming effect of long-wave cooling as for NF. As long as water vapor is condensing, the release of latent heat increases the temperature in NF (resulting in a negative contribution for CS minus NF). During fog dissipation, however, this leads to a temperature decrease in NF as water is evaporating. Integrated over time, microphysics is the largest contributor for warming the NFs, which is up to  $-0.45 \text{ K}$

**FIGURE 9** Integrated-in-time humidity difference within the air volume from the surface to HA contributions by evapotranspiration of plants, dewfall, droplet deposition, and the residual source versus maximum bulk humidity difference. Each dot represents the difference within a simulation pair at  $t_{a,q}$ . The sum of all contributions is shown by the black marker. Simulations with lower wind speeds are marked by asterisks [Colour figure can be viewed at [wileyonlinelibrary.com](http://wileyonlinelibrary.com)]

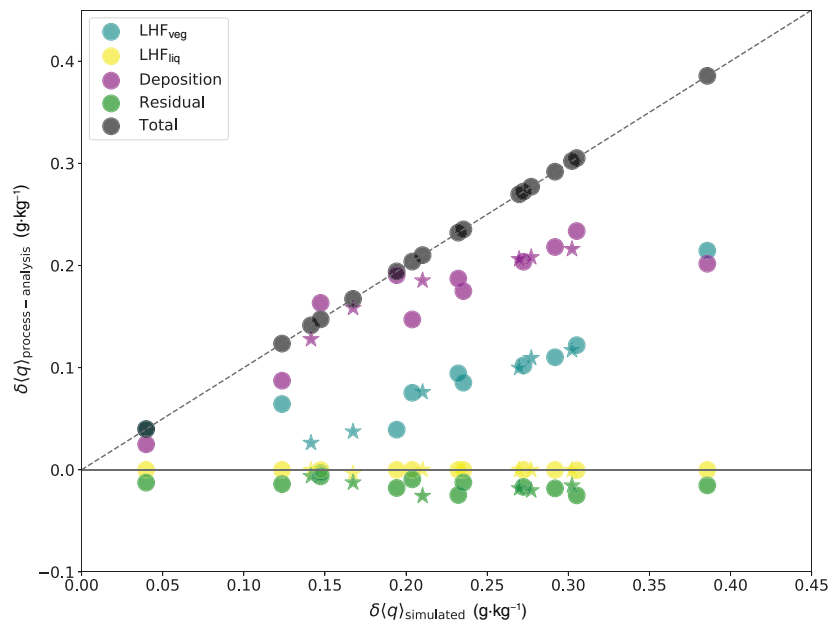


(Figure 8). If all condensed liquid were to completely evaporate during the fog life cycle, this contribution would be net zero. Deposition of fog droplets, though, constantly removes liquid from the atmosphere and consequently evokes an imbalance between latent heat by condensation and evaporation the NFs experience a net warming. Moreover, the SHF contributes for all simulation pairs to a larger energy input (equivalent to negative difference) in the NFs (Figure 8). This is mainly explained by the stronger surface cooling during night for the CSs (Figure 7), as the surface net radiation gets more negative (and in turn leads to a stronger negative SHF) for the CSs (due to less reflected long-wave radiation, as no cloud is present) than in the NFs. After sunrise, there is a short period in time where the SHF is larger in the CSs caused by a stronger heated surface, though this is mitigated by the reflection of the fog layer in the NFs (Figure 7). This contribution is one order of magnitude lower than the stronger surface cooling at night, as the period where the SHF in the CS is stronger than in the NF is very short (90 min) and the amplitude in the difference is smaller. Subsequently, the SHF difference becomes negative again (i.e., indicating that the NF cases are more strongly heated by the surface), which leads to a decrease in the temperature deviation between CS and NF (Figure 7). This is explained by larger values of the Bowen ratio for the NFs after fog dissipation; that is, more energy is transferred to sensible heat than to latent heat, resulting in a stronger temperature increase (and thus explaining the reduction in the difference between CS minus NF within the analysis period). Nonetheless, the contribution of the SHF shows relatively similar values in the range of

−0.15 to −0.4 K (Figure 8). After sunrise, heating due to atmospheric short-wave absorption also contributes to the temperature changes, which is larger for the NFs. Though the CS atmosphere is relatively transparent for short-wave radiation, the foggy atmosphere absorbs more short-wave radiation and leads to an increase in temperature. After fog dissipation, both NF and CS are cloud free and differences in heating rates due to short-wave absorption have vanished (Figure 7). Integrated-in-time differences between NFs can be quantified as −0.05 up to −0.2 K (Figure 8). Indeed, differences induced by short-wave heating are relatively small compared with contributions by long-wave cooling, microphysics, and SHF. Moreover, for all cases, a residual very close to zero is observed (Figure 9). This indicates that the process-level analysis covers the most relevant processes. To conclude, the temperature differences in the atmosphere between CS and NF have their origin in the night. The largest contribution to the temperature difference is cloud-top cooling, which in our case is a more powerful cooling process for the atmosphere than the nocturnal cooling from the surface. After fog dissipation, the temperature differences decrease due to the higher Bowen ratio for NF compared with CS.

### 3.3.2 | Process-level analysis on water vapor mixing ratio

Besides the temperature and BLH, the misrepresentation of fog also affects the water vapor content and the RH of the daytime CBL, and hence cloud formation during daytime.



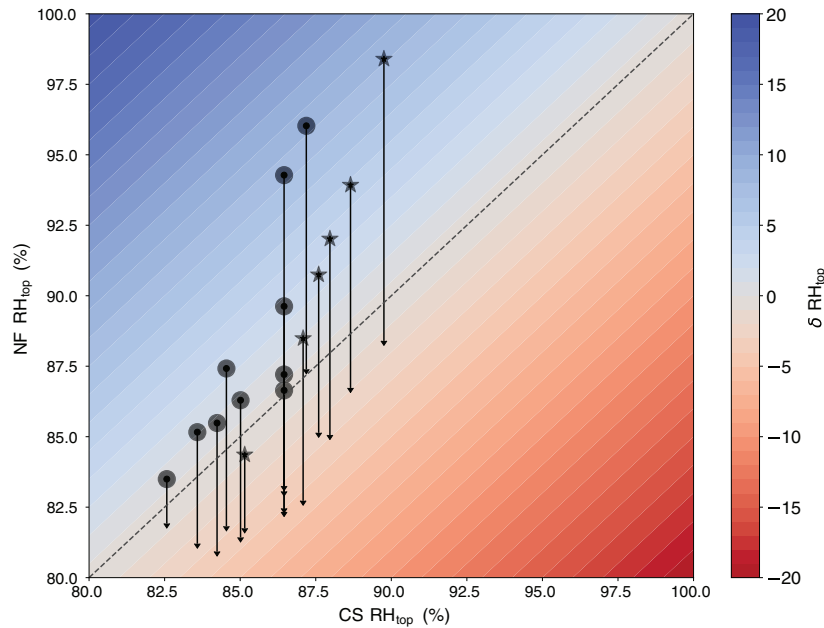


**FIGURE 10** Boundary-layer (BL) to relative humidity (RH) of nocturnal fog (NF) versus BL top RH of clear sky (CS) at noon (1200 UTC). The background illustrates the strength of the deviation between CS and NF, and the arrows indicate the RH drop by higher BL temperatures for the CS cases [Colour figure can be viewed at [wileyonlinelibrary.com](http://wileyonlinelibrary.com)]

In analogy to Figure 8, Figure 9 shows the decomposition of the change in terms of the water vapor mixing ratio change within  $H_a$ . Though we did not consider changes in the water vapor mixing ratio in the analyses discussed earlier herein, Figure 9 gives evidence that for all simulated cases there is a positive feedback; that is, the CSs display a higher water vapor mixing ratio than the NFs do. The evolution, however, is controlled by different processes partly counteracting each other, as presented in Equation (2). Deposition of fog droplets is the dominating process and makes up most of the net increase in water vapor mixing ratio of the difference between CS and NF (with values up to  $0.23 \text{ g}\cdot\text{kg}^{-1}$ ; Figure 9). Naturally, deposition of droplets is only present in the NF cases. The significance of this contribution is linked again to the strength of the fog and increases with increasing LWP and fog duration. It has been known that this process is strong in deep radiation fogs as the deposition rate is typically in the range of  $20 \text{ g}\cdot\text{m}^{-2}\cdot\text{hr}^{-1}$  (e.g., Boutle *et al.*, 2018), meaning the liquid water content within the fog layer is replenished every 0.5–2.0 hr, which is also seen in the present dataset ( $26 \text{ g}\cdot\text{m}^{-2}\cdot\text{hr}^{-1}$  for the baseline simulation during the mature phase of the fog). The second largest contribution to the differences is caused by the LHF due to evapotranspiration of vegetation ( $\text{LHF}_{\text{veg}}$ ). These differences in  $\text{LHF}_{\text{veg}}$  are driven in particular by the fact that the higher temperatures in CSs result in a higher saturation vapor pressure deficit, which causes higher evapotranspiration. As in both CS and NF almost all the dew produced during the night (which is in total more for the CSs due to a colder surface) is evaporated at  $t_{a,q}$ , the net contribution

is nearly zero (yellow markers,  $\text{LHF}_{\text{liq}}$ ). For all cases, a residual close to zero is observed.

As discussed earlier, we see a net gain in the water vapor mixing ratio when comparing the CS against NF cases. One thus might expect that the RH in the daytime becomes higher, but we observe the opposite (Figure 10) for almost all cases. This can be explained by the fact that we also find significantly higher BL temperatures (contribution of higher temperature to RH decrease is illustrated by the arrows in Figure 10) for the CSs compared with the NFs, so that the air can hold significantly more water vapor than gain due to non-existing fog development during nighttime. As a direct consequence, we can conclude that the misrepresentation of nocturnal radiation fog can lead to a too low RH during daytime. Therefore, failing to resolve fog fortunately does not favor an artificial cloud development during daytime. However, in some situations, when RH near the top of the CBL is close to 100% (assuming the NF as the reference), such errors in the RH might suppress the development of, for example, shallow cumulus clouds, which would develop if the fog were captured during nighttime.

#### 4 | SUMMARY AND CONCLUSION

Nocturnal radiation fog is frequently misrepresented in numerical models. The potential effect of failing to simulate a nocturnal deep radiation fog on the development of the daytime BL was studied in this article. High-resolution LESs were employed for this purpose. A set of typical

conditions prone to fog formation in spring and autumn seasons for the midlatitudes was simulated. By comparing pairs of simulations where deep fog was allowed to develop in one case of each pair and fog formation was suppressed in the other, the potential effects on the daytime CBL were analyzed. Here, cases in which fog did not dissipate completely and remained as low-level stratus during daytime were excluded.

The temperature within the CBL was found to be up to 2.5 K warmer for the CSs than in the NFs after fog dissipation, which was accompanied by a deeper CBL by up to 200 m. However, these differences decreased over time (due to approximately 25% larger Bowen ratios in the NFs) and were most extreme shortly after the dissipation of fog. Furthermore, water vapor mixing ratios were observed to be up to 10% lower in the NFs, whereas temperatures were significantly warmer. As the latter was the dominant effect, a generally lower RH at the top of the BL was produced in the CSs. As a direct consequence, the development of clouds during daytime (e.g., shallow cumulus clouds) might be suppressed by the misrepresentation of nocturnal fog. The differences between CSs and NFs during the day were exacerbated by fog thickness and duration. The thickness of the fog is neither an explicit parameter to be varied (or known a priori) nor an environmental condition, but rather an implicit result of the meteorological circumstances. Hence, a rather complex pattern emerges with respect whether other parameters (e.g., wind) influence the development of fog on CBL. Nevertheless, it can be concluded that the deviation in daytime CBL properties between CSs and NFs are amplified by circumstances that favor more extreme fog events (e.g., less incoming solar radiation during the day). Long-wave atmospheric cooling (in terms of temperature deviation) and droplet deposition (in terms of mixing ratio) were identified as the most important processes that can trigger differences between CSs and NFs. Therefore, special attention should be given to the representation of those processes in numerical models.

The error that is induced by failing to resolve a deep radiation fog event in the NBL (under spring and autumn conditions) can be significant for daytime CBL development. Thus, these findings are not following a potential straight conclusion based on the studies of van Stratum and Stevens (2015; 2018), who showed that misrepresentation of the NBL due to an underresolved NBL has no relevant implications for daytime convection (under summer conditions). Nevertheless, in agreement with van Stratum and Stevens (2015), artificial moist daytime convection is usually not initiated by non-resolved fog in the present study. However, how strong the error is in simulating the transition from deep fog to low-level stratus can only be conjectured, as such cases were excluded in this study. To

extend this work to account for such cases would be the starting point for a follow-up study.

Though perhaps impaired by limited horizontal extent (i.e., neglecting advection effects and non-local contributions) and idealized assumptions (i.e., fog misrepresentation is achieved by turning off cloud microphysics), the potential of nocturnal fog to effect CBL development is shown and quantified by the results presented here. It is likely that the feedback on the daytime BL that was identified in this idealized setting will also be present in operational models (e.g., NWP models). To assess this statement, a rigorous comparison of deep fog events that were not captured (or not captured adequately) by NWP models should be performed and respective daytime forecasts should be compared with in-situ observations of such situations.

#### ACKNOWLEDGEMENTS

All simulations were carried out on the computer clusters of the North-German Supercomputing Alliance (HLRN). Python 3.8 was used for data analysis and visualization. The PALM code can be accessed at <https://gitlab.palm-model.org/>. We sincerely thank Marie Mazoyer and Christine Lac for reviewing this article. Their numerous valuable comments helped to improve the manuscript. Open Access funding enabled and organized by Projekt DEAL. [Correction added on 28 September 2022, after first online publication: The Acknowledgements section has been amended in this updated version of the article.]

#### CONFLICT OF INTEREST

The authors declare no conflict of interest. The funders had no role in the design of the study, in the collection, analyses, or interpretation of data, in the writing of the manuscript, or in the decision to publish the results.

#### DATA AVAILABILITY STATEMENT

Model steering data and output files of the simulations presented are supplied at <https://doi.org/10.25835/0019390>.

#### ORCID

Johannes Schwenkel  <https://orcid.org/0000-0002-3985-4498>

#### REFERENCES

- Ackerman, A.S., vanZanten, M.C., Stevens, B., Savic-Jovicic, V., Bretherton, C.S., Chlond, A., Golaz, J.-C., Jiang, H., Khairoutdinov, M., Krueger, S.K., Lewellen, D.C., Lock, A., Moeng, C.-H., Nakamura, K., Petters, M.D., Snider, J.R., Weinbrecht, S. and Zulauf, M. (2009) Large-eddy simulations of a drizzling, stratocumulus-topped marine boundary layer. *Monthly Weather Review*, 137(3), 1083–1110.
- Beare, R.J., Macvean, M.K., Holtslag, A.A., Cuxart, J., Esau, I., Golaz, J.-C., Jimenez, M.A., Khairoutdinov, M., Kosovic, B.,

- Lewellen, D., Lund, T.S., Lundquist, J.K., McCabe, A., Moene, A.F., Noh, Y., Raasch, S. and Sullivan, P. (2006) An intercomparison of large-eddy simulations of the stable boundary layer. *Boundary-Layer Meteorology*, 118(2), 247–272.
- Bergot, T. (2013) Small-scale structure of radiation fog: A large-eddy simulation study. *Quarterly Journal of the Royal Meteorological Society*, 139(673), 1099–1112.
- Bergot, T. and Guedalia, D. (1994) Numerical forecasting of radiation fog. Part I: Numerical model and sensitivity tests. *Monthly Weather Review*, 122(6), 1218–1230.
- Boutle, I., Angevine, W., Bao, J.-W., Bergot, T., Bhattacharya, R., Bott, A., Ducongé, L., Forbes, R., Goecke, T., Grell, E., Hill, A., Igel, A.L., Kudzsotsa, I., Lac, C., Maronga, B., Romakkaniemi, S., Schmidli, J., Schwenkel, J., Steeneveld, G.-J. and Vié, B. (2022) Demistify: A large-eddy simulation (LES) and single-column model (SCM) intercomparison of radiation fog. *Atmospheric Chemistry and Physics*, 22(1), 319–333. <https://doi.org/10.5194/acp-22-319-2022>.
- Boutle, I., Price, J., Kudzsotsa, I., Kokkola, H. and Romakkaniemi, S. (2018) Aerosol–fog interaction and the transition to well-mixed radiation fog. *Atmospheric Chemistry and Physics*, 18(11), 7827–7840.
- Brown, A., Cederwall, R., Chlond, A., Duynkerke, P., Golaz, J.C., Khairoutdinov, M., Lewellen, D.C., Lock, A.P., MacVean, M.K., Moeng, C.-H., Nегgers, R.A.J., Siebesma, A.P. and Stevens, B. (2002) Large-eddy simulation of the diurnal cycle of shallow cumulus convection over land. *Quarterly Journal of the Royal Meteorological Society*, 128(582), 1075–1093.
- Clough, S.A., Shephard, M.W., Mlawer, E.J., Delamere, J.S., Iacono, M.J., Cady-Pereira, K., Boukabara, S. and Brown, P.D. (2005) Atmospheric radiative transfer modeling: a summary of the AER codes. *Journal of Quantitative Spectroscopy & Radiative Transfer*, 91(2), 233–244.
- Couvreur, F., Bazile, E., Rodier, Q., Maronga, B., Matheou, G., Chinita, M.J., Edwards, J., van Stratum, B.J.H., van Heerwaarden, C.C., Huang, J., Moene, A.F., Cheng, A., Fuka, V., Basu, S., Bou-Zeid, E., Canut, G. and Vignon, E. (2020) Intercomparison of large-eddy simulations of the Antarctic boundary layer for very stable stratification. *Boundary-Layer Meteorology*, 176(3), 369–400.
- Deardorff, J.W. (1980) Stratocumulus-capped mixed layers derived from a three-dimensional model. *Boundary-Layer Meteorology*, 18(4), 495–527.
- Fernando, H. and Weil, J. (2010) Whither the stable boundary layer? A shift in the research agenda. *Bulletin of the American Meteorological Society*, 91(11), 1475–1484.
- Gehrke, K.F., Sühling, M. and Maronga, B. (2021) Modeling of land-surface interactions in the PALM model system 6.0: Land surface model description, first evaluation, and sensitivity to model parameters. *Geoscientific Model Development*, 14(8), 5307–5329.
- Haefelin, M., Bergot, T., Elias, T., Tardif, R., Carrer, D., Chazette, P., Colomb, M., Drobinski, P., Dupont, E., Dupont, J.-C., Gomes, L., Musson-Genon, L., Pietras, C., Plana-Fattori, A., Protat, A., Rangognio, J., Raut, J.-C., RÁlmy, S., Richard, D., Sciare, J. and Zhang, X. (2010) PARISFOG: Shedding new light on fog physical processes. *Bulletin of the American Meteorological Society*, 91(6), 767–783.
- Izett, J.G., van de Wiel, B.J., Baas, P., van Hooft, J.A. and Schulte, R.B. (2019) Dutch fog: On the observed spatio-temporal variability of fog in the Netherlands. *Quarterly Journal of the Royal Meteorological Society*, 145(723), 2817–2834.
- Maronga, B., Banzhaf, S., Burmeister, C., Esch, T., Forkel, R., Fröhlich, D., Fuka, V., Gehrke, K.F., Geletič, J., Giersch, S., Gronemeier, T., Groß, G., Heldens, W., Hellsten, A., Hoffmann, F., Inagaki, A., Kadasch, E., Kanani-Sühling, F., Ketelsen, K., Khan, B.A., Knigge, C., Knoop, H., Krč, P., Kurppa, M., Maamari, H., Matzarakis, A., Mauder, M., Pallasch, M., Pavlik, D., Pfafferoth, J., Resler, J., Rissmann, S., Russo, E., Salim, M., Schrempf, M., Schwenkel, J., Seckmeyer, G., Schubert, S., Sühling, M., von Tils, R., Vollmer, L., Ward, S., Witha, B., Wurps, H., Zeidler, J. and Raasch, S. (2020a) Overview of the PALM model system 6.0. *Geoscientific Model Development*, 13(3), 1335–1372.
- Maronga, B. and Bosveld, F. (2017) Key parameters for the life cycle of nocturnal radiation fog: A comprehensive large-eddy simulation study. *Quarterly Journal of the Royal Meteorological Society*, 143(707), 2463–2480.
- Maronga, B., Knigge, C. and Raasch, S. (2020b) An improved surface boundary condition for large-eddy simulations based on Monin–Obukhov similarity theory: Evaluation and consequences for grid convergence in neutral and stable conditions. *Boundary-Layer Meteorology*, 174(2), 297–325.
- Maronga, B. and Li, D. (2022) An investigation of the grid sensitivity in large-eddy simulations of the stable boundary layer. *Boundary-Layer Meteorology*, 182(2), 251–273.
- Mazoyer, M., Lac, C., Thouron, O., Bergot, T., Masson, V. and Musson-Genon, L. (2017) Large eddy simulation of radiation fog: Impact of dynamics on the fog life cycle. *Atmospheric Chemistry and Physics*, 17(21), 13017–13035.
- Mellado, J.P. (2017) Cloud-top entrainment in stratocumulus clouds. *Annual Review of Fluid Mechanics*, 49, 145–169.
- Morrison, H., Curry, J.A. and Khvorostyanov, V. (2005) A new double-moment microphysics parameterization for application in cloud and climate models. Part I: Description. *Journal of the Atmospheric Sciences*, 62(6), 1665–1677.
- Nakanishi, M. (2000) Large-eddy simulation of radiation fog. *Boundary-Layer Meteorology*, 94(3), 461–493.
- Rémy, S. and Bergot, T. (2009) Assessing the impact of observations on a local numerical fog prediction system. *Quarterly Journal of the Royal Meteorological Society*, 135(642), 1248–1265.
- Schwenkel, J. and Maronga, B. (2019) Large-eddy simulation of radiation fog with comprehensive two-moment bulk microphysics: Impact of different aerosol activation and condensation parameterizations. *Atmospheric Chemistry and Physics*, 19(10), 7165–7181. <https://doi.org/10.5194/acp-19-7165-2019>.
- Schwenkel, J. and Maronga, B. (2020) Towards a better representation of fog microphysics in large-eddy simulations based on an embedded Lagrangian cloud model. *Atmosphere*, 11(5), 466.
- Seifert, A. and Beheng, K.D. (2001) A double-moment parameterization for simulating autoconversion, accretion and selfcollection. *Atmospheric Research*, 59–60, 265–281.
- Seifert, A. and Beheng, K.D. (2006) A two-moment cloud microphysics parameterization for mixed-phase clouds. Part 1: Model description. *Meteorology and Atmospheric Physics*, 92(1), 45–66. <https://doi.org/10.1007/s00703-005-0112-4>.
- Smith, D., Renfrew, I., Price, J. and Dorling, S. (2018) Numerical modelling of the evolution of the boundary layer during a radiation fog event. *Weather*, 73(10), 310–316.
- Steenefeld, G.J. and de Bode, M. (2018) Unravelling the relative roles of physical processes in modelling the life cycle of a warm

- radiation fog. *Quarterly Journal of the Royal Meteorological Society*, 144(714), 1539–1554.
- Steenefeld, G., Ronda, R. and Holtslag, A. (2015) The challenge of forecasting the onset and development of radiation fog using mesoscale atmospheric models. *Boundary-Layer Meteorology*, 154(2), 265–289.
- van Stratum, B.J. and Stevens, B. (2015) The influence of misrepresenting the nocturnal boundary layer on idealized daytime convection in large-eddy simulation. *Journal of Advances in Modeling Earth Systems*, 7(2), 423–436.
- van Stratum, B.J. and Stevens, B. (2018) The impact of vertical mixing biases in large-eddy simulation on nocturnal low clouds. *Journal of Advances in Modeling Earth Systems*, 10(6), 1290–1303.
- Toledo, F., Haefelin, M., Wærsted, E. and Dupont, J.C. (2021) A new conceptual model for adiabatic fog. *Atmospheric Chemistry and Physics*, 21(17), 13099–13117.
- Vilà-Guerau de Arellano, J. (2007) Role of nocturnal turbulence and advection in the formation of shallow cumulus over land. *Quarterly Journal of the Royal Meteorological Society*, 133(628), 1615–1627.
- Wainwright, C. and Richter, D. (2021) Investigating the sensitivity of marine fog to physical and microphysical processes using large-eddy simulation. *Boundary-Layer Meteorology*, 181(2), 473–498.
- Wærsted, E.G., Haefelin, M., Steeneveld, G.J. and Dupont, J.C. (2019) Understanding the dissipation of continental fog by analysing the LWP budget using idealized LES and in situ observations. *Quarterly Journal of the Royal Meteorological Society*, 145(719), 784–804.
- Wicker, L.J. and Skamarock, W.C. (2002) Time-splitting methods for elastic models using forward time schemes. *Monthly Weather Review*, 130(8), 2088–2097.
- Williamson, J. (1980) Low-storage Runge–Kutta schemes. *Journal of Computational Physics*, 35(1), 48–56.

## SUPPORTING INFORMATION

Additional supporting information can be found online in the Supporting Information section at the end of this article.

**How to cite this article:** Schwenkel, J. & Maronga, B. (2022) On the effect of nocturnal radiation fog on the development of the daytime convective boundary layer: A large-eddy simulation study. *Quarterly Journal of the Royal Meteorological Society*, 1–18. Available from: <https://doi.org/10.1002/qj.4352>

## APPENDIX A. PROCESS CONTRIBUTIONS TERMS

This appendix explains how we derive contributions for single processes of Equations 1 and 2 from the model output. SHF, LHF, LWP, and  $F_{\text{dep}}$  are given as horizontal

averaged time series, which are provided every  $\Delta t_{\text{ts}} = 10$  s. The short-wave heating rates due to absorption and the atmospheric long-wave cooling rates are provided as horizontally averaged and temporal mean profiles as model output every 5 min.

### A.1 Temperature

Following the approach presented in Section 2.3, the process contribution for the SHF is approximated by

$$\left\langle \frac{\delta\theta_{\text{SHF}}}{dt} \right\rangle = \frac{1}{\rho c_p} \frac{\text{SHF}_{\text{CS}} - \text{SHF}_{\text{NF}}}{H_a}, \quad (\text{A1})$$

where SHF has units of  $\text{W}\cdot\text{m}^{-2}$ ,  $\rho$  is the air density (approximated by  $1.29 \text{ kg}\cdot\text{m}^{-3}$ ), and  $c_p = 1,005 \text{ J}\cdot\text{kg}^{-1}\cdot\text{K}^{-1}$  the specific heat capacity of air. Moreover, it is assumed that  $T \approx \theta$ , which is justified for not too large values of  $H_a$ . Contributions for radiative heating rates are calculated as

$$\left\langle \frac{\delta\theta_{\text{lw}}}{dt} \right\rangle = \frac{\langle (R_{\text{lw}})_{\text{CS}} - (R_{\text{lw}})_{\text{NF}} \rangle}{H_a}, \quad (\text{A2})$$

$$\left\langle \frac{\delta\theta_{\text{sw}}}{dt} \right\rangle = \frac{\langle (R_{\text{sw}})_{\text{CS}} - (R_{\text{sw}})_{\text{NF}} \rangle}{H_a}, \quad (\text{A3})$$

with  $R_{\text{lw}}$  and  $R_{\text{sw}}$  as the long- and short-wave heating rates ( $\text{K}\cdot\text{hr}^{-1}$ ), respectively, which are directly calculated within the coupled RRTMG (Clough *et al.*, 2005). Moreover, the temperature is increased (decreased) by the release of latent heat from condensation (evaporation). However, phase transitions within the atmosphere are only simulated in the NFs. Subsequently, we can substitute the microphysics contribution to

$$\left\langle \frac{\delta\theta_{\text{micro}}}{dt} \right\rangle = \frac{1}{\rho c_p} \frac{-l_v \left( \frac{\text{LWP}(t)_{\text{NF}} - \text{LWP}(t-1)_{\text{NF}}}{\Delta t_{\text{ts}}} + F_{\text{dep,NF}} \right)}{H_a}, \quad (\text{A4})$$

where  $l_v = 2.5 \times 10^6 \text{ J}\cdot\text{kg}^{-1}$  is the specific latent heat of vaporization, LWP is the liquid water path, and  $F_{\text{dep}}$  is the surface droplet deposition flux ( $\text{kg}\cdot\text{m}^{-2}\cdot\text{m}\cdot\text{s}^{-1}$ ). Condensation and evaporation rates are implicitly calculated by the change in LWP and the loss due to deposition. For assessing which process is mostly responsible for temperature differences, Equations A1–A4 are integrated to the point in time where differences in temperature were the largest ( $t_{a,\theta}$ ). Exemplary Equation (A1) can be written as

$$\langle \delta\theta_{\text{SHF}} \rangle = \int_0^{t_{a,\theta}} \frac{1}{\rho c_p} \frac{\text{SHF}_{\text{CS}} - \text{SHF}_{\text{NF}}}{H_a} dt, \quad (\text{A5})$$

and Equations A2–A4 are integrated analogously. The time-integrated deviation between the modeled and calculated differences (of the resolved process analysis) is termed the residual and calculated as

$$\langle \delta\theta_{\text{Res}} \rangle = \langle \delta\theta_{t_{a,\theta}} \rangle - \langle \delta\theta_{\text{LHF,veg}} \rangle - \langle \delta\theta_{\text{LHF,liq}} \rangle - \langle \delta\theta_{\text{dep}} \rangle. \quad (\text{A6})$$

### A.2 Water vapor mixing ratio

As for the water vapor mixing ratio, the process contributions are only shown as time-integrated analysis equations and also presented in the integrated form. The difference of the gain (loss) due to a positive (negative) LHF<sub>veg</sub> between CS and NF is given by

$$\langle \delta q_{\text{LHF,veg}} \rangle = \int_0^{t_{a,q}} \frac{1}{\rho l_v} \frac{\text{LHF}_{\text{veg,CS}} - \text{LHF}_{\text{veg,NF}}}{H_a} dt, \quad (\text{A7})$$

where LHF<sub>veg</sub> has units of W·m<sup>-2</sup>. Analogously, for LHF<sub>liq</sub> we have

$$\langle \delta q_{\text{LHF,liq}} \rangle = \int_0^{t_{a,q}} \frac{1}{\rho l_v} \frac{\text{LHF}_{\text{liq,CS}} - \text{LHF}_{\text{liq,NF}}}{H_a} dt. \quad (\text{A8})$$

For the time-integrated analysis of the contribution by microphysics,  $F_{\text{micro}}$  can be substituted with the deposition rate  $F_{\text{dep}}$ . The underlying assumption is that (integrated over the life cycle of the fog) condensation and evaporation is net zero. Hence, the only sink for the water vapor mixing ratio is the deposited amount of liquid water to the surface. Since only the NF case suffers a loss of humidity to due deposition of fog droplets, this is considered by

$$\langle \delta q_{\text{dep}} \rangle = \int_0^{t_{a,q}} \frac{F_{\text{dep}}}{H_a} dt. \quad (\text{A9})$$

The residual is analogous to Equation (A6), calculated by

$$\langle \delta q_{\text{Res}} \rangle = \langle \delta q_{t_{a,q}} \rangle - \langle \delta q_{\text{LHF,veg}} \rangle - \langle \delta q_{\text{LHF,liq}} \rangle - \langle \delta q_{\text{dep}} \rangle. \quad (\text{A10})$$



## 7 Concluding Remarks

### 7.1 Summary

The superordinated subject of this thesis was to improve our understanding of small-scale processes in nocturnal radiation fog (in the following, termed "fog"). Small-scale processes significantly impact fog formation and development and are held responsible for the unsatisfying forecast quality in numerical weather prediction (NWP), as they are difficult to represent or parameterize in numerical models. Using highly-resolved large-eddy simulations (LES) with state-of-the-art methods, the representation of small-scale processes during fog within numerical models has been improved.

In particular, the first two studies focused on the microphysics and their implementation within the LES using different modeling techniques. The first study investigated the effect of various parametrizations for activation and diffusional growth on the development of fog. Three commonly used methods for calculating the supersaturation driving activation in LES have been implemented and tested for simulating fog: (i) the widely used saturation-adjustment scheme with approximated supersaturation (e.g., Cohard et al., 1998), (ii) a diagnostic scheme (e.g., Khvorostyanov, 1995), and (iii) a semi-analytic (also termed as prognostic) scheme (e.g., Clark, 1973; Morrison et al., 2005). While all the methods have their advantages and shortcomings (physically and in terms of computational cost), the feedback on the choice of parametrization was found to be large as fog is very sensitive to the number of activated cloud droplets. In particular, the widely used saturation-adjustment scheme in combination with approximated peak supersaturation overestimated activation, which resulted in 60% higher droplet number concentrations compared to the other two schemes. Consequently, using the saturation-adjustment scheme produced a thicker fog (in terms of a 70% higher liquid water path, LWP) and an about one hour later fog dissipation. Similar behavior has been observed by Thouron et al. (2012), who compared the aforementioned methods on activation in stratocumulus using LES. They reported up to twice the cloud droplet number concentrations for saturation-adjustment with an approximated peak supersaturation scheme.

Based on theory, the underlying assumption of equilibrium in the saturation-adjustment scheme is violated for very-small time steps. However, the error of disregarding the violation and applying saturation-adjustment on droplet growth and the feedback on radiation and dynamics was unknown. By isolating the effect of methods (i)-(iii) only on diffusional growth by prescribing a fixed cloud droplet number concentration, it was shown that differences between the methods were negligible. With only 1% or less difference in the LWP, droplet sizes remained nearly identical and consequently no relevant feedback on sedimentation nor radiation emerged.



In the last part of the first study, the influence of different realizations of the activation types were tested. While there are numerous implementations, the most simple original expression of Twomey (1959) was compared with frequently used extensions of Cohard et al. (1998) and Khvorostyanov and Curry (2006). Even though the activation formulations are similar when trying to reproduce a specific aerosol environment, it was shown that they resulted in different cloud droplet number concentrations. The reason was found in small differences within the activation spectrum.

The second study continued to focus on modeling microphysical processes in fog. A novel and advanced particle-based approach (a so-called Lagrangian Cloud Model, LCM) to simulate fog microphysics was used for the first time to overcome the immanent limitations of bulk cloud models, namely, the parameterized activation and fixed shape of the drop size distribution (DSD). In a comparison of the LCM and bulk cloud model, significant differences between the modeling approaches were observed. On the macroscopic scale, it was found that the onset of fog in the bulk cloud models is delayed compared to the LCM simulation. Furthermore, in agreement with the findings of Boutle et al. (2018), the bulk cloud model tends to overestimate the strength of the fog layer. As a result of both, the visibility drops down earlier in the LCM case, but is undercut by the bulk cloud model in the strengthening stage.

These observations can be linked to the different treatment of microphysics, which also revealed significant differences. As demonstrated by previous studies (e.g., Stolaki et al., 2015; Maalick et al., 2016; Poku et al., 2021), fog development is very sensitive to the cloud droplet number concentration. Although both LCM and the bulk cloud model have been initialized with identical aerosol conditions, lower cloud number concentrations of activated droplets are found for the LCM cases. Moreover, the study suggested that the bulk cloud model underestimated sedimentation as the parameterized relative sedimentation rates (normalized with the LWP) are lower than the ones explicitly calculated by the LCM.

With the benefit of a size-resolved microphysics treatment by the LCM, an analysis of the DSD was carried out. The explicitly resolved DSDs of the LCM showed a bi-modal behavior as also modeled by Bott et al. (1990) and partly observed from Wendisch et al. (1998) and Price (2011). It was found that this bi-modality divides the activated from the un-activated droplets. In contrast to the bulk schemes, where the shape of the DSD is constant by design, results of the study indicate that DSD shape shifts in time. In agreement with the observations of Fuzzi et al. (1992), the DSD is relatively narrow at the formation stage, but more platykurtic in the strengthening stage.

The LES model PALM, which was applied in the studies presented in Chapter 3-6, has been compared to other models in a model intercomparison study for radiation fog (Chapter 5). This was the first intercomparison study for LES and the second for single-column models (SCMs) simulating fog. The study highlighted the difficulties numerical models still have in simulating fog. While for other cloud types or atmospheric boundary layer (ABL) regimes the comparability of LESs was found to be much higher (Beare et al., 2006; Van der Dussen et al., 2013), differences between LES models for the simulation of fog are more distinct. The largest source for model uncertainties were found in the representation of microphysics,



which was differently parameterized by the five participating LES models. However, surface fluxes and turbulent structures also showed notable differences among the models. Although significant progress has been made in the SCMs since the previous intercomparison study (Bergot et al., 2007), SCM results are still unsatisfactory. In general, the SCMs produce a fog that is far too thick (in terms of fog height, liquid water content, and optical thickness).

The last study presented in this thesis focused on the influence of fog on the development of the daily boundary layer. The reasons for failing to represent fog in numerical models are manifold. However, the resulting biases on the daytime convection have not been investigated. The analysis of simulation in pairs, one in which fog develops during the night and one in which fog formation was prohibited, showed that failing to simulate fog results in an overestimation of ABL height and temperature during daytime. Depending on fog strength and environmental conditions, the difference in ABL temperature and height was estimated up to 2.5 K and 200 m, respectively. An analysis of individual physical processes revealed that differences in temperature and humidity between the clear-sky and nocturnal fog cases were mainly driven by differences in longwave cooling (amplified by fog) and droplet deposition (water vapor removal). In accordance with Van Stratum and Stevens (2015), artificial moist daytime convection is usually not initiated by unresolved fog.

All in all, the research presented in this thesis confirmed known issues, unveiled new insights, quantified relevant processes, and highlighted unprecedented perspectives in modeling fog. While extensively discussed in literature, a special focus has been set on microphysics in fogs. The need for improved parametrizations was demonstrated by presenting two studies on the performance of different microphysical parameterizations on modeling fog (Chapter 3 and 5). Moreover, new perspectives were highlighted by applying an advanced model technique for microphysics (the LCM) to simulate fog for the first time with that approach (Chapter 4). By demonstrating what effect failing to resolve fog has on the development of the daytime boundary layer (Chapter 6), the importance of not only the time-span of fog itself but also of the ongoing day was assessed. All these studies led to an increased knowledge of fog processes and their challenges while modeling and possibly ultimately contributing to improved fog forecasts in numerical weather prediction.

## 7.2 Outlook

This thesis aimed to improve understanding and representation of small-scale processes and their interaction during fog in numerical models. However, certain questions arose from the findings of the presented studies, which should be covered in future studies.

The representation of microphysical processes during fog have been improved and their uncertainties were evaluated. Although in Chapter 4 microphysics were depicted by a sophisticated state-of-the-art approach (the LCM), the results have only been qualitatively compared against observational data. Thus, a rigorous evaluation of how microphysical representation performs quantitatively against observational data is still pending. For such a comparison, a dataset containing both spatially and temporally high-resolved aerosol spectra and DSDs during fog is required. Although there is a lack of such datasets, the LANFEX

campaign (Price et al., 2018) provides measurements of aerosol and droplet distributions for one location. Thus, a future study could aim to compare model results with available observational data by initializing the model with measured aerosol distribution. This would help determine the accuracy of current state-of-the-art models in representing microphysics during fog and identify any missing or insufficiently resolved processes. Based on these results, recommendations could be made on how to improve microphysical parametrizations in numerical weather prediction models.

In Chapter 4, a LCM was used to simulate fog. As such an approach allows resolution of the DSD explicitly, it generally facilitates for consideration of more complex physical processes. One of these processes is the enhanced diffusional growth by radiative cooling of droplets (Roach, 1976). Under conditions where the droplet environment is being cooled by radiation, as is common for fog, droplets might become colder than their environment due to a radiative flux divergence. As a result, droplet growth is possible in an atmosphere in equilibrium or even in slightly subsaturated environments. To account for that, the diffusional growth equation must be extended by a term considering the radiative properties of the fog droplet. Numerical studies of Bott et al. (1990) and Bott (2021) showed that including this effect leads to quasi-periodic fluctuations in liquid water content of the fog layer. These are caused by the accelerated diffusional growth (due to the radiation term in the diffusional growth equation) which in turn amplifies sedimentation velocities and thus cause a faster reduction of liquid water from the fog layer. However, such investigations have only been carried out for SCMs. Therefore, a next step would be to extend the diffusional growth equation in the LCM by the explicit radiation term instead of parameterizing radiative cooling by the cloud droplet effective radius and liquid water content for each grid box as was done in the presented studies in this thesis (and as is usually done by other models). Moreover, it would be valuable to explore if fluctuations in liquid water content and related variables can be observed using the novel particle-based approach coupled with a three-dimensional (3D) LES. Additionally, the LCM provides the opportunity to evaluate the impact of the radiation term in the diffusional growth equation on environmental humidity and secondary activation.

Although column-based radiation schemes are commonly used (and also applied in the studies presented in this thesis), they are not able to represent the 3D-nature of radiative processes. In particular, such schemes neglect thermal cooling at the edge of clouds or fog layers by design. Moreover, the angle of incoming solar radiation can not be represented, i.e., shading effects are excluded. However, 3D-radiative processes might become important during fog formation and dissipation or for patchy fog patterns. Although a sophisticated 3D radiation-solver (the so-called Tensream scheme; Jakub and Mayer, 2016) was recently added to the used LES model, future work could evaluate the effect of lateral fog cooling and its impact on fog dynamics. The latter effect might be crucial for a lateral spreading mechanism of fog (posited by Price et al., 2015, based on the analysis of observation data), caused by a thermal circulation at the fog edge. Price et al. (2015) concluded that cold cloudy air subsides into and mixes with the warmer adjacent air, generating a saturated air mass. However, this hypothesis has not yet been proven by numerical models. Thus, investigating if the lateral fog spreading mechanism can be modeled and if so how relevant lateral cooling

is could be addressed in future work.

Beyond small-scale processes in fog, the used model is also a perfect tool to study the influence of surface heterogeneity and orographic effects on fog. As shown by observations for nearby sites different fog regimes (deep fog, shallow fog, and no fog) develop at the same time Bergot and Lestringant (2019). It was concluded that the main reason can be found by the surface properties and orography of the locations (e.g., Bergot and Lestringant, 2019). To evaluate the influence of heterogeneities systematically, the model could be initialized with idealized surface heterogeneity patterns (e.g., stripe-like or checkerboard pattern) as a first step. With such simulation data, surface conditions under which fog onset is preferred, advanced, or delayed could be identified. Moreover, the effect of surface heterogeneity-induced circulations on the fog structure could be analyzed. In the second step, a real environment with complex terrain could be simulated (e.g., the Lindenberg site area). While a former study by Maronga and Bosveld (2017) and the study presented in Chapter 5 could be understood as a validation of the model for fog in homogeneous terrain, future work should assess their performance for simulating fog in complex environments.



## Acknowledgements

Als Erstes möchte ich mich ganz herzlich bei Prof. Dr. Björn Maronga, meinem Doktorvater, bedanken, der mir das Vertrauen geschenkt hat, mich diesem Projekt anzunehmen. Ich bedanke mich vor allem für den konstruktiven fachlichen Austausch während dieser Zeit, die Unterstützung beim Fokussieren auf notwendige Zwischenschritte sowie die fachliche und finanzielle Förderung, die auch die Teilnahme an unterschiedlichen internationalen Konferenzen ermöglicht hat. Auch möchte ich mich für sein Verständnis bedanken, dass es während des Promotionszeitraums familiäre Situationen gab, in denen der Fokus nicht auf dieser Arbeit liegen konnte.

Ich bedanke mich auch herzlich bei Prof. Dr. Siegfried Raasch, der mich bereits als Masterstudent in die PALM-Arbeitsgruppe aufgenommen hat. Ich kann mich noch sehr genau an die Vorlesung zur theoretischen Meteorologie im zweiten Bachelor-Semester erinnern, die nachhaltig mein Interesse für atmosphärische Prozesse fernab des mit dem menschlichen Auge erkennbaren entfacht hat.

Mijn dank gaat ook uit naar Prof. Dr. Gert-Jan Steeneveld, die bereid was dit werk te evalueren. Auch danke ich Prof. Dr. Gunnar Friege, der sich bereit erklärt hat den Prüfungsvorsitz zu übernehmen.

Für das kritische Korrekturlesen dieser Arbeit bedanke ich mich herzlichst bei Micha Gryschka, Helge Knoop, Oliver Maas und Simon Ward.

Ich bin der Überzeugung, dass es einem besser gelingt, eine solche Arbeit zu erstellen, wenn man sich in einem schönen Arbeitsumfeld befindet. Für ein solches gilt mein Dank dem Kollegium und Studierenden des Instituts für Meteorologie und Klimatologie. Im Besonderen Berit und Petra für das offene Ohr zwischen Tür und Angel und das Korrigieren von sämtlichen Anträgen. Dem technischen und wissenschaftlichen Personal Uli, Notker und Micha für die Unterstützung, wenn es hakt, im Büro oder im Kopf. Sowie meinen lieben Kommilitonen und Kollegen für die gesamte Zeit, ob kurz oder lang. Ich denke da ganz speziell an Helge und die guten Büroabende sowie die nette Zeit am Deisterrand. Auch danke ich Katrin, Katja, Anna, Veit und Agnes für eine wunderbare Zeit im Studium. Egal ob im Büro oder nebenan, für fachlichen Austausch oder politische Gespräche und den guten Kaffee bedanke ich mich auch noch bei Oliver, Matthias, Fabian, Tobias, Farah, Basti, Lara, Charly, Giovanna, Pierre und Chris. Auch möchte ich mich herzlich bei drei ehemaligen Kollegen des Instituts bedanken: Christopher, Steffen und Simon. Schön, dass wir so viele gute Spiele mit den Frox bestreiten konnten, noch glücklicher bin ich, mit Euch freundschaftlich verbunden zu bleiben. In diesem Zuge sei auch dem gesamten Team der Flying Frox gedankt, mit dem ich die Ehre hatte, großartige Erfolge zu feiern und Niederlagen schön zu reden.

Ein ganz besonderer Dank gilt meiner Familie und meinen Freunden für die Liebe und Unterstützung in dieser Zeit. Meinen Eltern, Barbara und Hans-Georg, sowie Gosia und

meinen Schwiegereltern, Erika und Kurt, sei insbesondere gedankt für das Mitfiebern im Review-Prozess sowie das leckere Essen und das einfühlsame Dasein, falls es mal nicht so gut lief. Zuletzt möchte ich mich bei Dir, Sonja, bedanken. Ich bin sehr glücklich, dich kennengelernt zu haben und möchte Dir für die Art, wie du mich unterstützt und bestärkt hast, danke sagen. Schön, dass wir den Weg gemeinsam gehen konnten. Die Arbeit (oder zumindest das Ende davon) widme ich Dir, Felina. So fröhlich wie du in unser Leben gehüpft bist, mache ich mir keine Sorgen, dass sich der Nebel nicht jeden morgen aufs Neue lichtet.

## Bibliography

- Abdul-Razzak, H., Ghan, S. J., and Rivera-Carpio, C.: A parameterization of aerosol activation: 1. Single aerosol type, *J. Geophys. Res. Atmos.*, 103, 6123–6131, 1998.
- Ackerman, A. S., Stevens, B., Savic-Jovicic, V., Bretherton, C. S., Chlond, A., Golaz, J.-C., Jiang, H., Khairoutdinov, M., Krueger, S. K., Lewellen, D. C., et al.: Large-eddy simulations of a drizzling, stratocumulus-topped marine boundary layer, *Mon. Wea. Rev.*, 137, 1083–1110, 2009.
- Ambartzumian, V.: The effect of the absorption lines on the radiative equilibrium of the outer layers of the stars, *Publ. Obs. Astron. Univ., Leningrad*, 6, 7–18, 1936.
- American Meteorological Society: AMS Glossary, URL <https://glossary.ametsoc.org/wiki/Fog>, 2012.
- Andrejczuk, M., Reisner, J., Henson, B., Dubey, M., and Jeffery, C.: The potential impacts of pollution on a nondrizzling stratus deck: Does aerosol number matter more than type?, *J. Geophys. Res. Atmos.*, 113, 2008.
- Árnason, G. and Brown, P. S.: Growth of cloud droplets by condensation: A problem in computational stability, *J. Atmos. Sci.*, 28, 72–77, 1971.
- Balsamo, G., Beljaars, A., Scipal, K., Viterbo, P., van den Hurk, B., Hirschi, M., and Betts, A. K.: A revised hydrology for the ECMWF model: Verification from field site to terrestrial water storage and impact in the Integrated Forecast System, *J. Hydrometeorol.*, 10, 623–643, 2009.
- Beare, R. J., Macvean, M. K., Holtslag, A. A., Cuxart, J., Esau, I., Golaz, J.-C., Jimenez, M. A., Khairoutdinov, M., Kosovic, B., Lewellen, D., et al.: An intercomparison of large-eddy simulations of the stable boundary layer, *Boundary-Layer Meteorol.*, 118, 247–272, 2006.
- Bergot, T.: Small-scale structure of radiation fog: a large-eddy simulation study, *Quart. J. Roy. Meteor. Soc.*, 139, 1099–1112, 2013.
- Bergot, T.: Large-eddy simulation study of the dissipation of radiation fog, *Quart. J. Roy. Meteor. Soc.*, 142, 1029–1040, 2016.
- Bergot, T. and Lestringant, R.: On the predictability of radiation fog formation in a mesoscale model: A case study in heterogeneous terrain, *Atmosphere*, 10, 165, 2019.

- Bergot, T., Terradellas, E., Cuxart, J., Mira, A., Liechti, O., Mueller, M., and Nielsen, N. W.: Intercomparison of single-column numerical models for the prediction of radiation fog, *J. Appl. Meteor.*, 46, 504–521, 2007.
- Bott, A.: Comparison of a spectral microphysics and a two-moment cloud scheme: Numerical simulation of a radiation fog event, *Atmos. Res.*, 262, 105–178, 2021.
- Bott, A., Sievers, U., and Zdunkowski, W.: A radiation fog model with a detailed treatment of the interaction between radiative transfer and fog microphysics, *J. Atmos. Sci.*, 47, 2153–2166, 1990.
- Bougeault, P.: Modeling the trade-wind cumulus boundary layer. Part I: Testing the ensemble cloud relations against numerical data, *J. Atmos. Sci.*, 38, 2414–2428, 1981.
- Boutle, I., Price, J., Kudzsotsa, I., Kokkola, H., and Romakkaniemi, S.: Aerosol–fog interaction and the transition to well-mixed radiation fog, *Atmos. Chem. Phys.*, 18, 7827–7840, 2018.
- Briegleb, B., Minnis, P., Ramanathan, V., and Harrison, E.: Comparison of regional clear-sky albedos inferred from satellite observations and model computations, *J. Appl. Meteor.*, 25, 214–226, 1986.
- Clark, T. L.: Numerical modeling of the dynamics and microphysics of warm cumulus convection, *J. Atmos. Sci.*, 30, 857–878, 1973.
- Clough, S., Shephard, M., Mlawer, E., Delamere, J., Iacono, M., Cady-Pereira, K., Boukabara, S., and Brown, P.: Atmospheric radiative transfer modeling: A summary of the AER codes, *J. Quant. Spectrosc. Radiat. Transf.*, 91, 233–244, 2005.
- Cohard, J.-M., Pinty, J.-P., and Bedos, C.: Extending Twomey’s analytical estimate of nucleated cloud droplet concentrations from CCN spectra, *J. Atmos. Sci.*, 55, 3348–3357, 1998.
- Déqué, M., Drevet, C., Braun, A., and Cariolle, D.: The ARPEGE/IFS atmosphere model: a contribution to the French community climate modelling, *Clim. Dyn.*, 10, 249–266, 1994.
- Duynkerke, P. G.: Turbulence, radiation and fog in Dutch stable boundary layers, *Boundary-Layer Meteorol.*, 90, 447–477, 1999.
- Emanuel, K. A.: *Atmospheric convection*, Oxford University Press, 1994.
- Ferziger, J. H.: Large eddy numerical simulations of turbulent flows, *AIAA Journal*, 15, 1261–1267, 1977.
- Fick, A.: Über diffusion, *Ann. Phys.*, 170, 59–86, 1855.
- Flossmann, A. I., Hall, W., and Pruppacher, H.: A theoretical study of the wet removal of atmospheric pollutants. Part I: The redistribution of aerosol particles captured through



- nucleation and impaction scavenging by growing cloud drops, *J. Atmos. Sci.*, 42, 583–606, 1985.
- Fuzzi, S., Facchini, M., Orsi, G., Lind, J., Wobrock, W., Kessel, M., Maser, R., Jaeschke, W., Enderle, K., Arends, B., et al.: The Po valley fog experiment 1989, *Tellus B*, 44, 448–468, 1992.
- Gehrke, K. F., Sühling, M., and Maronga, B.: Modeling of land–surface interactions in the PALM model system 6.0: land surface model description, first evaluation, and sensitivity to model parameters, *Geosci. Model Dev.*, 14, 5307–5329, 2021.
- Ghan, S., Chuang, C., Easter, R., and Penner, J.: A parameterization of cloud droplet nucleation. Part II: Multiple aerosol types, *Atmos. Res.*, 36, 39–54, 1995.
- Goody, R. M. and Yung, Y. L.: *Atmospheric radiation: theoretical basis*, Oxford university press, 1989.
- Grabowski, W. W. and Morrison, H.: Toward the mitigation of spurious cloud-edge super-saturation in cloud models, *Mon. Wea. Rev.*, 136, 1224–1234, 2008.
- Grabowski, W. W. and Wang, L.-P.: Growth of cloud droplets in a turbulent environment, *Annu. Rev. Fluid Mech.*, 45, 293–324, 2013.
- Grabowski, W. W., Dziekan, P., and Pawlowska, H.: Lagrangian condensation microphysics with Twomey CCN activation, *Geosci. Model Dev.*, 11, 103–120, 2018.
- Grabowski, W. W., Morrison, H., Shima, S.-I., Abade, G. C., Dziekan, P., and Pawlowska, H.: Modeling of cloud microphysics: Can we do better?, *Bull. Amer. Meteor. Soc.*, 100, 655–672, 2019.
- Gultepe, I., Müller, M. D., and Boybeyi, Z.: A new visibility parameterization for warm-fog applications in numerical weather prediction models, *J. Appl. Meteor.*, 45, 1469–1480, 2006.
- Gultepe, I., Tardif, R., Michaelides, S. C., Cermak, J., Bott, A., Bendix, J., Müller, M. D., Pagowski, M., Hansen, B., Ellrod, G., et al.: Fog research: A review of past achievements and future perspectives, *Pure Appl. Geophys.*, 164, 1121–1159, 2007.
- Heus, T., van Heerwaarden, C. C., Jonker, H. J., Pier Siebesma, A., Axelsen, S., Van Den Dries, K., Geoffroy, O., Moene, A., Pino, D., De Roode, S., et al.: Formulation of the Dutch Atmospheric Large-Eddy Simulation (DALES) and overview of its applications, *Geosci. Model Dev.*, 3, 415–444, 2010.
- Hoffmann, F. and Feingold, G.: Entrainment and mixing in stratocumulus: Effects of a new explicit subgrid-scale scheme for large-eddy simulations with particle-based microphysics, *J. Atmos. Sci.*, 76, 1955–1973, 2019.

- Iacono, M. J., Mlawer, E. J., Clough, S. A., and Morcrette, J.-J.: Impact of an improved longwave radiation model, RRTM, on the energy budget and thermodynamic properties of the NCAR community climate model, CCM3, *J. Geophys. Res. Atmos.*, 105, 14 873–14 890, 2000.
- Izett, J. G., van de Wiel, B. J., Baas, P., van Hooft, J. A., and Schulte, R. B.: Dutch fog: On the observed spatio-temporal variability of fog in the Netherlands, *Quart. J. Roy. Meteor. Soc.*, 145, 2817–2834, 2019.
- Jaenicke, R.: Tropospheric aerosols, in: *Aerosol-Cloud-Climate Interactions*, edited by Hobbs, P. V., vol. 54, pp. 1–31, Academic Press, 1993.
- Jakub, F. and Mayer, B.: 3-D radiative transfer in large-eddy simulations—experiences coupling the TenStream solver to the UCLA-LES, *Geosci. Model Dev.*, 9, 1413–1422, 2016.
- Justo, J.: Fog structure in clouds: their formation, optical properties and effects, Academic Press, edited by PV Hobbs and A. Deepak, 187, 235, 1981.
- Khain, A., Ovtchinnikov, M., Pinsky, M., Pokrovsky, A., and Krugliak, H.: Notes on the state-of-the-art numerical modeling of cloud microphysics, *Atmos. Res.*, 55, 159–224, 2000.
- Khairoutdinov, M. and Kogan, Y.: A new cloud physics parameterization in a large-eddy simulation model of marine stratocumulus, *Mon. Wea. Rev.*, 128, 229–243, 2000.
- Khvorostyanov, V. I.: Mesoscale processes of cloud formation, cloud-radiation interaction, and their modelling with explicit cloud microphysics, *Atmos. Res.*, 39, 1–67, 1995.
- Khvorostyanov, V. I. and Curry, J. A.: Aerosol size spectra and CCN activity spectra: Reconciling the lognormal, algebraic, and power laws, *J. Geophys. Res. Atmos.*, 111, 2006.
- Khvorostyanov, V. I. and Curry, J. A.: Refinements to the Köhler’s theory of aerosol equilibrium radii, size spectra, and droplet activation: Effects of humidity and insoluble fraction, *J. Geophys. Res. Atmos.*, 112, 2007.
- Kogan, Y. L. and Martin, W. J.: Parameterization of bulk condensation in numerical cloud models, *J. Atmos. Sci.*, 51, 1728–1739, 1994.
- Köhler, H.: The nucleus in and the growth of hygroscopic droplets, *Trans. Faraday Soc.*, 32, 1152–1161, 1936.
- Koschmieder, H.: Theorie der horizontalen Sichtweite, *Beitrage zur Physik der freien Atmosphäre*, pp. 33–53, 1924.
- Larson, V. E., Kotenberg, K. E., and Wood, N. B.: An analytic longwave radiation formula for liquid layer clouds, *Mon. Wea. Rev.*, 135, 689–699, 2007.
- Liou, K.: *An Introduction to Atmospheric Radiation*, 392 Academic Press, Academic Press, 1980.

- Maalick, Z., Kühn, T., Korhonen, H., Kokkola, H., Laaksonen, A., and Romakkaniemi, S.: Effect of aerosol concentration and absorbing aerosol on the radiation fog life cycle, *Atmos. Environ.*, 133, 26–33, 2016.
- Maronga, B. and Bosveld, F.: Key parameters for the life cycle of nocturnal radiation fog: a comprehensive large-eddy simulation study, *Quart. J. Roy. Meteor. Soc.*, 143, 2463–2480, 2017.
- Maronga, B., Gryschka, M., Heinze, R., Hoffmann, F., Kanani-Sühring, F., Keck, M., Ketelsen, K., Letzel, M. O., Sühring, M., and Raasch, S.: The Parallelized Large-Eddy Simulation Model (PALM) version 4.0 for atmospheric and oceanic flows: model formulation, recent developments, and future perspectives, *Geosci. Model Dev.*, 8, 2515–2551, 2015.
- Maronga, B., Banzhaf, S., Burmeister, C., Esch, T., Forkel, R., Fröhlich, D., Fuka, V., Gehrke, K. F., Geletič, J., Giersch, S., Gronemeier, T., Groß, G., Heldens, W., Hellsten, A., Hoffmann, F., Inagaki, A., Kadasch, E., Kanani-Sühring, F., Ketelsen, K., Khan, B. A., Knigge, C., Knoop, H., Krč, P., Kurppa, M., Maamari, H., Matzarakis, A., Mauder, M., Pallasch, M., Pavlik, D., Pfafferoth, J., Resler, J., Rissmann, S., Russo, E., Salim, M., Schrempf, M., Schwenkel, J., Seckmeyer, G., Schubert, S., Sühring, M., von Tils, R., Vollmer, L., Ward, S., Witha, B., Wurps, H., Zeidler, J., and Raasch, S.: Overview of the PALM model system 6.0, *Geosci. Model Dev.*, 13, 1335–1372, 2020.
- Mazoyer, M., Lac, C., Thouron, O., Bergot, T., Masson, V., and Musson-Genon, L.: Large eddy simulation of radiation fog: impact of dynamics on the fog life cycle, *Atmos. Chem. Phys.*, 17, 13 017–13 035, 2017.
- Mellado, J. P.: Cloud-top entrainment in stratocumulus clouds, *Annu. Rev. Fluid Mech.*, 49, 145–169, 2017.
- Moin, P. and Mahesh, K.: Direct Numerical Simulation: A Tool in Turbulence Research, *Annu. Rev. Fluid Mech.*, 30, 539–578, 1998.
- Mordy, W.: Computations of the growth by condensation of a population of cloud droplets, *Tellus*, 11, 16–44, 1959.
- Morrison, H. and Grabowski, W. W.: Modeling supersaturation and subgrid-scale mixing with two-moment bulk warm microphysics, *J. Atmos. Sci.*, 65, 792–812, 2008.
- Morrison, H., Curry, J., and Khvorostyanov, V.: A new double-moment microphysics parameterization for application in cloud and climate models. Part I: Description, *J. Atmos. Sci.*, 62, 1665–1677, 2005.
- Morrison, H., van Lier-Walqui, M., Fridlind, A. M., Grabowski, W. W., Harrington, J. Y., Hoose, C., Korolev, A., Kumjian, M. R., Milbrandt, J. A., Pawlowska, H., et al.: Confronting the challenge of modeling cloud and precipitation microphysics, *J. Adv. Model. Earth Syst.*, 12, e2019MS001 689, 2020.

- Nakanishi, M.: Large-eddy simulation of radiation fog, *Boundary-Layer Meteor.*, 94, 461–493, 2000.
- Naumann, A. K. and Seifert, A.: A Lagrangian drop model to study warm rain microphysical processes in shallow cumulus, *J. Adv. Model. Earth Syst.*, 7, 1136–1154, 2015.
- Pilié, R., Mack, E., Kocmond, W., Eadie, W., and Rogers, C.: The life cycle of valley fog. Part II: Fog microphysics, *J. Appl. Meteor.*, 14, 364–374, 1975.
- Pincus, R., Barker, H. W., and Morcrette, J.-J.: A fast, flexible, approximate technique for computing radiative transfer in inhomogeneous cloud fields, *J. Geophys. Res. Atmos.*, 108, 2003.
- Poku, C., Ross, A. N., Hill, A. A., Blyth, A. M., and Shipway, B.: Is a more physical representation of aerosol activation needed for simulations of fog?, *Atmos. Chem. Phys.*, 21, 7271–7292, 2021.
- Porson, A., Price, J., Lock, A., and Clark, P.: Radiation fog. Part II: Large-eddy simulations in very stable conditions, *Boundary-Layer Meteor.*, 139, 193–224, 2011.
- Price, J.: Radiation fog. Part I: observations of stability and drop size distributions, *Boundary-Layer Meteor.*, 139, 167–191, 2011.
- Price, J., Porson, A., and Lock, A.: An observational case study of persistent fog and comparison with an ensemble forecast model, *Boundary-Layer Meteor.*, 155, 301–327, 2015.
- Price, J., Lane, S., Boutle, I., Smith, D., Bergot, T., Lac, C., Duconge, L., McGregor, J., Kerr-Munslow, A., Pickering, M., et al.: LANFEX: a field and modeling study to improve our understanding and forecasting of radiation fog, *Bull. Amer. Meteor. Soc.*, 99, 2061–2077, 2018.
- Pruppacher, H. R., Klett, J. D., and Wang, P. K.: *Microphysics of clouds and precipitation*, Kluwer Academic Publishers, 2 edn., 1998.
- Rémy, S. and Bergot, T.: Assessing the impact of observations on a local numerical fog prediction system, *Quart. J. Roy. Meteor. Soc.*, 135, 1248–1265, 2009.
- Richter, D. H., MacMillan, T., and Wainwright, C.: A Lagrangian cloud model for the study of marine fog, *Boundary-Layer Meteor.*, 181, 523–542, 2021.
- Riechelmann, T., Noh, Y., and Raasch, S.: A new method for large-eddy simulations of clouds with Lagrangian droplets including the effects of turbulent collision, *New J. Phys.*, 14, 065 008, 2012.
- Roach, W.: On the effect of radiative exchange on the growth by condensation of a cloud or fog droplet, *Quart. J. Roy. Meteor. Soc.*, 102, 361–372, 1976.
- Roach, W., Brown, R., Caughey, S., Garland, J., and Readings, C.: The physics of radiation fog: I—a field study, *Quart. J. Roy. Meteor. Soc.*, 102, 313–333, 1976.

- Rogers, R. and Yau, M.: A short course in cloud physics, Pergamon Press, 1989.
- Rogers, R., Baumgardner, D., Ethier, S., Carter, D., and Ecklund, W.: Comparison of raindrop size distributions measured by radar wind profiler and by airplane, *J. Appl. Meteor.*, 32, 694–699, 1993.
- Román-Cascón, C., Yagüe, C., Sastre, M., Maqueda, G., Salamanca, F., and Viana, S.: Observations and WRF simulations of fog events at the Spanish Northern Plateau, *Adv. Sci. Res.*, 8, 11–18, 2012.
- Rooth, C.: On a special aspect of the condensation process and its importance in the treatment of cloud particle growth, *Tellus*, 9, 372–377, 1957.
- Seifert, A. and Beheng, K. D.: A double-moment parameterization for simulating autoconversion, accretion and selfcollection, *Atmos. Res.*, 59, 265–281, 2001.
- Seifert, A. and Beheng, K. D.: A two-moment cloud microphysics parameterization for mixed-phase clouds. Part 1: Model description, *Meteorol. Atmospheric Phys.*, 92, 45–66, 2006.
- Seifert, A. and Stevens, B.: Microphysical scaling relations in a kinematic model of isolated shallow cumulus clouds, *J. Atmos. Sci.*, 67, 1575–1590, 2010.
- Shaw, R. A.: Particle-turbulence interactions in atmospheric clouds, *Annu. Rev. Fluid Mech.*, 35, 183–227, 2003.
- Shima, S., Sato, Y., Hashimoto, A., and Misumi, R.: Predicting the morphology of ice particles in deep convection using the super-droplet method: development and evaluation of SCALE-SDM 0.2.5-2.2.0, -2.2.1, and -2.2.2, *Geosci. Model Dev.*, 13, 4107–4157, 2020.
- Shima, S.-i., Kusano, K., Kawano, A., Sugiyama, T., and Kawahara, S.: The super-droplet method for the numerical simulation of clouds and precipitation: A particle-based and probabilistic microphysics model coupled with a non-hydrostatic model, *Quart. J. Roy. Meteor. Soc.*, 135, 1307–1320, 2009.
- Sölch, I. and Kärcher, B.: A large-eddy model for cirrus clouds with explicit aerosol and ice microphysics and Lagrangian ice particle tracking, *Quart. J. Roy. Meteor. Soc.*, 136, 2074–2093, 2010.
- Sommeria, G. and Deardorff, J.: Subgrid-scale condensation in models of nonprecipitating clouds, *J. Atmos. Sci.*, 34, 344–355, 1977.
- Steenefeld, G.-J., Ronda, R., and Holtslag, A.: The challenge of forecasting the onset and development of radiation fog using mesoscale atmospheric models, *Boundary-Layer Meteorol.*, 154, 265–289, 2015.
- Stevens, B., Ackerman, A. S., Albrecht, B. A., Brown, A. R., Chlond, A., Cuxart, J., Duykerke, P. G., Lewellen, D. C., Macvean, M. K., Neggers, R. A., et al.: Simulations of trade wind cumuli under a strong inversion, *J. Atmos. Sci.*, 58, 1870–1891, 2001.

- Stolaki, S., Haeffelin, M., Lac, C., Dupont, J.-C., Elias, T., and Masson, V.: Influence of aerosols on the life cycle of a radiation fog event. A numerical and observational study, *Atmos. Res.*, 151, 146–161, 2015.
- Straka, J. M.: *Cloud and precipitation microphysics: principles and parameterizations*, Cambridge University Press, 2009.
- Stull, R. B.: *An introduction to boundary layer meteorology*, vol. 13, Springer Science & Business Media, 1988.
- Teixeira, J.: Simulation of fog with the ECMWF prognostic cloud scheme, *Quart. J. Roy. Meteor. Soc.*, 125, 529–552, 1999.
- Thouren, O., Brenguier, J.-L., and Burnet, F.: Supersaturation calculation in large eddy simulation models for prediction of the droplet number concentration, *Geosci. Model Dev.*, 5, 761–772, 2012.
- Tudor, M.: Impact of horizontal diffusion, radiation and cloudiness parameterization schemes on fog forecasting in valleys, *Meteorol. Atmospheric Phys.*, 108, 57–70, 2010.
- Twomey, S.: The nuclei of natural cloud formation part II: The supersaturation in natural clouds and the variation of cloud droplet concentration, *Geofisica pura e applicata*, 43, 243–249, 1959.
- Unterstrasser, S., Hoffmann, F., and Lerch, M.: Collection/aggregation algorithms in Lagrangian cloud microphysical models: Rigorous evaluation in box model simulations, *Geosci. Model Dev.*, 10, 1521–1548, 2017.
- Van der Dussen, J., De Roode, S., Ackerman, A., Blossey, P., Bretherton, C., Kurowski, M., Lock, A., Neggers, R., Sandu, I., and Siebesma, A.: The GASS/EUCLIPSE model intercomparison of the stratocumulus transition as observed during ASTEX: LES results, *J. Adv. Model. Earth Syst.*, 5, 483–499, 2013.
- Van Stratum, B. J. and Stevens, B.: The influence of misrepresenting the nocturnal boundary layer on idealized daytime convection in large-eddy simulation, *J. Adv. Model. Earth Syst.*, 7, 423–436, 2015.
- van Stratum, B. J. and Stevens, B.: The Impact of Vertical Mixing Biases in Large-Eddy Simulation on Nocturnal Low Clouds, *J. Adv. Model. Earth Syst.*, 10, 1290–1303, 2018.
- Vilà-Guerau de Arellano, J.: Role of nocturnal turbulence and advection in the formation of shallow cumulus over land, *Quart. J. Roy. Meteor. Soc.*, 133, 1615–1627, 2007.
- Viterbo, P. and Beljaars, A. C.: An improved land surface parameterization scheme in the ECMWF model and its validation, *J. Clim.*, 8, 2716–2748, 1995.
- Von der Emde, K. and Wacker, U.: Comments on the relationships between aerosol spectra, equilibrium drop size spectra, and CCN spectra, *Contr. Atmos. Phys.*, 66, 157–162, 1993.

- Wærsted, E. G., Haeffelin, M., Steeneveld, G.-J., and Dupont, J.-C.: Understanding the dissipation of continental fog by analysing the LWP budget using idealized LES and in situ observations, *Quart. J. Roy. Meteor. Soc.*, 145, 784–804, 2019.
- Wainwright, C. and Richter, D.: Investigating the sensitivity of marine fog to physical and microphysical processes using large-eddy simulation, *Boundary-Layer Meteor.*, 181, 473–498, 2021.
- Wendisch, M., Mertes, S., Heintzenberg, J., Wiedensohler, A., Schell, D., Wobrock, W., Frank, G., Martinsson, B. G., Fuzzi, S., Orsi, G., et al.: Drop size distribution and LWC in Po Valley fog, *Contr. Atmos. Phys.*, 71, 1998.
- Zhou, B., Du, J., Gultepe, I., and Dimego, G.: Forecast of low visibility and fog from NCEP: Current status and efforts, *Pure Appl. Geophys.*, 169, 895–909, 2012.





# Curriculum Vitae

## Personal Details

Name	Johannes Schwenkel
Date of Birth	18.07.1989
Birthplace	Langenhagen
Nationality	German

## Education

2010-2013	B.Sc. in Meteorology, Leibniz Universität Hannover, Germany.
2013-2016	M.Sc. in Meteorology, Leibniz Universität Hannover, Germany.
since 2017	Ph.D. student, Leibniz Universität Hannover, Germany.

## Awards

2014	Lower Saxony scholarship
2013	Seilkopf price of the Institute for Meteorology and Climatology, Hannover.

## Publications

### Journals

Schwenkel, J., and Maronga, B.: On the effect of nocturnal radiation fog on the development of the daytime convective boundary layer: A large-eddy simulation study, *Quart. J. Roy. Meteor. Soc.*, 148, 3166-3183, doi: 10.1002/qj.4352, 2022.

Boutle, I., Angevine, W., Bao, J.-W., Bergot, T., Bhattacharya, R., Bott, A., Ducongé, L., Forbes, R., Goecke, T., Grell, E., Hill, A., Igel, A. L., Kudzotsa, I., Lac, C., Maronga, B., Romakkaniemi, S., Schmidli, J., Schwenkel, J., Steeneveld, G.-J., and Vié, B.: Demistify: a large-eddy simulation (LES) and single-column model (SCM) intercomparison of radiation fog, *Atmos. Chem. Phys.*, 22, 319-333, doi: 10.5194/acp-22-319-2022, 2022.

- Schwenkel, J. and Maronga, B.: Towards a better representation of fog microphysics in large-eddy simulations based on an embedded Lagrangian cloud model, *Atmosphere*, 11 (5), 466, doi: 10.3390/atmos11050466, 2020.
- Kral, S. T., Reuder, J., Vihma, T., Suomi, I., Haualand, K. F., Urbancic, G. H., Greene, B. R., Steeneveld, G., Lorenz, T., Maronga, B., Jonassen, M. O., Ajosenpää, H., Báserud, L., Chilson, P. B., Holtslag, A. A. M., Jenkins, A. D., Kouznetsov, R., Mayer, S., Pillar-Little, E. A., Rautenberg, A., Schwenkel, J., Seidl, A. W., and Wrenger, B.: The Innovative Strategies for Observations in the Arctic Atmospheric Boundary Layer Project (ISOBAR) - Unique fine-scale observations under stable and very stable conditions, *Bull. Am. Meteor. Soc.*, 102(2), 218-243, doi: 10.1175/BAMS-D-19-0212.1, 2020.
- Maronga, B., Banzhaf, S., Burmeister, C., Esch, T., Forkel, R., Fröhlich, D., Fuka, V., Gehrke, K. F., Geletič, J., Giersch, S., Gronemeier, T., Groß, G., Heldens, W., Hellsten, A., Hoffmann, F., Inagaki, A., Kadasch, E., Kanani-Sühring, F., Ketelsen, K., Khan, B. A., Knigge, C., Knoop, H., Krč, P., Kurppa, M., Maamari, H., Matzarakis, A., Mauder, M., Pallasch, M., Pavlik, D., Pfafferoth, J., Resler, J., Rissmann, S., Russo, E., Salim, M., Schrempf, M., Schwenkel, J., Seckmeyer, G., Schubert, S., Sühring, M., von Tils, R., Vollmer, L., Ward, S., Witha, B., Wurps, H., Zeidler, J., and Raasch, S.: Overview of the PALM Model System 6.0, *Geosci. Model Dev.*, 13, 1335–1372, doi: 10.5194/gmd-13-1335-2020, 2020.
- Schwenkel, J., and Maronga, B.: Large-eddy simulation of radiation fog with comprehensive two-moment bulk microphysics: Impact of different aerosol activation and condensation parameterizations, *Atmos. Chem. Phys.*, 19, 7165-7181, doi: 10.5194/acp-19-7165-2019, 2019.
- Schwenkel, J., Hoffmann, F., and Raasch, S.: Improving collisional growth in Lagrangian cloud models: development and verification of a new splitting algorithm, *Geosci. Model Dev.*, 11, 3929-3944, doi: 10.5194/gmd-11-3929-2018, 2018.

## Conference Contributions

- Schwenkel, J., and Maronga, B.: Demystifying fog microphysics: A high-resolution Large-Eddy Simulation study with coupled particle based microphysics, oral presentation, EMS Annual Meeting, 9-13 September 2019, DTU Lyngby, Denmark, 2019.
- Veith, S., and Schwenkel, J.: Climate Future Day 2020 at Leibniz Universität Hannover: concept and framework, EMS Annual Meeting 2019, 9-13 September 2019, DTU Lyngby, Denmark, oral presentation, 2019.
- Schwenkel, J., and Maronga, B.: Demystifying fog microphysics: A high-resolution Large-Eddy Simulation study with coupled particle based microphysics, poster presentation, Workshop on Eulerian vs. Lagrangian methods for cloud microphysics, 15-17 April 2019, Cracow, Poland, 2019.

Schwenkel, J., and Maronga, B.: Untersuchungen von Aerosolaktivierung in Strahlungsnebel mit einem Lagrangschen Wolkenphysik Modell, oral presentation, DACH 2019, 18-22 March 2019, Garmisch-Patenkirchen, Germany, 2019.

Schwenkel, J.: Wolken - und ihre Mikrophysik: Ein Versuch der Entmystifizierung durch numerische Modelle, oral presentation, Stumeta, 25 May - 2 June 2019, Hannover, Germany, 2019.

Schwenkel, J., and Maronga, B.: Investigating the Development of Fog Droplet Size Distributions and Aerosol Activation in Radiation Fogs Simulated By a Lagrangian Cloud Model, poster presentation, 15th AMS Conference on Cloud Physics, 9-13 July, Vancouver, BC, Canada, 2018.

Maronga, B., Schwenkel, J., and Bosveld, F. C.: Key Parameters for the Life Cycle of Nocturnal Radiation Fog: Results from a Comprehensive Large-Eddy Simulation Study, 23rd Symposium on Boundary Layers and Turbulence/21st Conference on Air-Sea Interaction, poster presentation, 11-15 June 2018, Oklahoma City, OK, USA, 2018.

## **Theses**

Schwenkel, J.: Entwicklung, Implementierung und Validierung eines Algorithmus für das Spalten und Zusammenfassen von Partikeln im einem Lagrangschen-Wolkenphysik-Modell, Master thesis, Leibniz Universität Hannover, Hannover, Germany, 2016.

Schwenkel, J.: Vereisungswarnung mit ADWICE in den bodennahen Modellschichten, Bachelor thesis, Leibniz Universität Hannover, Hannover, Germany, 2013.